Measurement of OID During Blowdown Transients

MEASUREMENT AND PREDICTION OF THE ONSET OF INTERMITTENT DRYOUT DURING BLOWDOWN TRANSIENTS FOR UPWARD ANNULAR FLOW

by

B.A. Statham,

A Thesis

Submitted to the School of Graduate Studies

in Partial Fulfilment of the Requirements for the Degree

Doctor of Philosophy in Engineering Physics

McMaster University

DOCTOR OF PHILOSOPHY (2014)   MCMASTER UNIVERSITY

(Engineering Physics)   Hamilton, Ontario, Canada

Title: Measurement and Prediction of the Onset of Intermittent Dryout
     During Blowdown Transients For Upward Annular Flow

Author: Bradley Allan Statham, B. Eng. & Scty., M. A. Sc. (McMaster University)

Supervisor: Dr. D.R. Novog

Number of Pages: xxiv, 166

Abstract

The effect of pressure transients on the onset of intermittent dryout in upward annular flow was experimentally investigated in order to resolve the conflict between the observations drawn from two major data sets in the literature. A delay in time to the onset of dryout at the test section exit relative to the time predicted based on steady-state data was observed in the R-12 experiments of Celata *et al* [1, 2]. Steady-state prediction methods were sufficient to predict the upstream progression of a pre-existing dryout front in the water experiments of Lyons and Swinnerton [3].

Steady state and pressure transient dryout experiments were performed using water with outlet pressures of 2–6 MPa and mass fluxes of 1000–2500 kg m^{-2} s^{-1} in an electrically heated 1.32 m long 4.6 mm ID vertical Inconel 600 tube with depressurisation rates of up to 1.0 MPa s^{-1}. Transient experiments were performed with a small margin to dryout and with post-dryout initial conditions in order to test the hypothesis that these initial conditions influenced the onset of dryout during transients.

The results of a comparison between the steady dryout data and two dryout prediction methods—the Biasi *et al* correlation [4] and the 2006 CHF look-up table [5]—were used to develop correction factor correlations to reduce systematic error when these methods were used to predict the transient time to dryout. The transient prediction performance of these two methods for all of the transient data is summarized in the table below. There was no statistically significant variation between the pre- and post-dryout initial conditions. Based on this result it was concluded that the initial conditions did not affect the observed time to dryout.

The mean wall temperature exhibited a discontinuous *decrease* as the heat flux

Method	Mean Error	Standard Deviation	Prediction Uncertainty
LUT*	-1.5 s	3.0 s	±4.2 s
Biasi*	-0.1 s	2.8 s	±1.5 s

approached 92–95% of the dryout value. It was postulated that this was caused by a heat transfer regime change from liquid film evaporation to droplet evaporation based on the observations of Hewitt [6], Doroschuk *et al* [7] and Groeneveld [8]. For the range of conditions of the present work the onset of intermittent dryout [9] was caused by deterioration of droplet evaporation heat transfer.

Celata *et al* [1] noted that in their pressure transient experiments the decrease in saturation temperature drove a rapid increase in the heat flux to the fluid. This was caused by the release of stored thermal energy as the test section wall cooled. Celata *et al* [2] stated that the systematic dryout delay was observed for depressurisation rates greater than 0.2 MPa s^{-1}. By applying this criteria to Celata *et al*'s pressure transient data [1] it was concluded that the stored thermal energy transient does not influence the onset of intermittent dryout when $\rho_w c_{pw} L_w \frac{dT_{sat}}{dt} < 0.3 \cdot \ddot{q}_a$. This criteria clearly separated the R-12 data of Celata *et al* [1] from the water data of Lyons and Swinnerton [3] and the present work.

Acknowledgements

I would like to sincerely thank my supervisor, Dr. D. R. Novog, for his technical advice and support over the last six and a half years that I have been his student. My supervisory committee, Dr. J. S. Cotton, Dr. R. L. Judd and Dr. A. Robinson, asked great questions that helped guide me through this research. I am grateful to all of them for being helpful, flexible and understanding that we are all only human.

Thanks to all of the other graduate students in Engineering Physics, especially Ken, Kurt, Hummel, James and Matt in the Nuclear Engineering groups, for sharing equipment and tools, answering questions and bouncing ideas around.

Much of what I have learned in graduate school had nothing whatsoever to do with the contents of this thesis. I have made some amazing friends during my time at McMaster and I am in eternal debt to all of you for your love and support. Dave, Laura, Rene, Janice, Derek, Sara, Alex, Scott, Robbie, Deb, Brian—thanks. I owe a profound debt of gratitude to Brent and Laura; you guys have been patient and supportive and I've learned a lot from both of you through our meals, conversations and adventures together.

My Mom and Dad have always been proud and supportive of my sister, Laurel, and I. Thank you for always being there for me despite the long times between visits home.

Last but certainly not least, Steph: you inspire me to be a better person, to dream and to love. Or, if you prefer, maybe the Weakerthans said it better: "I know/you might roll your eyes at this/but I'm so/glad that you exist."

Contents

List of Figures

List of Tables

List of Symbols and Abbreviations

Symbols

Bo	Boiling Number
c_p	Specific heat capacity
C_i	Constant
C	Vapour core droplet concentration
d	Diameter
d_{hyd}	Hydraulic diameter
D	Deposition rate
E	Entrainment rate
E	Expectation value
L_h	Heated length
L_B	Boiling length
G	Mass flux
h	Heat transfer coefficient
h	Enthalpy
k	Thermal conductivity
$\dot{m}$	Mass flow rate
z	Axial length
p	Pressure
$\ddot{q}$	Heat flux
$\ddot{q}_a$	Applied heat flux due to electrical power

$\ddot{q}_{st}$	Additional heat flux at the heater surface due to the release of stored thermal energy
S_{mc}	Mean core slip ratio
T	Temperature
t	Time
u	Fluid velocity
x	Thermodynamic quality
x_i	Dummy independent variable
y	Dummy dependent variable
W_f	Liquid supply rate to the liquid sublayer in the model of Pasamehmetoglu *et al*

Greek letters

Γ	Thermal energy storage number
Δ	Adjustment of or change in a value
δ	Prediction method error
ϵ	Critical value used to linearise test section boundary conditions for RELAP5 input
η	Correction factor
μ	Dynamic viscosity
ξ	Dummy variable
ρ	Density
σ	Standard deviation
σ	Surface tension
τ_c	Shear stress at the vapour-liquid interface in annular flow
ϕ_ϵ	Fraction of RMS fluctuations from the moving average of a boundary condition measurement used to calculate ϵ

Subscripts

L	Liquid saturation property
V	Vapour saturation property
$crit$	Critical value
CHF	Value at the critical heat flux
CHF-SS	Value at the steady-state critical heat flux
BLA	Boiling length average value
DO	Value at dryout
EXP	Experimental value
DSM	Value based on the CHF calculated using the DSM
HBM	Value based on the CHF calculated using the HBM
w	Value at the heated wall or referring to physical properties of the test section wall material
∞	Value in the ambient away from any source or sink
OAF	Value at the position of the onset of annular flow
PRED	Predicted value
sat	Referring to the value at saturation for a given pressure or temperature
lf	Value referring to a quantity in the liquid film
LFC	Value referring to the critical liquid film value
$lfeq$	Value referring to a quantity in the liquid film in thermal and/or mechanical equilibrium
E	Value at mechanical equilibrium
u	Referring to a value related to 'upstream' conditions
t-max	The maximum value of a time-dependent quantity
0	Initial or steady-state value

Abbreviations

BLA	Boiling length average. The spatial average over the fraction of a channel undergoing boiling.
CHF	Critical heat flux. Heat flux beyond which the heat transfer rate begins to deteriorate rapidly.

DNB	Departure from nucleate boiling. CHF mechanism for heated surfaces undergoing nucleate boiling.
DSM	Direct substitution method. Method to evaluate CHF prediction methods. Equivalent to comparing observed CHF and prediction method at constant quality.
EHL	End of heated length
FS	Full scale
HBM	Heat balance method. Method to evaluate CHF prediction methods. Equivalent to comparing observed CHF and prediction method with constant boundary conditions.
HEM	Homogeneous equilibrium model. A simplification used in two-phase flow models that assumes the liquid and vapour phases are in thermodynamic equilibrium and travel as a homogeneous mixture through the channel.
LUT	Look-up table. Specifically the 2006 CHF look-up table [5]
MTD	Referring to experiments that were conducted with a margin to dryout at the initial conditions
OID	Onset of intermittent dryout. Defined by Groeneveld [9] and associated with a gradual deterioration of heat transfer.
PDO	Post-dryout. Refers to both post-dryout heat transfer and experiments conducted with initial conditions beyond the onset of intermittent dryout
PDT	Predicted during transient. This refers to experimental dryout data where dryout was predicted to occur by a CHF correlation during the transient itself rather than before the transient started or not at all. Only PDT data were included in the final analysis of the transient data.
RMS	Root mean square
SD	Standard deviation
URL	Upper range limit
VFD	Variable frequency pump drive

Declaration of Academic Achievement

The academic contribution of the work within this thesis was conducted by the author with assistance from others.

The experiment described in Chapter 3 was reconstructed by the author from the experimental apparatus described in the author's Master's thesis [10] that was originally based on a design sketch and component specification by S. T. Yin. Substantial modifications including a new pump, flow meter, condenser, differential pressure gauge, power measurement instrumentation, secondary cooling loop, blowdown valve, data acquisition system, control system, preheater power supply, and instrumentation and control software were designed and/or added since 2009 in order to conduct the present work.

The 2-D conduction model used in the present work was originally implemented in `FiPy` [11] by K. Boniface as part of an undergraduate summer research project under the author's supervision. The geometry and boundary conditions were modified by the author in order to model the effects of the bus bars and of post-dryout heat transfer that are presented in this dissertation.

The author's supervisor, Dr. D. R. Novog, suggested the author include several papers on transient heat transfer that are described in the literature review and provided valuable feedback and editing input on this dissertation. The author's supervisory committee members, Dr. J. S. Cotton, Dr. R. L. Judd, and Dr. A. Robinson also provided editorial and technical feedback on the first completed version of this document. Dr. A. Robinson suggested the idea of using the standard deviation as a quantitative dryout criteria based on the paper by Del Col and Bortolin [12].

The design and construction of the experimental apparatus and the execution, analysis and synthesis of the results of the experiments was performed entirely by the author.

Chapter 1

Background and Motivation

1.1   Introduction and Overview

The subject of this thesis is the measurement and prediction of heat transfer deterioration in a channel undergoing forced flow boiling in the annular flow regime during depressurisation. This heat transfer deterioration is associated with the partial or complete dryout of the heated surface. The present work provides new insight into the effect of transient thermalhydraulic conditions on the cooling of fuel during postulated nuclear reactor accidents. As part of this work a new high pressure heat transfer test facility was constructed that was capable of transient and steady state heat transfer and dryout measurement.

This facility was used to conduct pressure transient experiments in order to observe the time at which dryout occurred at the exit of the test section and as the dryout front moved upstream. The test section was a 1.321 m long uniformly heated vertical 4.6 mm ID Inconel 600 tube. Experiments were conducted at initial conditions slightly beyond dryout at the exit of the test section and with a small margin to dryout. The purpose of the experiments was to determine whether or not these initial conditions had an influence on the apparent contradictions in the conclusions drawn from two databases of pressure transient dryout data from the literature. Celata *et al* [1] observed a delay in the onset of dryout for their experiments with a margin to dryout. In contrast Lyons and Swinnerton [3] concluded that the quasi-steady method was sufficiently accurate to predict the progression of a dryout

front moving upstream in a uniformly heated tube when there was a pre-existing dryout condition at the outlet before the initiation of the transient.

This chapter gives some background information on the relevance of transient dryout prediction. Specific reference is made to safety analysis in nuclear power reactors. Then, a review of the existing literature on transient heat transfer and dryout is presented. The review establishes the author's hypothesis that the initial conditions for transient dryout experiments played a role in the differing conclusions drawn by Celata *et al* [1] and of Lyons and Swinnerton [3]. This is followed by a chapter that gives details about the experimental apparatus. Steady state dryout data is presented in Chapter 4. The steady dryout data was used to modify two existing dryout prediction methods to better fit data from this facility. This was necessary to reduce bias when the transient data was analysed. Chapter 5 presents transient data and the results of the data reduction. The data reduction compares the distribution of the observed dryout time relative to the dryout time predicted using the quasi-steady method. Finally a discussion of some relevant phenomena and a comparison of the present work with the work of Lyons and Swinnerton and of Celata *et al* is presented in Chapter 6. Conclusions and recommendations for future work are presented in Chapter 7.

1.2   Nuclear Reactors, Safety, and Regulation

The quality of life for the majority of human beings on Earth has been significantly improved over the last few centuries partly due to the availability of abundant and affordable energy. The unintended consequence of this prosperity has been the pollution of Earth's land, water, and air including the emission of heat-trapping gases like carbon dioxide that is believed to be a primary driving force behind anthropogenic climate change. Electricity is one form of energy among several that has transformed the way people live and work but its generation is also the single largest source of global carbon dioxide emissions [13]. The vast majority of these emissions come from fossil-fuel fired power plants. Reducing the carbon intensity of the electricity sector will allow more people to benefit from it while simultaneously reducing its potential negative effects on Earth's climate [14]. Many low-carbon alter-

natives to fossil fuels exist but only two are proven, reliable, and price-competitive at current market electricity prices: hydro-electric dams and nuclear power reactors.

Nuclear energy provided approximately 12% of global electricity from 437 operating reactors with an installed capapcity of 394 GW at the end of 2012. The International Energy Agency expects installed nuclear generating capacity to grow to 578 GW by 2035 [15]. This estimate includes the fact that some countries have passed legislation to phase out the use of nuclear power in their energy supply due to safety concerns raised in the wake of the recent nuclear accident at Fukushima in Japan. Nuclear energy provided 56.4% of Ontario's electricity supply in 2012 from 14 operating reactors [16]. Nuclear fission is a significant contributor to global electricity supply and its role will become more important as governments move to decarbonise their energy supplies while simultaneously keeping up with growing demand.

At the most basic level a nuclear reactor produces heat that is used to create steam that spins a turbine and drives a generator to produce electricity. The heat is released in the fuel where the nuclei of fissile atoms are split. The fuel atoms may also absorb neutrons and transmute into different heavy isotopes. The atoms that are left after the fission reaction takes place are radioactive. The public safety risk associated with an operating nuclear reactor is largely based on the ability of the reactor system to keep the public from being exposed to these fission products and other heavy elements.

In order to minimise safety risks while maximising the benefits to the public most countries that take advantage of nuclear power generation have developed robust regulatory regimes that reactor operators must comply with in order to retain their operating licence. In Canada the Canadian Nuclear Safety Commssion (CNSC)—formerly the Atomic Energy Control Board (AECB)—oversees compliance with the operating licences of nuclear power reactors and other nuclear installations in accordance with the Nuclear Safety and Control Act [17].

Regulations have evolved along with the safety analysis techniques used to assess the consequences of postulated accidents. Early regulations were prescriptive but also incorporated risk as safety limits and reflected the conservative assumptions used when modelling the behaviour of a reactor under abnormal or accident

conditions. These prescriptive regulations were largely based on experience from accidents and operating experience from research reactors. These early experiences led the designers of the early generations of CANDU reactors to implement diversity and separation of important reactor systems that were intended to reduce risk due to common cause failure [18]. Accumulated operating experience and exponential increases in computing power gradually allowed more realistic and detailed probability-based analyses to be performed [19]. The current licensing environment, under CNSC RD-337 [20], is based on quantitative estimates of the risk of specific radioactive releases and risk estimates for several classes of postulated anomalous behaviour.

1.2.1 Postulated Reactor Accidents

A large portion of the analysis required for reactor licensing is related to the prediction of consequences that result from the behaviour of the reactor during postulated accidents. The computer codes used to simulate these conditions must be verified and validated to meet CNSC guidelines [21]. The goal of these analyses is to demonstrate that a given reactor design will withstand these events with an acceptable outcome. These outcomes include but are not limited to the prevention of environmental contamination and risks to public health.

Specific details for each hypothetical accident vary with the reactor type and regulatory framework but several classes are common to all water-cooled reactors: loss of forced flow accidents (LOFAs), loss of power regulation (LORs), loss of heat sink, or loss of coolant accidents (LOCAs). LOCAs are particularly important because they are a result of the reactor pressure boundary being compromised. Depending on the type of reactor and how they occur LOCAs can negatively affect the ability of reactor operators to maintain long term fuel cooling. Preventing and mitigating the consequences of these main types of reactor accidents are a fundamental component of nuclear power reactor design.

The tools and methodologies used to assess these conditions rely heavily on empirical information derived from experiments. These experiments and consequently the resulting empirical correlations are largely conducted with steady or near-steady

state conditions. As indicated above this thesis examines the acceptability of using this steady-state data to predict heat transfer deterioration under specific transient conditions.

1.2.2 Fuel Cooling in Nuclear Reactors

Defence in depth is one important concept that is used to help power plant designers prevent the release of radioactive material. It is based on the idea that by using multiple, overlapping barriers to the release of radioactive material the possibility of public radiation exposure due to the failure of a single barrier will be significantly reduced [22]. These barriers include the fuel sheath that prevents radioactive fission products and heavy isotopes from entering the coolant and being transported throughout the plant and the pressure boundary of the heat transport system itself.
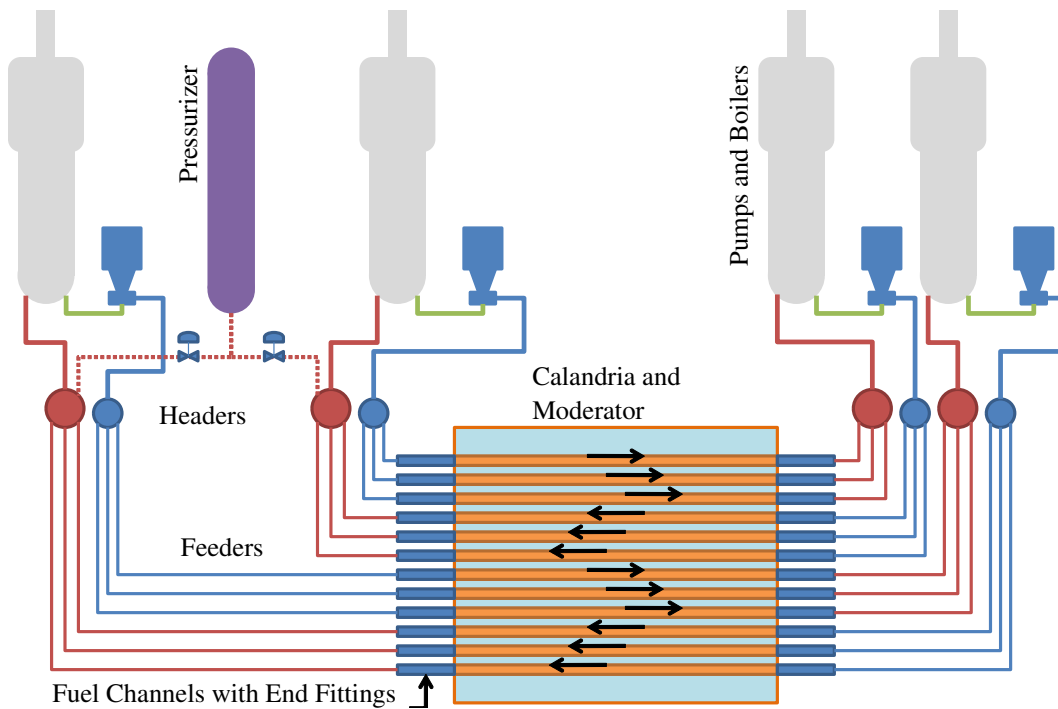
Figure 1.1: Schematic representation of the primary heat transport system in a CANDU®nuclear power reactor. Arrows in fuel channels denote direction of flow.

The present work focusses on the ability to predict when the fuel sheath may be compromised due to heat transfer deterioration in a postulated accident. The

work is specifically concerned with transient conditions that result from a breach
of the primary heat transport system pressure boundary. A schematic diagram of
the primary heat transport system of a CANDU pressurized heavy water reactor is
shown in Figure 1.1. The flow path for 12 channels in two figure-of-eight loops
is shown in the diagram. CANDU reactors typically have between 360 and 480
individual fuel channels. A centrifugal pump drives liquid water into an inlet header
where it is distributed to the inlets of one-quarter of the reactor's fuel channels. The
thermal energy released by the fission chain reaction in the reactor core heats the
water as it flows through the channel. The heated water from each channel in each
pass through the core is mixed in an outlet header before the heat from the reactor
is transferred through the walls of U-tubes in the steam generator. In the steam
generator saturated water at a lower pressure than the primary heat transport system
evaporates to make steam and drive the power plant turbune.

Inside the fuel channel heat is transferred from the fuel by conduction through
the solid fuel, the gap between the fuel pellet and the sheath, and the sheath to
the sheath's surface. From the sheath's surface the cooling water removes heat by
forced convection. The nuclear reaction is strongest in the centre of the reactor core
so the heat removed per unit surface area of the fuel—the heat flux—is highest at
the centre of each fuel channel and lowest at the ends. When the coolant first enters
the channel it is relatively cool—below the saturation temperature at the operating
pressure of the reactor—and the heat flux is low compared to its value near the
axial centre of each channel. Under normal circumstances the coolant leaves a
CANDU reactor as near-saturated liquid or a low-quality saturated mixture. In
many postulated accidents, however, additional boiling may occur due to reduced
flow rate, reduced pressure, or increased reactor power.

As the coolant is heated in the channel it may begin to boil and generate vapour.
Descriptions of the two-phase topology based on the configuration of liquid and
vapour are called flow regimes. Some relevant regimes for vertical two-phase flows
are illustrated in Figure 1.2. At the initial stages of boiling bubbles are generated
by nucleation at the heated surface and may collapse and condense in the bulk flow
which may be below the saturation temperature. As the bulk fluid heats up and
the heat flux increases the point of net vapour generation may be reached [23].
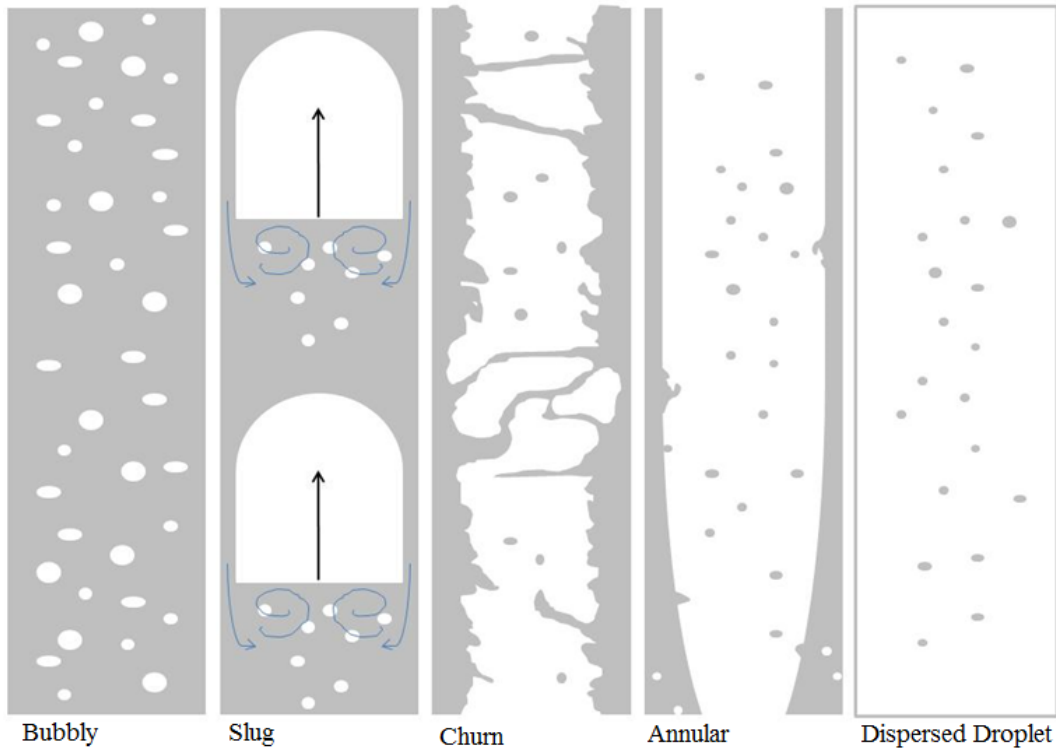
Figure 1.2: Flow regimes that have been observed in vertical upward forced flow.

When enough small vapour bubbles are present they can agglomerate into larger slug bubbles that flow periodically. As these vapour slugs grow they may begin to further agglomerate and form the churn flow regime. When enough vapour exists—10–20% of the total mass flow—the annular flow regime is formed where liquid flows as a film along surfaces and vapour flows through the centre or core of the channel with entrained droplets.

If, under abnormal or accident conditions, enough heat is added through the walls of the channel to cause the annular film to completely evaporate the dispersed droplet flow regime may occur. The transition from annular to dispersed droplet flow coincides with the termination of the continuous liquid film flow on heated surfaces in the channel. A partial annular flow may remain from the flow of liquid film on unheated surfaces. Depending on the heat flux the deposition of the remaining liquid as droplets from the vapour core may or may not be able to continue cooling the fuel. When the droplets are no longer able to continuously wet the

surface it begins to intermittently dryout and the heat transfer will begin to deteriorate [9]. This has important ramifications for fuel cooling and therefore the overall safety of nuclear power reactors.

1.2.3   Critical Heat Flux

In nuclear reactors a primary public safety priority is to keep fuel cool. Satisfying this criteria substantially reduces the risk of a release of radioactive material because it ensures the physical boundaries, including the fuel sheath, fuel channels (in a pressure tube reactor), and reactor vessel, remain intact. Therefore the limitations to fuel cooling are of great interest and importance to nuclear power plant designers, operators, safety analysts, and regulators.

One of the primary limits to heat transfer and fuel cooling in a nuclear reactor during the progression of an accident or abnormal operating occurence is generically called the critical heat flux (CHF). The CHF is the rate of heat transfer per unit surface area where a deterioration in the convective heat transfer coefficient is observed. The prevention of CHF is specifically cited in CNSC regulatory guide G-144 [24] as a permissible acceptance criteria for the primary reactor trip mechanism. The heat transfer coefficient is defined in Equation 1.1 where h is the heat transfer coefficient, $\ddot{q}$ is the thermal power per unit area of the heater—*i.e.* fuel—surface, T_{surf} is the surface temperature of the heater, and T_{∞} is the coolant temperature; this expression is commonly referred to as 'Newton's law of cooling'.

$$\ddot{q} = h(T_{surf} - T_{\infty}) \tag{1.1}$$

In a heat-flux controlled system the heat throughput is an independent variable. The coolant temperature, T_{∞}, is nominally constrained to the local liquid or saturation temperature. With these constraints it is evident that if h decreases the only remaining independent variable, T_{surf}, must increase in order to satisfy Equation 1.1. This is undesirable in a nuclear reactor where maintaining fuel cooling is paramount.

A great deal of work that is available in the literature has been done to obtain experimental CHF data over a wide range of operating conditions, fluids and geometries. These experimental data have been analysed to identify and model the

underlying physical phenomena and to correlate and compile the data so that it may be used to predict the CHF over a similarly wide range of relevant conditions. Several general features have been identified in the literature. CHF may nominally be parametrically represented as a function of pressure, *i.e.* the fluid properties, mass flux, quality, and diameter, *i.e.* geometry, as shown in Equation 1.2 [25].

$$\ddot{q}_{CHF} = f(p, G, x, D) \tag{1.2}$$

Each of the terms in Equation 1.2 contain many layers of complexity: in a nuclear fuel bundle any or all of them may vary with axial, radial and azimuthal position in the channel. At a given position in a heated channel each of these terms ultimately depends on the upstream history of the flow. In a uniformly heated channel the heated length, CHF, and quality are related and the CHF condition will be met at the exit of the channel where the steam quality is highest and thus corresponds to the lowest CHF. For a given geometry, therefore, it is possible to eliminate one or more of these variables from a model or correlation. There is also evidence that suggests that the CHF may be influenced by the heated length, boiling length, or annular flow length in the channel [25, 26, 27, 28].

CHF correlations may fall into two broad categories: those based on the local conditions hypothesis and those that include upstream history effects. The local conditions hypothesis postulates that the CHF at any point in a channel is dependent only on the conditions at that point in the channel and independent of 'how' those conditions arose. History-based methods, such as the boiling length average approach, tend to include integral information over part or all of the channel.

CHF may also be divided into two broad phenomenological categories: the departure from nucleate boiling (DNB) and the liquid film dryout. These are depicted in Figure 1.3. DNB is associated with subcooled coolant conditions or saturated conditions where nucleate boiling is the dominant heat transfer mechanism. At the point where DNB occurs the heat transfer mechanism switches from nucleate boiling to transition or film boiling. The heat transfer deterioration associated with DNB is dramatic and may result in near-immediate failure of the heater under test.

Two possible underlying DNB mechanisms are denoted in Figure 1.3. In the
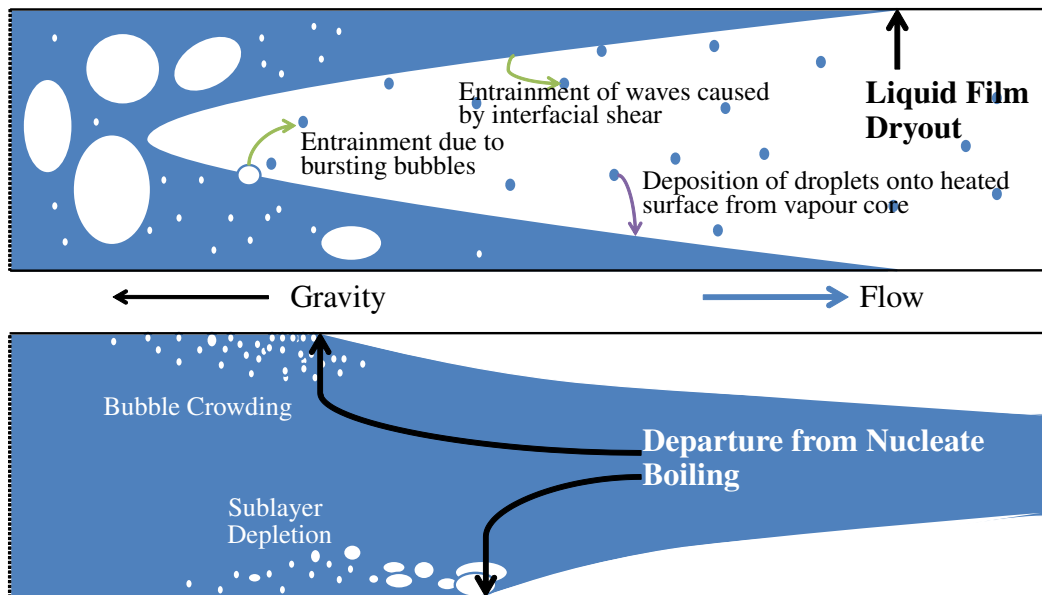
Figure 1.3: Schematic representation of DNB and liquid film dryout CHF mechanisms.

sublayer instability model [29, 30] a thin liquid layer separates the heated surface from a near-wall vapour layer. The critical heat flux is predicted to occur when the sublayer-vapour interface becomes unstable and the vapour blanket causes a dry patch on the heater surface. The bubble crowding hypothesis [31] is based on the observed phenomena of bubbles being generated at the heater surface before detaching and flowing down the channel. Since the bulk fluid is subcooled the vapour is concentrated near the wall: bubbles that enter the liquid core of the flow will condense. As bubbles accumulate near the surface they prevent liquid from the core of the channel from reaching the surface which then becomes liquid deficient and leads to DNB.

Dryout may also specifically refer to the depletion of the liquid film that flows along the surface of the heater in annular flow. This CHF mechanism occurs under saturated conditions with relatively high steam quality. It is usually associated with a smaller discontinuous change in the heat transfer coefficient or even a gradual transition to post-dryout heat transfer behaviour. Groeneveld [9] called the gradual deterioration of the heat transfer coefficient the 'onset of intermittent dryout' or OID and suddenly- or fully-depleted heat transfer the 'onset of dry sheath' or ODS

when liquid contact with the wall ceased altogether.

In an annular flow liquid flows as both a liquid film and as entrained droplets. The liquid film is depleted mainly by two processes: the entrainment of droplets into the vapour core due to the interfacial shear stress between the two phases and by the evaporation of the liquid due to the applied heat flux. The liquid film is simultaneously replenished by droplets deposited onto the film from the vapour core. Dryout is predicted to occur when the flow rate of the liquid film is zero. This is calculated by integrating a mass balance equation over the length of the test section where annular flow occurs.

A comprehensive correlation must be able to predict both types of CHF: often this results in using two or more equations, as in the Biasi *et al* correlation [4], or comparing and combining the results of different expressions, as in the Katto-Ohno correlation [32], in order to be comprehensive and accurate. As a result the look-up tables for CHF in 8 mm tubes for vertical upward flow of water by Groeneveld *et al* are widely used [33, 34, 5]. The look-up table has the advantage of being comprehensive, accurate and easy to use.

1.2.4   CHF in Nuclear Safety Analysis

Most of the existing CHF data has been collected using steady-state experiments. These steady-state experiments form the basis of the understanding of underlying CHF phenomena used for modelling, correlation development and as the foundation for the CHF look-up tables. In nuclear safety analysis and other relevant applications of CHF prediction, however, the CHF will not be reached under steady state conditions. Instead it will occur under abnormal or accident conditions where the input power, channel pressure or mass flow rate change rapidly with time. The behaviour of the CHF under transient conditions is the focus of this dissertation.

Codes like RELAP5, TRACE, and CATHENA are based on one-dimensional finite volume methods to simultaneously solve the time-dependent mass, energy, and momentum transport equations for both liquid and vapour. These codes are used to predict the local conditions in the reactor during accidents. CHF is predicted by using these transient conditions as input to the steady-state based methods. This

is referred to as the quasi-steady method.

1.3 Basis of the Present Work

1.3.1 Transient Heat Transfer

The quasi-steady method may also be used to predict heat transfer in the same way that it is used to predict dryout: by using transient local conditions and fluid properties as input to a correlation that is based on steady-state data. There is evidence in the literature, however, that single phase and nucleate boiling heat transfer does not behave in a quasi-steady manner under transient conditions. Several studies [35, 36] from the literature have found that the response of convective heat transfer is delayed with respect to the prediction of heat transfer based on local instantaneous values of fluid properties and mass flow. Furthermore pool boiling curves have been observed to exhibit surface temperature overshoot under conditions of exponentially increasing power input [37]. These examples and others will be presented in more detail in Chapter 2.

These studies demonstrate that some heat transfer mechanisms experience lag during transients: the underlying phenomena do not behave in a quasi-static manner. In multiphase flow additional layers of complexity are added on top of the two examples cited above: additional liquid may be supplied to a nucleate boiling surface by radial turbulent flow fluctuations [38] and a continuous liquid-vapour interface exists in annular flow through which energy from the heated surface is exchanged with the vapour and droplets in the core. It is possible that the phenomena that govern the locus of dryout, since they are fundamentally related to the underlying heat transfer phenomena, may experience a similar non-quasi-steady behaviour under transient boundary conditions. Therefore the investigation of transient effects is not unique to the locus of dryout but is a common pursuit in all aspects of convective heat transfer.

1.3.2   Objectives and Benefits of the Present Work

The present work aims to answer two questions. How well does the quasi-steady method predict the onset of intermittent dryout under transient conditions? Secondly, what physical phenomena may be responsible for any discrepancy in the predicted conditions compared to conditions observed from experimental data? The research presented in this thesis focusses specifically on the onset of intermittent dryout in annular flow during pressure transients. Two major pressure transient dryout experimental data sets were available prior to the present work. The conclusions of the authors of the two major existing datasets, however, seem to disagree: Whalley, Lyons and Swinnerton's [39] results suggest that steady-state prediction methods are sufficient to predict the progression of a dryout front up a uniformly heated tube. Celata *et al* [1]show that transient effects are important in delaying the onset of dryout. These two major works and other relevant literature are are summarised in Chapter 2.

A new experimental apparatus was designed and used to perform experiments to resolve these issues. The relevant details of the experimental apparatus, instrumentation and measurement uncertainties, and the experimental procedure are presented in Chapter 3. Experiments were conducted at pressures of 2–6 MPa, mass fluxes from 1000–2500 kg m^{-2} s^{-1}, and inlet flow quality of -0.148 in a 1.321 m vertical, uniformly heated 4.6 mm inside diameter tube. The results obtained for steady-state heat transfer, steady-state pressure drop, steady-state dryout and outlet depressurisation experiments are presented.

The experiments were performed to test what underlying physical phenomena were responsible for the difference, if any, between the observed and predicted time that dryout occurs. The predicted times were based on the CHF values calculated using methods derived from steady state data. In an annular two-phase flow of a single-component pure fluid the liquid flows both as a film along the channel boundaries and as droplets entrained in the vapour at the centre or core of the channel. It is widely believed that the heat transfer transition associated with the critical heat flux occurs when a dry patch develops on the surface of the heater due to liquid film depletion.

In this thesis it will be argued, based on the evidence in the literature and the

data that has been collected, that *for the conditions under investigation* any surface wetting before the onset of dryout is maintained solely due to the deposition of droplets onto the heated surface as described by Hewitt [6]. This is in constrast to dryout caused by the depletion of a continuous liquid film. Any delay observed in the critical heat flux was therefore due primarily to the thermal and mechanical disequilibrium of entrained droplets. Transport delays in the liquid film itself were of secondary importance.

Improving the understanding of CHF during transient conditions will make an important contribution to the nuclear industry in several ways. The uncertainty associated with CHF prediction during transients will be reduced or better understood. An immediate benefit will be improved safety margins for existing reactors without any changes to reactor operating procedures or conditions. Secondly, this may allow more realistic accident models to be created that, combined with reduced uncertainty, may allow reactor safety margins to be more precisely quantified. Most importantly, however, this work will help to resolve the discrepancy in the literature.

1.3.3 Summary

CHF refers to the point in a boiling system where a small change in local or system boundary conditions—pressure, mass flow rate, heat flux, inlet temperature— results in a marked decrease in the rate of heat transfer. It is usually associated with the termination of contact of the liquid phase with the heated surface. In a heat flux controlled system this results in a substantial rise in the heater surface temperature. Depending on the post-dryout condtions this could lead to damage, *e.g.* melting, or thermal stress if the heat input is not decreased quickly. CHF prediction is therefore an important safety and economic criteria for the design and operation of many industrial process systems. Collier and Thome [25] provide a summary of major results and prediction methods.

The CHF is particularly important in the licensing of nuclear power plants. For example, the Canadian Nuclear Safety Commission regulatory guide G-144 [24] for CANDU nuclear power plants suggests that primary and and secondary reactor trip parameters should be accepted if: the first parameter is chosen so that the onset

of intermittent dryout is not reached, and the second parameter chosen so that a fuel sheath will operate in post-dryout conditions for no longer than 60 s and reach a temperature no greater than 600°C.

Most dryout prediction methods are based on data collected under steady-state conditions. In nuclear power plants the CHF may only be reached under abnormal operating conditions such as a loss of forced flow, an uncontrolled power increase, or a breach in a pressure boundary resulting in a system depressurisation. The study of dryout phenomena during these transient situations has been more limited than under steady-state condtions and the existing database of pressure transient data is largely composed of two investigations with contradictory conclusions. An improvement in the understanding of depressurisation transient CHF will help determine the degree—or lack—of conservatism that is present in predictions of system transients based on steady-state CHF prediction methods.

The work presented in this thesis aims to aid the understanding of the uncertainty in predicting CHF during pressure transients by resolving the inconsistencies in the existing literature. Experimental results will be presented that fill these gaps and clarify discrepancies between different authors' work.

Existing work on CHF during transients is summarised in Chapter 2. The experiment used to test the hypotheses developed from the existing body of work is described in Chapter 3 along with a detailed operating procedure for collecting steady-state and transient CHF data. The steady-state results including heat balance and heat transfer data are presented in Chapter 4 while transient results are presented and discussed in Chapter 5. The conclusions drawn from the experimental results of this work are presented in Chapter 7.

Chapter 2

Literature Review

This chapter will present experimental results and analyses from the literature that frame the objectives of the present work. The information from these works will be used to develop the author's hypothesis that pre-existing dryout at the initial conditions of Lyons and Swinnerton's [3] flow boiling depressurisation experiments negated the effects that caused the delay in the onset of dryout that was observed by Celata *et al* [1, 2]. A set of experiments are then proposed to test this hypothesis.

The focus of the present work is on transient conditions. Steady-state experiments and models are not presented in detail except where they are directly relevant or have been applied to the measurement and prediction of transient dryout. An overview of dryout prediction methods and data may be found in works such as [25], [40], [41], [33], [34], [5] and [42].

This chapter is divided into four sections. An introduction provides some background on transient heat transfer as well as the applicability of dryout prediction methods to transient conditions and the evaluation of steady-state data. This is followed by a section that outlines experimental results on transient dryout available in the literature. The third section describes some of the available prediction methods, models and analyses that have been developed to predict the onset of dryout during transients. The final section develops the author's hypothesis based on the experimental and phenomenological evidence presented in the literature.

2.1 Transient Dryout and Heat Transfer

2.1.1 Application of Dryout Prediction Methods

The quasi-steady method for predicting dryout during transients used in the present work involves two major steps. First, the mass, energy and momentum conservation equations must be solved to obtain the local instantaneous conditions. The second step uses these local values of pressure, mass flow rate, quality, and heat flux to determine whether or not dryout has occurred. In many earlier works—*e.g.* [43], [44], [45] *etc.*—the solution of the transport equations was simplified based on the assumption that the pressure drop is zero and the phases are in thermodynamic equilibrium. In this case the momentum equation becomes a linear combination of the mass and energy equations and effectively eliminates it from the solution method. Some of these models incorporate the effects of differing phasic velocities or slip [46]. Others further simplify the model by assuming that the liquid and vapour flow with the same velocity. This simplification is referred to as a homogeneous equilibrium model (HEM) [2].

When the local conditions in a channel—pressure, mass flux and quality—at the observed OID in a steady-state experiment are directly used as input to a CHF prediction method in order to assess the method's performance it is referred to as the direct substitution method (DSM). This is similar to the way CHF or dryout prediction methods are used in the quasi-steady method for transient conditions. However there is some justification in the literature that when evaluating the representativeness of dryout correlations for experimental data the iterative heat balance method (HBM) is more effective.

These two methods are equivalent to assessing the error of prediction methods at constant dryout quality and constant inlet conditions respectively. A brief discussion of these methods is included here; they were discussed in depth during the round table discussion on reactor power margins that may be found in volume 163 of Nuclear Engineering and Design: [47, 48, 49, 50, 51, 52, 53, 54, 55, 56]. In response to this discussion Hejzlar and Todreas [55] made a recommendation to use the HBM to compare the performance of different prediction methods against steady-state experimental data and each other but, when the DSM is to be used, to

specify the steady-state DSM performance for each correlation used as well. These recommendations are followed in the present work.

The HBM involves performing a heat balance on the test section of interest to evaluate the quality at a given location as a function of test section heat flux. The predicted dryout point is the intersection between the heat balance and the CHF-quality curve for the prediction method. The HBM is implicitly used in dryout prediction methods based on the inlet quality or subcooling and heated length rather than the local quality.

The difference between the accuracy of the HBM and the DSM is illustrated in the performance evaluation of the 2006 CHF look-up table [5]. The LUT's RMS error when evaluating the data from which the table is derived in comparison with the compiled table is 39% for the DSM compared to 7% for the HBM. The reason for this discrepancy is illustrated in Figure 2.1 where the differences between the predicted and observed CHF are denoted by δ_{DSM} and δ_{HBM} for the DSM and the heat balance respectively. The CHF predicted by the HBM occurs at a lower local quality than the observed CHF. Conversely the CHF predicted by the DSM is based on the local quality for the observed CHF. In most cases—see [25] or [8] for example exceptions—the CHF decreases with quality. As a result the error in the DSM is doubly compounded by any deviation from the prediction curve. The HBM error is proportional only to the deviation between the observed CHF and the heat balance–CHF curve intersection which is fixed for constant boundary conditions.

Celata [50] justified the use of the HBM for evaluating dryout data based on the approach that the predicted value with which the observed dryout data are to be compared should not be based on the parameters from the observed data point. Instead it should be based on an unbiased evaluation of the predicted value based on the boundary conditions of the experiment, *i.e.* the inlet temperature, mass flow rate and system pressure.

The use of the HBM *vs* DSM is controversial—*e.g.* Olekhnovitch *et al* [57] provided an argument that neither of these methods are ideal with respect to nuclear reactor power margins to dryout. This debate is limited to the evaluation of steady-state data. The HBM is fundamentally ill-suited for predicting dryout during dynamic conditions since it is based on constant mass flow rate throughout the test
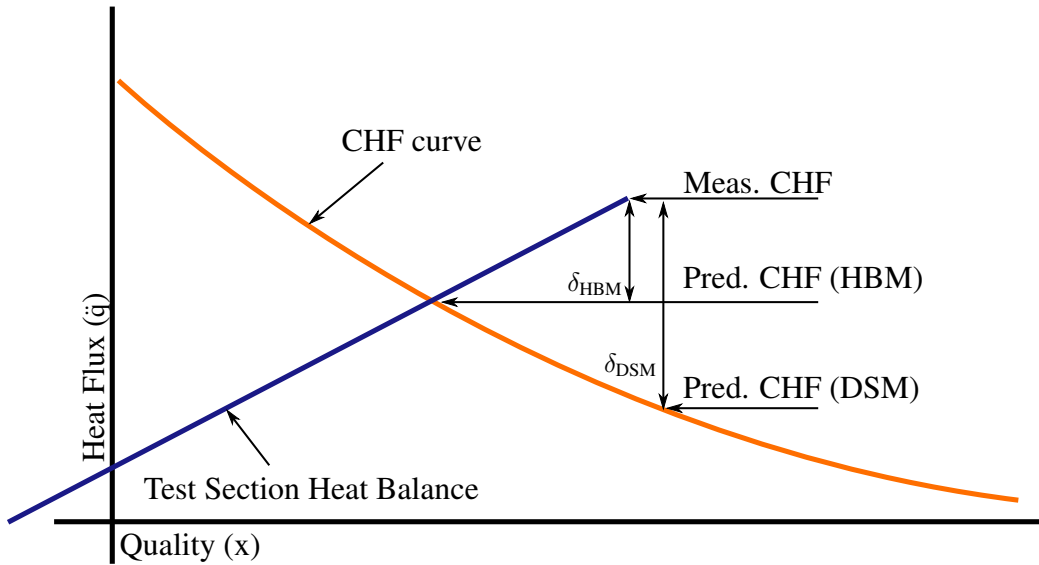
Figure 2.1: Depiction of the steady-state prediction error for HBM and the DSM. The steady-state prediction error using the HBM, δ_{HBM}, is generally much smaller than the error in the same prediction of the DSM, δ_{DSM}. δ_{DSM} is compounded by the deviation of both the experimental dryout heat flux *and* the dryout quality from the CHF prediction curve.

section. Therefore the quasi-steady method that implicitly uses the DSM should be used to realistically predict the time-to-dryout under transient conditions.

2.1.2 Transient Heat Transfer and Turbulence

When investigating the measurement and prediction of dryout under transient conditions it is important to examine transient heat transfer since it will dictate the local conditions in the fluid. Experimental data from the literature indicates that, for both single-phase and boiling cases, transient heat transfer rates differ somewhat from the values that are predicted based on local conditions and assuming a quasi-steady state. Some of these works are reviewed here.

Sparrow and Siegel [58] solved the unsteady energy conservation equation in radial co-ordinates for a tube with steady flow and uniform temperature distribution at the inlet for an arbitrary variation in wall temperature. The solution was based on first integrating the equation in the radial dimension and then finding the eigenvalues and eigenfunctions of the resulting expression for a series solution in the

axial and time dimensions. Their results were compared to a solution of the energy conservation equation that assumed constant values of heat transfer coefficient. It was concluded that the accuracy of the constant heat transfer coefficient assumption depended on the severity of the transient and that entrance region effects—for $z/D < 30$—were important when this assumption was used.

Kalinin and Dreitser [36] conducted experiments in a variety of both heated and cooled test sections with diameters of 5.4–42.9 mm and Reynolds numbers of 6×10^3–6×10^5. Their experiments included variations in fluid inlet temperature for cooled channels, applied wall heat flux in heated channels, flow rate transients, and combinations thereof for both liquids and gases. They developed complex relations based on local conditions and found that the deviation from steady-state values of heat transfer were proportional to the rates of change of the varied parameters.

Jackson *et al* [35] conducted ramp flow increase experiments in a 48.3 mm ID tube with an upstream calming length of 3.7 m and a uniformly heated length of 3.0 m. They found that both the wall and fluid temperature showed a delayed response to the transient when transient conduction effects were taken into account in the wall. To explain this delay they cite an earlier work, [59], where it was found that the axial turbulent velocity fluctuations responded promptly to flow transients while radial velocity fluctuations showed a delayed response.

He and Seddighi [60] reviewed existing literature and performed a DNS study on turbulence structures in Poiseuille flow with rapidly increasing mass flow rate. Their results complemented those of Jackson *et al* [35]. They found the turbulence did not follow a straightforward path to the higher Reynolds number flow but rather that a transition similar to a laminar to turbulent transition with three phases occurred. Stream-wise streaks with large axial velocity fluctuations near the boundary layer formed in the first phase which was followed by the development of structures similar to turbulent spots in laminar-to-turbulent flow transitions. These structures grew until they spanned the entire channel at which time the transition was complete. He and Seddighi [61] extended their DNS study to a range of initial and final conditions and were able to correlate the critical equivalent Reynolds number that relates the channel flow to the boundary layer bypass phenomenon observed in external flows as a simple function of the initial turbulence intensity.

Kang and Chang [62] performed heat transfer experiments in supercritical HFC-134a at pressures of 4.1 to 4.5 MPa, mass fluxes of 600–2000 kg m^{-2} s^{-1}, inlet temperature from 50–110°C and heat fluxes of 10–160 kW m^{-2} in a vertical uniformly heated 2.0 m by 9.4 mm ID tube. They developed a new steady-state heat transfer correlation based on 7022 of their own data points for the normal heat transfer—*i.e.* rather than enhanced or deteriorated modes that are also observed in supercritical diabatic flow. This correlation predicted 94% of their data and 86.4% of 1073 data from the literature within ±20%. They then performed ramp pressure transient experiments—both increasing and decreasing—from the subcritical pressure of 3.8 MPa to the supercritical pressure of 4.5 MPa at ramp rates of 1.1 to 13.6 kPa s^{-1}. The critical pressure of HFC-134a is 4.06 MPa. They found that the steady-state correlation overestimated the heat transfer coefficient by between 10 and 40% at supercritical local pressures during both increasing and decreasing pressure transients.

Johnson [37] reviewed a series of transient nucleate boiling experiments with exponentially increasing heat input to 0.1 mm thick by 76.2 mm long and 2.5–6.4 mm wide ribbons both with and without forced flow. It was found that for exponential periods less than 0.005 s that the wall superheat values would overshoot the values expected from steady-state nucleate boiling curves. This is also noted and classified into several different types of overshoot later by Serizawa [63].

Sakurai and Shiotsu [64] performed pool boiling experiments with exponentially increasing heat input on a horizontal platinum wire heater with a diameter of 1.2 mm and an effective length of 45.8 mm. Incipient boiling was observed at lower superheats but higher heat fluxes than that for steady-state boiling. For exponential periods less than 1 s the heat transfer coefficient due to natural convection was independent of subcooling and found to increase with decreasing period. For longer periods it approached a constant subcooling-dependent value. These trends of pre-boiling heat transfer coefficient were modelled with good success by modelling the water as an infinite solid and solving the transient conduction equation for short periods and using a correlation for natural convection heat transfer for longer periods. Temperature overshoot—the maximum amount by which the transient wall superheat exceeded the wall superheat for the same heat flux on the steady boiling

curve—and incipient boiling superheat both increased with decreasing period.

Osman and Beck [65] performed non-boiling quenching experiments on a hollow sphere of high-purity copper plunged into water and ethylene glycol. The sphere had an OD of 7.42 cm and an ID of 2.20 cm fabricated from two hemispheres. It was instrumented with three radially distributed equatorial thermocouples embedded at a depth of 2.6 mm from the surface. They solved the inverse heat transfer problem—transient conduction—to find the time-dependent value of the surface heat transfer coefficient. The boundary conditions for the solution were based on the mean temperature of the readings of the three thermocouples at each time and an adiabatic boundary condition at the air-copper interface on the inside surface of the sphere. Early in the quenching period—*i.e.* the first 1–2 s—the surface heat transfer coefficients exceeded values predicted based on correlations from the literature by 100–120%. After this initial period the correlations predicted the results within $\pm 15\%$ for ethylene glycol and $\pm 20\%$ for water.

Auracher and Marquardt [66] summarised a number of steady and transient experimental results for pool boiling and boiling under an impinging jet for both well-wetting and poorly wetting fluids—water, FC-72 and isopropanol—under saturated conditions. They used a finely-tuned surface temperature controller and surface with embedded thermocouples and solved the transient inverse heat conduction problem in order to obtain surface heat fluxes at all regions of the boiling curve. They found that, for linear rates of temperature increase up to 50 K s^{-1}, the CHF occurred at similar wall superheats but the value of the CHF increased with the heating rate. They postulated that the increased heat transfer rates up to the CHF observed during transients was due to the increased thermal gradient in the fluid adjacent to the wall. Conversely they also claimed that the enhanced heat transfer was not the result of a change in the two-phase structure near the wall since it was not observed to be strongly affected by the surface temperature transients. They later, [67], used these observations to propose a heat transfer model up to and including the prediction of CHF based on the dynamic stability of the interactions between the interfacial area on the heater surface—based on observations from the literature that a great deal of the heat transfer from a boiling surface occurs at the three-phase contact line in the microlayer below growing bubbles—and conduction in the heater

surface.

Ragheb *et al* [68] summarised a series of transition boiling experiments that were performed using a transient technique to obtain complete boiling curves. Copper and brass blocks with embedded cartridge heaters were used that were heated above the Leidenfrost temperature before a flow was introduced. In order to collect transition boiling data a flow was introduced and the cartridge heaters were turned off so that a cooling curve was obtained. The data from the transient cooldown of the test sections were used to generate boiling curves in the film boiling, transition boiling and nucleate boiling regions. They performed both 1-D radial and 2-D radial and axial transient conduction analyses of their data. At the mid-plane of the test section axial conduction losses through the ends of the test section could be neglected. Ragheb *et al* determined that data collected near the mid-plane of their test sections were representative of the mean boiling curve for the entire test section and that 1-D conduction analysis was sufficient. They were able to obtain a steady-state boiling curve for one of the test sections using a temperature controller and obtained similar results for the transient and steady-state curves. The exception to this was that steady-state data showed higher heat fluxes than the transient data for the same wall superheat in the nucleate boiling region.

Green [69], and Green and Lawther [70], performed power transient heat transfer experiments at 1.0 MPa for mass fluxes of 150–3270 kg m^{-2} s^{-1} in 7.1–26.6 mm ID tubes with 0.9–2.0 mm wall thicknesses and lengths of 0.9–3.9 m with exit qualities of 0.3–1.0. These experiments investigated post-dryout heat transfer including transition boiling, minimum heat flux film boiling, and stable film boiling heat transfer by examining the transient thermal response of the test section wall to small step changes of 2–12% of test section power from pre to post-dryout conditions in Freon-12 using thermocouples fixed to the outside of the test section wall. They analysed their results using a HEM numerical model coupled with a transient heat conduction model with 4 radial and 27 axial nodes. Axial conduction was not modelled. Axial nodes were concentrated near the exit of the test section with 9 axial nodes in the 76 mm nearest the end of the heated length where dryout had been experimentally observed. They found that the transient response predictions of their model were most sensitive to the time of the predicted onset of dryout—*i.e.*

the accuracy of the dryout prediction method. The transition boiling region where the heat flux decreased with increasing wall temperature was found to have a minimal influence on the transient response possibly due to the short period of time over which it was observed. The accuracy of heat transfer predictions before the onset of dryout had no influence on the post-dryout transient response. When the steady-state correlations for the onset of dryout, minimum film boiling heat transfer and stable film boiling heat transfer were modified to better match their data they obtained excellent agreement between their model predictions and their experimental results. The CISE and Groeneveld (1969) dryout correlations for R-12 were modified by providing alternate forms of their fitting functions and/or by adjusting some of their coefficients while a unique boiling length function was applied to the Dougall and Rohsenow, Miropolskii and Groeneveld film boiling correlations. These results suggest that transient effects do not have a significant influence on convective boiling heat transfer since good transient response results were obtained using modified versions of steady-state correlations.

This brief review of transient heat transfer literature demonstrates that the underlying phenomena of single phase and nucleate boiling heat transfer do not respond in a quasi-steady way to imposed transients. The work of Green and Lawther [69, 70] suggests that the quasi-steady method is sufficient for modelling two-phase convective heat transfer although the step changes of power in their experiments were relatively small. These works in the literature suggest that transient effects on heat transfer may be more significant in channels where single phase or nucleate boiling heat transfer are dominant whereas they are less important for convective boiling in annular flow.

2.2   Experimental Studies

2.2.1   Pool and Nucleate Boiling Experiments

The experimental studies discussed in this section are summarised in Table 2.1 except for the work of Kataoka *et al* [71] and Roemer [72] which are shown in Table 2.3 since their test sections were immersed in a flow channel rather than a static

pool.

Roemer [72] performed power transient experiments on 9.5 mm outside diameter tubes with wall thicknesses of .25 and 0.04 mm mounted perpendicular to the flow axis of a 30.5 by 203 mm water flow channel. Transient tests were performed with rapid increases in applied voltage in the form $V(t) = V_0 + V_f(1 - e^{\frac{t}{\tau}})$ with a time constant of 0.1 s. Both aged and unaged test sections were used: heater aging was accomplished by applying a test section power of approximately 40% of the CHF value for 40 minutes. The transient CHF values for the unaged heaters were approximately 37% and 25% of the steady-state values for the 0.25 and 0.04 mm wall thickness heaters respectively. High speed photography was used to observe the behaviour of the boiling surface. Low transient values of the CHF for the unaged heaters was attributed to the presence of air bubbles on the heated surface that did not condense when they came into contact with the subcooled flow of water. These bubbles continued to agglomerate and formed a gas blanket on the surface during the transient tests. The aged heaters did not exhibit this behaviour: the bubbles would grow and either condensed or were transported away from the surface after a period of growth. Roemer concluded that for the aged heaters the dominant transient effect was due to conduction in the heater and that, for the aged heaters, the transient peak heat flux did not differ from the steady-state value. No surface temperature overshoot was observed during the transients in contrast to the work of, *e.g.*, Johnson [37].

Gerliga and Tokarev [73] performed steady-state and power-on transient pool boiling experiments on flat plates of varying thickness. They found that the transient CHF was 12–1.5% less than the steady-state CHF as the plate thickness was increased from 0.1 mm to 0.8 mm. From the description of the experimental procedure it is possible that the steady-state CHF was taken during a slow ramp transient and the transient CHF was taken as the value that film boiling ceased when the applied power was slowly decreased following a power-on transient. A better conclusion from this study may be that there is a hysteresis between the onset and suppression of film boiling when the applied heat flux is increased and decreased respectively. No indication was made to suggest that transient conduction and energy storage in the heater was accounted for in their analysis. Therefore the inference

Data	Fluid	Transient Type	Geometry	Pressure (MPa)	Mean Heat Flux (kW m^{-2})	Transient Effect
Gerliga and Tokarev (1971)	Water	Power	0.09–0.80 mm thick 10 mm×30 mm plates	0.1	1200–2300	CHF Decrease
Fukuda et al (1994)	Water	Pressure	42 mm by 1.2 mm wire 49 mm by 3.0 mm wire	1.08–1.57	100–800	25–37% CHF Decrease
Auracher & Marquardt (2002)	FC-72	Surface Temperature	5 mm thick by 18.2 mm diameter copper surface	0.13	0–900	CHF Increase
Deev et al (2007)	Water	Power	25 mm by 0.1 mm platinum wire	0.1	700–3100	None

Table 2.1: Summary table of transient pool boiling dryout data from the literature.

with regard to the onset and suppression of film boiling hysteresis is not conclusive.

Deev *et al* [74] similarly performed power-on transients in a 25 mm platinum wire heater at atmospheric pressure. They were able to accurately predict the time to CHF using a nucleate boiling model that included transient conduction and energy storage within the heater. No transient delays or increases in CHF were observed.

Fukuda *et al* [75] performed pool boiling pressure transient experiments on horizontal platinum wire heaters 1.2 and 3.0 mm in diameter and 42 and 49 mm in length respectively. Their test apparatus was equipped with rupture disks to facilitate the pressure transient experiments with very fast exponential decay periods of between 1×10^{-3} and 0.025 s. Boiling behaviour at the surface was recorded using a high speed camera operating at 200 frames per second. The heat generation rate was kept constant. In the analysis the observed heater temperature was used as input to the solution of the transient conduction equation that was used to calculate the total surface heat flux as a function of time. They found that the transient CHF was as little as one quarter of the corresponding steady-state value at the corresponding transient pressure and estimated the error in the observed wall superheat to be ± 1 K and $\pm 2\%$ for the surface heat flux. During the transients the onset of nucleate boiling was delayed to higher wall superheats than their steady state values. The wall superheat values exceeded the steady-state values after the initiation of explosive boiling while the surface heat flux approached but never reached the steady-state nucleate boiling heat flux at the corresponding wall superheat and pressure. The decrease in observed heat flux—*i.e.* the temperature overshoot—and similarly the reduction in the maximum (critical) heat flux was attributed to a delay in the activation of flooded nucleation sites.

Kataoka *et al* [71] performed experiments with exponentially increasing power on wire heaters in a vertical upward flow channel over a wide range of mass flow rates. They modelled transient conduction with heat generation in the wire heaters. They found that CHF occurred at transient heat fluxes up to twice that of the steady state values when the heat increase exponential period was as small as 0.007 s and approached the steady values as the period increased.

2.2.2   Annular Film Dryout Experiments

Annular film dryout experiments require an experimental apparatus that is capable of establishing an annular flow upstream of the dryout locations before dryout occurs. This requires a test section with relatively long heated length—$z/D > 100$—in order to avoid exceeding the CHF before enough vapour is generated to create an annular flow unless the fluid is a saturated two-phase mixture at the test section inlet. As the flow quality increases with increases in heat flux the liquid film that flows along the heated surface may dry out and heat transfer deterioration may occur thereafter. The experiments discussed in this section are summarised in Tables 2.2, 2.3, 2.4, 2.5 and 2.6.

Moxon and Edwards [46] performed flow and power transient tests using water with an inlet pressure of 6.9 MPa in several uniformly heated tubes with heated lengths of 1.52 and 3.05 m with inside diameters of 9 and 10.8 mm respectively, a 3.05 m long non-uniformly heated tube with an inside diameter of 9.5 mm and a 37-rod cluster. The inlet subcooling was approximately 54 kJ kg^{-1} below the liquid saturation enthalpy for all tests except the power transient tests on the uniformly heated 1.52 m tube that were performed with a higher inlet subcooling value of 264 kJ kg^{-1}. They used steady state results from each test section to generate analytical expressions based on local conditions from which the transient dryout could be predicted based on local values of mass flux, heat flux, and quality. Local conditions during the transients were calculated using a numerical solution of the mass and energy conservation equations using a homogeneous equilibrium model that incorporated the effects of interfacial slip. Their model underpredicted the time to dryout in every case except for two power transient tests in the 1.52 m uniformly heated with the least underprediction in time to dryout observed in the non-uniformly heated 3.05 m tube.

Smirnov *et al* [76] performed flow transient experiments in 0.5 and 1.4 m tubes with 4.0 mm inside diameters at 9.8 MPa. They reduced the flow by 40–70% of its initial value over a perdio of 0–3 s and computed local conditions in the test section by integrating the energy and mass conservation equations. This included a lumped capacity model of the test section wall. It was assumed that pressure drop in the test section was negligible. They found that the transient dryout conditions

Data	Transient Type	Geometry	Pressure (MPa)	Mass Flux (kg m^{-2} s^{-1})	Mean Heat Flux (kW m^{-2})	Transient Effect
Moxon & Edwards (1967)	Flow	3.05 m by ⌀10.8 mm uniformly heated tube		2700	1150–1400	Delayed OID
	Flow	3.05 m by 9.5 mm non-uniformly heated tube	6.9	2710	1170–1380	Slightly Delayed OID
		37 rod bundle 36 × ⌀15.9 mm rods with radially varied heating		2370	880–1050	Delayed OID
	Power	3.05 m by ⌀10.8 mm uniformly heated tube		2700	870–1820	Delayed OID
	Power	3.05 m by ⌀9.5 mm non-uniformly heated tube		2700	1150–1890	Slightly Delayed OID
		1.52 m by ⌀9.0 mm uniformly heated tube		2000	1670–3120	Slight-No OID Delay
Roemer (1969)	Power	51–152 mm long ⌀9.5 mm horizontal tubes with 0.25 and 0.04 mm walls in a vertical 31 by 203 mm channel	0.1	970	0–827	None for aged heaters
Smirnov, Pashkov & Zaitsev (1972)	Flow	0.5 and 1.4 m by ⌀4.0 mm uniformly heated tubes	9.81	1000–3000	292–3400	Increase in x_{crit} with $d\dot{m}/dt$
Smirnov, Zaitsev & Serov (1977)	Flow	1.2 and 2.5 m by ⌀8.0 mm uniformly heated tubes	1.5–15.7	100–600	NA	Increase in x_{crit} with $d\dot{m}/dt$

Table 2.2: Summary table of transient flow boiling water dryout data from the literature (1).

differed from steady-state conditions as the flow decay rate increased. Smirnov *et al* [77], with different co-workers, later performed experiments at lower mass fluxes but a very wide pressure range—1.5–15.7 MPa—in 1.2 and 2.5 m long 8 mm ID tubes. They analysed the results using a method similar to their earlier publication but instead characterized the transient effect using the critical quality ratio x_{tr}/x_{ss} and found that this ratio increased with the rate of the transient.

Gaspari *et al* [78] conducted inlet flow stoppage, inlet flow stoppage with depressurisation and also power transients in a 4.0 m long annulus with an outer heater 21 mm in diameter and an unheated inner rod 13.5 mm in outer diameter for an equivalent hydraulic diameter of 7.5 mm. They analysed their data using local conditions calculated using a computer code TILT. They demonstrated good performance of this code by comparing its predictions to some flow transient parameters. Local conditions from this code were used to predict the time-to-dryout using a correlation that was well-tuned to their steady-state dryout results. The code was able to accurately predict the time-to-dryout for the constant pressure flow stoppage tests. It underpredicted the time to dryout for the flow stoppage transients with exit depressurisation. When they re-analysed the transients using a tube dryout correlation they attained better results and postulated that the pressure transient caused a dramatic redistribution of liquid from the unheated to the heated wall that caused the observed delay in the onset of dryout. Based on this discussion they postulated that this effect would only be relevant in geometries with unheated surfaces and would not be observed in tubes.

Iwamura and Kuroyanagi [79] performed flow transient dryout experiments with ramp flow decrease rates of 0.6–35% s^{-1} in a uniformly heated tube. They analytically solved the mass and energy equations assuming a constant slip ratio between the liquid and vapour phases to obtain local parameters. They obtained a pressure-dependent relationship on the ratio of the local mass flux at the time of dryout to the mass flux under steady state conditions with otherwise similar boundary conditions. A later work by Iwamura [44] re-analyses the earlier results and also includes some experiments performed in water at atmospheric pressure in a transparent annular test section. When the local conditions computed using the same method as in the earlier work were combined with a local-conditions dryout corre-

Data	Transient Type	Geometry	Pressure (MPa)	Mass Flux ($kg\ m^{-2}\ s^{-1}$)	Mean Heat Flux ($kW\ m^{-2}$)	Transient Effect
Gaspari, Granzini & Hassid (1973)	Flow Stoppage	4.0 m annulus 13.5 mm OD by 21 mm ID (7.5 mm D_h) external uniform heating	4.9	407–2565	237–830	None
	Flow and Pressure			700–2565	341–972	OID Delay
	Power			700–1490	352–1290	None
Iwamura & Kuroyanagi (1982)	Flow	0.8 m by ⌀10 mm uniformly heated tube	0.5–3.9	1240–3050	2160–3860	None
Lyons & Swinnerton (1983)	Pressure	3.66 m by ⌀12.7 mm uniformly heated tube	3.1–6.7	490–2260	740–1570	None
Iwamura, Watanabe & Murao (1994)	Flow	0.6 and 1.5 m 7 rod bundles of ⌀9.5 mm rods with axially and radially non-uniform heating	13.0–15.5	2000–3200	760–5200*	None
	Power			1430–2400	760–4020*	None
	Power and Flow		15.5	2000-3100		None
Kataoka, Serizawa & Sakurai (1983)	Power	39.3–100.4 mm by ⌀0.8–1.5 mm axially-oriented wires in a 1.425m by 38 mm channel	0.1–2.0	0–4900	3000–20 000	100% CHF Increase for Fast Transients
Lee & Lin (1993)	Flow	3.6 m by ⌀13.4 mm uniformly heated tube	6.9 and 15.5	1960–3800	1100 and 1460	None

Table 2.3: Summary table of transient flow boiling water data from the literature (2).

Data	Transient Type	Geometry	Pressure (MPa)	Mass Flux (kg m^{-2} s^{-1})	Mean Heat Flux (kW m^{-2})	Transient Effect
Ozawa, Umekawa, Yoshioka & Tomiyama (1993)	Flow Oscillations (0–400% of mean flow)	0.9 m 5.0 mm ID by 1.0 mm wall uniformly heated tube	0.1	70–450	<514	Decrease in CHF with increasing oscillation period and amplitude
Zhao, Su, Liang, Zhang, Tian & Siu (2011)	Flow Oscillations (0–300% of mean flow)	1.8 m 10 mm ID by 2.0 mm wall uniformly heated tube	0.5–3.0	100 and 170	300–900	Decrease in CHF with increasing oscillation period and amplitude

Table 2.4: Summary table of oscillating flow dryout experiments from the literature.

lation the time to dryout was predicted within $\pm 20\%$ similar to the R-12 results of Cumo *et al* [43].

Lyons and Swinnerton [80, 3] performed pressure transient experiments in a vertical uniformly heated tube over a range of pressures with depressurisation rates of up to 5.0 MPa s^{-1} . Their experiments were analysed using the Whalley *et al* film flow model, which will be discussed in the next section, see also [39], and the inlet conditions based Bowring correlation to predict the dryout *length*. The dryout length was used because it made numerical integration of the film flow model's governing equations easier. The film flow model predicted their steady results with a mean error of -3.0% and an RMS error of 6.7%. The Bowring correlation performed worse with a mean error of 12.1% and an RMS error of 14.5%. These transient experiments were unique in that the pressure transients were initiated from steady-state conditions with a small section in dryout at the furthest downstream thermocouple position. It was noted that before the initiation of the transients the surface temperature occasionally exceeded 400°C. Their observations were of the progression of the dryout front rather than the onset of dryout. They found that both the model and the correlation's predictions of the dryout length during the transients was consistent with their performance for their steady-state data.

Cumo *et al* [43] conducted exponentially decreasing flow transient experiments using R-12 in a uniformly heated tube with half-flow decay times of 0.7–3.2 s. They were able to predict the time to DNB, as they characterised the dryout phenomena, within approximately $\pm 20\%$ by solving the mass and energy conservation equations to obtain local conditions within the test section and applying a DNB correlation for R-12.

Leung [81] performed flow transient, outlet break—pressure—plus flow stoppage, inlet break—pressure and flow reversal—and simultaneous inlet and outlet break experiments in several vertical test sections using R-11. The results were analysed using the CODA HEM code that solved the mass, energy, and momentum conservation equations in one dimension coupled with a transient heat conduction calculation in the wall of the tube. Leung found that the CISE refrigerant correlation could predict the steady data within $\pm 10\%$ of the observed CHF. It consistently underpredicted the time to dryout in the flow transient experiments by approximately

Data	Transient Type	Geometry	Pressure (MPa)	Mass Flux (kg m^{-2} s^{-1})	Mean Heat Flux (kW m^{-2})	Transient Effect
Leung (1980) [R-11]	Flow	2.74 m by ⌀11.7 mm uniformly heated tube	2.14–2.86	1270–2640	57–113	10% Time Delay
	Flow Stoppage	2.74 m by ⌀11.7 mm non-uniformly heated tube	1.81–1.97	620–1000	52–64	NA
	Exit Break plus Flow Stoppage	2.74 m by ⌀11.7 mm non-uniformly heated tube	2.2	1260	NA	NA
	Inlet Break	2.74 m by ⌀11.7 mm uniformly heated tube	2.21	1230	50.3	NA
	Inlet and Outlet Break	2.74 m by ⌀11.7 mm uniformly heated tube	2.21–2.85	1220–2710	49–67	NA

Table 2.5: Summary table of Leung's R-11 pressure and flow transient experiments.

34

10%. The pressure-flow transient data were generally slightly underpredicted by the CISE correlation; no quantification is given but the experimental times to dryout were graphically shown to be bracketed by the CISE prediction and local equilibrium quality equal to unity. Leung also noted a dramatic increase in power-to-fluid early in the transients as the thermal energy stored in the test section wall was released. This release of thermal energy was due to the decreasing saturation pressure with nominally constant heat transfer coefficient.

In addition to performing a series of experiments Leung [81, 82] also used the CODA HEM code to evaluate the results of many earlier PWR integral blowdown experiments. The local conditions computed using this code were used to predict the onset and progression of dryout using 8 different correlations: the Bowring, Biasi and CISE correlations for tubes and the B&W-2, CONDIE MOD7, GE and Hsu-Beckner correlations for rod bundles and the Griffith-Zuber correlation based on results from annuli with short heated lengths at low flow conditions. The performance of the correlations varied for each set of experiments but overall it was found that the Biasi and CISE correlations were able to predict—usually slightly early—the onset of dryout at the beginning of the blowdown transients while the Griffith-Zuber low flow correlation was best for predicting dryout that occurred near the end of the transients. Leung also noted, however, that the dryout that occurred early in the blowdown was nearly as well predicted by assuming dryout would occur when the equilibrium quality reached 1.0 as it was by the correlations. Due to the variation in conditions of the experiments evaluated in Leung's work it is difficult to make a conclusion about the ability of the quasi-steady method to predict dryout during transients. It lends credence to the argument that, in order to evaluate the ability of the quasi-steady method to predict dryout, the time-to-dryout must be predicted by a method that has been shown to be representative of dryout under steady-state conditions for the channel of interest: *i.e.* as Leung did for the CISE correlation and the reported R-11 experiments.

Celata *et al* [83, 1, 84, 85, 2] conducted approximately 1000 transient experiments in a vertical uniformly heated tube with heated lengths of 1.18 and 2.30 m using R-12 as the working fluid to simulate the two-phase flow of water. This included flow, pressure and power transients as well as every combination thereof.

Summarily all of their experimental data were published in [86] and their analyses in [87]. These experiments simulated water at initial pressures of approximately 8–16 MPa for mass fluxes of 1000–1470 kg^{-2} s^{-1} in a 7.7 mm diameter, 2.3 m long tube by using R-12 at 1.2–2.75 MPa. The rate of change of fluid parameters with respect to pressure for R-12 was similar to that of water at lower pressures.

Flow transients with half-flow decay times less than 5 s were reported in [83]. Celata *et al* analysed these results using an inlet-conditions correlation that predicted 96% of their steady-state results within $\pm10\%$. They conclude that the inlet-conditions approach is inadequate unless the ratio of the half-flow decay time of the exponential flow decrease to the transit time of single phase liquid through the heated length before the beginning of the transient is on the order of 8.

Pressure-only transients with constant power and mass flux were conducted for four initial pressures spanning the full available range, three mass fluxes, and depressurisation rates of 0.05 to 0.9 MPa s^{-1} [1]. If the depressurisation rate is extrapolated by linearly interpolating the range of pressures using R-12 to the simulated range of water experiments then these depressurisation rates correspond roughly to 0.3–5 MPa s^{-1}. They used the same inlet conditions based correlation described above to analyse the results. In a pressure-only transient this is more relevant than in a flow transient since the inlet enthalpy is only a weak function of pressure and therefore the exit quality based on the outlet pressure is a reasonable approximation. The exception is that it would not account for flow acceleration due to increased evaporation. If the applied test section power was considered on its own an 'unexpected' dryout occurred. The authors then took the release of stored energy from the wall into account by assuming a constant heat transfer coefficient at the heated surface and using a lumped capacity model for the wall. They found that the heat flux exceeded the predicted dryout value very early in the transient but that dryout was not observed until several tenths of a second later. They concluded that these pressure transient experiments were similar to a fast power transient and that there was a delay in the onset of dryout for pressure transients. This illustrates that conjugate heat transfer effects, *e.g.* the reciprocal relationship between conduction and thermal energy storage in the wall with convective or pool boiling at the surface, are equally important when analysing thermalhydraulic transient effects in channels as

they are for pool boiling experiments such as those by Fukuda *et al*.

Similarly, power-only transient results were presented and analysed using the inlet conditions correlation in [84]. Transients with margins to dryout of 4.5–15.3 kW m^{-2} and final state excesses to dryout of 1.8–18 kW m^{-2} were conducted as step-power increases and linear power ramps with times to increase to 150% of the initial power of 1.3–3.6 s. The thermal lag effect on the power delivered to the fluid due to energy storage to the wall was modelled. The time to dryout was significantly underpredicted for the step-power transients but by a smaller, nominally constant, margin of about 0.1–0.2 s was evident in the ramp transients.

Combined power and flow transients with flow decay and power change rates similar to those in the publications described above were reported in [85]. When the inlet-conditions approach was used it was again found to be inadequate. The combination of power and flow transients reduced the difference between the observed and predicted dryout times compared to flow and power transients alone. In this paper, however, the data is also analysed with a local conditions approach using the ANATRA code. This code is described in [2] as a HEM model that solves the mass, energy, and continuity equations in one dimension and is coupled with a 2-D transient conduction model of the wall. When the local conditions method was used the transient time to dryout could be predicted for the combined flow-power transients with a typical uncertainty of ±20%.

The local conditions approach was used again in a later work by Celata *et al* [2] to analyse pressure transients combined with flow, power and flow-power transients. The maximum depressurisation rate in all three cases was 0.3–0.32 MPa s^{-1}. This work again demonstrated the inadequacy of the inlet conditions approach. The additional power-to-fluid caused by the release of stored energy in the test section wall caused faster secondary power transients than the applied step power transients. For depressurisation rates of 0.2 MPa s^{-1} or less the code predicted the time to dryout within ±20% without any observable systematic dependence on transient parameters. However the quasi-steady method using local conditions increasingly underpredicted the time to dryout as the depressurisation rate increased beyond this value. Celata *et al* [2] note that this may be due a limitation of the HEM formulation that does not accurately represent the local conditions during fast pressure

transients.

Ozawa *et al* [88] performed dryout experiments under flow oscillation conditions in 900 mm long 5.0 mm ID by 1.0 mm wall electrically heated vertical and horizontal test sections. They used water as the test fluid and the exit conditions were maintained at atmospheric pressure for mass fluxes of 70 to 450 kg m^{-2} s^{-1}. They applied mass flow rate fluctuations of up to 4 times the amplitude of the mean flow so that in many cases the instantaneous inlet flow was in the reverse direction. Oscillation periods of 2, 4, and 6 s were tested. As the amplitude and period of the oscillations were increased the observed value of the onset of CHF based on time-average boundary conditions decreased to as little as 40% of the steady-state value for the highest mean mass fluxes. The CHF decreased by a greater degree for the horizontal channels than the vertical channels. No comparison was made of their observed CHF values with values obtained from local instantaneous conditions in the test section.

Lee and Lin [89] performed linear flow transient experiments in a uniformly heated tube at nominal BWR and PWR operating conditions with ramp rates of 0.1–30% s^{-1}. They analysed their results using several correlations from the literature based on the CODA HEM code described by Leung [81]. They found that their was little influence of the flow decay rate on the prediction capability of any of the correlations: the ratio of predicted to observed CHF at the time of the observed CHF was nearly constant for the full range of ramp rates. The GE correlation performed best for BWR conditions while the B&W-2 correlation performed best for PWR conditions. These results may be expected since GE largely developed the commercial BWR and B&W had developed its own PWR design.

Iwamura *et al* [90] conducted flow, power and flow-power transient experiments in an axially and radially non-uniform hexagonal 7-rod bundle near PWR operating conditions. They found that several mechanistic models did not predict their steady-state data well but the KfK correlation predicted their steady-state data within ±10%. This correlation achieved the same performance for the transient experiments with local conditions calculated using the COBRA-IV subchannel code.

Zhao *et al* [91] performed dryout experiments with sinusoidally oscillating inlet flow boundary conditions somewhat similar to those of Ozawa *et al* [88] in a vertical

Data	Transient Type	Geometry	Pressure (MPa)	Mass Flux (kg m^{-2} s^{-1})	Mean Heat Flux (kW m^{-2})	Transient Effect
Cumo et al (1977)	Flow	2.0 m by ⌀7.5 mm uniformly heated tube	1.1–1.8	760–900	29–75	None
Celata et al (1992)	Flow	1.18 and 2.30 m by ⌀7.7 mm uniformly heated tubes	1.2–2.75	1000–1470	32–85	OID Delay (Inlet Conditions)
	Pressure	1.18 and 2.30 m by ⌀7.7 mm uniformly heated tubes	1.2–2.75	1000–1470	28–89	OID Delay (Inlet Conditions)
	Power	1.18 and 2.30 m by ⌀7.7 mm uniformly heated tubes	1.2–2.75	1000–1470	21–151	OID Delay (Inlet Conditions)
	Power and Flow	1.18 and 2.30 m by ⌀7.7 mm uniformly heated tubes	1.2–2.75	1030–1500	27–126	None (Local Conditions)
	Power and Pressure	2.30 m by ⌀7.7 mm uniformly heated tube	2.02	1470	42–103	OID Delay for dp/dt >0.2 MPa s^{-1}
	Flow and Pressure	2.30 m by ⌀7.7 mm uniformly heated tube	1.25–2.02	1470	42–82	OID Delay for dp/dt >0.2 MPa s^{-1}
	Flow, Power and Pressure	2.30 m by ⌀7.7 mm uniformly heated tube	1.25–2.02	1470	36–94	OID Delay for dp/dt >0.2 MPa s^{-1}

Table 2.6: Summary table of transient R-12 flow boiling data from the literature.

39

1.1 m by 10 mm ID uniformly heated tube with mean inlet mass fluxes of 100 and 170 kg m^{-2} s^{-1} and pressures from 0.5 to 3.0 MPa. The inlet mass flux oscillation period varied from 1.04–10.6 s with amplitudes up to 3 times the amplitude of the mean inlet flow. They normalized their results to the 2006 CHF look-up table for both the onset of periodic dryout—intermittent dryout during the troughs of the inlet mass flux oscillations at constant applied power—and continuous dryout where the wall temperature progressively increased without returning to a fixed value between mass flow minima. Similar to Ozawa *et al* they found that increasing period and amplitude resulted in an asymptotic decrease in the periodic onset of dryout. The value of the periodic dryout decreased below the value predicted based on the steady-state value of the minimum mass flux that had previously been stated as a theoretical limit by Okawa et al [92]. They also found that increasing period and amplitude decreased the continuous dryout below the steady-state value based on the mean mass flux while the value approached the steady value as period decreased to zero. The cause of this decrease in CHF with increasing period was attributed to increased droplet entrainment from wave crests in the liquid film whose amplitudes were magnified by the flow oscillations and resulted in lower liquid film flow and a thinner periodic liquid film thickness that allowed earlier complete evaporation of the liquid film than under steady conditions. The earlier the liquid film evaporated during the flow oscillation the greater the amplitude of the temperature variation. Based on the work of Fukano *et al* [93] it was then proposed that continuous dryout resulted when the amplitude of the temperature oscillations exceeded the Leidenfrost temperature.

2.3 Transient-Effects and Phenomenological Models

This section summarises the major experimental and theoretical works on transient dryout. Chang and Baek [94] summarise several of the mechanisms and studies discussed below in their review where they identify improving the database of transient data as one area for future R&D in CHF.

2.3.1   Pool and Nucleate Boiling

Serizawa [63] proposed a model to predict dryout during power transients for pool boiling. Serizawa postulated that dryout occurred when the liquid layer underneath a vapour blanket was completely evaporated. A finite time is required to evaporate the liquid film after the steady CHF has been exceeded. In the meantime the heat flux continues to increase and the transient CHF is considered to occur when this liquid layer dries out. The finite time to evaporate the liquid layer after the steady state CHF has been exceeded accounts for the increased value of the CHF observed in power transient pool boiling. The model was then based on the premise that the liquid supply rate to the liquid layer matched the evaporation rate up to a limiting value. This value was a function of fluid properties and heater geometry. Dryout was then predicted by integrating over time until evaporation completely exhausted the supplied liquid once the liquid supply rate had reached this critical value. They compared their data with power transient pool boiling data from the literature and were able to model transients with exponential periods greater than about 0.01 s. Faster transients than this were not as accurately predicted but, based on observations from the experimental data, these data corresponded to conditions where the transient boiling curve departed from the steady-state curve before the onset of dryout.

Pasamehmetoglu *et al* [95, 38] later modified a steady-state model by Haramura and Katto to predict power transient pool boiling CHF. This model assumed that no liquid was supplied to the layer underneath bubbles except during the time between the departure of a bubble and the beginning of the next bubble growth period. Their model incorporated both hydrodynamic thinning of the liquid sublayer—based on Helmholtz instability of vapour jets in the thin layer—and evaporation. Dryout occurred if the liquid layer was depleted before the end of the bubble growth period. Similar performance is achieved to that of Serizawa's model but with the improvement that no empirical correlations are required for saturated boiling data and their basic model is derived from an existing steady-state model.

Pasamehmetoglu *et al* [38, 96] also extended this model to situations with forced convection by adding a liquid supply model. Their liquid supply model was based on several assumptions. They assumed, from Weisman and Pei [31], that the only

liquid that reached the surface would be due to the turbulent radial velocity fluctuations that exceeded the vapour escape velocity $(u' > u_v)$. They then further assumed that the liquid supply rate, *e.g.* at steady-state CHF denoted by W_{f0}, was proportional to the expectation value of the radial velocity fluctuations in excess of the vapour escape velocity as shown in Equation 2.1. They then assumed that the probability density function of the radial velocity fluctuations for $u' > u_v$ could be represented by a hyperbolic distribution for ease of calculation as shown in Equation 2.2. Furthermore they assumed that the vapour escape velocity was directly proportional to the surface heat flux as shown in Equation 2.3 where $\ddot{q}_{CHF-SS}$ has replaced the escape velocity and the velocity fluctuations have been replaced by the dummy variable ξ to reflect the absorbed proportionality constants. This equation can then be integrated and re-arranged in terms of another single constant as in Equations 2.4 and 2.5. If the equation is integrated for both the steady state CHF and a time-varying heat flux then an expression for the liquid supply rate during a transient based on the liquid supply rate at steady-state CHF—that can be derived from steady-state data—can be formed. When this liquid supply model was added to their pool boiling transient CHF model excellent overall agreement with the data of Kataoka *et al* [71] was achieved. The liquid supply rate model may overspecify the model since the agreement is nearly as good for $n = 2$ where the liquid supply rate is equal to the constant steady-state CHF value as it is for larger values of n where the liquid supply rate varies with time.

$$W_{f0} \propto E(u') = \int_{u_v}^{\infty} p(u')(u' - u_v)du' \tag{2.1}$$

$$p(u') \approx \frac{C_1}{u'^n} \tag{2.2}$$

$$W_{f0} \propto \int_{\ddot{q}_{CHF-SS}}^{\infty} \frac{\xi - \ddot{q}_{CHF-SS}}{\xi^n}d\xi \tag{2.3}$$

$$W_{f0} = C_2 \cdot \ddot{q}_{CHF-SS}^{(2-n)} \tag{2.4}$$

$$W_{f0} \cdot \ddot{q}_{CHF-SS}^{(n-2)} = C_2 = W_f(t) \cdot \ddot{q}(t)^{(n-2)} \tag{2.5}$$

$$W_f(t) = W_{f0} \cdot \left(\frac{\ddot{q}_{CHF-SS}}{\ddot{q}(t)} \right)^{n-2} \tag{2.6}$$

2.3.2   Annular Film Dryout

For channels with steam quality in excess of approximately 0.1–0.2 the flow regime is annular. *e.g.* Olekhnovitch [28] cites a correlation, shown in Equation 2.7, for the onset of annular flow by Levitan and Borevskiy. Dryout in the annular flow regime is widely believed to occur when the liquid film is completely depleted through evaporation and entrainment of droplets into the vapour core. Hewitt and Hall-Taylor summarise the results of experimental and theoretical work on annular flow up to 1970 in [97].

$$x_{OAF} = (2.7 \pm 0.3) \cdot \left(\frac{G^2 d}{\rho_V \sigma} \right)^{-0.25} \left(\frac{\rho_L}{\rho_V} \right)^{-0.33} \tag{2.7}$$

Biasi *et al* [98] used a steady-state annular flow model based on a mass balance of the superficial liquid film mass flux as shown in Equation 2.8. They derived an expression for the deposition rate based on the concentration of liquid and the turbulent velocity fluctuations in the vapour core as well as the vapour-liquid density ratio. They then proposed that the entrainment rate was equal to the deposition rate at equilibrium and that the difference in the entrainment and deposition rates at non-equilibrium would be proportional to the difference between the local and equilibrium values of the liquid film flow rate. They obtained the expression shown in Equation 2.9 where τ_c is the vapour-film interfacial shear stress and S_{mc} is the mean core slip ratio. The resulting expression for the liquid film flow rate was integrated to the point where the liquid film flow rate decreased to zero. This equation was coupled to an energy conservation equation—a heat balance—and using appropriate initial and boundary conditions. Dryout was predicted to occur at the point where the film flow rate reached zero.

$$\frac{dG_{lf}}{dz} = \frac{4}{d} \left(D - E - \frac{\ddot{q}}{h_{LV}} \right) \tag{2.8}$$

$$D - E = 9.2 \frac{\rho_V^{\frac{3}{2}} \tau_c^{\frac{1}{2}} S_{mc}}{\rho_L G x d} \left(G_{lfeq} - G_{lf} \right) \tag{2.9}$$

With the empirical constant shown in the equation Biasi *et al* predicted some

positive inlet quality dryout data collected with a long unheated length preceding the heated section within approximately ±10%. Another set of 135 dryout data with subcooled inlet conditions but exit quality greater than 20% were predicted with an overall RMS error of 7.5%. A qualitatively accurate representation of the data of Bennet *et al* was also achieved. For this data a uniformly heated test section was interrupted by an adiabatic section in the centre. When heating was resumed downstream of the adiabatic section a higher heat flux was required in order to achieve dryout than was observed if the same heated length was continuous. It was believed that the liquid film flow rate increased in the adiabatic section as the annular flow was allowed to relax towards equilibrium values of entrained droplet and liquid film flow thereby increasing the heat flux necessary to completely evaporate the liquid film. The success of the liquid film flow model at predicting this phenomena supports the argument that the liquid film flow theory is representative of the underlying phenomena related to dryout.

Many correlations have since been proposed for both droplet deposition and entrainment from the liquid film since the work of Biasi *et al* outlined above. Attention in this work is focussed primarily on the work of Whalley *et al* and others in the UK. The annular film flow model developed there has been used to predict dryout for a range of transient conditions.

In addition to the depletion of the liquid film Hewitt [6] proposed that at a minimum the liquid film dryout is governed by the ability of deposited droplets to maintain a wetted surface at very high qualities. Hewitt presented experimental entrained liquid flow rate data for steam-water with a mass flux of 279 kg m^{-2} s^{-1} in a 9.3 mm tube at 0.247, 0.343, and 0.446 MPa. The data shows that the equilibrium entrained liquid fraction increases to a maximum then decreases with quality. Figure 2.2 shows the entrained fraction in a diabatic flow—as a function of heated length—and the corresponding equilibrium value for an adiabatic section. The rate of change of the entrained fraction in the diabatic flow causes it to increase or decrease toward the co-plotted equilibrium value. This partially supports Biasi *et al*'s assumption that the rate of change of the liquid film flow is proportional to its difference from the equilibrium value.

Doroschuk *et al* [7] found that for a diabatic flow there is a mass quality, be-
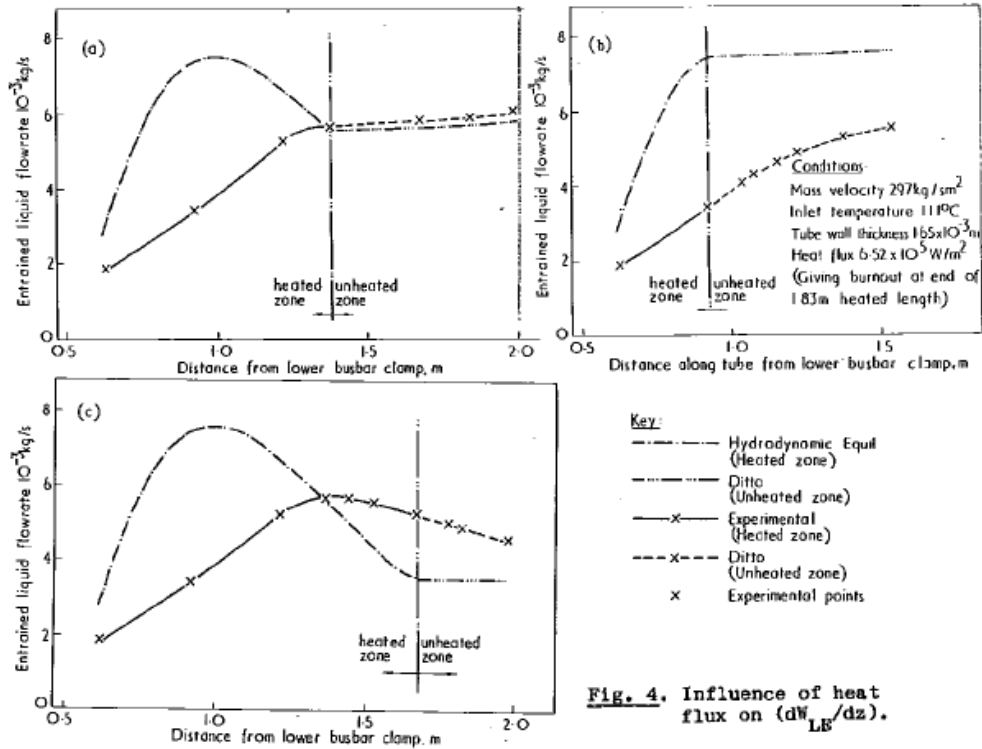
Figure 2.2: Hewitt's [6] entrained liquid fraction data for a uniformly heated diabatic flow plotted against axial position. The axial dependence of the equilibrium entrained fraction at the same local quality is also plotted. At all positions the diabatic entrained fraction changes to minimise the difference with the equilibrium value.

fore dryout occurs, where the two-phase multiplier begins to decrease with increasing quality and which is a function of liquid and vapour saturation density, mass flux, liquid viscosity, and surface tension. A similar phenomena of decreasing two-phase multiplier for high-quality, high mass flux flows before the onset of dryout was observed recently by Leung *et al* [99]. Doroschuk *et al* also defined a limiting quality for liquid film dryout using the same mathematical relationship with a slightly higher constant than for the change in slope of the two-phase multiplier. This relationship with the constant chosen for dryout in 8 mm tubes, is shown in Equation 2.10. This implies that this value of the limiting quality for dryout is related to the decrease in two-phase multiplier with increasing quality.

$$x_{DO}^2 G \frac{\nu_L}{\sigma} \left(\frac{\rho_L - \rho_V}{\rho_L} \right) = 0.0031 \tag{2.10}$$

These observations are consistent with the limiting quality regime (LQR) as referred to by Groeneveld *et al* in the 2006 CHF look-up table [5] and as observed in the dryout experiments of Olekhnovitch *et al* [100]. In the LQR the CHF changes drastically over a very small range of quality. The LQR is considered by Groeneveld to be one of the anomalies in CHF prediction that is not taken into account by existing empirical CHF prediction methods [8]. He states that it is widely believed that the limiting quality represents a transition from liquid film depletion or entrainment-controlled dryout to deposition controlled dryout. This is supported by the evidence presented by Hewitt [6] that is discussed above. The LQR is relevant to transient dryout in that it may represent a change in the governing phenomena— from liquid film depletion to droplet-deposition limited heat transfer—of dryout. This could contribute to uncertainty in the prediction of dryout during transient conditions if a finite time is required for this regime change to happen.

Whalley *et al* [101] also developed an annular flow model similar to that of Biasi *et al*'s [98] earlier model based on mass conservation of the liquid film, entrained liquid and vapour phases and thermodynamic equilibrium energy conservation. In order to close their liquid film flow model the deposition rate, D, and entrainment rate, E, were estimated using a mass transfer approach as shown in Equations 2.11– 2.12. C represents the homogeneous vapour core droplet concentration and C_E the equilibrium droplet concentration that was correlated by Hutchinson and Whalley [102] using a dimensionless group $\tau_i \delta / \sigma$. The mass transfer coefficient, k, was taken from experimental data for steam-water flow at 6.9 MPa. For other fluid systems k was estimated by optimizing the model for each fluid based on k for most of the results presented in the paper. A correlation of k as a function of surface tension was also presented and tested against data for water at 9.1 MPa and R-12 at 2.33 MPa with good results for dryout qualities greater than 30%. Their model did not include momentum conservation. Overall prediction accuracy was claimed to be equal to the empirical correlations available at the time.

$$D = kC \tag{2.11}$$

$$E = kC_E \tag{2.12}$$

The Whalley *et al* [101] model was expanded in 1978 [103] to include mass flow and pressure transients and the effects of flashing. They found that the influence of flashing on the predicted dryout length was negligible until the flow rate approached the critical value. They also reformulated the mass conservation equations for liquid film, entrained droplets and vapour for transient conditions. They tested their transient model against one of Moxon and Edwards flow transient experiments and found that their model underpredicted the time to dryout by a smaller amount than the quasi-steady method used by Moxon and Edwards.

James and Whalley performed a numerical experiment by superimposing a postulated pressure transient onto one of the Moxon and Edwards flow transient experiments [104]. They found that the predicted time to dryout—at the heated length of 3.66 m as used in the Moxon and Edwards experiments—was slightly shorter with the additional pressure transient but that the dryout length—in an hypothetical extension in the heated length simulated in the model—increased in the early stages of the transient. They ascribed the early increase in the dryout length to acceleration of the vapour core due to liquid flashing into vapour during the pressure transient.

Whalley, Lyons and Swinnerton [39] modelled the pressure transient experiments of Lyons and Swinnerton [3, 80] and observed the same initial increase in predicted dryout length at the beginning of their transient experiments. The observed increase in dryout length was attributed in this case to the mass flux increase observed in the experiments at the beginning of the transients. The same vapour acceleration would have been present in these modelled experiments as were in the hypothetical pressure transient experiment modelled by James and Whalley.

The dryout model was improved by Govan *et al* [105] by using a large database of equilibrium experimental entrainment and deposition data to develop correlations for the deposition mass transfer coefficient, k, and a droplet concentration-independent entrainment correlation shown in Equations 2.13 and 2.14 below. These correlations save the calculation steps required to estimate the interfacial shear stress and film thickness that were needed in the earlier model to determine the entrainment rate and also hypothetically allow any fluid to be modelled whose properties are known.

47

$$k\sqrt{\frac{\rho_V d}{\sigma}} = \begin{cases} 0.18, & \text{if} \frac{C}{\rho_V} \le 0.3 \\ 0.083 \left(\frac{C}{\rho_V} \right)^{-0.65}, & \text{if} \frac{C}{\rho_V} > 0.3 \end{cases} \tag{2.13}$$

$$E = \begin{cases} 5.75 \times 10^{-5} G_V \left((G_{LF} - G_{LFC})^2 \frac{d\rho_L}{\sigma \rho_V^2} \right)^{0.316}, & \text{if} G_{LF} > G_{LFC} \\ 0, & \text{if} G_{LF} \le G_{LFC} \end{cases} \tag{2.14}$$

$$\frac{G_{LFC} d}{\mu_L} = Re_{LFC} = \exp \left(5.8504 + 0.4249 \frac{\mu_V}{\mu_L} \sqrt{\frac{\rho_L}{\rho_V}} \right) \tag{2.15}$$

For a set of over 5000 dryout data points in six different fluids—over 95% from water and R-12—Govan *et al* found that the 'original' Harwell model performed better than the new model when the boundary conditions of Whalley and co-workers were used—onset of annular flow at $x_e = 0.1$ with an entrained fraction, ϵ, of 0.99—with mean underpredictions of 6.7% and 9.7% and standard deviations of 16.4% and 16.3% respectively. However, the new model improved to an underprediction of 0.8% with a standard deviation of 15.4% when the following boundary conditions were used:

$$\epsilon_0 = \begin{cases} 0.99, & \text{if } {}^{G}\!/_{G_{crit}} \le 0.2 \\ 0.90, & \text{if } {}^{G}\!/_{G_{crit}} > 0.2 \end{cases} \tag{2.16}$$

$$G_{crit} = 1.42 \left(\frac{z}{d} \right)^{0.85} \left(\frac{\rho_L}{\sigma} d \right)^{0.6} \tag{2.17}$$

The considerable improvement in prediction accuracy afforded by this relatively simple correction may be related to the entrainment fraction at the onset of annular flow. It may also be due to a dependency of the onset of annular flow on the mass flux as per the correlation that is shown in Equation 2.7 [28]. If it is assumed that $\epsilon_0 \approx 0.99$ then as the mass flux increases the onset of annular flow will occur at lower qualities so that the entrained fraction at $x \approx 0.1$ will decrease.

Hewitt and Govan [106] compared the results of this model with flow transient data from Moxon and Edwards [46] and Celata *et al* [83] in water at 6.9 MPa and R-12 at 1.3 and 2.8 MPa respectively. The prediction of the time to dryout for

the Moxon and Edwards data is underpredicted by a reduced amount compared to the original Whalley *et al* model [103] while the time to dryout of Celata *et al*'s data [83] was predicted generally within $\pm 20\%$ although several data points are overpredicted by more than this.

In addition to the liquid film transport models of Whalley and coworkers Chang *et al* [107] proposed a boiling length average analogy as a correction factor for flow and power transient annular film dryout. The form of their proposed correction factors are shown in Equations 2.18–2.19. The exponent 0.6 in the mass flux term is derived from the same exponent on the mass flux term of the high-quality region for the Biasi *et al* correlation [4]. Chang *et al* [107] computed the local conditions for several of Moxon and Edwards [46] power transient experiments and compared the time to dryout prediction between the Biasi *et al* correlation and the Biasi *et al* correlation with their correction factor. It was found that the Biasi *et al* correlation consistently underpredicted the time to dryout but that this underprediction was improved when it was modified with the boiling length average correction factor. No comparison was made between the steady-state data of Moxon and Edwards [46] and the Biasi *et al* or modified Biasi *et al* correlations.

$$\eta_u = \frac{\ddot{q}}{\ddot{q}_{BLA}} \left(\frac{G}{G_{BLA}} \right)^{0.6} \tag{2.18}$$

$$G_{BLA} = \frac{4L_B \ddot{q}_{BLA}}{x d h_{LV}} \tag{2.19}$$

Le Corre *et al* [108] compared the results of simulations for synthetic—with a single varying parameter—and realistic—pump trip and load rejection—transients for nominal BWR operating conditions using four different thermalhydraulic models using three computer codes: BISON, VIPRE-W and TRACE. The transients included a linear 0.2 MW s^{-1} power decrease, a 1 kg s^{-1} linear flow rate ramp and a 1.0 MPa s^{-1} increasing pressure ramp. Each transient began from steady state and was run for 1 s before the transient was stopped. The code continued to run with steady boundary conditions at the end of transient values for 3 s beore the transient was reversed. BISON is a four-equation one-dimensional system thermalhydraulics code that solves the momentum and energy equations for a two-phase mixture and

separate mass conservation equations for each phase using proprietary interphasal slip and heat transfer correlations. VIPRE-W is a subchannel code that was run using both a 3-equation model with one equation for each of mass, momentum and energy of the two-phase mixture using a drift flux model for slip and also a 4-equation model that had separate mass conservation equations for each phase. Both models assumed thermodynamic equilibrium. Finally, TRACE uses a six-equation two-fluid model with separate mass momentum and energy conservation equations for each phase and incorporates many closure relationships to model interfacial slip and heat transfer. The most significant differences in code behaviour were attributed to the selection of interfacial slip and void fraction models. It was concluded that the assumption of thermodynamic equilibrium between the phases was valid for the range of transients that were investigated.

2.4   Discussion

2.4.1   Dryout Onset Delay in Pressure Transients

There is evidence in the literature to suggest that, in many cases, the onset of dryout during transients can be well predicted using the quasi-steady method but in some cases there may also be an increase in CHF or delay in OID. Examples of CHF increase or dryout delay include the power and flow transients of Moxon and Edwards, the pressure and inlet flow stoppage experiments of Gaspari *et al* [78] and the pressure transient experiments of Celata *et al* [1]. Some analyses have shown that the Moxon and Edwards data can be well-predicted using the quasi-steady method—*i.e.* Iwamura [44] and Chang *et al* [107]. Without a systematic test of how well a method is able to predict steady state data from the same facility it is difficult to judge whether or not the accurate prediction of transient data is a coincidence or actually a good demonstration of the quasi-steady method. A major contribution of this work is that it compares transient results to self-consistent steady state CHF data from the same experimental facility and test section.

There are two data sets from the literature that show a transient effect in the onset of dryout for pressure transients: the data of Gaspari *et al* [78] and the data of

Celata *et al* [1, 2]. As described above Gaspari *et al* [78] proposed that the super-position of depressurisation onto an inlet flow stoppage transient caused a redistribution of liquid from the unheated to the heated wall in their annular test section. They believed that this resulted in the observed delay in the onset of dryout and that this would not be observed in a geometry that lacked unheated surfaces like a tube. When Celata *et al* [1] analysed their pressure transient data and included the discharge of thermal energy from the wall due to the decrease in saturation temperature with pressure they also observed a delay in the onset of dryout. Their inlet conditions correlation predicted that the total heat delivered to the fluid exceeded the dryout value very early in their transients while the increase in wall temperature associated with dryout was not observed until several tenths of a second later as illustrated in Figure 2.3 from [1].
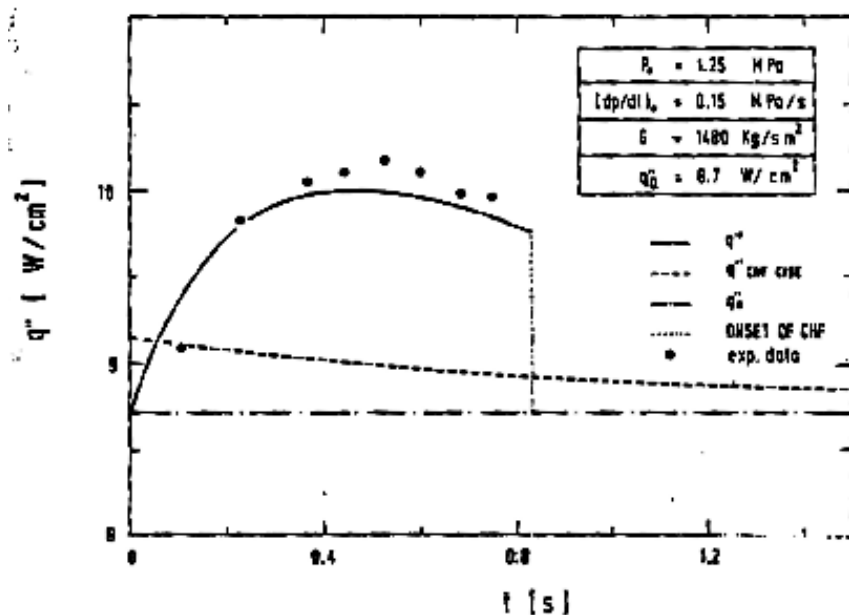
Figure 2.3: Pressure transient data from Celata *et al* [1]. The time-dependent additional heat flux caused by the release of stored thermal energy in the test section wall caused the predicted CHF to be exceeded early in the transient. The temperature excursion that indicated the onset of dryout was not observed until nearly 0.8 s after CHF was predicted.

Celata *et al*'s [1] pressure transient data were not analysed using the quasi-steady DSM. Their later work [2], that presented analyses of flow and power transients when combined with pressure transients, was performed using a local con-

ditions analysis based on a HEM formulation for the mass, momentum and energy conservation equations. For these transients they concluded that the quasi-steady method was insufficient for any of the transients where the maximum depressurisation rate exceeded 0.2 MPa s^{-1}. This suggests that within the limits of the HEM formulation the pressure transients could not be predicted using the quasi-steady model.

In contrast, Lyons and Swinnerton [3] and Whalley *et al* [39] found that removing the transient terms from the Whalley annular flow model had a minimal effect on its prediction of the dryout length for their pressure transient experiments. An example of a slow transient from Whalley, Lyons and Swinnerton [39] is shown in Figure 2.4. Figure 2.5 shows an example fast transient from the same work. In this latter figure the prediction results of the Bowring correlation and the transient annular film model are plotted against the observed dryout length. Figure 2.5 also shows the prediction results of the annular film flow model without any transient terms— these results were nearly identical to the results of the transient model. They found that the Bowring correlation, based on inlet conditions, was able to successfully predict the rate of dryout front progression although it overpredicted the length to dryout in the transients as it did for their steady-state results. These results suggest that not only did Lyons and Swinnerton not observe a delay in the onset of dryout but furthermore that the onset of dryout could be predicted by treating the transient as a series of steady states. These observations can be directly compared with those made by Celata *et al* [1] that were based on their inlet conditions correlation. These results beg the question of which observations are correct?

One major difference between the analyses of Lyons and Swinnerton [3] and that of Celata *et al* [1] is the effect that the release of thermal energy stored in the test section wall has on the dryout. In all except for a handful of Celata *et al*'s [86] pressure transient experiments dryout would not occur at all if not for the additional heat due to the stored energy. Lyons and Swinnerton [3] did not account for the additional heat due to stored energy in their computation of the dryout length. They did calculate the additional heat flux using the transient heat conduction equation for one moderate transient: Lyons and Swinnerton estimated that the energy storage resulted in an 8% peak in heat flux. For their fastest transient—with a maximum
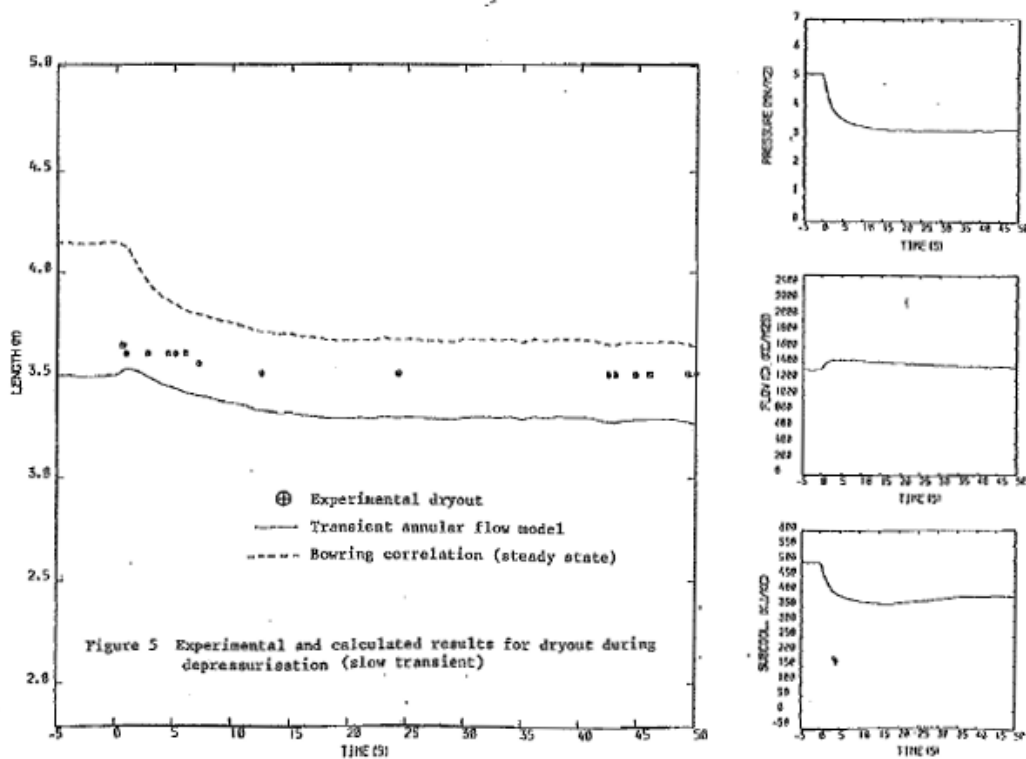
Figure 2.4: The progression of a dryout front during a slow transient from Whalley *et al* [39]. The predictions of the Bowring correlation and the annular film dryout model with time are also depicted. They respectively over and under-predict the dryout length as they did for Lyons and Swinnerton's [3] steady data.
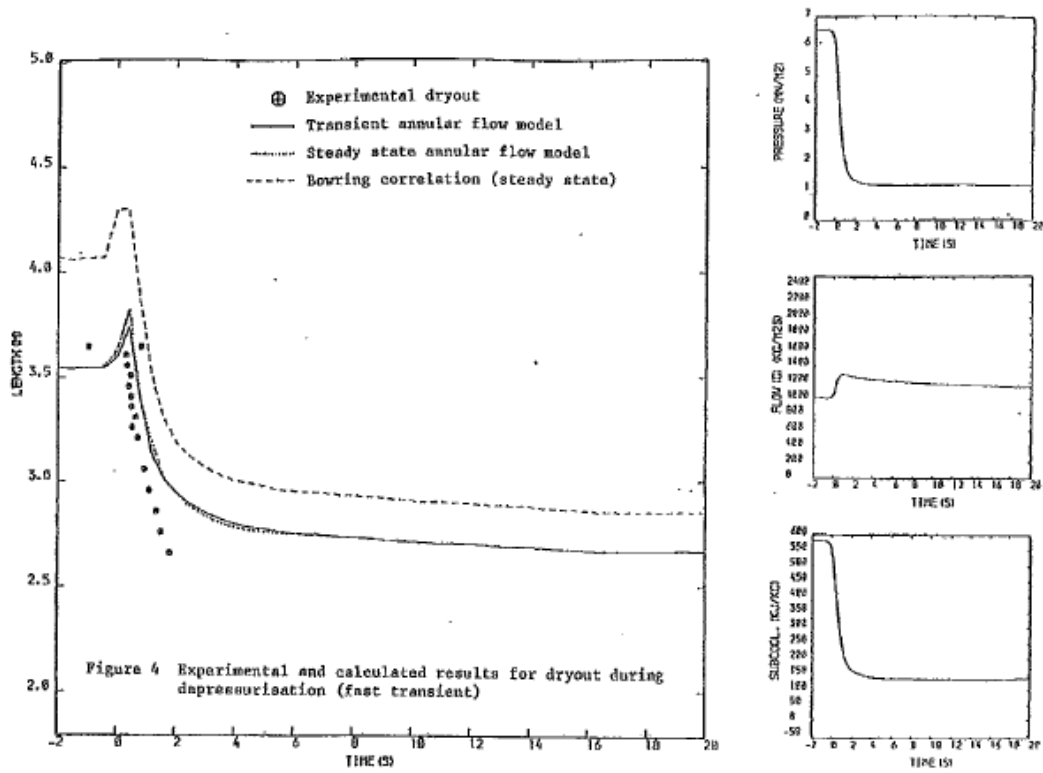
Figure 2.5: The progression of a dryout front during a very fast transient from Whalley *et al* [39]. In addition to the Bowring correlation and the transient annular film flow model the predictions of a steady version of the model are shown. The steady version's prediction was nearly identical to the transient version's.

depressurisation rate of more than 5 MPa s^{-1}—they estimated that the heat flux may increase by as much as 40% due to this effect [3].

Celata *et al*'s experimental loop [83, 1, 85, 2, 86] consisted of a positive displacement piston pump, an air bladder accumulator used as a flow oscillation damper, two parallel flow meters and flow control valves, a bypassable heat exchanger used to preheat the inlet fluid using the latent heat of the outlet fluid, a 10 kW electric preheater and a 15 kW electrically heated test section. The fluid passed through a regulating valve in parallel with the fast-acting valve used to initiate the pressure transients. Downstream of the test section the fluid was cooled by the 'preheater' and a water cooled condenser and passed back to a water-cooled holding tank. The Lyons and Swinnerton [3] loop was nearly identical except that a much greater amount of power is needed for a water experiment. Furthermore the Lyons and Swinnerton [3] loop was open: steam and water were discharged to atmosphere downstream of the test section for both steady and transient operation rather than into a closed-loop holding tank. Therefore it is unlikely that the design of the experimental loop influenced the difference in results between Lyons and Swinnerton and Celata *et al*.

Aside from the difference in the working fluid the only major difference in the experiments of Celata *et al* [1] and Lyons and Swinnerton [3] were the initial conditions. Celata *et al* conducted experiments with a margin to dryout and investigated the onset of dryout at the outlet of their uniformly heated test section. Lyons and Swinnerton increased the test section power until dryout was observed at its exit and then established steady-state with these conditions before initiating the blowdown. Therefore there are two possibilities for the difference in their conclusions: the effect of pre-existing dryout at their initial conditions or the relative magnitude of the thermal energy storage effect in the test section wall due to the different working fluids.

Experiments, like Celata *et al*'s [1], whose initial conditions have a margin to dryout may represent a slower dryout front progression for two reasons. First: droplets are able to wet the entire heated surface until the surface reaches intermittent dryout. The surface is relatively cool before OID so that radiative evaporation of droplets is minimized. The minimum film boiling temperature has not been ex-

B.A. Statham
Ph. D. Thesis

Chapter 2
Literature Review

McMaster University
Engineering Physics

ceeded so the droplets are able to wet the surface. Second: the later the dryout occurs the more likely that the peak in additional heat flux due to the release of stored thermal energy in the test section wall has already passed. This is illustrated in the top of Figure 2.6 where the local conditions before OID are shown.
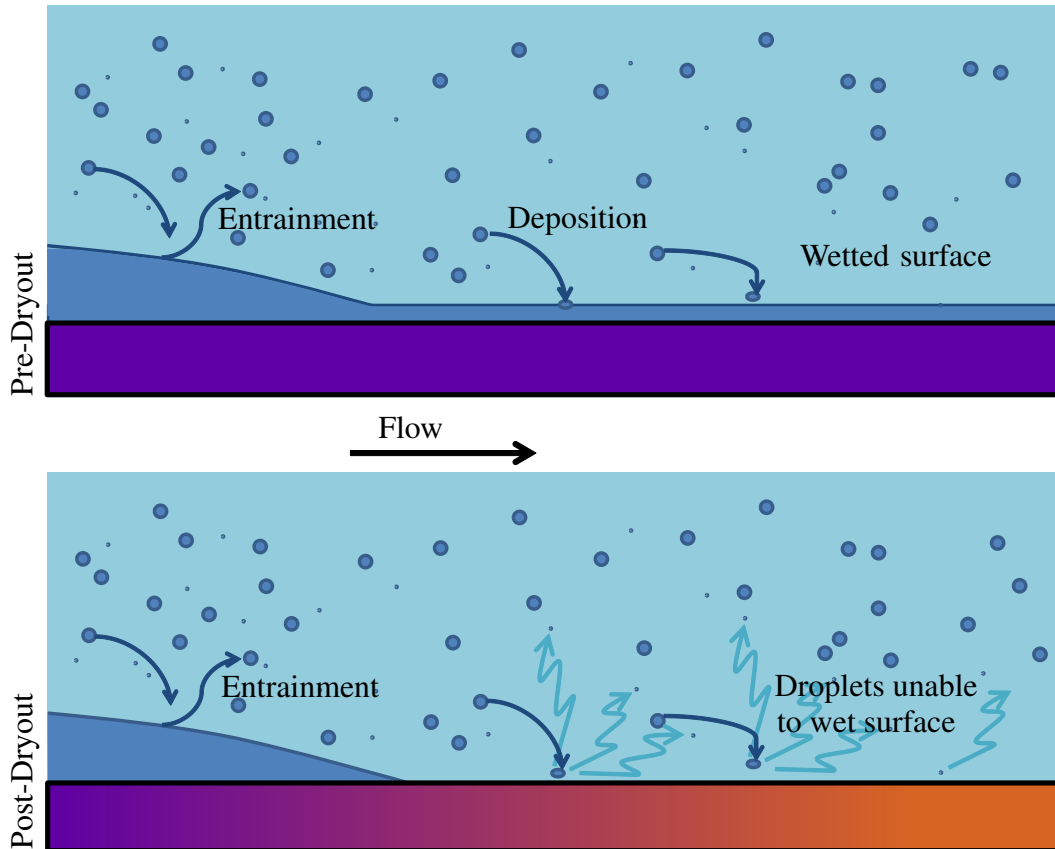
Figure 2.6: Depiction of pre- and post-dryout surface conditions before transient initiation. For pre-dryout initial conditions (top) the surface is cool and wetted by a continuous liquid film that must evaporate before dryout can occur. Post-dryout conditions have a hot wall that may cause additional dryout front progression due to axial conduction, prevents droplets from wetting the surface and lacks the continuous liquid film that is present before the onset of dryout.

Lyons and Swinnerton [3] state that the wall thermal storage effect for the fast transients may result in a peak heat flux as much as 40% in excess of the applied value early in the transient. Their experimental data should represent a limiting rapid case of dryout front progression for two reasons: the liquid film takes a finite time to evaporate if, *e.g.*, the liquid sublayer modelled by Serizawa [63] and

by Pasamehmetoglu *et al* [96] is used as an analogy. This film has already completely or partly evaporated at the test section exit at the initial conditions of Lyons and Swinnerton's transient experiments. Secondly, the test section wall is at an elevated temperature. Axial conduction may locally increase the extent of the region of dryout beyond what would be predicted based on the local conditions—heat flux, pressure, mass flux, quality—alone if the wall temperature is increased beyond the minimum film boiling temperature. This is illustrated in the lower portion of Figure 2.6 where the hot wall prevents the droplets from wetting the surface and there is an axial temperature gradient in the test section wall.

The Whalley *et al* model [39] is representative of the case without pre-existing dryout. It does not take the stored energy released into the fluid nor the hot-wall effects that prevent rewetting based on thermalhydraulic parameters alone. Hot wall effects were theoretically demonstrated by Hewitt and Govan [106] who modelled rewetting in a reversal one of the Moxon and Edwards flow transient experiments. They added a rewetting model that took into account the effects of post-dryout (PDO) superheat to the liquid film conservation equations. In this case there was a delay in the rewet transient compared to the predictions of the film flow alone. This makes the prediction capability of the Whalley model—without rewet—for the Lyons and Swinnerton data more remarkable since these phenomena are not represented.

2.4.2   Objectives of the Present Work

The objective of the present work is to clarify whether a delay in the onset of dryout is present, as observed by Celata *et al* [1, 2], or if quasi-steady methods are sufficient for predicted the onset of dryout during pressure transients as observed by Lyons and Swinnerton [3, 80]. An hypothesis that the initial conditions of these two sets of experiments was responsible for the differing conclusions of the two sets of authors was proposed based on the observations discussed above. It was proposed that a finite time would be required to evaporate the liquid film near the exit of the test section under MTD conditions while the effect of axial conduction may accelerate the initial rate of dryout front progression in PDO conditions as

illustrated in Figure 2.6.

In order to test this hypothesis a series of experiments were proposed. Pressure transient dryout experiments were conducted in a 4.6 mm ID tube with a heated length of 1.321 m and a wall thickness of 0.9 mm at initial pressures from 2 to 6 MPa and mass fluxes of 1000 to 2500 kg m^{-2} s^{-1}. The transients were conducted at conditions just beyond the onset of intermittent dryout (OID) and just below the onset of intermittent dryout. The experimental apparatus and procedure that was used is described in Chapter 3, steady state and transient results are presented and analysed in Chapters 4 and 5. The results are discussed in Chapter 6. Conclusions are made and future work is suggested in Chapter 7.

In order to quantitatively test the applicability of the quasi-steady method to transient data it is necessary to establish a reliable method of predicting the onset of dryout for the test section(s) used to conduct the transient experiments as Celata *et al* [83, 1, 85, 2, 86] did to reduce bias in the predicted times to dryout. Once an effective steady-state dryout prediction method based on the DSM or local conditions method is established the local conditions during the transient experiments must be computed. These local conditions can then be used to predict the time to dryout. The predicted time to dryout may then be compared to the experimentally observed dryout time in order to determine how well the quasi-steady method predicts the time to dryout.

The transient local conditions must be predicted using a method that includes the phenomena that are relevant to the parameters used in the chosen dryout prediction method(s). Based on the work of Celata *et al* [1] and Lyons and Swinnerton [3, 80] this must include the effects of thermal energy released from the wall due to the decrease in saturation temperature with pressure. In nuclear safety analyses these local conditions are computed using a thermalhydraulic systems code such as RELAP5, CATHENA, or TRACE. This approach was adopted for the present work. These codes incorporate heat structures that may be used to model the energy storage and thermal mass of solid components that are solved in parallel with the solution of the time-dependent mass, momentum, and energy conservation equations for both liquid and vapour phases in the fluid flow channel.

Chapter 3

Experiment

The experimental facility described in this chapter, including the hydraulics, instrumentation and control and data acquisition system, was designed, constructed and commissioned as part of this work. All components were pressure rated to at least 10.0 MPa and all instruments were calibrated before testing and after testing where possible. Calibration data has been included in Appendix D. It should be noted that the measurements in this text are written with SI units and prefixes. [1]

3.1   Flow Boiling Hydraulic Circuit

A schematic diagram of the entire circuit used to perform the experiments described in this text is shown in Figure 3.1. General features, operating specifications and components are described in the following subsection.

---

[1]Typically pressure is given in MPa, temperature in $^\circ$C, length in mm, mass in kg, energy in kJ, time in s and so on with other derived units. Most of the tubing and Swagelok tube fittings used to construct the experiment were manufactured according to the US imperial measurement system and their dimensions as given in this text were converted to metric. For example: the Inconel 600 tubing used for the test section was received as a 6 ft length of $1/4$ in tubing with a wall thickness of 0.035 in. This was converted, respectively, to a 2.835 m length of 6.4 mm outside diameter tubing with an inside diameter of 4.6 mm which is how it appears in the text. It should also be noted that the original pump performance data was also received with head in ft and flow in US gpm although the complete specifications were a mixture of metric and imperial units. This disclosure is made to facilitate those who might wish to duplicate the experiments in order to reduce the difficulty in sourcing components with what at first may appear to be esoteric dimensions.
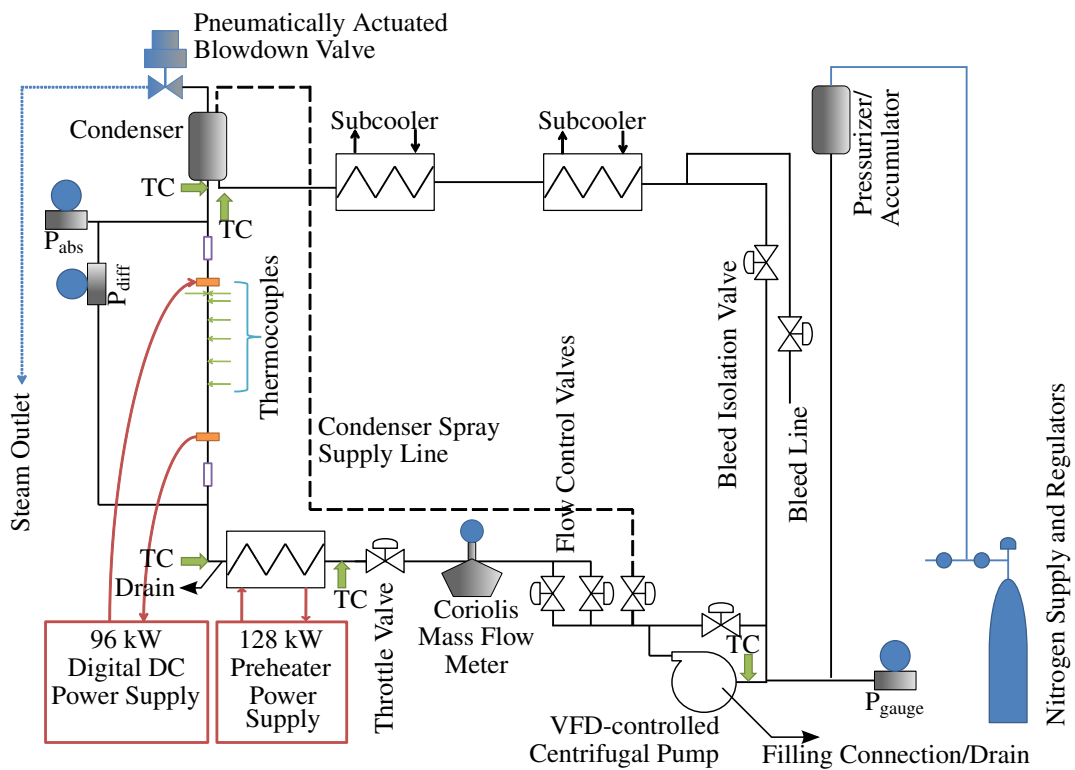
Figure 3.1: Schematic diagram of the Flow Boiling Hydraulic Circuit.

3.1.1   Pressurisation

The experiment was pressurised using a Hydac SB330-10A1/02S-210C 10 L nitrogen filled bladder accumulator mounted with its bottom connector 2.28 m above the level of the pump suction line. The process connection from the accumulator to the loop was made at the end of flow loop slightly upstream of the return connection from the experimental loop using 6.4 mm outside diameter tubing. Connecting the pressuriser to the loop at this location allowed close coupling of the applied pressure with the pressure in the condenser while simultaneously reducing the possibility that hot fluid would enter it. Close pressure coupling was possible because the head losses in the tubing and components between the condenser and the suction line of the pump recirculation loop were small compared to the head loss in the test section.

3.1.2   Pump and Recirculation Loop

A Klaus Union SLM NVHO 040-025-200-09E04 sealless magnetic drive centrifugal pump with a design operating point of 75 m head at 833 cm^3 s^{-1} volumetric flow was used to supply the driving force for the fluid through the circuit. Its nominal operating curve at 58.3 Hz for 1 mPa s, 1 Mg m^{-3} water at 23.2°C is provided in Table 3.1; these data may be scaled using the pump affinity laws in order to obtain pump curves at different operating frequencies. The calibration data used by the manufacturer to derive this nominal curve is given in Appendix D. The nominal operating range of the pump is: suction pressure 2.0 to 14 MPa, fluid temperature 50 to 205°C, total volumetric flow range approximately 2.5 to 8 m^3 h^{-1} and nominal kinematic viscosity of 15×10^6 m^2 s^{-1}.

The pump was driven by a 7.5 kW Siemens SD100 TEFC 215T electric motor that was supplied with power from a Siemens MicroMaster 440 variable frequency drive (VFD). The VFD was supplied with 575 V 3-phase AC power at 60 Hz. Using the VFD allowed soft was that it permitted the motor frequency to be controlled in 0.1 Hz increments over a typical range of 30 to 60 Hz via the buttons on the "Basic Operator Panel" or BOP. This allowed the operating point to be controlled to match the loop and test conditions. The VFD allowed the pump to be operated at lower

B.A. Statham
Ph. D. Thesis

Chapter 3
Experiment

McMaster University
Engineering Physics

Q (Lpm)	Head (m)	Pump Power (kW)	Motor Power (kW)
18.7	77.30	4.60	5.98
50.0	76.57	4.96	6.34
133	75.35	5.87	7.25
250	71.51	7.08	8.46
335	67.54	7.96	9.34
436.8	62.76	8.89	10.27

Table 3.1: Nominal pump curve data for operation at 58.33 Hz with water at 23.2°C, 1 mPa·s and 1 Mg m^{-3}.

frequencies but this was not recommended by the pump manufacturer.

Most of the fluid in the system circulated in the short recirculation loop near the pump; this maintained a minimum allowable flow through the pump to keep the pump head cool while acting as a pressure reservoir for the experimental flow path. 38 by 3 mm tubing was used exclusively in the recirculation loop aside from the parallel flow paths for the needle valves where 19 by 1 mm tubing was used. The test section flow was a small portion of the total flow circulated by the pump; *i.e.* the total flow through the test section and condenser spray line was on the order of 83 cm^3 s^{-1} compared to the minimum manufacturer specified pump flow of approximately 694 cm^3 s^{-1}.

Small changes in the flow through the experimental loop therefore had a negligible effect of the position on the pump operating curve and consequently little effect on the output head of the pump. The flatness of the head-flow curve at low flows, as shown by the data in Figure 3.1, also contributed to the head supply stability. The position on the pump operating curve, since each pump speed corresponded to a different head *vs* flow curve, could be adjusted using the two SS-18RS12 needle valves. These valves were connected in parallel in the recirculation flow loop immediately downstream of the pump discharge. The flatness of the pump curve was particularly important for transient conditions because it fixed the pump head supply to a relatively narrow region throughout the transient.

3.1.3   Condensing Spray Line

Part of the flow from the recirculation loop was diverted to the condenser to condense the steam generated in the test section. 6.4 by 0.9 mm SS316 tubing was used for this branch. Flow was controlled by adjusting a Swagelok SS-1RS4 needle valve. A BETE L80 spray nozzle distributed the discharge flow to the condenser in a cone spray pattern to increase the interfacial area and consequently the condensation rate.

3.1.4   Experimental Flow Path

The flow path from the recirculation line to the test section included two parallel flow control valves: one SS-1RS4 needle valve for fine control and one SS-1RS8 for coarse control. In practice the flow control valves were mainly used for throttling the flow upstream of the test section in order to damp two-phase instabilities by increasing the single-phase pressure drop relative to the two-phase pressure drop. 12.7 mm tubing is used for all intermediate connections except where noted or where the flow path is reduced down to 6.4 mm tubing when SS-1RS4 throttle valves were used. The inlet mass flow rate was then measured using an AW-Lake ACM1500 coriolis mass flow meter. Another SS-1RS4 throttle valve follows the flow meter before the fluid enters the preheater.

Following the preheater the flow enters a U-tube with a total flow length of 3.05 m that was used to provide a delay between the preheater exit and the text section inlet. This stored fluid at the correct temperature so that the inlet temperature remained constant for most of the duration of the transient tests.

Downstream of the test section the flow area was increased by adapting the flow path to 19 mm tubing before entering the centre of the condenser through the bottom. Steam was condensed there before leaving as liquid through an off-centre process connection in the bottom of the condenser vessel. It was then cooled in two counterflow co-axial heat exchangers before it was returned to the pump recirculation loop.

3.1.5   Preheater

The preheater consisted of 9.5 mm SS316 tubing fabricated into a 7-turn 191 mm diameter coil with a coil pitch of approximately 30 mm. It was electrically heated by passing a current through the coil supplied by a 128 kW DC power supply with all specifications similar to that of the test section power supply. It was electrically isolated using Conax EG-375-A-XX-L electrode glands.

3.1.6   Test Section

Heated Length

The test section was a 1.575 m length of Inconel 600 tubing with an inside diameter of 4.6 mm and a wall thickness of 0.9 mm. The total heated length was 1321 mm and thermocouples were silver-soldered to the test section 955, 1113, 1229, 1276, 1293, 1305 and 1316 mm from the beginning of the heated length as depicted in Figure 3.2. These heated lengths non-dimensionally correspond to 209, 242, 267, 277, 281, 284 and 286 diameters (z/D). Heat was generated in the test section wall by the resistance of the metal when a DC current of up to 1600 A was supplied by a 96 kW DC power supply. Electrical connections were made by a two-piece copper clamp. This clamp consisted of two 30 mm long by 100 mm wide by 13 mm thick bars with a 6.4 mm round half-channel routed lengthwise in each one and 13 mm bolt holes located centrally between the channel and the edge of the width as shown in Figure 3.3. The clamps were fastened tight using 13 mm hex-head screws, nuts, one lock washer, and two regular washers. The heated length was considered to be the distance between the interior edges of each clamp along the running length of the Inconel tube.

Process Measurement Locations

The inlet temperature was measured using a 1.6 mm diameter K-type thermocouple immersed in the fluid at a 90 degree bend in the flow path. This arrangement helped to ensure well mixed conditions existed at the thermocouple measurement location. A schematic diagram of the flow path upstream and downstream of the test section,
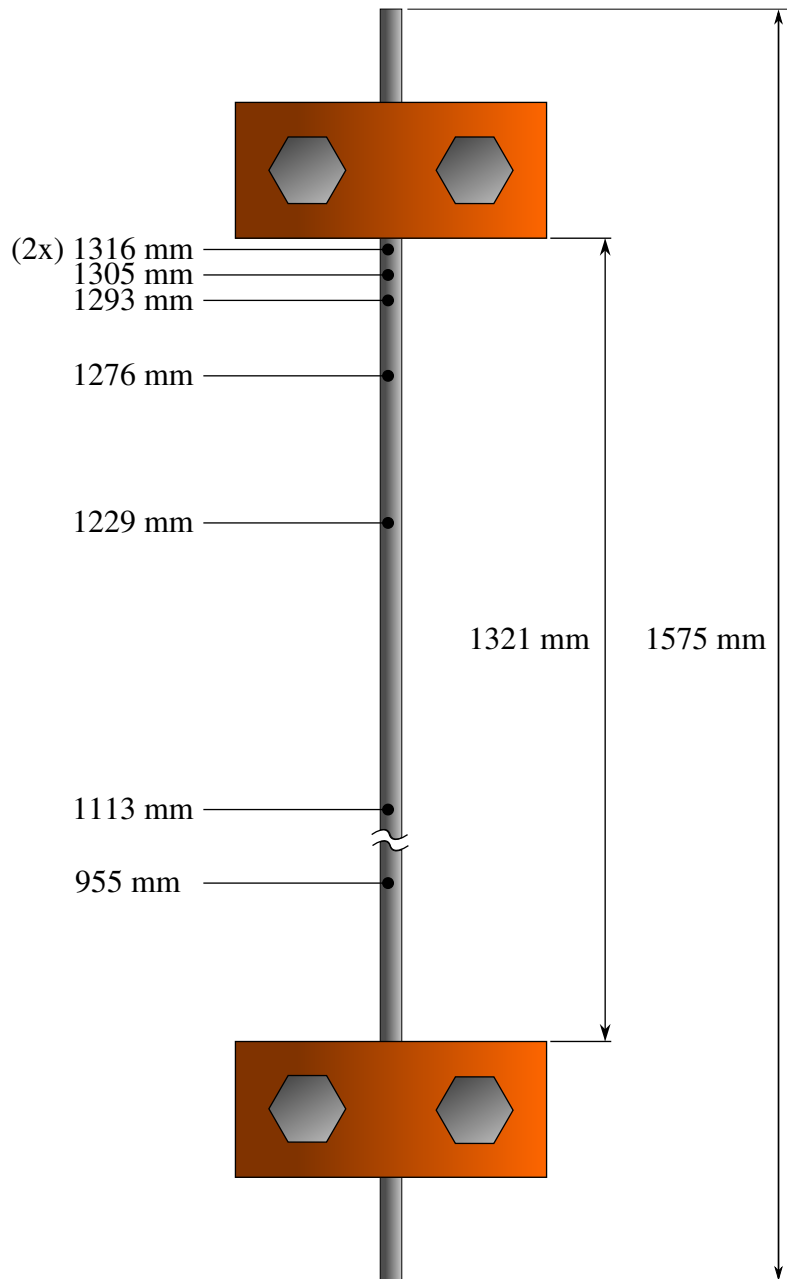
Figure 3.2: Test section diagram showing full length, heated length, and thermocouple locations.
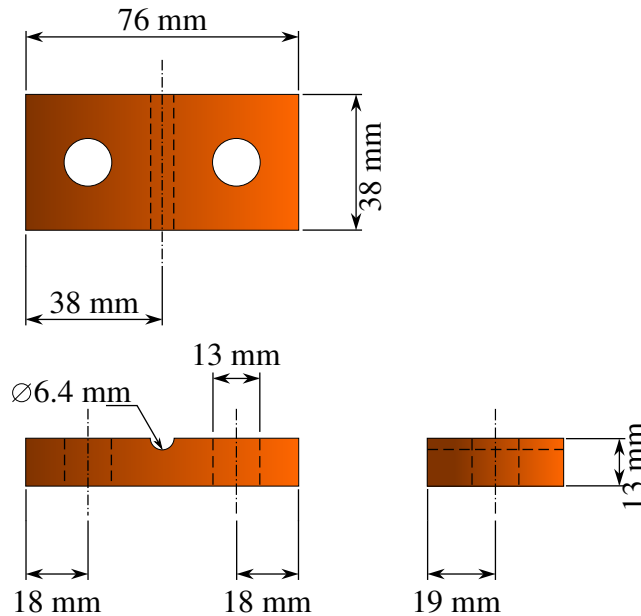
Figure 3.3: Schematic diagram of half of a bus bar clamp. Two each of these are used at the beginning and end of the heated length.

including the locations of the inlet temperature measurement and the sense line connections for the outlet and differential pressure, is shown in Figure 3.4.

Downstream of the last fitting in the flow path shown in Figure 3.4 the temperature is measured using a 3.2 mm K-type thermocouple inserted through a Swagelok SS-200-R-8BT bored-through fitting installed in the branch connection of an SS-810-3 tee. Before the two-phase flow enters the condenser the flow area was increased again by increasing the tubing diameter from 13 mm to 19 mm using an SS-1210-6-8 fitting.

3.1.7　Condenser

At the test section exit steam was condensed by a spray of subcooled droplets in the condenser depicted in Figure 3.5 and manufactured by Sleegers Engineered Products. The condenser was manufactured from a 229 mm length of 168 mm outside diameter by 11 mm wall SS316 tubing—ANSI schedule 80 6" pipe—with a 13 mm wall by welding on round 38 mm thick end plates. This resulted in a cylindrical condensation volume with an internal length of 203 mm and diameter of

Out to Test Section

SS-400-6

164 mm long tube
6.4 mm x 0.9 mm

Conax EG-250-A-XX-L

SS-400-7-8

48 mm long tube
6.4 mm x 0.9 mm

Inlet Pressure
(Differential)

SS-400-3

48 mm long tube
6.4 mm x 0.9 mm

SS-810-6-4

330 mm long tube
13 mm x 1 mm

SS-810-3TFT
+SS-6-RB-4
+SS-100-1-4BT

Flow Inlet

Inlet Temperature
(K-type TC)

Outlet Pressure
(Absolute)

SS-810-3-8-4

48 mm long tube
13 mm x 1 mm

SS-810-7-8

Conax EG-250-A-XX-L

94 mm long tube
6.4 mm x 0.9 mm

SS-400-6

From Test Section

(a) Upstream of Test Section   (b) Downstream of Test Section

Figure 3.4: Flow path upstream and downstream of the test section. Not to scale.

147 mm for a total volume of 3.42 L. Fluid entered the centre of the bottom of the condenser via a 19 mm tube that extended approximately 95 mm from the bottom of the inside of the volume. This was done using a Swagelok SS-1210-1-12BT bored-through MNPT to Swagelok adapter fitting.

Under normal conditions all fluid left the condenser through a neighbouring process connection in the bottom of the condenser whose centre was offset by 51 mm from the centre of the condenser. The fluid temperature at the condenser exit/subcooler entrance was measured using a 1.6 mm diameter K-type thermocouple immersed in the fluid through an SS-100-1-4BT fitting adapted to the NPT run connection of an SS-810-3TFT fitting using an SS-6-RB-4 bushing similarly to the inlet fluid temperature measurement described below and shown in Figure 3.4.

During blowdown transients fluid could also leave the condenser as a two-phase mixture through the top central process connection that led to the pneumatically actuated blowdown valve. One 51 mm-offset on each of the top and bottom was used for the sense lines of a level sensor in order to keep track of the liquid level. Steam was condensed by flow delivered to a BETE L80 spray nozzle that was supplied with subcooled liquid from the condenser spray supply line. A Swagelok bored-through fitting was used to allow the 6.4 mm tubing of the condenser spray line to penetrate through the top of the vessel head and was bent so that the spray was aimed towards the two-phase inlet.

3.1.8 Blowdown Valve

A High Pressure 10-11-AF4-MPO-NC electrically controlled pneumatically operated valve was used to perform blowdown transient experiments. It was connected to the top centre process connection of the condenser. Its opening time was estimated to be 90 ms using a high-speed video camera as shown in Appendix G. The valve is actuated using an electrical solenoid valve supplied with 24V DC power. Power was switched using a National Instruments (NI) 9481 relay module controlled by an NI LabVIEW Virtual Instrument (VI) that is described below. The solenoid shuts the air supply on and off. Air was supplied at 0.6 MPa by a pressure regulator connected to a high pressure medical air tank.
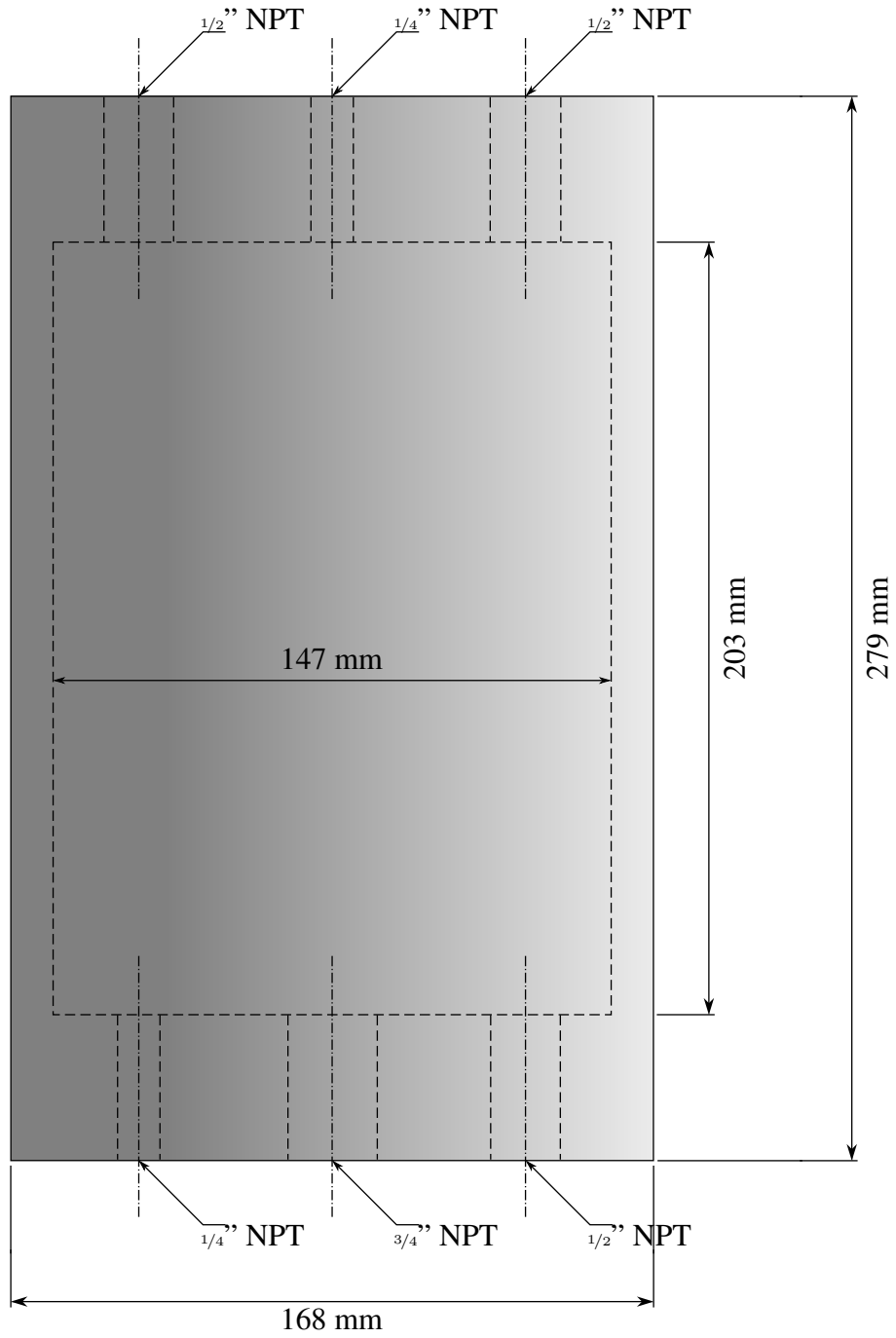
Figure 3.5: Condenser Schematic.

3.1.9 Subcoolers

Under normal operation, *i.e.* any condition other than blowdown, the flow from both the test section and the condensing spray line left the condenser as saturated or nearly saturated liquid. Two counterflow co-axial heat exchangers were used to subcool the liquid before it returned to the pump.

The first subcooler was an Exergy model 00528 which consists of a 13 mm by 2 mm wall inner tube with a 25 mm by 2 mm wall outer tube arranged in 9.5 oval-coils with straight runs of approximately 102 mm each and an end radius of 152 mm. The estimated heat removal capacity is 43 kW based on 100 g s^{-1} flows in each branch with cooling fluid entering the inner tube at 80°C and hot fluid entering the outer tube at 250°C. The heat exchanger was set up with the inner tube as the hot side and the cooling flow in the outer tube. Cooling water was supplied in a closed loop by a Micropump GC-41 gear pump with an estimated maximum mass flow rate of 110 g s^{-1} assuming it was equipped with the 'M25' gear set [109]. This closed loop was cooled by an Armstrong tube-in-shell heat exchanger supplied on the shell side with university chilled water at 5–7°C that cooled the flow to between 20 and 50°C.

The second heat exchanger was made from 9.5 mm SS316 tubing on the inner side and 25 mm copper tubing on the outer low pressure side. The outer tubing was a coil with 6 turns approximately 203.2 mm in diameter. The outer tube of this heat exchanger was provided with cold water from the municipal supply. The exact performance of this heat exchanger was unknown but operating experience suggests its capacity was approximately half that of the Exergy model.

During the tests that were performed to obtain the data in this text the maximum steady state heat removal demand for these two heat exchangers was approximately 65 kW. This supports the argument that the second heat exchanger capacity was approximately half that of the first.

3.2 Instrumentation

Four types of process measurements were made in order to record data from the Flow Boiling Hydraulic Circuit: wall and fluid temperature, differential, absolute and gauge pressure, mass flow rate, and voltage measurements in order to calculate test section and preheater power. The instruments used for each of these process measurements are described below.

3.2.1 Temperature

All temperature measurements were made using Omega type K thermocouples. The supplier stated accuracy of these probes is the greater of $\pm 1.1°$C or $\pm 0.4\%$ for 0 to 1250°C. Specific details about how the probes were configured is outlined below.

Fluid Temperature

Fluid temperatures were measured by immersing thermocouple probes directly in the fluid using bored-through Swagelok fittings in the locations outlined in the Flow Boiling Circuit described above. The inlet temperature, condenser outlet temperature, and preheater inlet temperature probes were 1.6 mm in diameter with Omega-clad XL probe cladding material while the outlet temperature probe was 3.2 mm in diameter with Inconel 600 cladding material.

Fluid temperature was also estimated in unheated sections using outer tube surface measurements where it was necessary to have a process measurement that was not critical to the experimental results. The first was on the tube surface near the pump suction flange as an indicator of the temperature of the fluid entering the pump. Similarly the outer tube surface temperature at the entrance of the U-tube immediately downstream of the preheater was also measured using a 0.25 mm thermocouple to aid with preheater control since the inlet temperature thermocouple was located several metres downstream of the preheater exit.

Wall Temperature

Test section wall temperatures were measured using Omega KMQIN-010U-6 and KMQIN-010U-12 K-type 0.25 mm diameter Inconel 600 sheathed thermocouples. They were silver-soldered to the outside of the tube surface. Before performing experiments this technique was tested on two thermocouples. They were calibrated, soldered to a test piece of Inconel, and then cut out from the tubing surfaces where the thermocouples were attached. Once they were removed—along with small pieces of the tube—they were re-calibrated and found to be within specification.

The thermocouples used to obtain the results presented in this text were silver soldered to the test section surface in the locations shown in Figure 3.2.

3.2.2 Pressure

Outlet Pressure

A Rosemount 3051CA absolute pressure transducer with an output current of 4-20 mA for an input of 0–13.8 MPa was used to measure the pressure downstream of the end of the test section heated length. Quoted experimental pressures in this text refer to measurements made by this sensor. The process connection for this sensor is shown in Figure 3.4.

Instrument	Reference Accuracy	Five-Year Stability	Temperature Effect per 28°C	Response Time
3051CA	0.065%FS	0.125%URL	0.025%URL +0.125%FS	100 ms
3051CG	0.065%FS	0.125%URL	0.0125%URL +0.0625%FS	100 ms
3051S1CD	0.025%FS	0.20%URL[*] *10 years	0.009%URL +0.025%FS	100 ms

Table 3.2: Pressure transducer uncertainties. FS refers to the calibrated span while URL refers to the upper available range limit for the instrument. The manufacturer specifies uncertainties to $\pm 3\sigma$

.

The measurement uncertainties for this sensor are shown in Table 3.2. This

instrument was received from the distributor on 13 February 2009. Tests were performed over the period from 2009–2013 and recalibrated by Cal-Matrix Metrology on 11 October 2013 using NIST traceable reference standards. It was found to be within specifications and no change was made to the zero or range settings. Calibration data can be found in Appendix D.

Differential Pressure

A Rosemount 3051S1CD differential pressure transducer calibrated to 0–0.8 MPa input for 4–20 mA output was used to measure the test section pressure drop. The sense lines for this transducer were connected to the upstream process connection shown in Figure 3.4 while the downstream (low) pressure connection was made at the same point as for the outlet pressure.

This instrument was received from the distrbutor on 2 August 2011. Tests and experiments were performed from 2009–2013. It was then calibrated by Cal-Matrix using NIST traceable standards on 21 Oct 2013. The instrument was received in tolerance at that time and no adjustments were made. Instrument uncertainty is listed in Table 3.2 and calibration data is available in Appendix D.

Gauge Pressure

The suction pressure was measured upstream of the suction run of the pump recirculation line—co-located with the accumulator process connection—using a Rosemount 3051CG gauge pressure transducer. This sensor provided a check against the absolute pressure transducer, allowed the pump head to be checked at startup by blocking the test section and condenser spray return line using a plug valve, and enabled the NPSH available to be estimated in conjuction with a temperature measurement made on the surface of the pump suction line near the pump entrance.

This instrument was calibrated to 0–13.00 MPa by Stern Laboratories on 20 March 2009. It was re-calibrated on 11 October 2013 by Cal-Matrix using NIST traceable instruments and found to be within specifications; no changes in zero or span were made. Uncertainty values for this instrument may be found in Table 3.2 and the most recent calibration data in Appendix D.

3.2.3 Mass Flow Rate

An AW-Lake ACM-1500 coriolis mass flow meter configured to output 4–20 mA for 0–50 g s-1 measured the test section inlet flow. The uncertainty specifications are shown in Table 3.3. It was received on 4 May 2010 with manufacturer's calibration curve dated 30 April 2010 as shown in Appendix D.

Basic Accuracy	0.5%
Zero Stability	0.01%URL
Zero Drift per °C	0.002%URL
Repeatability	0.1%
Resolution (bits)	14
Linearity	0.05%FS
Temperature Drift per 10°C	0.05%

Table 3.3: Flow transducer and transmitter uncertainties.

3.2.4 Voltage (Power)

The electrical power supplied to the test section and preheater were calculated using the product of measured voltage drop and current measurements. The voltage drop measurements were taken from leads sandwiched between the bus bar clamps very near the outside edge of the test section and preheater tubes, *i.e.* the heated length beginning and ending points. Current measurements were made indirectly by measuring a 0–50 mV voltage drop on a calibrated 0–2000 A current shunt resistor.

Model	Accuracy	Temperature Effect per 10°C	Response Time
WAP-DS-99A-3	0.10%FS	0.15%FS	25 ms
WAP-DS-16A-3	0.10%FS	0.15%FS	25 ms

Table 3.4: Watanabe isolator measurement uncertainties.

Voltage

The test section and preheater voltage were measured using 0–100 V WAP-DS-99A-3 Watanabe isolation transformers that converted the voltage into a 4–20 mA current signal. Both the preheater and test section unit were received with calibration data dated 7 March 2013. Uncertainties for these transmitters can be found in Table 3.4 and calibration data is listed in Appendix D

Current

The supply current was converted into voltage signals using model #90000-1143 2000 A calibrated shunt resistors from Canadian Shunt Industries. These shunts were calibrated to 0–50 mV. The unit that was used for the test section current measurement was received in March 2012 with a calibration certificate dated 27 March 2012. The certificate specified a resistance of $25\mu\Omega\pm0.1\%$ with a confidence interval of 95% measured using an applied current of 100 A. The preheater shunt was received in October 2012 with a calibration certificate dated 24 October 2012 and specified a resistance of $25\mu\Omega\pm0.1\%$ with a confidence interval of 95% measured using an applied current of 22 A. Both certificates specify that the measurements are traceable to the reference standards at the Canadian Natural Research Council or the US NIST.

The 0–50 mV voltage drop across each shunt was coverted into a 4–20 mA signal using Watanabe WAP-DS-16A-3 isolation transformers. Both units were received with calibration data dated 7 March 2013. Their uncertainties are listed in Table 3.4 and calibration data is listed in Appendix D.

3.3 Power Supplies

Two TopCon programmable DC power supplies supplied by Magnavolt, Inc. were used to power the test section and preheater respectively. Their configurations were slightly different but their specifications were nearly identical. The test section unit was a TCP96.100.480.SHMI 96 kW supply and the preheater unit was a TCP128.100.480.SHMI unit. Both had internal 3-phase transformers to reduce the

input voltage from the supplied value of 600 V to the unit input requirement of 480 V. Some specifications common to both units are given in Table 3.5; for more information see [110].

Static Accuracy	0.1%FS
Transient Reponse Time	2 ms
Stability	0.05%FS
Temperature Coefficient	$0.03^{\%FS}/_{\circ C}$
Output Ripple	V_{pp}: 1.1%FS @300 Hz
Output Noise	V_{pp}: 1.5 V 0.04–1 MHz

Table 3.5: Power supply output specifications. Values correspond to the current regulation operating mode that was used exclusively for both power supplies during all experiments.

Current was conducted by 373.7 kcmil diesel locomotive stranded copper flexible cable from the power supplies to the test section and preheater. Four each of these cables were used for the send and return to the preheater current shunt and the return from the preheater bus bar. Two 1 m lengths were used to connect the preheater shunt to the preheater inlet bus bar. Three cables were used to connect the positive output of the test section output to the test section shunt, a single 1 m cable was used as a connector from the shunt to the test section outlet bus bar, and two cables connected the test section inlet bus bar to the negative terminal of the power supply.

3.4   Data Acquisition and Control Interface

LabVIEW was used extensively for both data acquisition and control. This section describes first, the hardware used for data acquisition, and secondly the LabVIEW VI and associated user interface used to display process measurements and to control the prehater and test section.

All instrument signals were sampled using National Instruments (NI) Compact DAQ (cDAQ) modules arranged in a cDAQ-9178 8-slot chassis. Signals from the

chassis were communicated via a USB cable with 32-bit resolution to a PC running NI LabVIEW software. The relevant specifications for the NI 9203 and NI 9213 modules used to measure current output from process measurements and to convert thermocouple EMF to temperature are shown in Table 3.6. Typical values are given in the table; see [111] and [112] for more information. Sample rates are for the entire module and must be divided by the number of channels used. Two of each module were used: one NI 9203 for the test section and preheater power measurements and one for pressure and flow process measurements. Similarly one NI 9213 was used for wall thermocouples and one for fluid temperature measurements. In the case of the NI 9213 this was done partially to increase the available sample rate to 150 Hz per channel and also to electrically isolate the test section from the rest of the loop since the NI 9213 has channel-to-ground but not channel-to-channel isolation.

Model	NI 9203	NI 9213
Channels	8	16
Measurement Range	21.5 mA	78.125 mV
Gain Error	0.66%	0.08%
Offset Error	$99\mu A$	$14\mu V$
ADC bits	16	24
Gain Drift/ Sensitivity	± 14 ppm/$^\circ$C	0.25°C
Offset Drift/ CJC Accuracy	63 nA/$^\circ$C	0.8°C
Maximum Sample Rate	200 kHz	1200 Hz

Table 3.6: cDAQ module specifications.

A LabVIEW Virtual Instrument (VI) was created in order to display and record all process measurements and to control the blowdown valve solenoid. Unless otherwise specified this will henceforth be referred to as 'the VI' in the text. A screenshot of the VI's main display is shown in Figure 3.6. The data display consisted of both large text boxes for several temperature measurements and time-series plots. The text boxes displayed the temperature measurements from the flow meter's internal resistance temperature device (RTD), the preheater inlet thermocouple, the

77
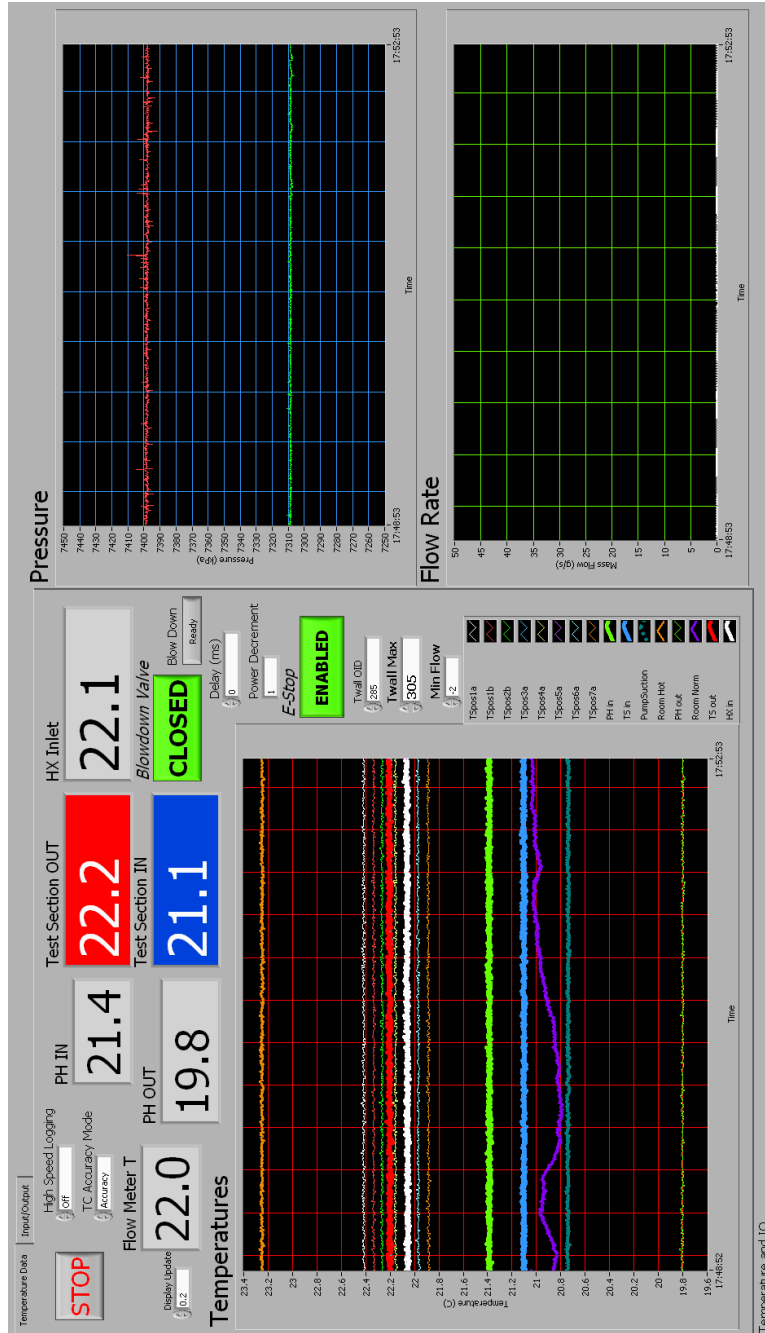
Figure 3.6: LabVIEW VI for process measurement visualisation and experiment control.

preheater outlet surface temperature thermocouple, the test section inlet temperature, test section outlet temperature, and the condenser outlet temperature. All temperature measurements were displayed on one large plot, the outlet pressure, pump suction pressure, differential pressure, and condenser level were displayed on another, the mass flow rate was displayed on a third, the preheater and test section power were displayed on a plot in a separate window, and the condenser level was displayed a second time in its own plot in another separate window.

The VI was able to control the sample rate and range parameters for each of the DAQ modules and the user could specify the frequency at which displayed values—both plots and text boxes—were updated. All process signals were written to plain-text ASCII files—one file for each DAQ module—using the same samples and sample rate displayed in the text boxes and on the plots. Data could be recorded at the full sample rate by switching high speed logging on from the GUI. High speed data was logged to an NI proprietary binary format Technical Data Management Streaming (TDMS) file that could later be read and translated into a tab-delimited file using another VI.

The blowdown valve was controlled and its status was indicated by three controls on the VI: A manual open/close button, a blowdown delay time control that allowed a predetermined opening period to be set in ms, and a blowdown button that initiated the blowdown of predetermined length. The manual open/close button displayed the status of the valve regardless of the method used to set its position. One channel of an NI 9481 4-channel electro-mechanical relay module was used to trigger the 24V solenoid that allowed air from a medical gas cylinder to pressurise and open the blowdown valve and to relieve the pressure and allow the valve spring to return the valve to the closed position.

Several emergency power supply shutoff features were also built in to the VI. This included a manual power supply emergency stop button on the VI interface, power supply step and power supply shutdown signals triggered by test section wall temperature measurements, and a low flow preheater shutoff triggered by the measured flow rate. The manual emergency stop made use of the remaining three channels in the NI-9481 relay module. Two of these channels were required for the preheater power supply's dual parallel emergency stop switch circuit and one for

that of the test section power supply. The temperature and flow measurement-based power supply trips made use of LabVIEW global variables to change the state of the state-machine based power supply control VIs that are described below. The wall temperatures and the low flow rate that would trigger the power supply trips could be specified on the VI's user interface while the VI was running. The low flow trigger set the output current setting on the preheater to 33.2 A corresponding to a total output of approximately 165 W. The test section step change trigger—labelled 'Twall OID' on the VI where the temperature setting could be adjusted—caused the power supply control VI to reduce test section power by 1.5% by multiplying the current output setpoint by 0.9925. The shutdown trigger—labelled 'Twall Max'— instructed the test section power supply VI to set the output to off without changing the actual output setpoints.
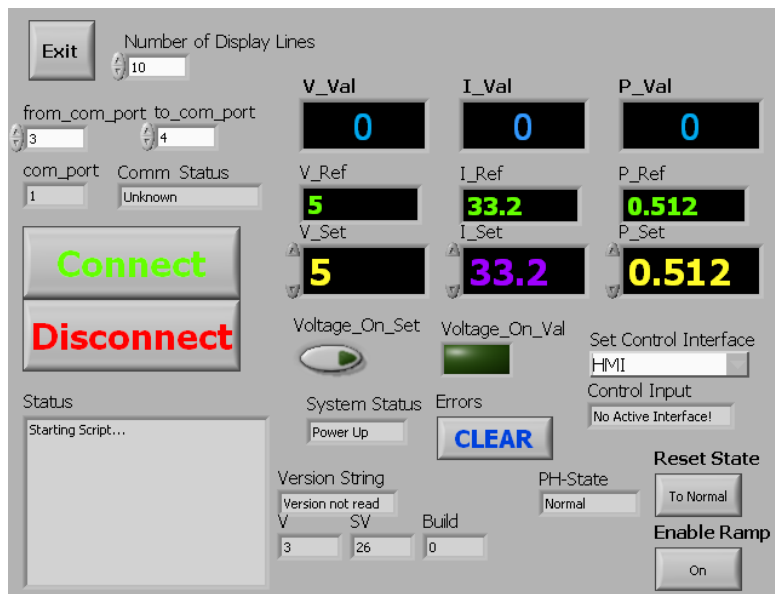
Figure 3.7: LabVIEW VI for preheater power supply control.

Both the test section and preheater power supplies were controlled by LabVIEW VIs during experimental runs using a manufacturer-supplied C library that could be compiled into LabVIEW function blocks [113]. A screenshot is shown in Figure 3.7. This VI was created using state-machine principles with two main states— connected and disconnected—and several substates including: Normal, Blowdown,

Ramp, Dryout (test section only), CHF (test section only) and Low Flow (preheater only). In all modes the voltage and power output setpoints could be adjusted freely from the power supply VI.

In Normal mode the current limit setting was adjusted in the same way. The Ramp state was activated by selecting a button on the power supply VIs. It allowed an external VI to control the current limit setting; the VIs created for this purpose linearly increased the supplied power in time as implied by the name. The power supply VIs would be triggered to switch to the Blowdown state whenever the predetermined-length blowdown was initiated from the main VI. This suspended control of the current output from the power supply VIs and automatically decremented the power to both power supplies to a user-supplied fraction of the initial power at the same time as the relay was triggered to close the blowdown valve. The CHF, Dryout, and Low Flow states were triggered as described above. A button on the power supply control interfaces allowed the user to reset the state to Normal whenever any of the other modes was active. Clicking this button returned exclusive control to the power supply VI itself.

In addition the power supply control itself could be set from within the VI to several states: HMI, RS-232, and Analog Input. Control signals—aside from changing the control interface selection itself—from the VI would be ignored in the HMI and Analog Input modes but the output values and limit settings measured by the power supply would continue to be updated.

3.5 Experimental Uncertainty

All experimental uncertainties were calculated by propagating the variances and sensitivities of the components of each measurement with respect to the measured value using the error propagation equation shown in Equation 3.2 [114]. Covariances were assumed to be small enough to be disregarded. The sources of error include the instrument accuracy, linearity, and zero stability, DAQ bit precision and DAQ random and systematic gain uncertainties and DAQ reference junction accuracy. The manufacturers' specified values were used unless otherwise specified. Typical values for total uncertainties in boundary condition measurements are

shown in Table 3.7.

$$y = f(x_0, ...x_i, ...x_n) \tag{3.1}$$

$$\sigma_y^2 = \sum_{i=0}^{n} \sigma_i^2 \left(\frac{\partial y}{\partial x_i} \right)^2 \tag{3.2}$$

Measurement	Uncertainty
Outlet Pressure	± 0.1 MPa
Mass Flux	± 25 kg m^{-2} s^{-1}
Heat Flux	± 45 kW m^{-2}
Inlet Temperature	± 1.4°C

Table 3.7: Typical values of measurement uncertainties to 1 standard deviation.

3.6   Experimental Procedure

This section lists the experimental procedures for both the approach to steady state CHF and the collection of transient data. Standard operating procedures including the loop filling procedure, startup procedure and shutdown procedure from two-phase conditions are listed in Appendix B

3.6.1   Approach to Steady State CHF

For the approach to CHF the same procedure was followed for steady-state data collection listed in Appendix B except that the intervals between test section power were reduced from several kW to approximately 100 W.

1. The approach to CHF begins when the test section power exceeds the CHF look-up table CHF value by 1–2 kW. This was based on preliminary experiments that found the look-up table underpredicted the data by approximately 10%.

2. Change the 'Twall OID' and 'Twall Max' settings so that the former exceeds the current wall temperatures by approximately 10°C rounded up to the nearest 5°C and the latter is 100°C greater. This will set the power back 1.5% if the lower limit is exceeded and shut off the power supply before the test section is damaged if the wall temperature begins to increase dramatically.

3. Obtain steady-state boundary conditions.

4. Record data for 1 minute.

5. Increment test section power by 0.6 A. The current can be adjusted in steps of 0.3 A but 0.6 A was approximately the minimum change that resulted in an observable change in the measured power output.

6. Repeat previous three steps until the desired CHF/OID criteria have been met. There were two criteria for ending the steady-state portion of the experiment by ceasing power increases. Either: one thermocouple's temperature regularly and rapidly varied over a range of 3–5°C or temperature jumps in excess of 8°C were periodically observed. This corresponded to conditions slightly in excess of OID.

3.6.2 Transient Experiment Procedure

Transient data were collected at the maximum test section power for a given steady-state experiment and with the power reduced from this value by 1.5%.

1. Establish steady-state for the desired initial conditions.

2. Set 'Twall Max' to a value slightly below material failure limits. Usually this was somewhere between 700–800°C corresponding approximately to the melting point of silver solder. Set 'Twall OID' to a value approximately 100°C below Twall Max—usually this was sufficient to stop excessive temperature transients from reaching 'Twall Max' and causing the power supply to be tripped.

3. Set 'Delay' to the desired duration of the blowdown in ms.

4. Set 'decrement' to the desired fraction of preheater and test section power desired immediately upon closure of the blowdown valve. Usually this was simply set to 1.0.

5. Record Steady-State Data for 40–60 s. The time data collection was initiated, the test section and preheater measured power, the test section and preheater power supply current limit settings, the Twall Max and Twall OID settings, the pump frequency, the blowdown duration and the power decrement were recorded on paper for future reference.

6. Initiate blowdown by depressing the Blow Down button. When the preset delay time had elapsed the blowdown valve would close and the loop pressure would recover. Continue recording data until the wall temperatures return to approximately their pre-blowdown values. The total duration of the steady-state plus blowdown transient and recovery to steady state was approximately 240 s in most cases.

7. In some cases the pressure and flow rate may require some adjustment to return to the previous steady state.

8. Adjust test section power to 98.5% of the maximum power. Repeat the steps above to obtain transient data for initial conditions with a small margin to dryout.

3.7   Summary

This chapter described the experimental apparatus and operating procedure used to obtain the experimental data presented later in this thesis. The experimental loop was constructed using SS316 tubing and Swagelok fittings and pressurised using a nitrogen charged bladder accumulator. The flow was driven by a Klaus Union high-pressure centrifugal pump capable of supplying over 0.8 MPa of delivery head at pressures up to 15 MPa. The test section was constructed of a 4.6 mm inside diameter length of Inconel 600 tubing with a heated length of 1321 mm. Blowdown experiments were performed with the use of a electronically controlled pneumatic

valve that simulated a break in the pressure boundary of a nuclear power reactor heat transport system at the test section outlet. Power was supplied to the test section and preheater using Regatron digitally-controlled DC Power supplies.

Process measurements were made using Rosemount 3051C and 3051S pressure transducers, an AW-Lake coriolis mass flow meter and Omega K-type thermocouples. The data from these instruments were recorded using a NI Compact DAQ 8-slot chassis equipped with two 16-channel 9213 thermocouple modules and two 8-channel 9203 0-20 mA current modules. This chassis also housed an NI-9481 electromechanical relay module that was used for both emergency power supply shutdown and to actuate the blowdown valve solenoid.

Process measurements were displayed on a LabVIEW VI that also facilitated control of the blowdown valve and emergency shutdown of the power supplies if process measurement limits were exceeded. Separate VIs were used to control the digital power supplies.

Commissioning data including heat balance, pressure drop, and heat transfer data are presented in Appendix C. Steady critical heat flux data is presented in Chapter 4. Transient experimental data follows in Chapter 5.

Chapter 4

Steady-State Results

4.1 Dryout Data

4.1.1 Boundary Conditions at Dryout

Steady-state dryout data were collected so that they could be compared to dryout prediction methods from the literature. The data was used to modify or adjust the methods from the literature to eliminate any systematic error in predicted *vs* observed CHF values. The elimination or reduction of systematic error was important for transient experiments since this would be directly reflected in a systematic bias in the predicted times to dryout. A large systematic underprediction of CHF would result in the transient dryout being predicted before the transient was initiated and a large systematic overprediction could lead to no dryout prediction during the transient at all.

In total, 22 dryout data points were collected for 15 different sets of boundary conditions at pressures of 2–6 MPa and mass fluxes of 1000–2500 kg m^{-2} s^{-1}. This is representative of the entire range of initial conditions for the transient experiments that were conducted. Dryout was observed at a heated length of 1316 mm—the nearest thermocouple position to the end of the total heated length of 1321 mm.

The boundary conditions for all dryout points were controlled to within ±0.5°C, ±10 kg m^{-2} s^{-1}, and ±0.005 MPa for the inlet temperature, inlet mass flux, and outlet pressure, respectively. This corresponded to a standard deviation in the inlet

quality of less than 0.1% over all observed dryout points. A table of the boundary conditions for all of the experimental dryout points are shown in Table 4.1.

Run ID	P_{out} (MPa)	Mass Flux (kg m^{-2} s^{-1})	T_{in} (°C)	Heat Flux (kW m^{-2})
0826-no004	4.0 ±0.1	1490±20	195.6±1.4	1770 ±40
0827-no005	5.0 ±0.1	1990±30	212.5±1.4	1950 ±50
0827-no019	6.0 ±0.1	2490±30	227.2±1.4	2010 ±50
0827-no028	6.0 ±0.1	1490±20	227.6±1.4	1620 ±40
0829-no007	5.0 ±0.1	990±20	212.5±1.4	1400 ±40
0829-no013	6.0 ±0.1	1490±20	227.8±1.4	1620 ±40
0904-no010	4.0 ±0.1	1490±20	195.7±1.4	1780 ±40
0904-no023	3.0 ±0.1	1490±20	175.2±1.4	1820 ±40
0906-no015	4.0 ±0.1	1990±30	195.6±1.4	2050 ±50
0906-no028	3.0 ±0.1	1990±30	175.4±1.4	2110 ±50
0908-no010	2.0 ±0.1	1990±30	149.5±1.4	2110 ±50
0909-no009	2.0 ±0.1	990±20	149.1±1.4	1450 ±40
0909-no031	2.0 ±0.1	1500±20	148.9±1.4	1830 ±40
0910-no008	4.0 ±0.1	990±20	195.6±1.4	1450 ±40
0910-no021	3.0 ±0.1	1000±20	175.4±1.4	1480 ±40
0911-no006	4.0 ±0.1	1490±20	195.7±1.4	1790 ±40
0913-no006	4.0 ±0.1	1490±20	195.6±1.4	1780 ±40
0917-no004	4.0 ±0.1	1000±20	195.4±1.4	1430 ±40
0917-no015	4.0 ±0.1	1490±20	195.5±1.4	1780 ±40
0918-no010	4.0 ±0.1	2490±30	195.4±1.4	2280 ±50
1113-no015	6.0 ±0.1	1990±30	227.5±1.4	1800 ±40
1114-no017	4.0 ±0.1	1490±20	195.5±1.4	1770 ±40
1115-no027	2.0 ±0.1	2000±30	149.5±1.4	2100 ±50

Table 4.1: Table of steady CHF boundary conditions and run ID numbers.

The steady state dryout data point for 4 MPa and 1500 kg m^{-2} s^{-1} was repeated six times. The standard deviation of the CHF was 7.5 kW m^{-2} or 0.4%. This was approximately one third of the total uncertainty for the heat flux and indicates that the experimental apparatus had very good repeatability for steady state data.

4.1.2   Dryout Data Selection

The OID data shown in Table 4.1 were chosen from steady state data points based on two criteria. The first criteria was based on the evidence of heat transfer deterioration, *i.e.* an increased rate of change of wall temperature with heat flux. The second criteria was based on the standard deviation of the wall temperature over the total sampled time. An increase in standard deviation was indicative of intermittent dryout. The processes that were used to collect the steady state data and to select the dryout data from each data set are outlined in this section.

Figure 4.1 shows the progression of boundary conditions as the CHF was approached for one series of steady state experiments. The boundary conditions excursion at an approximate time of 29 000 s was caused by the power supply current being decreased due to a wall overtemperature trip. As CHF was approached the overtemperature trip was kept within 10–20°C of the nominal observed maximum wall temperature and a single sample that exceeded this value would trigger a power decrease.

If the short power excursion is disregarded Figure 4.1 shows the applied test section heat flux increasing in steps and the adjustment of boundary conditions over time. Smaller steps generally required less time to reach steady state with the boundary conditions within acceptable limits, *e.g.* there is one power step at approximately 28 000 s and 1785 kW m^{-2} where steady state was obtained quickly. The reduced data that were taken from the data shown in this figure are discussed below and displayed in Figure 4.2.

At each intermediate steady state the process measurements were recorded at high frequency for approximately 1 minute. This recorded data was then reduced to a single data point composed of mean values for process measurements and two measures of the standard deviation of the wall temperature. Appendix A describes the data processing methods in detail.

The standard deviation of the wall temperature remained roughly constant until the slope of the mean wall temperature *vs* heat flux curve began to increase. As the heat flux was increased the standard deviation then also began to increase rapidly. The wall temperature was plotted against heat flux on the primary axis of Figure 4.2. Figure 4.2 also contains a simultaneous plot on the secondary y-axis—in reversed
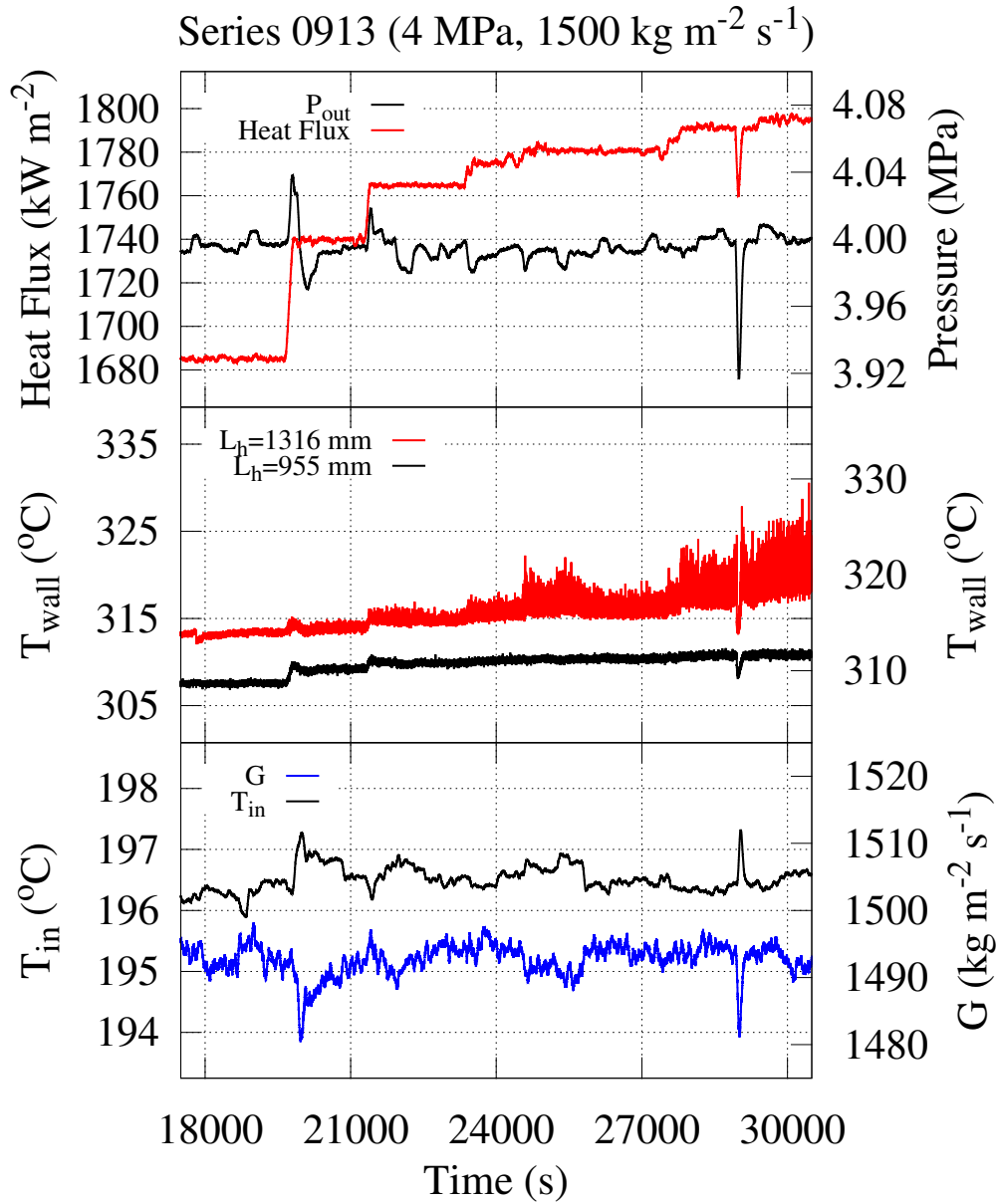
Figure 4.1: Variation of the controlled boundary conditions during the steady approach to dryout. The test section heat flux is increased in steps while the outlet pressure, inlet mass flux, and inlet pressure are controlled within a prescribed range before data is recorded at high frequency. In the middle section of the figure the variation in wall temperature near the EHL (L_h=1316 mm) and upstream (L_h=955 mm) as a result of the increased test section power are shown. The variance of the wall temperature near the EHL increases substantially as OID is approached and exceeded.
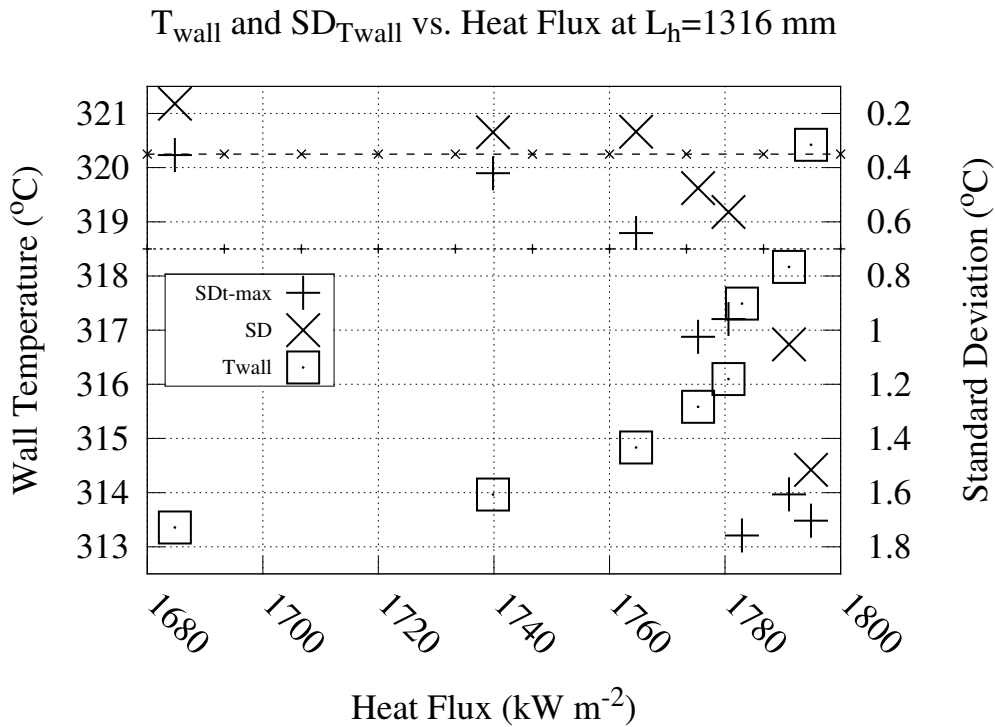
Figure 4.2: Wall temperature and its standard deviation *vs* Heat Flux for the reduced data from the experiment depicted in Figure 4.1. The change in slope of the wall temperature *vs* heat flux curve was accompanied by an increase in the overall and maximum time-dependent standard deviations of the wall temperature. Threshold values of standard deviation for OID are depicted as dashed lines with $\times$ and $+$ markers for steady and transient dryout conditions, respectively. The variation in wall temperature was due to intermittent surface dryout and rewetting.

co-ordinates—of the overall standard deviation of the wall temperature based on all high frequency samples for each data set. The reduced data in this figure may be compared to the data in Figure 4.1 that are from the same experiment series. When these two figures are compared the increasing variability of the wall temperature with increasing heat flux that is evident in Figure 4.1 translates into the increasing wall temperature standard deviation in Figure 4.2. All of the steady-state data from the present work was plotted on wall temperature and standard deviation *vs* heat flux axes and have been included in Appendix C.

The standard deviation was previously used as a dryout criteria by Del Col and Bortolin [12]. Their experiment used R245fa, R134a and R32 as the working fluids to simulate two-phase flow at a wide range of reduced pressures in a microchannel heated externally by a counterflow of hot water. They calculated the standard deviation based on 50 samples taken at 1 s intervals. The wall temperature standard deviation in the region of intermittent dryout was triple its value in the pre and post-dryout regions of their test section. The test section in the present work was heat flux controlled rather than temperature controlled so that no transition boiling region is observed in the steady state experiments. As a result the standard deviation was observed to continuously increase in the region of intermittent dryout.

The standard deviation of the wall temperature was calculated two different ways in the present work. The first method calculated the overall standard deviation of the wall temperature for all time values in each recorded data set. The second method calculated the standard deviation at each sample time step using all samples in the preceding 0.1 s and taking the maximum value of these sampled values over all times. This was done in order to establish a basis for determining the onset of dryout during transients.

The OID data that were selected satisfied two criteria: the overall wall temperature standard deviation was at least $0.35°C$ and the wall temperature lay in the region of increased wall temperature sensitivity to heat flux. Based on these data a criteria was developed for the 0.1 s windowed standard deviation that was used to detect OID during transients: $\sigma_{\Delta t = 0.1\ s} > 0.7$. The application of this method to the transient data is described in Chapter 5 and Appendix F.

4.1.3   Pre-Dryout Wall Temperature Discontinuity

For all boundary conditions the wall temperature increased steadily with heat flux in the two-phase region until it reached 90–95% of the steady CHF. When the heat flux was increased beyond this value a discontinuous decrease in the steady value of the wall temperature of up to 5°C was observed. This behaviour is shown in Figures 4.3–4.5. These figures contain plots of the heat flux plotted against the mean outside wall temperature. As the heat flux increased in these figures the observed mean steady-state wall temperature jumped downwards to a minimum value. When the heat flux increased beyond this local minimum the observed temperature resumed increasing. Initially the wall temperature increased more slowly with increasing heat flux than before the jump and then gradually began to increase more rapidly as the surface dried out with increasing frequency.

Figures 4.3 and 4.4 show wall temperature data for experiments conducted at 2 and 5 MPa respectively for a mass flux of 1000 kg m^{-2} s^{-1}. At 2 MPa the decrease in wall temperature when the jump occurs is less than 1°C while at 5 MPa it is nearly 5°C which suggests that this phenomena increases in magnitude with pressure. Figure 4.5, that contains a similar plot of data collected at 4 MPa with an inlet mass flux of 2500 kg m^{-2} s^{-1}, shows that this phenomena was observed at the highest tested mass flux in addition to the lowest tested mass flux as in Figures 4.3 and 4.4.

4.1.4   Parametric Trends of Dryout Data

At constant pressure the CHF increased with mass flux and decreased with local quality as shown in Figure 4.7 for all mass fluxes at 4 MPa. For constant mass flux, as shown in Figure 4.6 for 2000 kg m^{-2} s^{-1} the CHF decreased with pressure above 3 MPa. The CHF value at 2 MPa was slightly lower than the value at 3 MPa. The presence of a local maximum in CHF in the region below 5 MPa, as seen in Figure 4.6 and the dependency of CHF on mass flux and quality at constant pressure as shown in Figure 4.7 is consistent with the description of parametric trends described in [25]. Therefore the steady state data from the present work were consistent with available descriptions of parametric trends from the literature.

T_{wall} Discontinuity Before OID
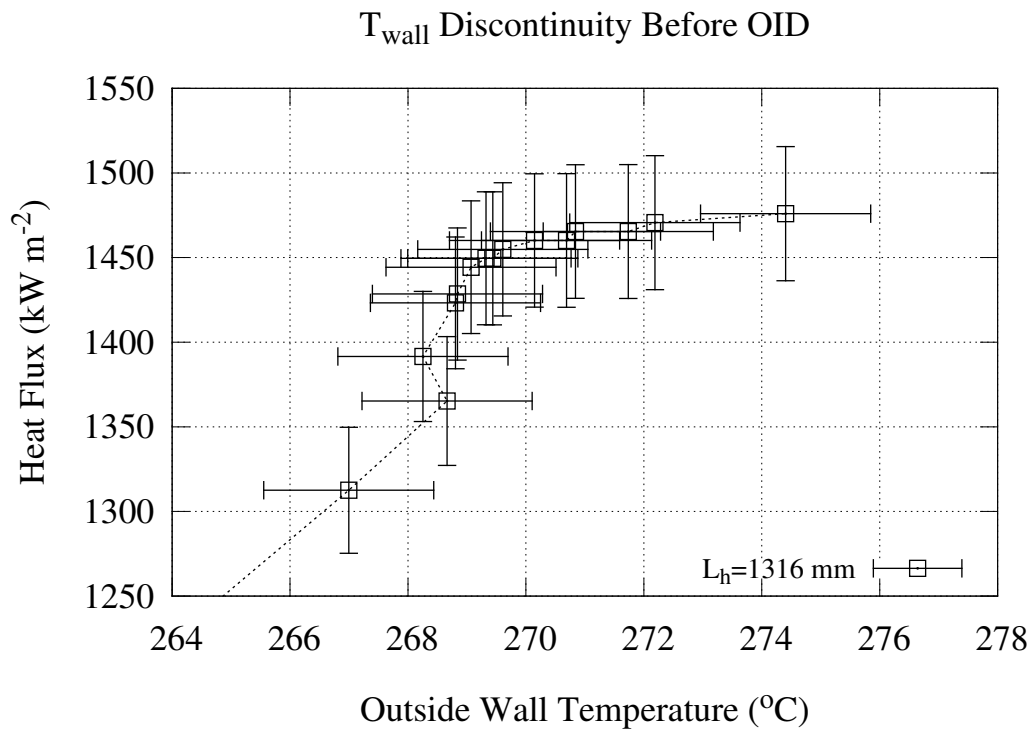
Figure 4.3: The measured outside wall temperature from an experiment conducted at 2 MPa with a mass flux of 1000 kg m^{-2} s^{-1} discontinuously jumped from 269 to 268°C when the heat flux increased from 1360 to 1390 kW m^{-2}. This signified a change from liquid film evaporation to droplet evaporation heat transfer. The data at heat fluxes below the jump followed a continuous line of steadily increasing wall temperature with heat flux.

T_{wall} Discontinuity Before OID
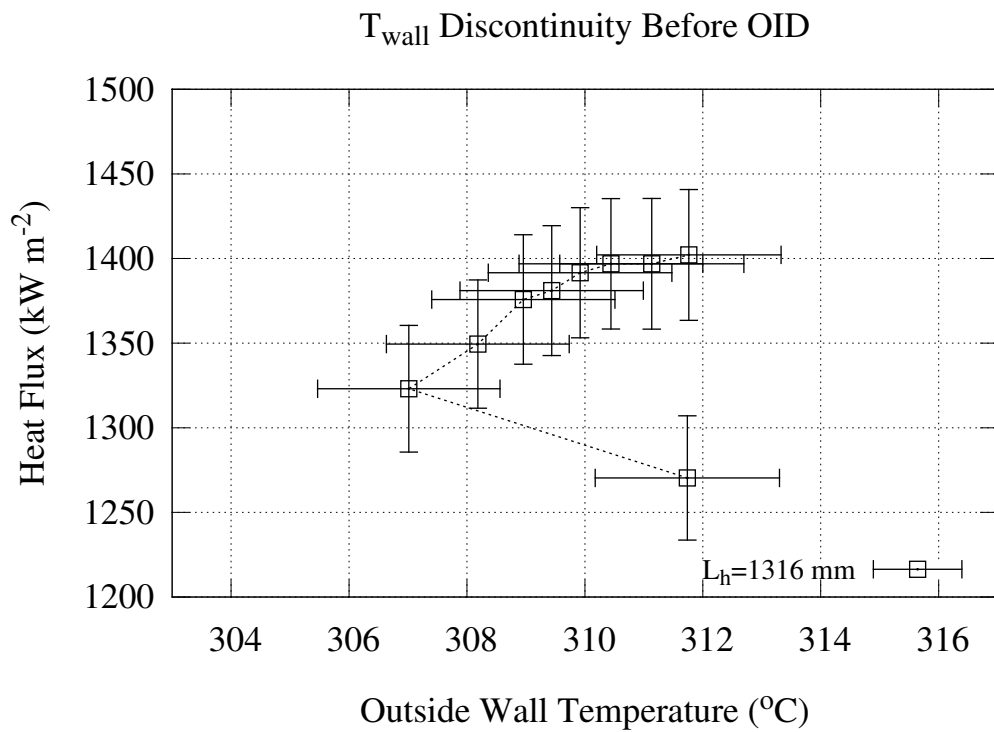
Figure 4.4: The measured outside wall temperature from an experiment conducted at 5 MPa with a mass flux of 1000 kg m^{-2} s^{-1} shown on this plot discontinuously jumped from 312 to 307°C when the heat flux increased from 1260 to 1320 kW m^{-2}. This discontinuity was larger at 5 MPa in this figure than for the 2 MPa data plotted in Figure 4.3.

T_{wall} Discontinuity Before OID
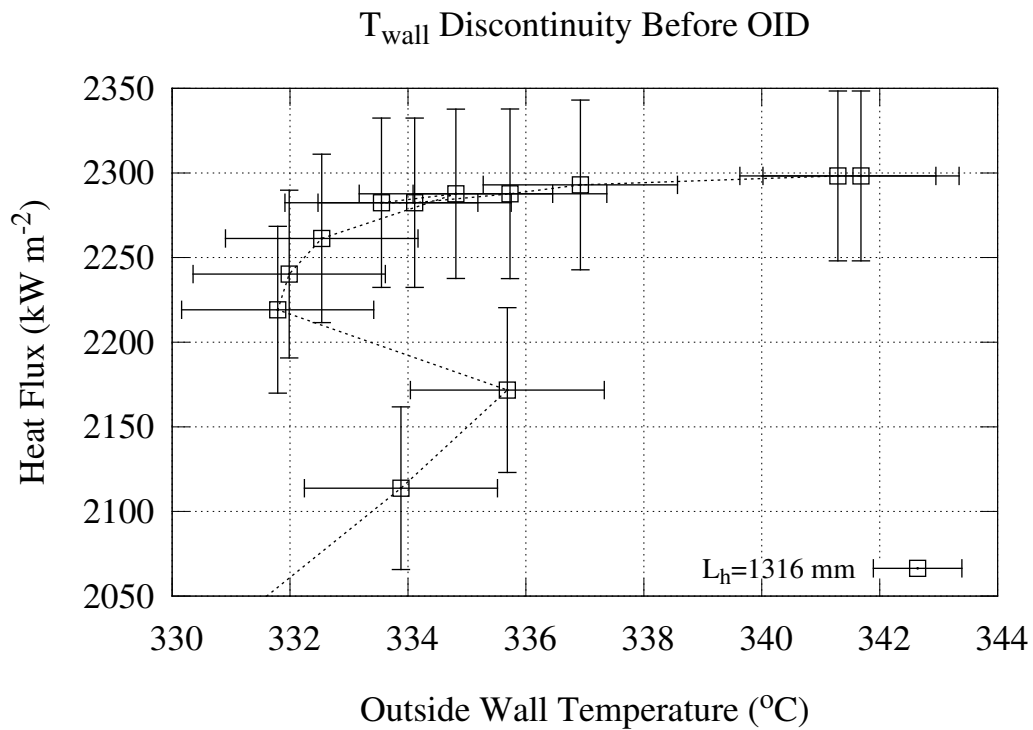
Figure 4.5: The measured outside wall temperature, from an experiment conducted at 4 MPa with a mass flux of 2500 kg m^{-2} s^{-1} jumped from 336 to 332°C when the heat flux increased from 2170 to 2220 kW m^{-2}. This figure shows that the wall temperature discontinuity associated with a transition to droplet evaporation heat transfer was observed at the highest tested mass flux as well as the lowest tested mass flux that was shown in Figures 4.3 and 4.4.
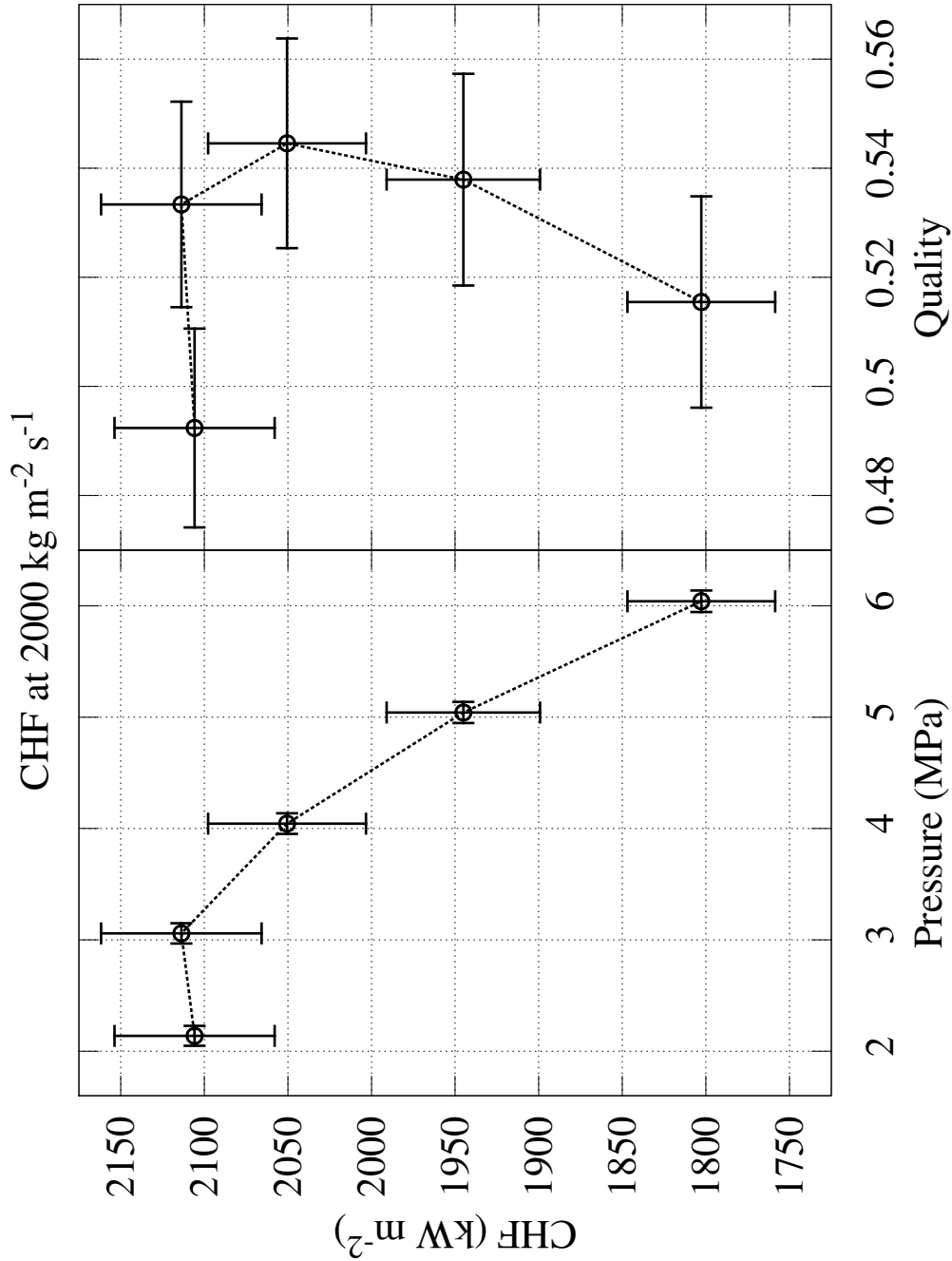
Figure 4.6: Variation of steady experimental CHF with pressure at constant mass flux. The CHF generally decreased with pressure although there was a local maximum at 3 MPa. The dryout quality for constant inlet flow quality had a local maximum at 4 MPa.
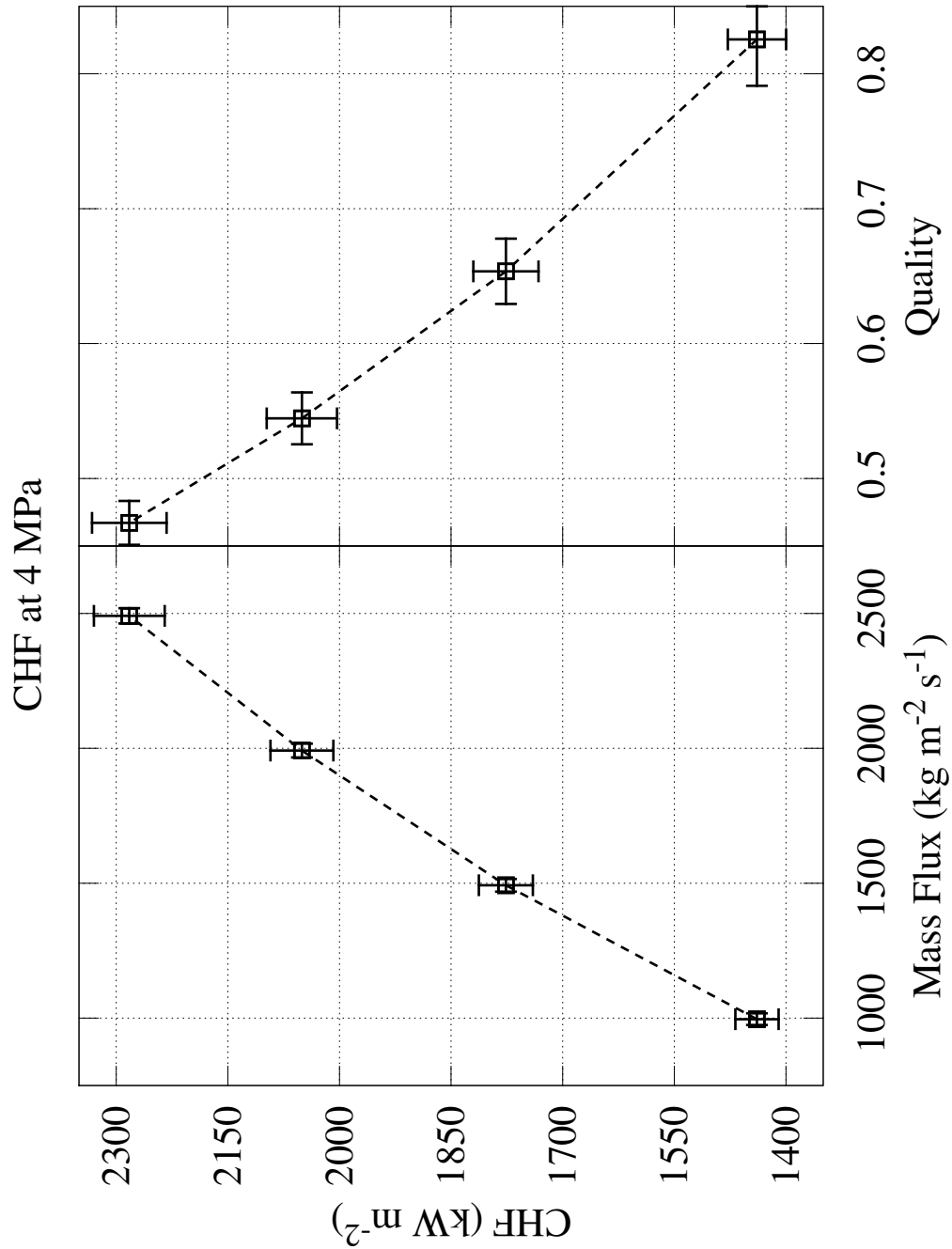
Figure 4.7: Variation of steady experimental CHF with mass flux at constant pressure. In keeping with parametric trends described in the literature the CHF increased with mass flux and decreased with quality.

4.2   Dryout Prediction

The 2006 CHF look-up table [5], the Biasi *et al* correlation [4] and the Katto-Ohno
correlation [32] were compared with experimental data from the present work. Both
the direct substitution method (DSM) and heat balance method (HBM), which were
discussed in Chapter 2, were used. Data points from repeated measurements, from
similar experiments performed on different days, were combined by taking the
mean value of their boundary conditions and predicted values for statistical eval-
uation so that these points would not bias the results—*i.e.* repeated test conditions
were counted as single points. As a result the 22 dryout points were reduced to
15 comparison conditions. The results are shown in Table 4.2. Some deviation in
the predictions relative to the measurements was expected since the conditions and
geometry may be different than those tested in other works on which the prediction
methods were based.

Method	Mean Error	Standard Deviation	RMS Error	Within $\pm10\%$	Within $\pm5\%$
LUT (DSM)	-46%	7.7%	46%	0%	0%
Biasi *et al* (DSM)	15%	21%	25%	7%	0%
Katto & Ohno	6.2%	4.8%	7.8%	73%	53%
LUT (HBM)	-8.4%	2.4%	8.7%	80%	7%
Biasi *et al* (HBM)	4.0%	4.5%	5.9%	100%	47%

Table 4.2: Steady CHF prediction overall performance for both the HBM and the
DSM for unmodified prediction methods.

The DSM yielded poor results for both the look-up table and the Biasi *et al* cor-
relation although the precision of the look-up table is relatively good with a standard
deviation of 7.7%. $^{\text{CHF}_{\text{PRED}}}/_{\text{CHF}_{\text{EXP}}}$ for these correlations using the DSM are plotted
against pressure and mass flux respectively in Figures 4.8 and 4.9. Figure 4.9 shows
a slight systematic dependence of the Biasi *et al* correlation on mass flux.

In contrast the HBM yielded much better comparisons: this includes the Katto
and Ohno correlation since it relies on the inlet subcooling instead of the local
quality and therefore performs an implicit heat balance during its calculation. The
CHF prediction ratios for the HBM are plotted against pressure and mass flux in

CHF Ratio (DSM) vs. Pressure
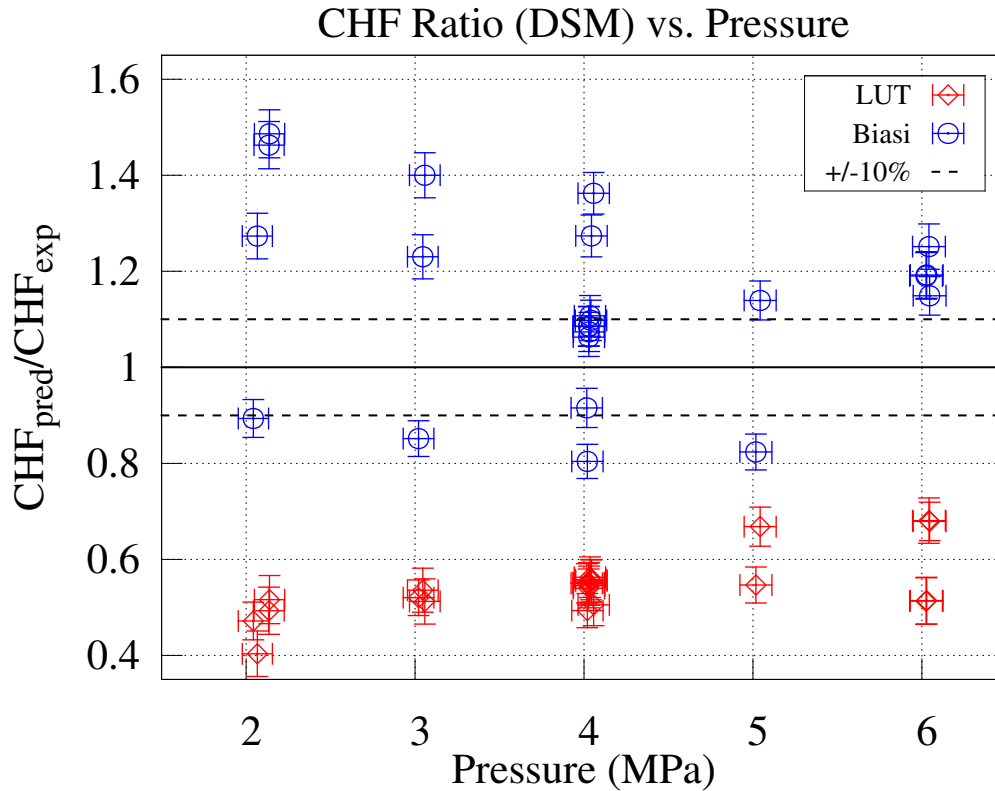
Figure 4.8: CHF prediction ratio *vs* pressure using the DSM for unmodified correlations. The LUT consistently underpredicts the data but the degree of underprediction is consistent at each pressure value. The Biasi *et al* correlation generally overpredicts the data but there is a considerable amount of scatter at each pressure.

Figures 4.10 and 4.11 respectively. The look-up table underpredicts all of the data by 8% but with very good precision: the standard deviation is just over 2%. The Katto-Ohno correlation overpredicts the data overall by 6% but performs very well at pressures above 4 MPa. The Biasi *et al* correlation overpredicts the data by 4% with a similar standard deviation and predicts nearly half of the data within less than $\pm 5\%$. In Figure 4.11 the Biasi *et al* correlation predictions are grouped tightly together at each value of the mass flux while the value about which the predictions are grouped increases as the mass flux increases from 1000 to 2000 kg m^{-2} s^{-1}. This systematic effect of the mass flux on the prediction performance of the Biasi *et al* correlation contributes a large part of its RMS error.

The reason for the much larger deviation from unity in the ratio of predicted to

CHF Ratio (DSM) vs. Mass Flux
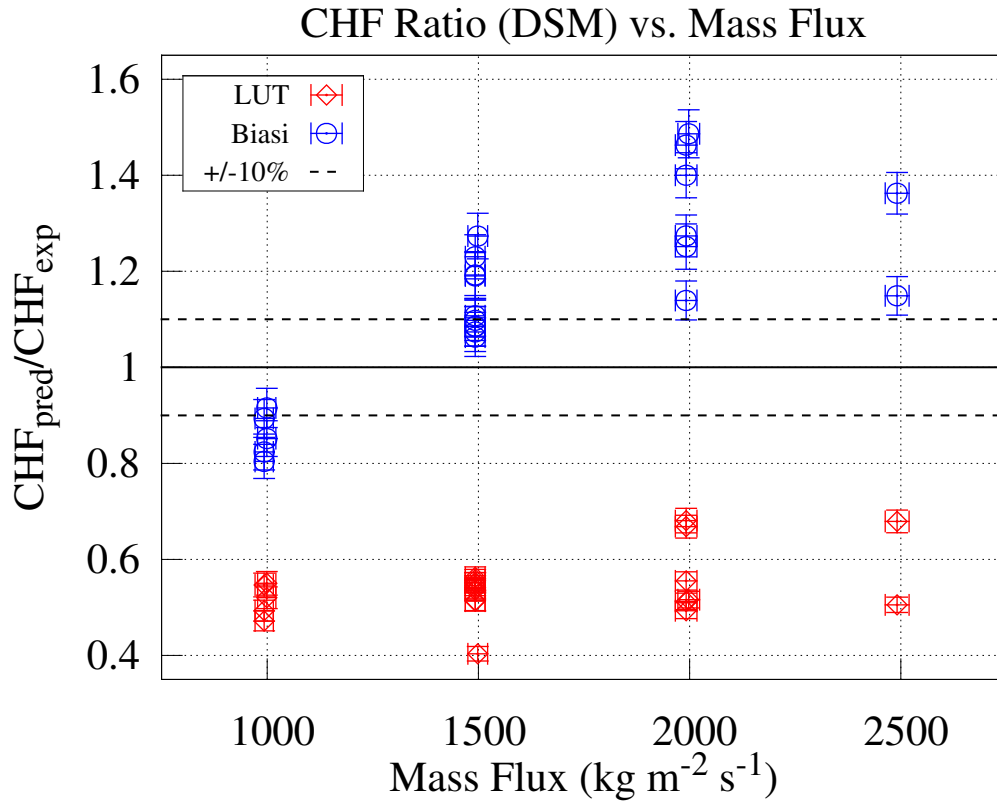
Figure 4.9: CHF prediction ratio *vs* mass flux using the DSM for unmodified correlations. The CHF look-up table is relatively self-consistent at each mass flux value with a slightly greater degree of underprediction for the two lowest mass fluxes. A systematic dependence of the prediction error on mass flux is evident in the Biasi *et al* correlation.

experimental CHF for the DSM *vs* HBM is due to the slope of the CHF *vs* outlet quality curve as explained in [48]. For the HBM there is only a single value of the CHF for each channel location under steady-state conditions and it is based on the boundary conditions of the channel: inlet temperature, inlet mass flow rate, and outlet presure. The *local* value of pressure may be used to evaluate the heat balance but the single value of the CHF is still dependent on the boundary condition or outlet pressure. Any difference in the observed value of the CHF is relative to this single value for the HBM.

For the DSM, however, the predicted CHF at any position in the channel depends on the local conditions so that for every value of channel power there is a unique value of the predicted CHF. This is not a problem if the observed CHF is
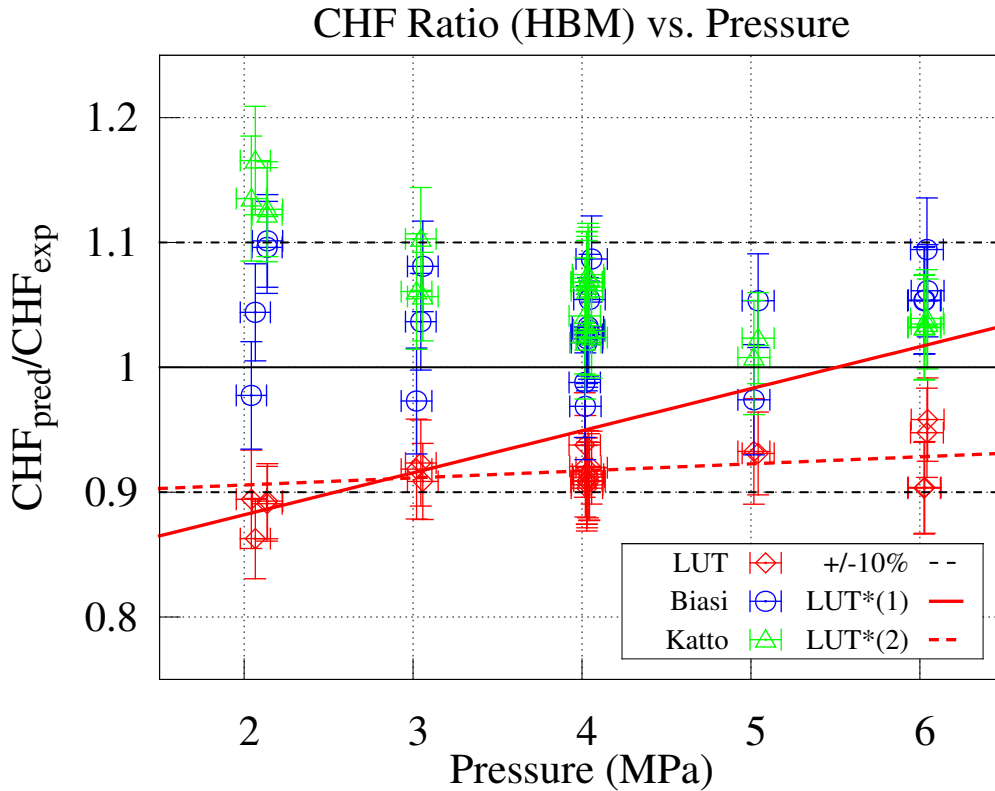
Figure 4.10: CHF prediction ratio for unmodified correlations *vs* pressure using the HBM. Compared to the DSM—see Figure 4.8—the prediction ratios are much closer to unity. In this figure the inverse of the LUT pressure correction factor—see Section 4.3—was plotted and denoted by * in the legend. The LUT had a slight pressure dependence on its prediction ratio using the HBM.

precisely equal to the predicted CHF. In general the CHF varies inversely with the local quality, however, so as the observed CHF varies from perfect agreement with the correlation's CHF *vs* quality curve the error is compounded: not only does the observed CHF vary from perfect agreement with the CHF *vs* quality curve but the predicted CHF varies in the opposite way. This was illustrated in Figure 2.1 from Chapter 2.

4.3   Modified Dryout Prediction Methods

In order to credibly compare the influence of the experimental initial conditions on the time to dryout a prediction method with good accuracy is needed. If a prediction

B.A. Statham
Ph. D. Thesis

Chapter 4
Steady-State Results

McMaster University
Engineering Physics
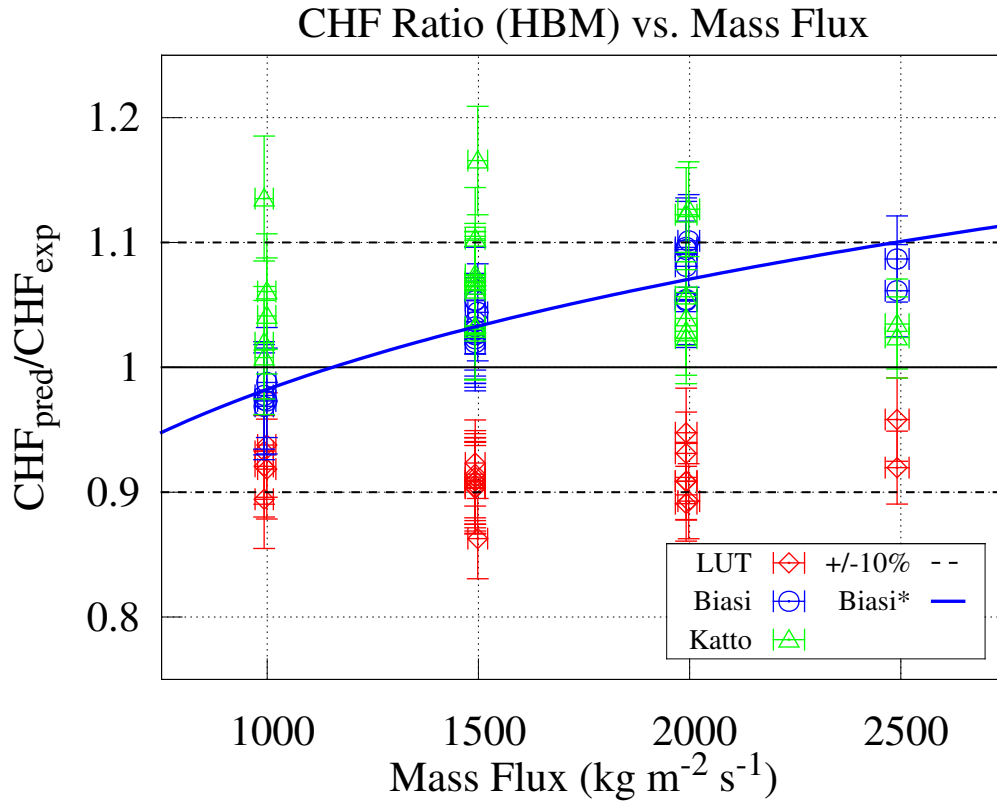
Figure 4.11: CHF prediction ratio for unmodified correlations *vs* mass flux using the HBM. A mass flux dependent HBM correction factor was derived for the Biasi *et al* correlation—see Section 4.3. Its inverse is plotted here denoted by *.

method consistently over or underpredicts the steady-state data with good precision then the predicted times to dryout may largely yield values of infinity or zero respectively. This makes it difficult to quantify the overall effect the initial conditions have on the ability to predict the onset of intermittent dryout during a transient. The methods tested in the previous section all exhibited systematic errors in their predictions of the onset of dryout. It was necessary to modify them, or develop a new correlation, in order to reduce these systematic errors before they were applied to the transient data for the test section used in the present work.

During a transient the inlet conditions are not a reliable indication of the local conditions in the test section: mass fluxes may depart from the inlet value, the evaporation rate may change, and the vapour, droplet, and liquid film fluxes may

respond differently to the changing boundary conditions. This dynamic disequilibrium means that the HBM is physically unrealistic during transients. This was acknowledged in the example cited above [48] and, in the discussion on the application of CHF prediction methods that this example was part of, was used as an argument against the use of the HBM by Siman-Tov and Weisman and in favour of the DSM and mechanistic models, respectively [53, 54]. The following compromise was proposed by Hejzlar and Todreas: when different CHF prediction correlations or look-up tables are compared to steady-state data in order to evaluate their performance the HBM should be used. In situations where the DSM must be used, such as during transient analysis, the performance of these methods should be explicitly evaluated and stated when implemented this way [55].

For the main thrust of the present work, comparing the observed to predicted times to dryout for pressure transients, the DSM must be used. The performance of the Biasi *et al* correlation and the look-up table have been compared using both the DSM and the HBM. Both prediction methods implemented in both ways have exhibited systematic biases or errors that had to be eliminated before they could be used to evaluate transient data. Instead of adjusting or modifying these correlations a new correlation based on the steady-state data that was collected could have been developed. The validity of this method would be limited to the conditions of the steady-state data. It made the most sense to modify an existing correlation that was based on the observed trends of a wide range of data.

One way it was possible to modify the correlations that were tested was to apply a simple power multiplication factor to the predicted CHF values based on the DSM. This would have resulted in overall multiplication factors from 0.7 to 1.25 for the Biasi correlation and 1.5 to 2.5 for the look-up table. This was deemed unreasonable if it is assumed that the CHF curves are representative of the underlying CHF phenomena—the same phenomena may not be responsible for dryout if the quality is the same but the observed heat flux is 250% of the value reported by a prediction method. This is a consequence of using the quality as analogue for the phase distribution that may be highly geometry dependent. This does not undermine the dryout prediction methods overall representativeness of the underlying phenomena with respect to changing quality—it merely means that the relationship between the

quality and the phase distribution evolves at a different rate in different test section geometries.

The author's solution was to make use of the CHF values predicted using the HBM to shift the CHF *vs* quality curve into better agreement with the data. Eliminating the overall bias in the HBM should, in theory, also eliminate bias when the DSM is applied to the shifted CHF curve. This process is illustrated Figures 4.12–4.13 and outlined below:

1. Use the error in the CHF value predicted by the HBM to derive a CHF correction factor. See Figures 4.10 and 4.11 for continuous plots of the correction factors used in the present work.

   - This correction factor alone will not eliminate the prediction bias as illustrated in Figure 4.12.

2. The local quality in the test section is directly related to the channel heat flux. Use the derivative of the quality with respect to the heat flux to derive an expression that relates a change in heat flux to a change in quality as shown in Equations 4.1–4.2.

3. Calculate the CHF using the DSM with the quality equal to $x - \Delta x$. This effectively shifts the entire CHF-quality curve in the positive direction along the quality axis by calculating the CHF at a quality that is shifted to a lower value.

4. Multiply the calculated CHF by the power correction factor to obtain a CHF value that has resulted from a shift in both the quality and the power based on the linear relationship between power and quality.

   - This is true for any position in a channel with any axial power profile provided that the relative power profile does not change as power is increased [48].

$$\frac{\partial x}{\partial \ddot{q}} = \frac{\pi D L_h}{\dot{m}(h_V - h_L)} \approx \frac{\Delta x}{\Delta \ddot{q}} \tag{4.1}$$
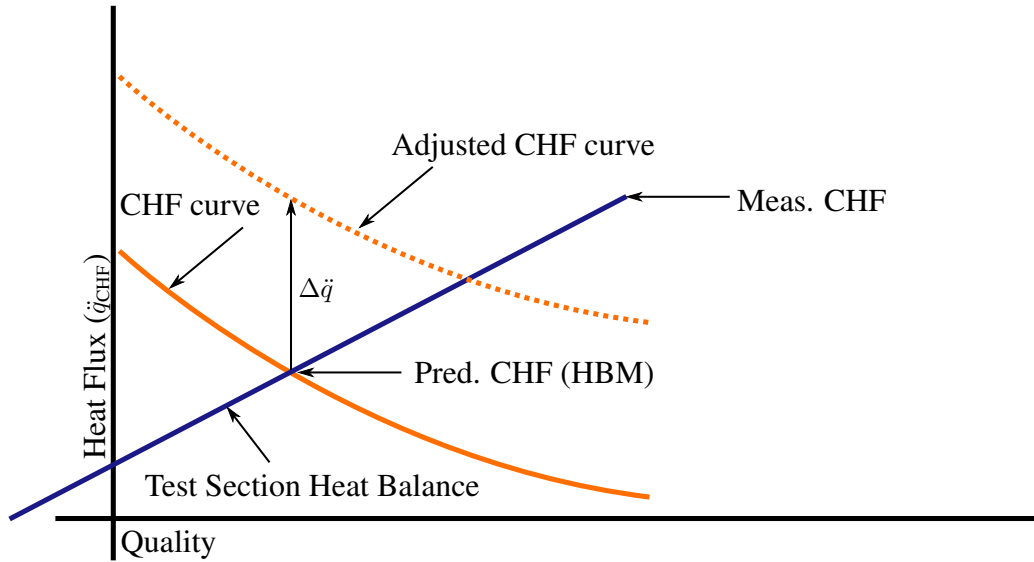
Figure 4.12: The first step in the technique used to modify the Biasi correlation and CHF look-up table. This step consists of multiplying the predicted CHF value by the correction factor.
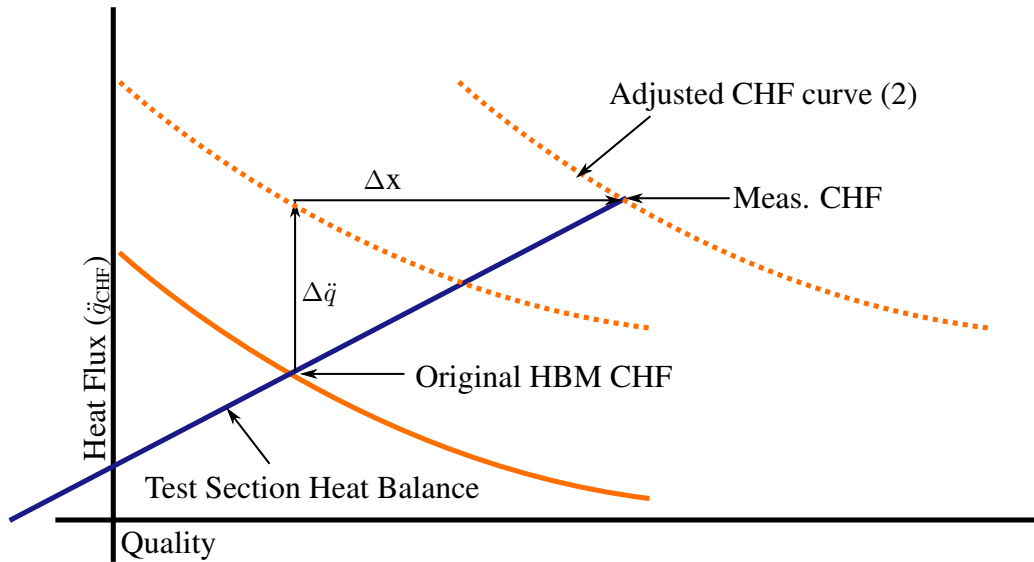
Figure 4.13: The second step in the technique used to modify the Biasi correlation and CHF look-up step. In this step the CHF curve is shifted along the quality axis so that the experimental CHF value lies on the prediction curve. This is implemented by subtracting the value of the quality shift, Δx from the input local value of the quality when the CHF is calculated so that $\ddot{q}_{CHF-PRED} = f(x - \Delta x)$.

$$\Delta x = \frac{(\Delta \ddot{q})\pi D L_h}{\dot{m}(h_V - h_L)} \tag{4.2}$$

Equations 4.3 to 4.5 illustrate how the correction factors derived from the HBM with unmodified correlations were used to find the modified value of the CHF using the DSM and the shifted value of the quality. The CHF correction factors illustrated in Figures 4.10 and 4.11 for the the LUT and the Biasi *et al* correlation are given mathematically in Equations 4.6 and 4.7 respectively.

$$\ddot{q}_{CHFexp} = \ddot{q}_{CHFHBM} + \Delta \ddot{q}_{CHFHBM} \tag{4.3}$$

$$\eta = \frac{\ddot{q}_{CHFEXP}}{\ddot{q}_{CHFHBM}} \tag{4.4}$$

$$\ddot{q}_{CHFDSM} = \eta \cdot f(p, G, x - \Delta x, D) \tag{4.5}$$

$$\frac{1}{\eta_{LUT}} = \begin{cases} a = 0.0337 \cdot p + 0.814 & a <= b \\ b = 0.00565 \cdot p + 0.894 & a > b \end{cases} \tag{4.6}$$

$$\frac{1}{\eta_{Biasi}} = 0.694 \cdot G^{0.124} \tag{4.7}$$

A disadvantage of this method was that the DSM CHF value was *a priori* unknown and became a function of itself within the calculation of Δx. The power correction factor, η, was independent of the CHF value but $\Delta \ddot{q}$ was not. Therefore the values of $\Delta \ddot{q}$ and Δx had to be determined through iteration. The iterative process that was used to evaluate the CHF based on this method is shown in Figure 4.14.

Method	Mean Error	Standard Deviation	RMS Error	Within ±10%	Within ±5%
LUT* (DSM)	87%	151%	170%	6.7%	0%
Biasi* (DSM)	-0.01%	5.8%	5.6%	93%	40%
LUT* (HBM)	1.1%	2.0%	2.2%	100%	93%
Biasi* (HBM)	0.4%	1.7%	1.6%	100%	100%

Table 4.3: Modified CHF prediction method performance.

The CHF prediction ratios produced when this correction method was applied
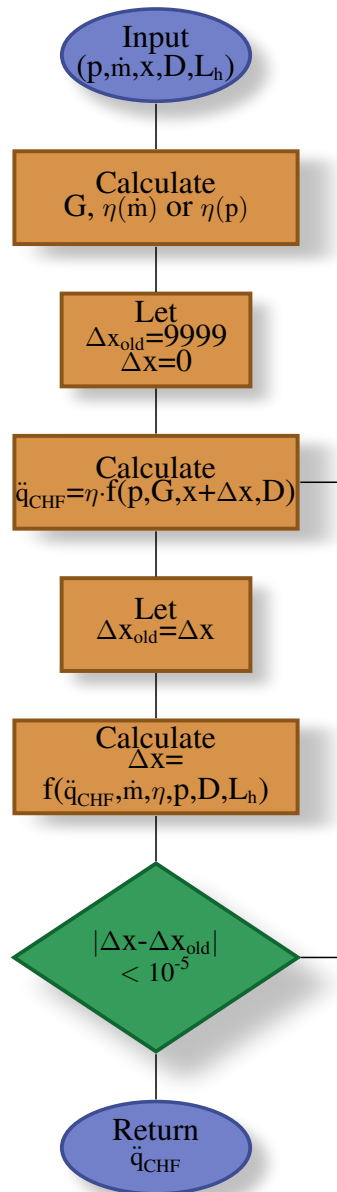
Figure 4.14: Flow chart of the iterative method used to find the modified predicted CHF using the DSM. Iteration is required to compute the value of Δx because the CHF is *a priori* unknown. The heat flux correction factor η was fixed for each value of mass flux or pressure depending on whether the Biasi *et al* correlation or the LUT was being used.

to the look-up table and the Biasi *et al* correlation were plotted against pressure and mass flux are shown in Figures 4.15 and 4.16 respectively. The overall prediction performance is shown in Table 4.3 denoted as LUT* and Biasi*. Observing only the overall performance of the look-up table is deceptive: Figures 4.15 and 4.16 demonstrate that the performance is skewed by a few points at low flow and low pressure that are dramatically overpredicted although even then only 7% of the data points are predicted within $\pm10\%$. Figures 4.17 and 4.18 show the same data on reduced prediction ratio scales that more clearly show how well the modified Biasi *et al* performed with little evident systematic prediction bias.
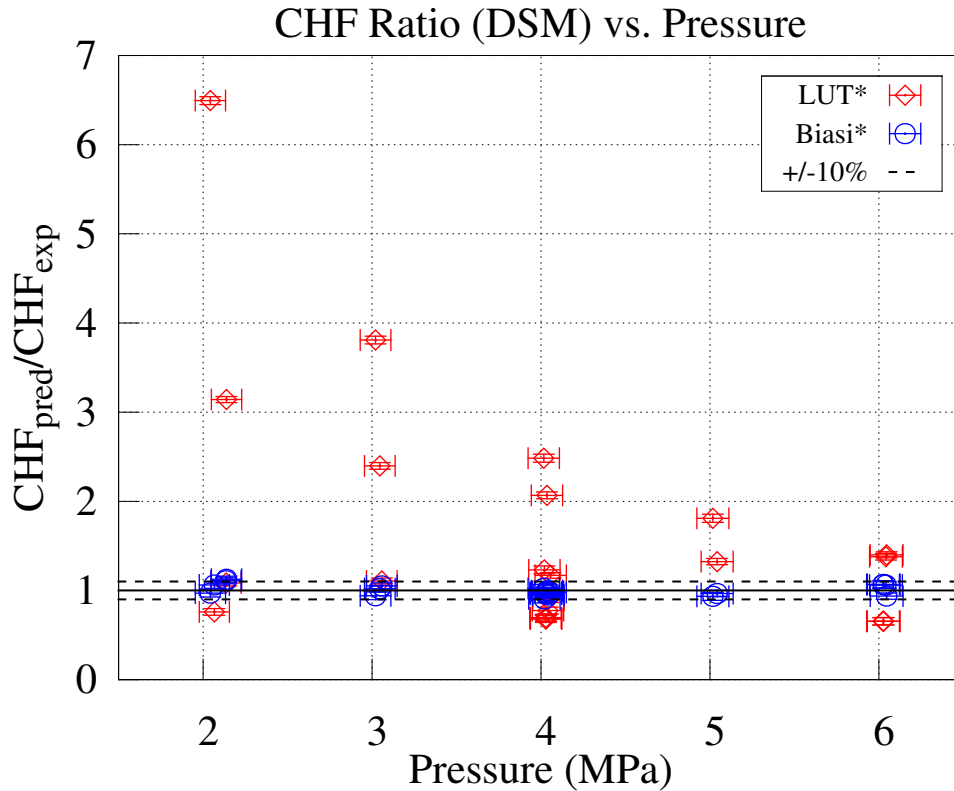
Figure 4.15: CHF prediction ratio for modified prediction methods *vs* pressure using the DSM. The performance of the modified look-up table appears to be worse than it was before modification. However the modification has the effect of compressing the CHF-quality curve in the quality dimension so that the prediction error becomes even more sensitive to small changes in local quality.

The poor performance of the modified CHF look-up table wass because of the implicit assumption in this correction method that the slope of the CHF *vs* quality
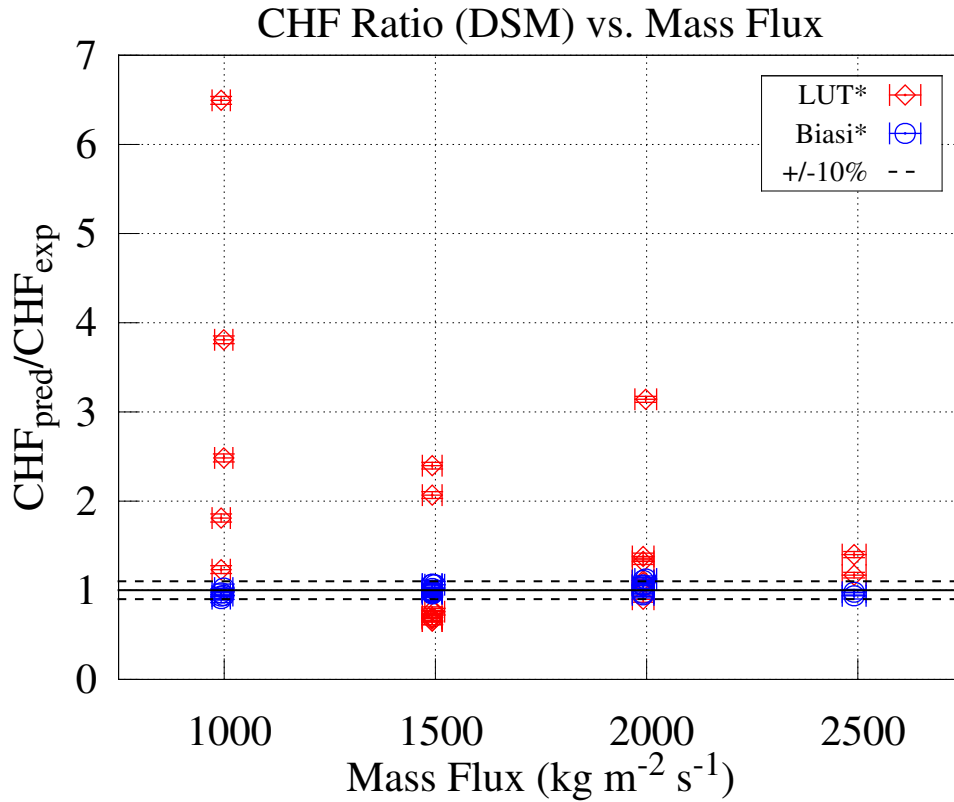
Figure 4.16: CHF prediction ratio for modified prediction methods *vs* mass flux using the DSM. Comparing this figure and Figure 4.15 it is evident that the modified LUT performs worst for 1000 and 2000 kg m^{-2} s^{-1} at 2 MPa.

curve is constant. The experimental data presented in this thesis fall on the higher-quality end of the limiting quality regime (LQR) that was discussed in Chapter 2. It has been noted by the primary author of the LUT [5] as a remaining source of uncertainty in dryout prediction [8]. In the region of the present investigation both the slope of the CHF *vs* quality curve for the LUT and the value of the CHF increased rapidly as the quality decreased. This presented a problem for the data points that lie away from the CHF correction curve(s). This was especially true for the overpredicted points where Δx was also overpredicted and thus compounded the problem. In practical terms this resulted in an upper limit of 10 000 kW m^{-2} being placed on the value of $\ddot{q}$ used to evaluate Δx and an upper limit of 1000 iterations through the process shown in Figure 4.14 to determine the modified dryout point. For the

CHF Ratio (DSM) vs. Pressure
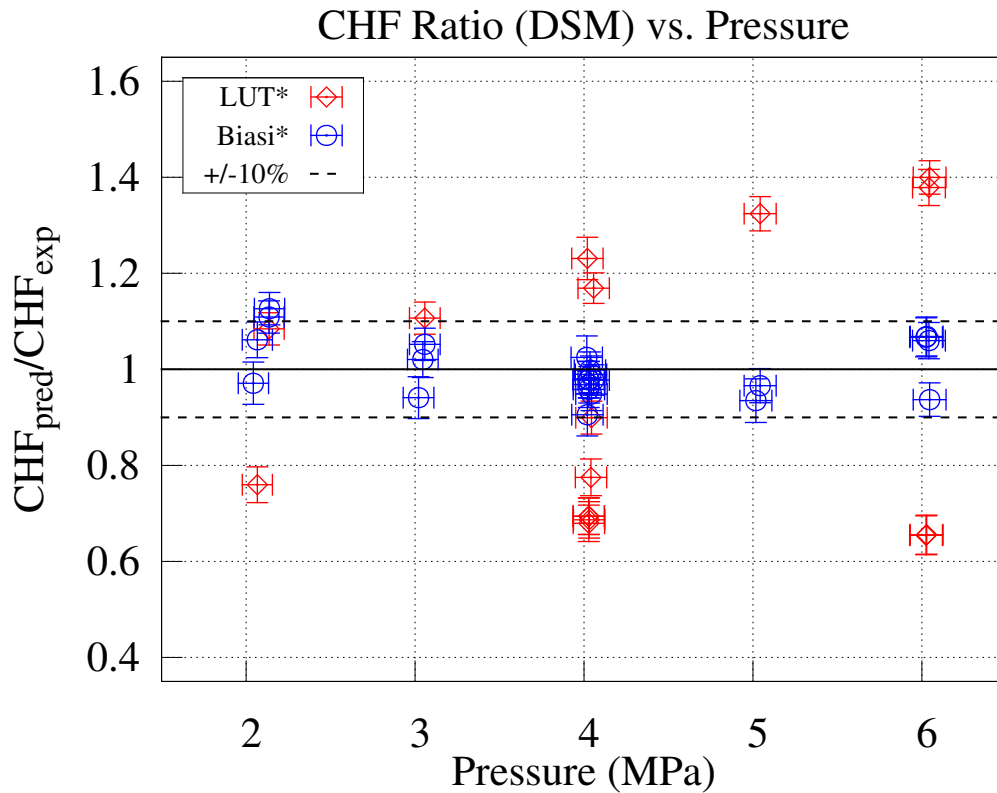
Figure 4.17: CHF prediction ratio over a reduced range for modified prediction methods *vs* pressure using the DSM. The scale of Figures 4.15 and 4.16 obscured the data that were predicted well by the DSM. In this figure it is evident that nearly all of the data were predicted within $\pm10\%$ by the Biasi *et al* correlation while very few of the data were predicted within this range by the modified look-up table.

present data this limited the degree of overprediction permitted for points that were already overpredicted by a factor of 4–7 based on the range of steady-state CHF data.

The strong sensitivity of the modified CHF look-up table to the precision of the correction method relative to the steady-state data is a double edged sword in the present work: the performance is very poor for the steady state data because a small imprecision in the modification factor leads to a gross error in the predicted dryout point. In a transient this is beneficial with respect to the time-to-dryout prediction: if the predicted CHF is a strong function of quality then even a large error in steady-state prediction could lead to a relatively small inaccuracy in time for even slow
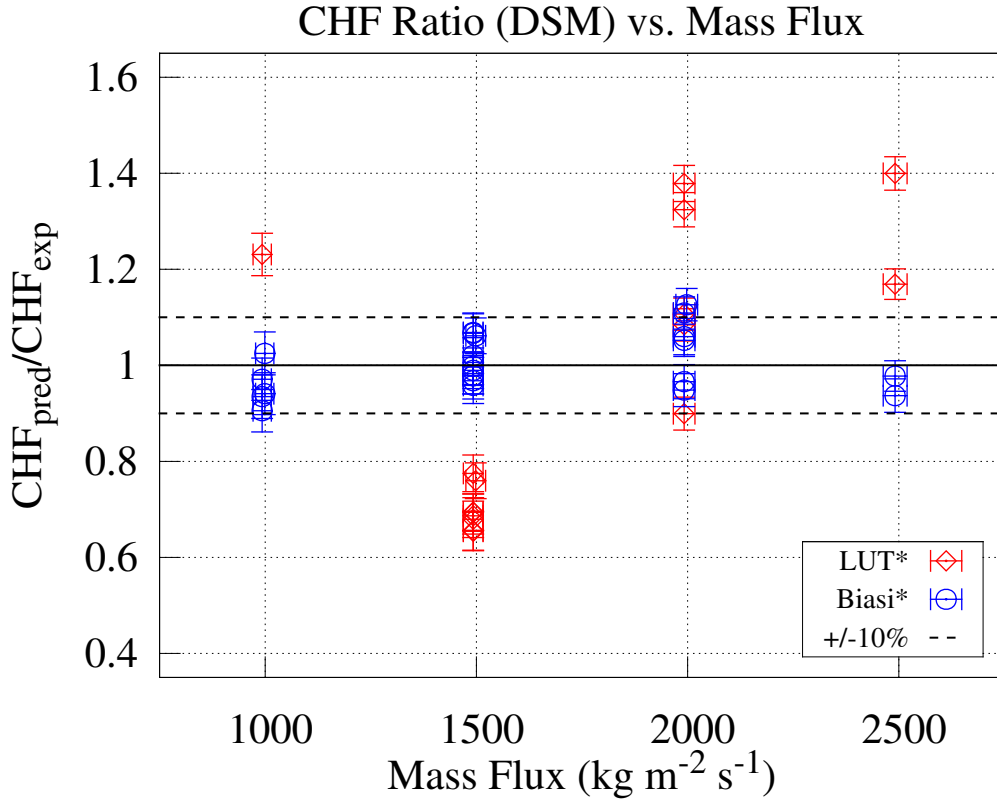
Figure 4.18: CHF prediction ratio over a reduced range for modified prediction methods *vs* mass flux using the DSM. In this figure it is evident that the CHF modification method has nearly eliminated the systematic effect of mass flux on the CHF prediction of the Biasi *et al* correlation.

transients. This can be illustrated using the error propagation equation and the chain rule as shown in Equation 4.9 where it was assumed that the uncertainty in time measurement is negligible even though this is not strictly true. Equation 4.9 shows that the uncertainty in the predicted time to CHF is inversely proportional to the slope of the CHF *vs* quality curve.

$$t_{CHF} = f(\ddot{q}_{CHF}(x), t) \tag{4.8}$$

$$\sigma_{tCHF}^2 = \sigma_{\ddot{q}CHF}^2 \left(\frac{\partial \ddot{q}_{CHF}}{\partial t} \right)_{tCHF}^{-2} \approx \sigma_{\ddot{q}CHF}^2 \left(\frac{\partial \ddot{q}_{CHF}}{\partial x} \frac{\partial x}{\partial t} \right)_{tCHF}^{-2} \tag{4.9}$$

4.4 Summary

22 experimental dryout data points representing 15 boundary conditions were collected and were compared with three correlations from the literature. The DSM yielded poor results: the CHF look-up table and the Biasi *et al* correlation underpredicted the data by 46% and overpredicted the data by 15% respectively. The HBM—including the Katto and Ohno correlation—performed much better. The look-up table, Biasi *et al* correlation, and the Katto-Ohno correlation had overall mean prediction errors of -8.4%, 4.0% and 6.2% respectively. This performance was satisfactory to prove that the present experiment is representative of previous experimental investigations for similar boundary conditions.

The purpose of the present work was to test how accurately the quasi-steady method was capable of predicting dryout during depressurisation transients for two different initial conditions. The results of this test were used to compare the influence of the intial conditions on the prediction accuracy. The DSM must be used for transient analysis since the instantaneous inlet conditions are not representative of the downstream conditions in the test section during a transient. This is because significant dynamic disequilibrium exists under transient conditions. The author developed a method to improve the prediction capabilities of the Biasi *et al* correlation and the look-up table using the DSM based on the results of the HBM from the steady-state data. This was successful for the Biasi *et al* correlation but dramatically decreased the overall performance of the look-up table. The poor performance of the modified LUT was largely due to the sensitive and complex relationship of CHF to quality in the region of the LUT where the data lay. The ability of these two modified dryout prediction methods to predict the onset of intermittent dryout during depressurisation transients is tested against experimental data in the next chapter.

Chapter 5

Transient Results

5.1 Introduction

Depressurisation experiments were conducted to test the author's hypothesis that a pre-existing dryout condition was responsible for the lack of dryout delay observed by Lyons and Swinnerton [80, 3] in contrast to the work of Celata *et al* [1, 2]. Transient runs were conducted by following the procedure for transient data collection outlined in Chapter 3. The range of boundary conditions were nearly identical to those of the steady-state data: pressures from 2–6 MPa, mass fluxes of 1000–2500 kg m^{-2} s^{-1} and initial inlet quality of -0.148±0.006. The two initial conditions tested were termed margin-to-dryout (MTD) and post-dryout (PDO) for the pre and post-CHF initial conditions respectively.

This chapter presents a summary of the transient experimental data and the results of the data reduction. Some relevant parts of the data reduction are described and illustrated here. The techniques used to process the data including post-processing the data to detect transients and calculate transient characteristics, determination of the dryout time, modelling of the test section in RELAP5, preparation of boundary and initial conditions data for the RELAP5 simulations, and post-processing of the RELAP5 results using the modified dryout prediction methods presented in Chapter 4 are described in detail in Appendix A.

The reduced data demonstrate there is no difference between the two initial conditions tested within the limits of the experimental uncertainty and the range of data

in the present work. The quasi-steady method of dryout prediction is satisfactory within the same limits.

5.2 Transient Data

5.2.1 Boundary Conditions and Data Selection

All transient runs are listed in Tables 5.1 and 5.2 for PDO and MTD initial conditions, respectively. Note that in some cases transient runs were repeated for longer durations in order for the dryout front to progess further upstream. Some PDO cases do not have direct MTD counterparts where the experiment was terminated prematurely by a test section wall overtemperature trip during the PDO transient run.

Data from two thermocouples were eliminated from the data set. This was done due to the observation from Figure 6.2 that the second thermocouple at a heated length of 1316 mm and the thermocouple at 1305 mm exhibited a delay in the rewetting curve. This may have been due to a poor silver solder joint between the edge of the test section and the thermocouple or the location of the thermocouple joint itself may have been located some distance up the thermocouple sheath away from the tip of the thermocouple. In either case this conduction delay would produce a bias in the experimental results and so their data was discarded in the present analysis.

The closing of the blowdown valve occasionally triggered dryout at the end of the pressure transient runs. This may have been due to the pressure shockwave caused by the rapid closing of the valve or the ensuing rapid decrease in flow. The flow transient observed when the valve was closed was opposite—but not equal—to the rapid increase observed at the moment of valve opening. Data for dryout times observed within less than 0.4 s of the end of each transient were eliminated from the overall data analysis.

Some of the transient times-to-dryout were over or under-predicted enough that dryout was predicted before the beginning of the transient or dryout was not predicted at all. This was despite the modifications that were made to the LUT and

Run Identifier	Upstream Position (mm) (#)	Heat Flux ($\frac{kW}{m^{-2}}$)	T_{in} (°C)	Mass Flux ($\frac{kg}{m^2\ s}$)	P_{out} (MPa)	BD_{max} ($\frac{MPa}{s}$)	BD Time (s)
0826-no007	1276 (3)	1780	195.7	1460	4.0	-0.28	12
0827-no007	1276 (3)	1950	212.6	1960	5.0	-0.31	12
0827-no020	1316 (1)	2010	227.2	2500	6.0	-0.32	12
0827-no022	1276 (3)	2010	227.3	2490	6.0	-0.34	16
0829-no010	1230 (4)	1400	212.4	990	5.0	-0.34	12
0829-no017	1293 (2)	1630	227.7	1500	6.0	-0.45	16
0904-no016	1230 (4)	1790	195.5	1500	4.0	-0.25	12
0904-no026	1276 (3)	1830	175.2	1490	3.0	-0.19	12
0906-no019	1276 (3)	2060	195.6	1990	4.0	-0.24	12
0906-no031	1276 (3)	2120	175.0	2000	3.0	-0.20	12
0909-no016	1276 (3)	1470	149.2	1000	2.0	-0.13	12
0909-no037	1276 (3)	1850	149.2	1500	2.0	-0.13	12
0910-no013	1276 (3)	1460	195.3	1000	4.0	-0.29	12
0910-no028	1276 (3)	1500	175.0	1000	3.0	-0.21	12
0911-no011	1276 (3)	1800	195.5	1490	4.0	-0.31	12
0913-no012	1230 (4)	1790	195.7	1500	4.0	-0.42	8
0917-no011	1230 (4)	1450	195.4	1000	4.0	-0.48	8
0917-no020	1230 (4)	1800	195.5	1500	4.0	-0.41	9
0918-no015	1230 (4)	2300	195.7	2490	4.0	-0.39	10
1113-no019	1316 (1)	1820	227.5	1990	6.0	-0.82	10
1113-no020	1293 (2)	1820	227.5	1990	6.0	-0.88	16
1113-no021	1276 (3)	1820	227.5	1940	6.0*	-0.99	20
1114-no022	1230 (4)	1790	195.6	1500	4.0	-0.57	16
1115-no031	955 (6)	2120	149.1	2000*	2.0	-0.24	16

Table 5.1: Blowdown runs with PDO initial conditions.

Run Identifier	Upstream Position (mm) (#)	Heat Flux ($\frac{kW}{m^{-2}}$)	T_{in} (°C)	Mass Flux ($\frac{kg}{m^2\,s}$)	P_{out} (MPa)	BD_{max} ($\frac{MPa}{s}$)	BD Time (s)
0826-no008	1276 (3)	1750	195.6	1490	4.0	-0.26	12
0827-no009	1293 (2)	1920	212.7	2000	5.0	-0.31	16
0827-no023	1316 (1)	1980	227.4	2490	6.0	-0.30	16
0829-no011	1276 (3)	1380	212.8	1000	5.0	-0.34	14
0829-no018	1316 (1)	1600	227.8	1500	6.0	-0.40	16
0829-no019	1276 (3)	1600	227.6	1500	6.0	-0.36	20
0904-no017	1276 (3)	1770	195.9	1490	4.0	-0.25	18
0904-no027	1276 (3)	1800	175.1	1500	3.0	-0.21	18
0906-no020	1276 (3)	2030	195.6	1990	4.0	-0.25	18
0906-no032	1230 (4)	2090	175.2	1990	3.0	-0.18	18
0909-no017	1276 (3)	1450	149.1	990	2.0	-0.14	18
0909-no038	1276 (3)	1820	148.9	1500	2.0	-0.11	18
0910-no014	1276 (3)	1440	195.6	1000	4.0	-0.30	18
0910-no029	1276 (3)	1470	174.9	990	3.0	-0.19	18
0911-no012	1276 (3)	1770	195.5	1490	4.0	-0.24	18
0913-no013	1230 (4)	1770	195.4	1500	4.0	-0.42	10
0917-no012	1230 (4)	1430	195.4	1000	4.0	-0.45	10
0917-no022	1230 (4)	1770	195.4	1490	4.0	-0.43	10
0918-no016	1230 (4)	2260	195.4	2500	4.0	-0.37	10
1113-no022	1276 (3)	1790	227.4	2000	6.0	-0.80	30
1114-no023	1230 (4)	1760	195.7	1500	4.0	-0.50	20

Table 5.2: Blowdown runs with MTD initial conditions.

Biasi *et al* correlations to reduce the overall bias in dryout prediction that were discussed in the previous chapter. Data points where dryout was predicted before the beginning of the transient or where dryout was not predicted before the end of the transient were eliminated from the data sets that were analysed for each correlation. The points that were eliminated based on this criteria were unique to each prediction method.

The data set consisted of 174 points after all of the data points from the two poorly joined thermocouples were eliminated. The total number of data to analyse using each prediction method was further reduced when the data with pre- or non-predicted dryout and the experimental dryout points that may have been triggered by the closing of the blowdown valve were eliminated. This left 89 data including 37 PDO data and 52 MTD data for the modified Biasi *et al* correlation and 99 data points including 46 PDO and 53 MTD points for the modified LUT that were predicted during the transients (PDT).

5.2.2   Example Data

Data from several transient runs are shown in Figures 5.1, 5.2 and 5.3. These transients displayed a rapid initial mass flow rate increase followed by a gradual decay as the transient progressed. The initial mass flux increase was caused by the initiation of the blowdown at the exit of the test section. The mass flux decay is closely associated with the pressure: the flow rate decays more quickly during faster transients. Some data from the literature suggests that there is a delay in the onset of dryout during rapid mass flow transients. For example, Moxon and Edwards [46] reported a delay in the onset of dryout but their mass flow decayed to half its initial value in less than 1 s. In the present work the flow was never observed to decrease to half of its original value even over the course of transients up to 30 s long.

Another typical property of these transients is the decrease in measured wall temperature with time before the onset of dryout. The heat transfer coefficient may change slightly as the pressure and mass flow decay and the quality consequently increases. These effects played only a minor role; the decrease in wall temperature was primarily caused by the change in saturation temperature as the pressure de-
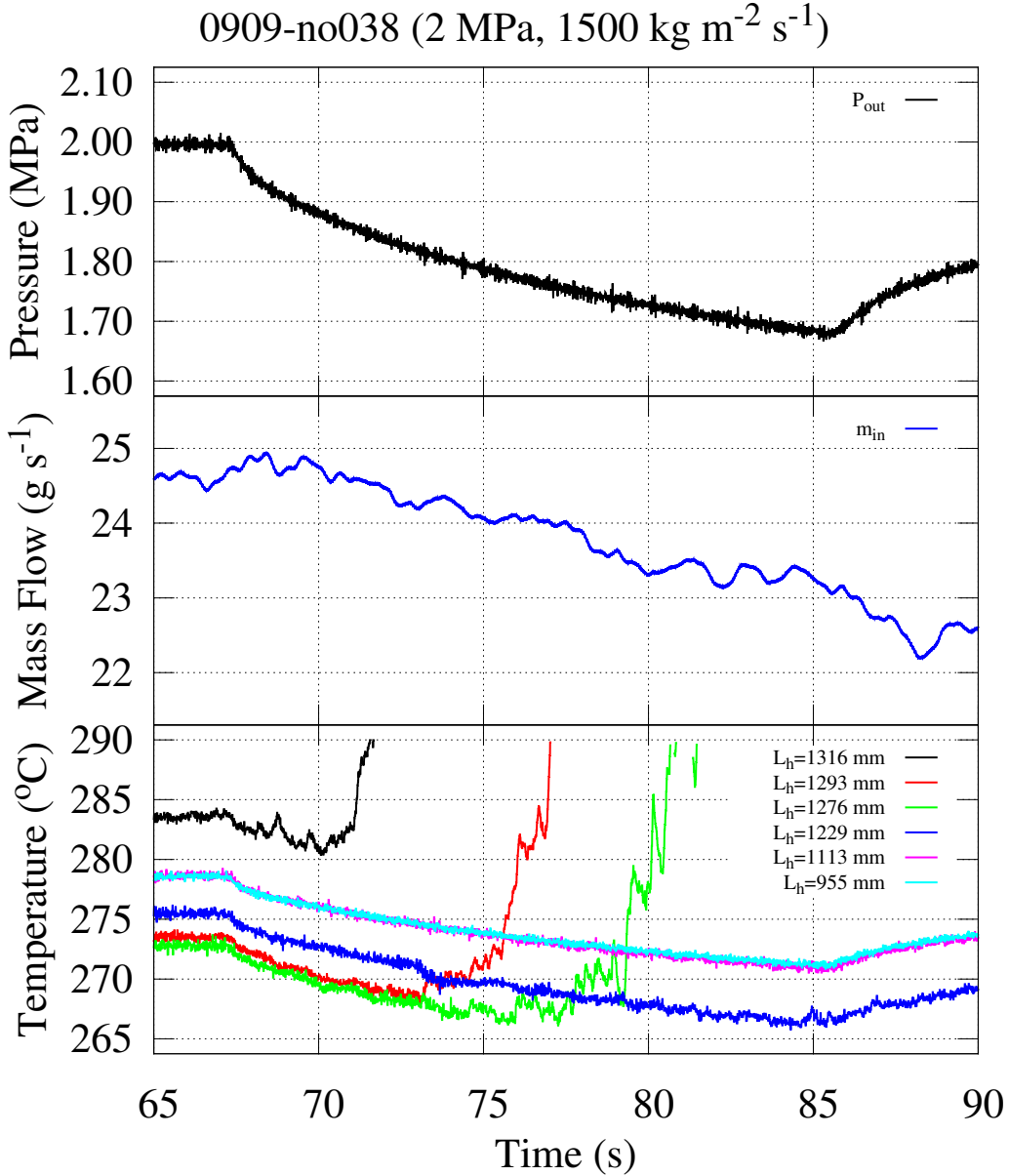
Figure 5.1: MTD transient data with an initial pressure of 2 MPa. From top to bottom the outlet pressure, inlet mass flow rate, and outside wall temperatures for 7 test section positions are plotted against time. In 18 s the pressure decays from 2 to 1.7 MPa; the pressure decay rate was smaller at lower initial pressures. The temperature measured at L_h=1316 mm began to noticeably dry out only after the transient was initiated. The discontinuous decrease in the measured temperature at 74 s for L_h 1229 mm was typical of the transition to droplet heat transfer that was observed in the steady data.
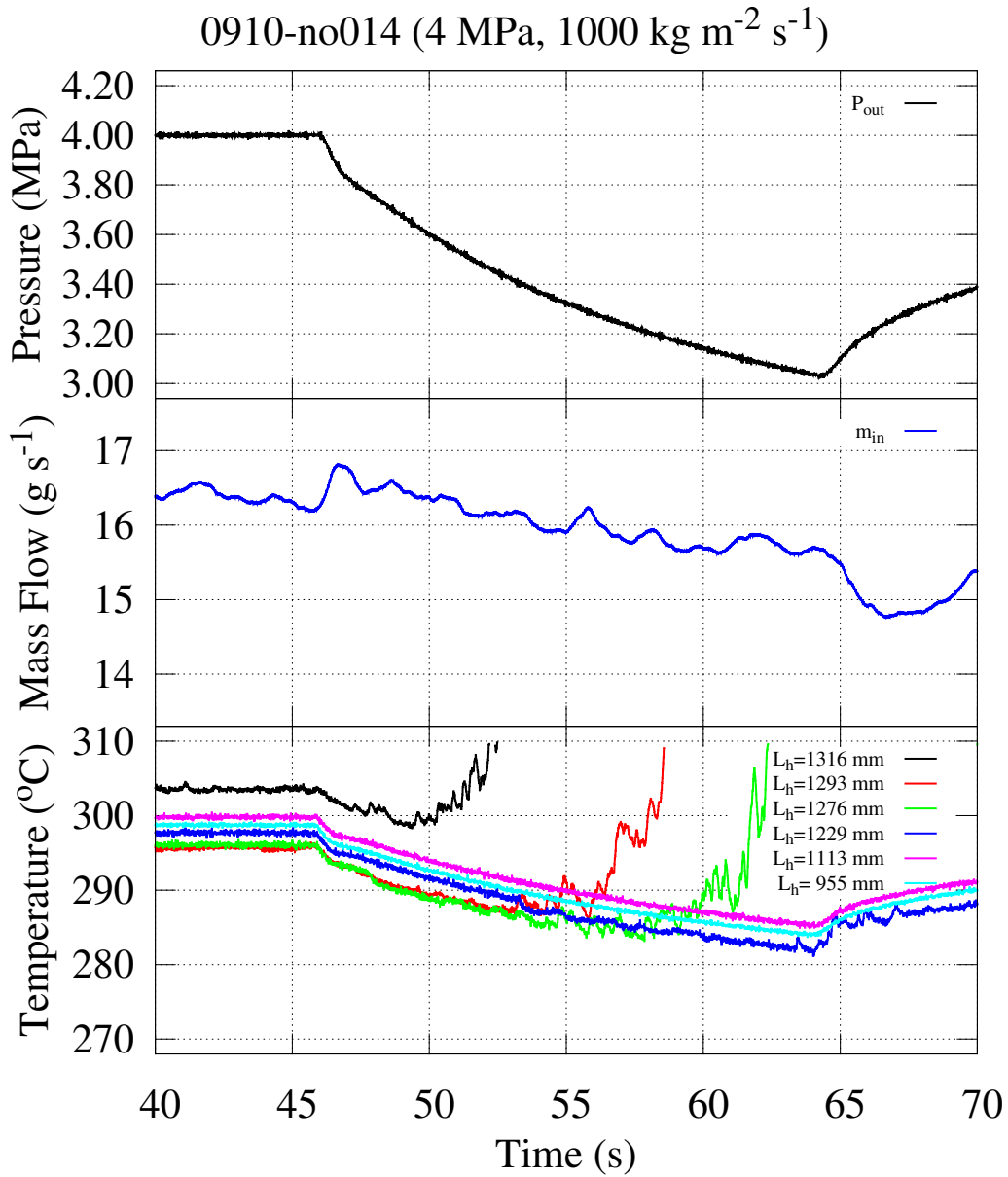
Figure 5.2: MTD transient data with an initial pressure of 4 MPa. When the top of this figure is compared with the top of Figure 5.1 it is evident that the depressurisation rate was much higher at higher pressures. In both of these figures the response of the outlet pressure, mass flow rate, and wall thermocouples to the blowdown transient is similar.

1113-no021 (6 MPa, 2000 kg m^{-2} s^{-1})
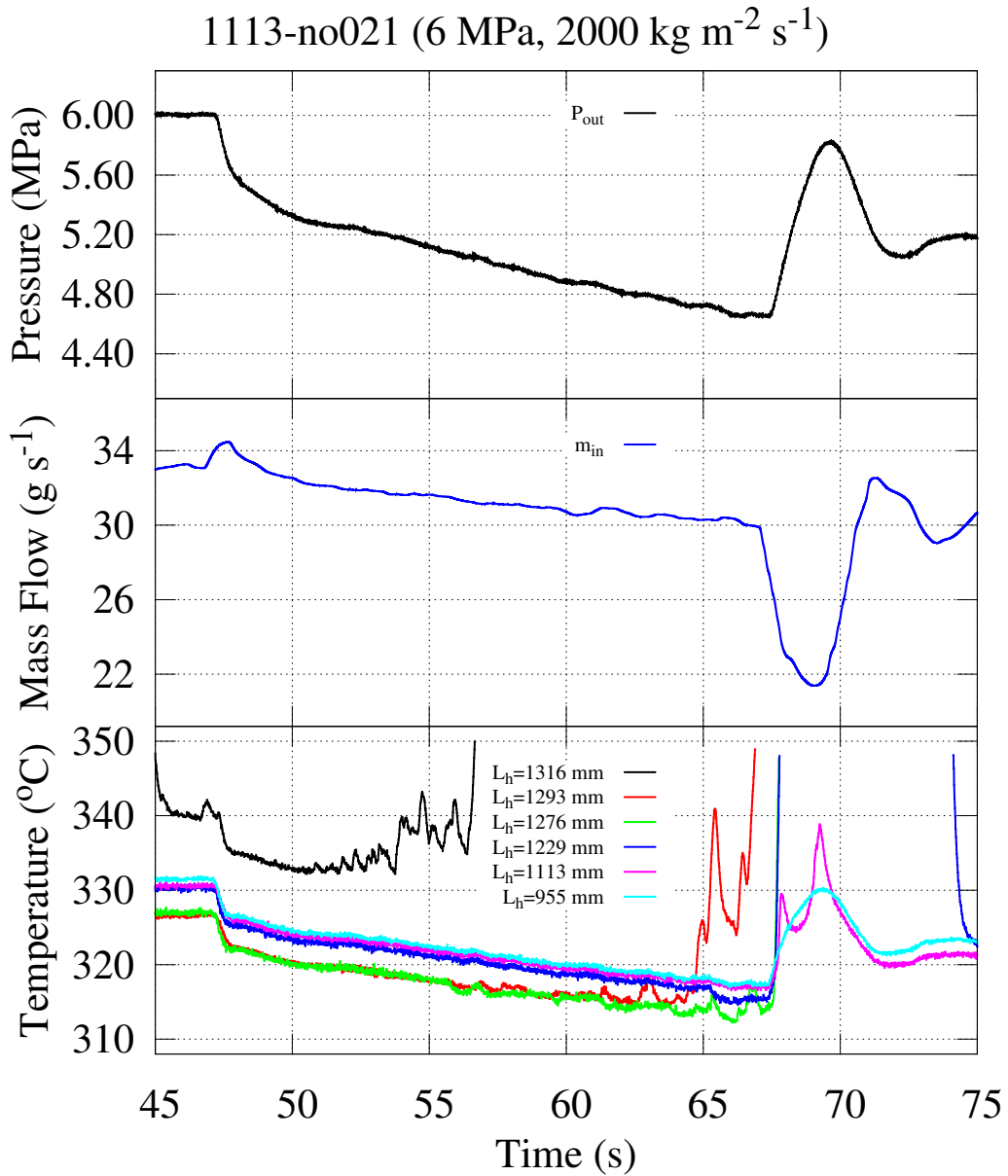
Figure 5.3: PDO transient data with an initial pressure of 6 MPa. At the top of this figure, in comparison to Figures 5.1 and 5.2, the pressure transient is very rapid during the first 3 seconds. The wall temperature fluctuates noticeably before the initiation of the transient when it rewets and dries out again after 4–5 s. At the end of the transient the closing of the blowdown valve causes a very rapid mass flow rate transient and also triggers dryout at L_h=1229 mm and 1113 mm.

creased. This decrease in wall temperature complicated the data analysis somewhat because thermal energy stored in the wall of the test section was released as the fluid temperature changes.

In the present work RELAP5 predicted an increase in convective heat flux of 1.6% due to thermal inertia in the test section wall for the fastest tested transient with a maximum depressurisation rate of approximately 1.0 MPa s^{-1}. The time evolution of the convective heat flux for this experiment is displayed in Figure 5.4. This figure shows the total heat flux, including the effect of stored energy, delivered to the fluid over time at the simulated test section volume nearest the end of the heated length for the same experiment as shown in Figure 5.1. This increase in heat flux to the fluid is the same order of magnitude as the overall uncertainty in the measured test section heat flux based on electrical power alone.

For the data presented in this thesis the power transient effect due to thermal energy storage was negligible. This is in contrast to what was observed in the pressure transient experiments of Celata *et al* [1] where the thermal energy storage transient was the main reason dryout was observed. This effect was also discussed briefly by Lyons and Swinnerton [3] but not modelled during their analysis of the predicted *vs* observed dryout time. An analysis of this effect is presented in Chapter 6.

5.3   Predicted and Observed Times to OID

5.3.1   Time Distributions

The data was analysed as an ensemble of all data points—one data point per thermocouple where dryout was observed per transient experiment—and separately for each initial condition. The techniques used to determine the predicted and observed times to dryout are illustrated in Figure 5.5. In the upper plot the predicted CHF was plotted with the convective heat flux computed by RELAP5. The convective heat flux included both the applied heat flux and the effects of thermal energy storage. CHF was predicted at the time when the predicted critical and convective heat flux curves intersected. The lower plot shows the wall temperature at one test section position plotted in parallel with its time-dependent running standard deviation
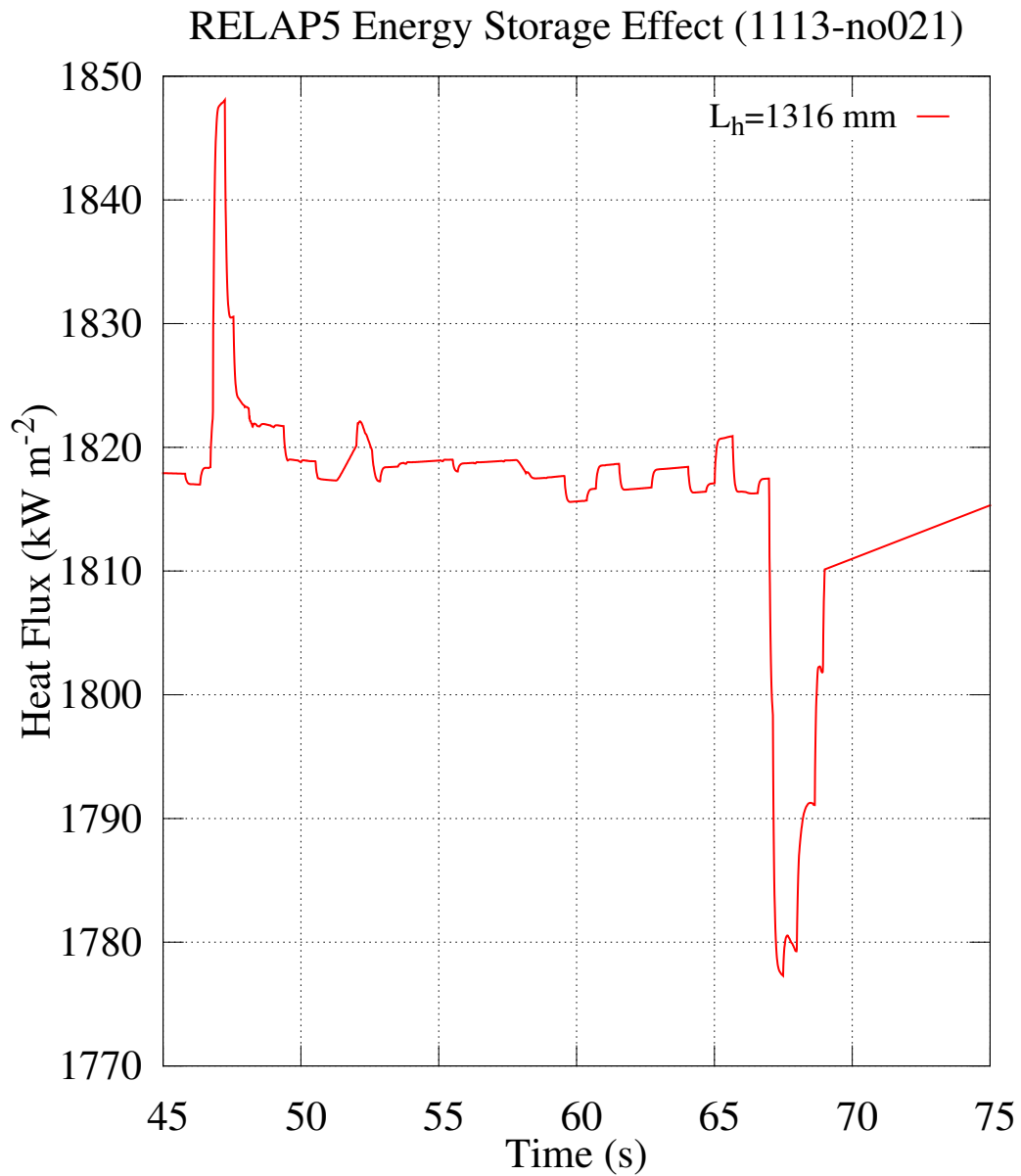
Figure 5.4: The transient surface heat flux due to the release of stored energy from the test section wall calculated by RELAP5 is plotted here for the fastest transient in the present work. Both the pressure decrease at the beginning of the transient and the pressure recovery at the end of the transient cause the surface heat flux to, respectively, increase and decrease due to energy being released from and stored in the test section wall.

calculated over the previous 0.1 s. The time of the experimental OID was marked when this 0.1 s standard deviation value exceeded $0.7°C$. For the example transient that is shown in Figure 5.5 OID was predicted to occur earlier in the transient than it was observed. The predicted dryout times for both modified prediction methods are plotted against the observed dryout times in Figures 5.6–5.9 sorted first by the nominal pressures and then by the nominal mass fluxes.

From Figures 5.6 and 5.8 it is evident that the modified look-up table predicted dryout to occur later than it was observed for more than half of the data. This is to be expected since several of the steady-state data were substantially overpredicted using this method—refer to Figures 4.15 and 4.16 in Chapter 4—and would therefore correspond to a later predicted dryout time.

The dryout delay for all of the transient data was then plotted on a histogram for all points, PDO points only and MTD points only for each dryout prediction method as shown in Figures 5.10 and 5.11. From the histograms the inferences drawn from looking at the predicted *vs* observed dryout times can be confirmed: the distribution for all initial conditions shows a bias towards slightly negative values of dryout delay for both dryout prediction methods.

It is evident that the dryout delay distributions were centred near the same values. This is true both for all of the data together and for the MTD and PDO initial conditions separately. This suggests that the author's hypothesis that the initial conditions played a role in the differing observations made by Celata *et al* [1, 2] and Lyons and Swinnerton [80, 3] is null.

Method–ICs (# of points)	Mean Delay (s)	Median Delay (s)	Standard Deviation (s)	Prediction Uncertainty (s)	Predicted Within ±2 s
LUT*–All (99)	-1.5	-1.0	3.0	±4.2	66%
LUT*–PDO (46)	-1.6	-1.1	2.8	–	70%
LUT*–MTD (53)	-1.3	-0.9	3.1	–	62%
Biasi*–All (89)	-0.1	-0.6	2.8	±1.5	53%
Biasi*–PDO (37)	-0.5	-0.6	2.8	–	49%
Biasi*–MTD (52)	0.2	-0.6	2.8	–	56%

Table 5.3: Dryout prediction performance for PDT (transient) data.
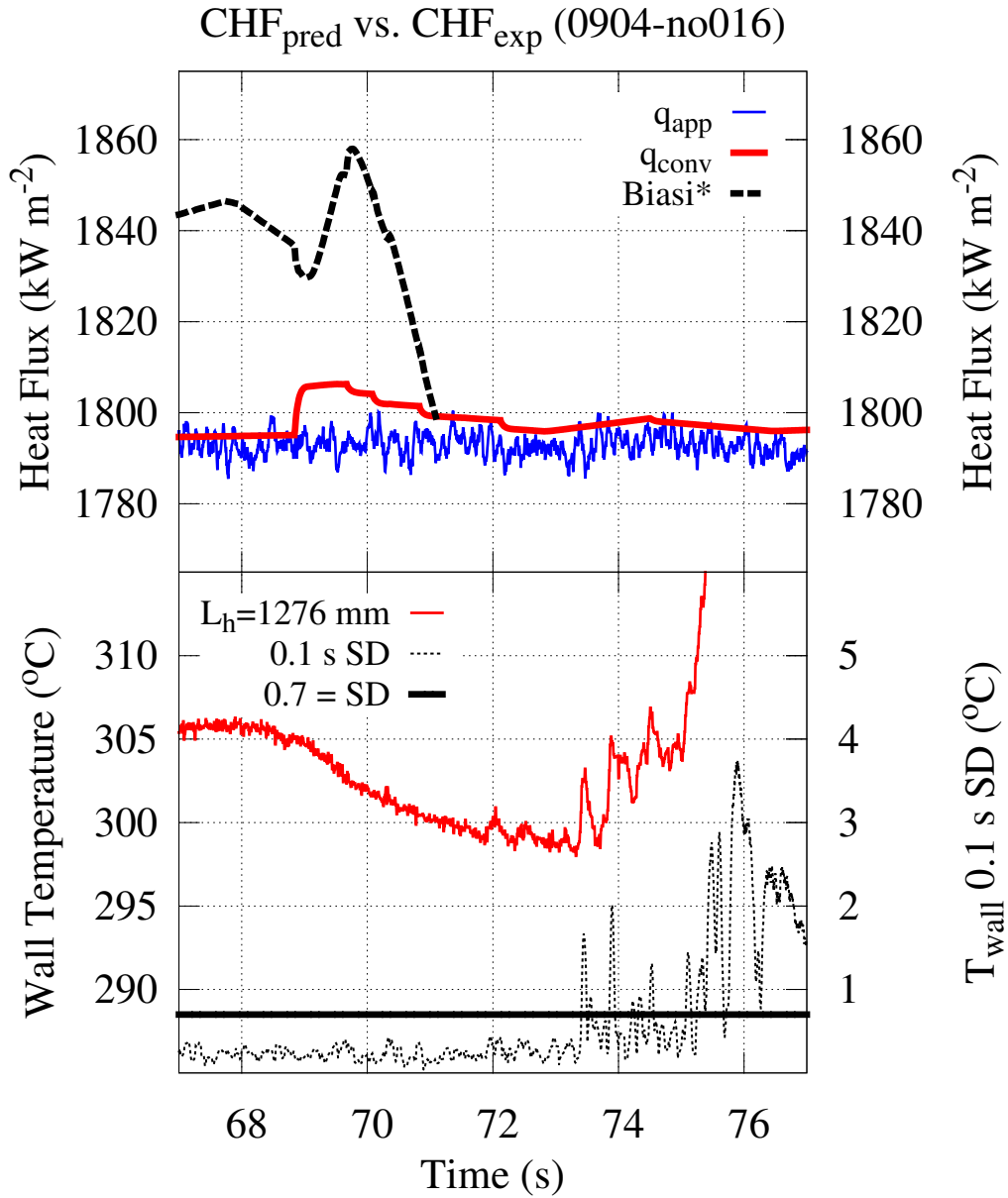
Figure 5.5: In the upper plot the electrical power measured during the transient is plotted along with the convective heat flux at one test section location calculated by RELAP5 that includes the thermal energy storage effect. The red line shows the predicted local value of the heat flux *vs* time. The predicted time to dryout was marked when the convective heat flux exceeded the predicted local CHF. The bottom of the figure shows the wall temperature for L_h=1276 mm and its standard deviation on the same time axis for the same transient. Experimental CHF was recorded when the transient standard deviation exceeded 0.7°C. The increase in standard deviation was well correlated with the beginning of large wall temperature fluctuations at OID.

B.A. Statham
Ph. D. Thesis

Chapter 5
Transient Results

McMaster University
Engineering Physics

LUT*
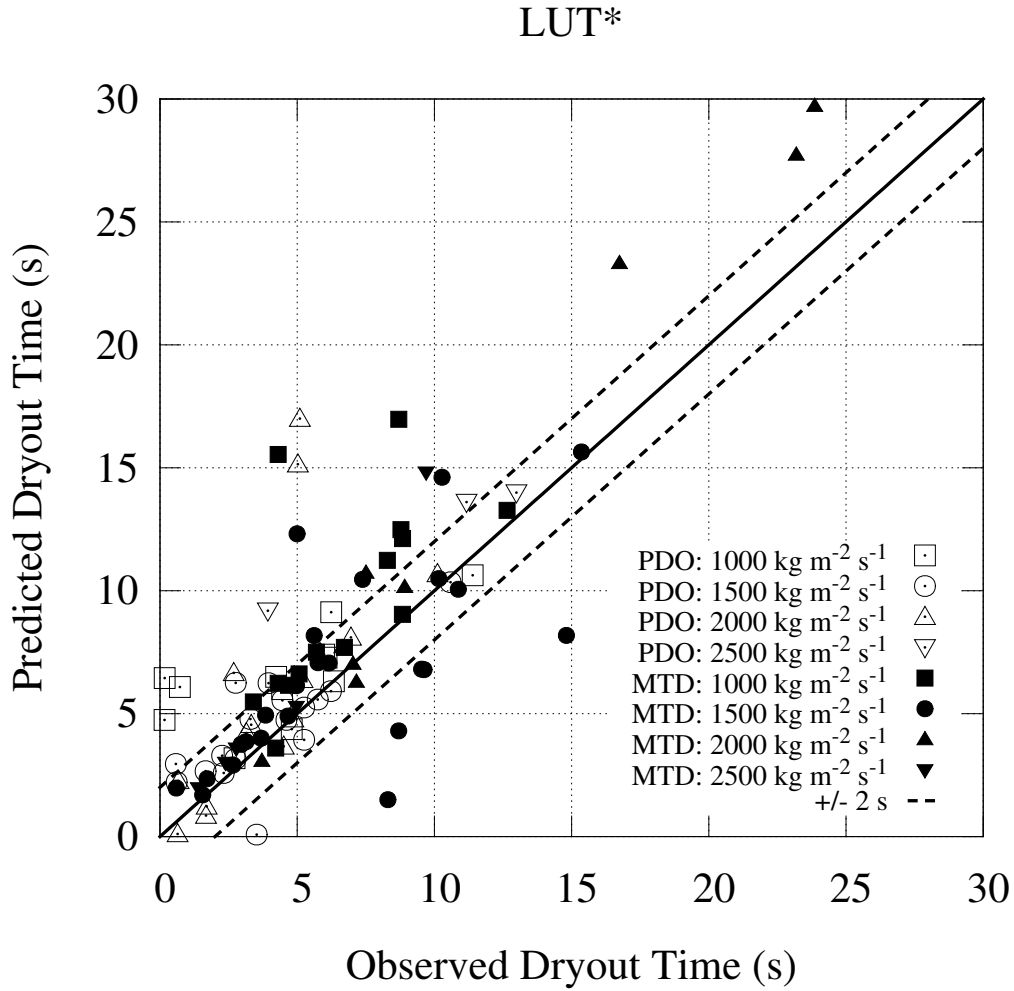
Figure 5.6: Predicted *vs* observed dryout time by mass flux for PDT data using the modified look-up table. No clear grouping of the predicted *vs* observed dryout times by mass flux or by initial conditions is apparent for the modified look-up table. There is a bias towards overprediction of the dryout time. This was due to the fact that many of the data that were underpredicted for steady-state conditions were predicted to experience dryout before the beginning of the transient and were eliminated from the final data analysis.
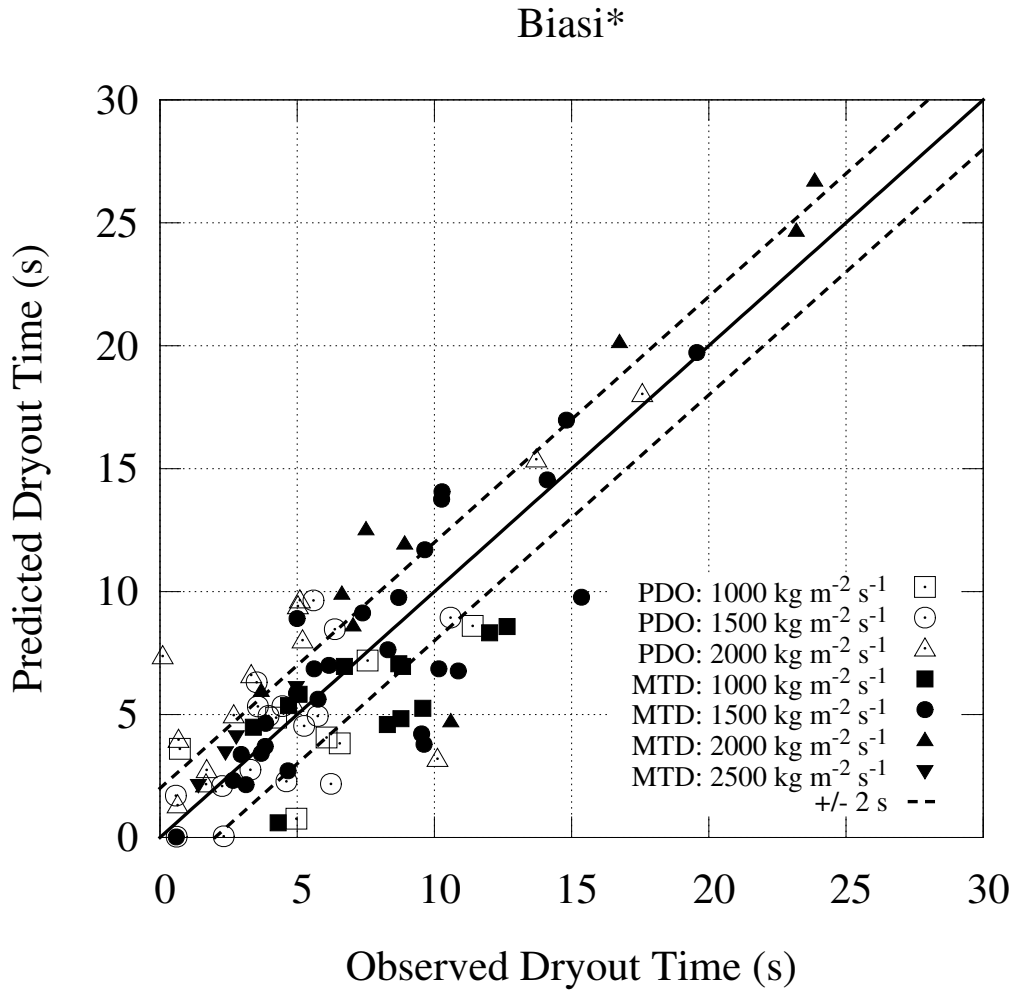
Biasi*

Figure 5.7: Predicted *vs* observed dryout time by mass flux for PDT data using the modified Biasi *et al* correlation. This figure is similar to Figure 5.6 in that there was no clear grouping by mass flux nor initial conditions—PDO or MTD—apparent when the predicted dryout time was plotte against the observed dryout time.
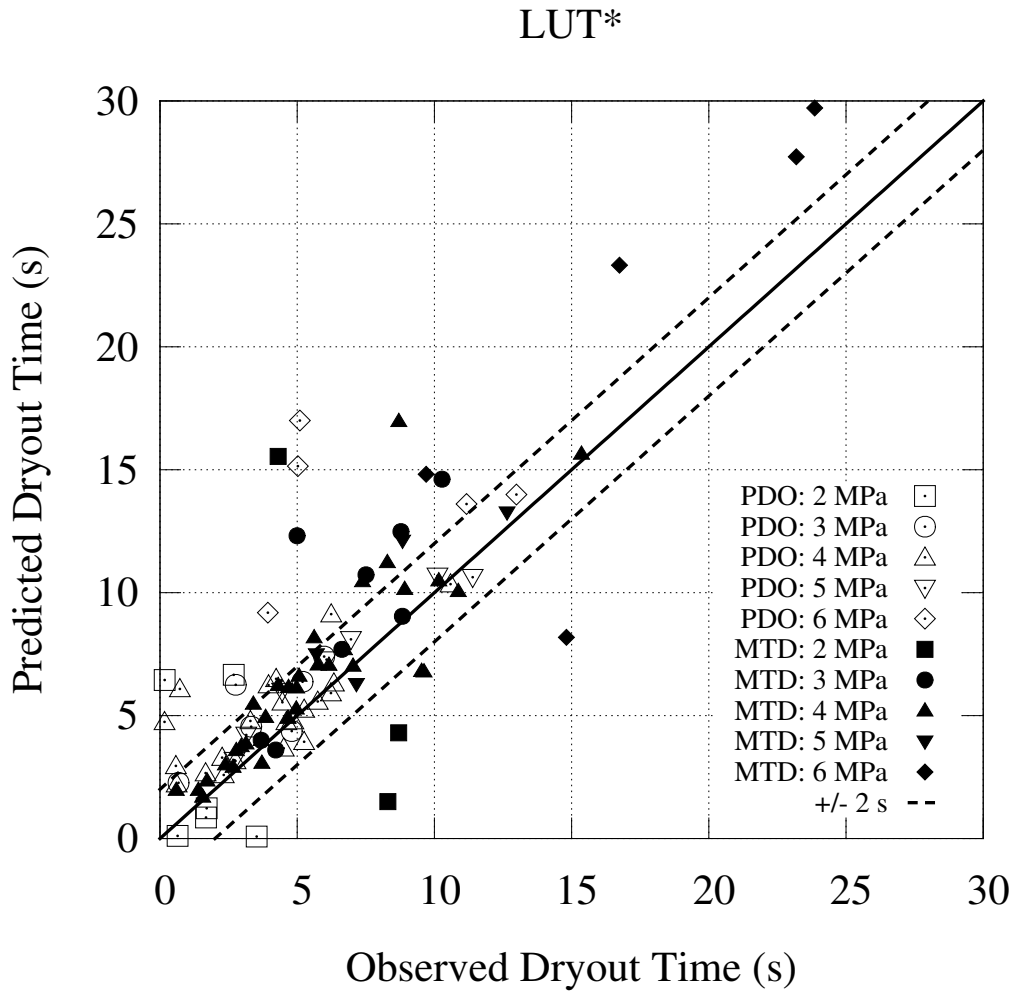
Figure 5.8: Predicted *vs* observed dryout time by pressure for PDT data using the modified look-up table. This is the same data as ploted in Figure 5.6 sorted by initial pressure. Again there is no apparent grouping of initial pressure nor initial conditions. Both this figure and Figure 5.6 for the modified LUT show a high concentration of data near the line of perfect prediction but with a number of data outside of ± 5 s.
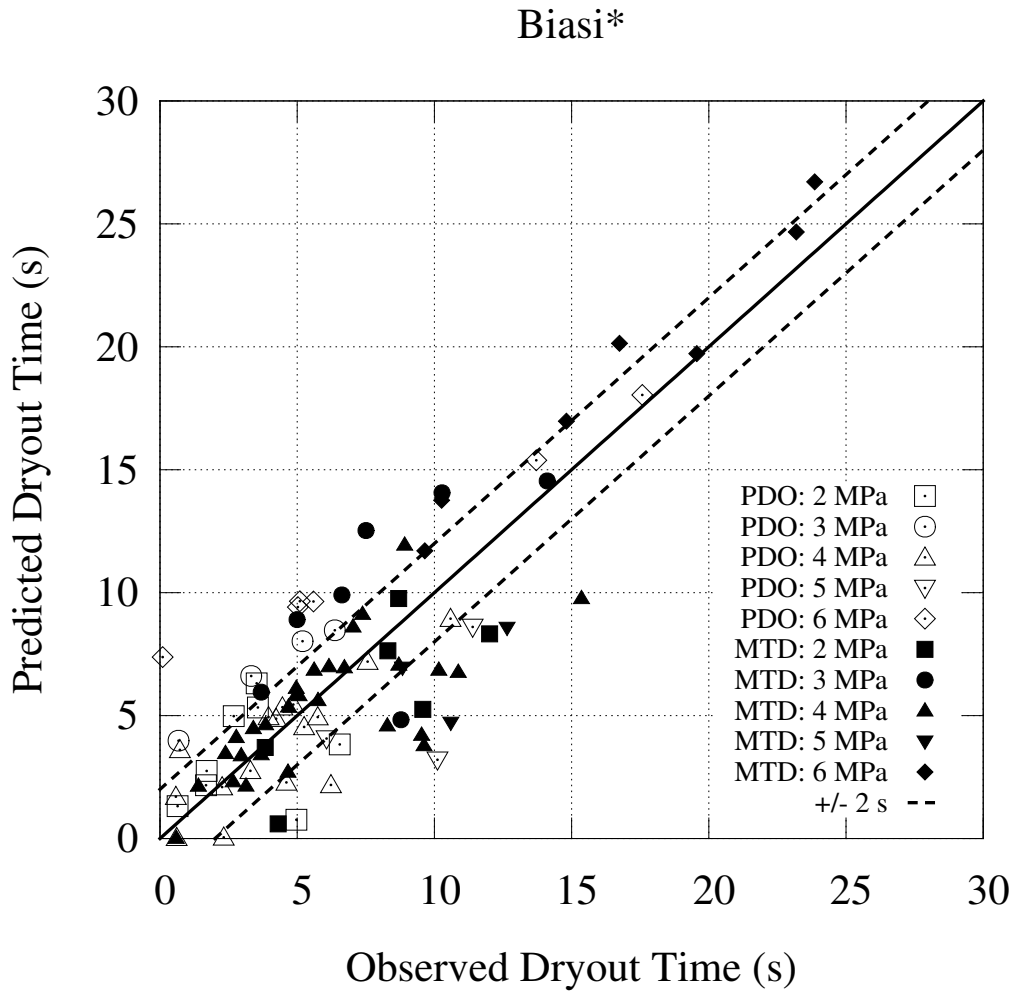
Figure 5.9: Predicted *vs* observed dryout time grouped by initial pressure for PDT data using the modified Biasi *et al* correlation. No distinct grouping of initial pressure nor initial conditions is obvious from this figure. Note that overall the distribution of data for the modified Biasi *et al* correlation is less tightly grouped than the modified LUT's data distribution but also that very few data are predicted outside of ± 5 s of the observed time.
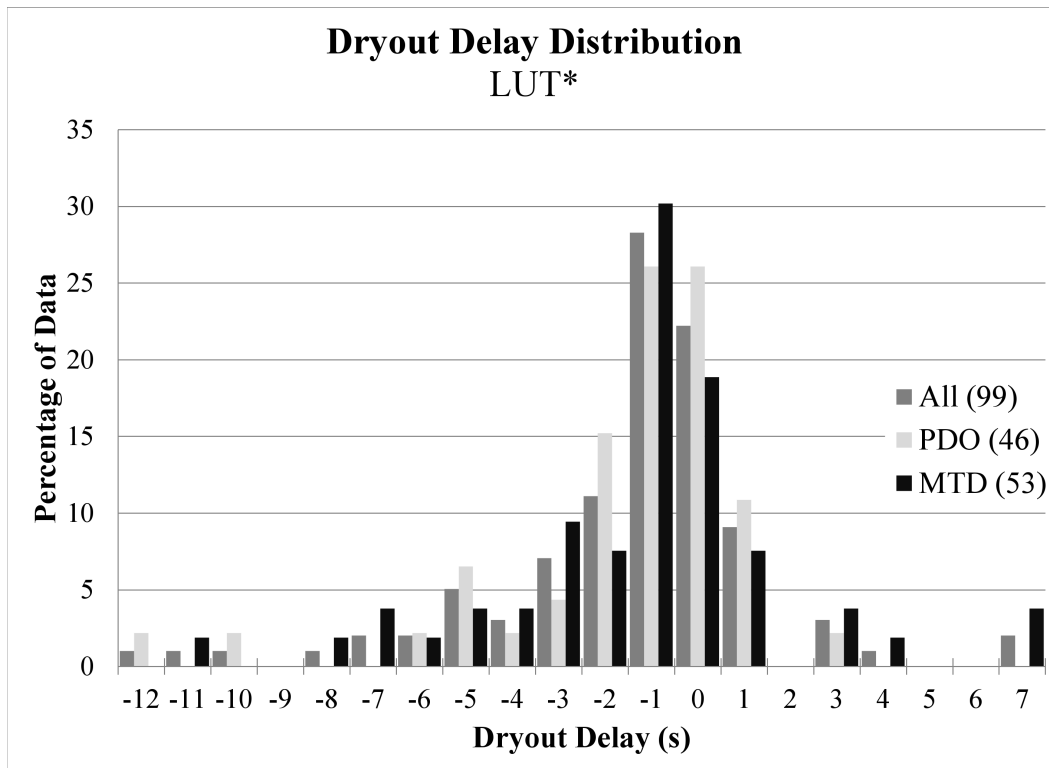
Figure 5.10: Dryout delay histogram for PDT data using the modified LUT. This figure shows the *difference* between the predicted and observed dryout times for the modified LUT. The distribution shapes for each initial condition are very similar to each other and, consequently, to the overall distribution of data with both initial conditions. Note the very strong peak at -1 s.
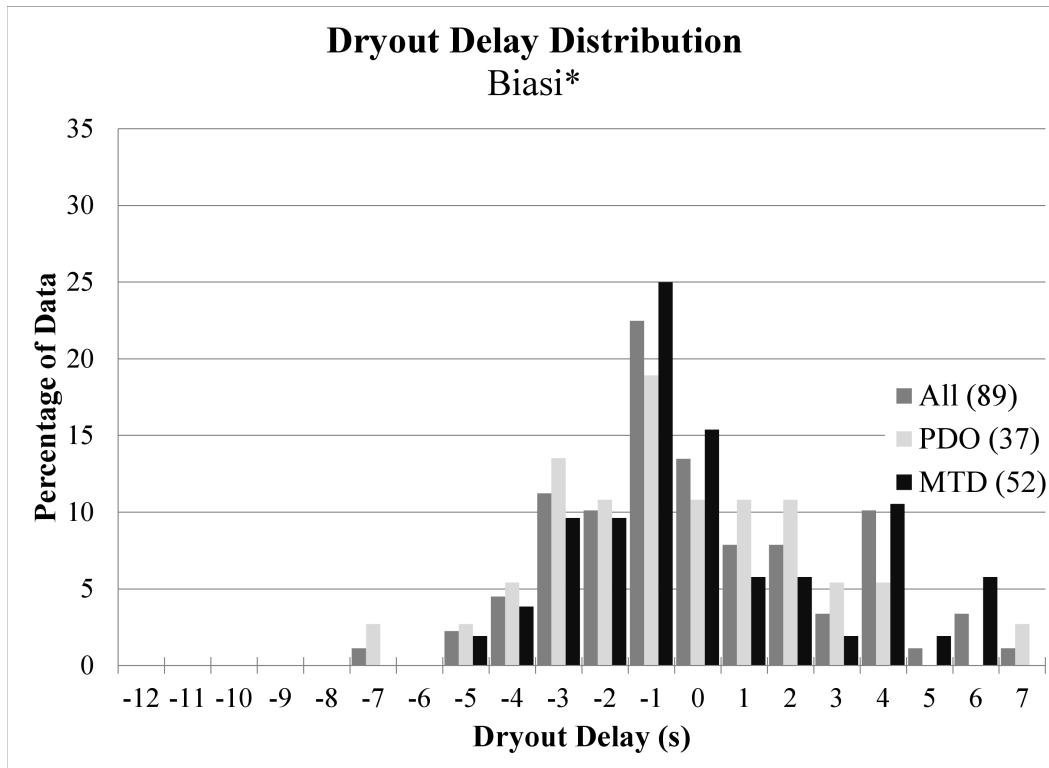
Figure 5.11: Dryout delay histogram for PDT data using the modified Biasi *et al* correlation. In comparison to Figure 5.10 for the modified look-up table the distribution of the dryout delay for the modified Biasi *et al* correlation has fewer outliers. Overall the dryout distributions for each initial condition—PDO and MTD—are similar although for positive values the PDO data have a relatively flat distribution while the MTD data has a distinct peak near 4 s.

The overall dryout time prediction performance of each method is listed in Table 5.3 for PDT data. It is sorted into categories of all data, PDO points only and MTD points only. The prediction uncertainty in time was estimated by calculating the time uncertainty using Equation 4.9 for every data point and computing the median value of all of these estimates. The standard deviation of the steady-state DSM predictions was used as an estimate of the relative CHF prediction errors. These were 5.8 and 151% of the instantaneously predicted CHF values respectively for the modified Biasi and LUT methods. The time derivative of the predicted CHF was calculated using a simple backwards finite difference estimate at the time CHF was predicted.

The time uncertainty estimates ranged from 0.06 to 30.9 s for the modified Biasi correlation and from 0.01 to 1980 s for the modified LUT. The median error estimate values for all of the data are shown in Table 5.3 to reduce bias due to the extreme high error estimates for data points whose predicted CHF varied slowly with time. The mean error estimates were 2.7 and 28.4 s for the modified Biasi correlation and the modified LUT. The mean time error for the modified LUT was approximately 10 times larger than the mean time error for the modified Biasi correlation while the standard deviation of the prediction error in the steady state data was nearly 30 times larger for the modified LUT than for the modified Biasi correlation. This was due to the very steep negative slope of the CHF *vs* quality curve in the LUT in the region that was investigated. This resulted in very fast rates of change in the predicted CHF with time for the modified LUT which, with reference to Equation 4.9, corresponded to a reduced time error estimate.

From the table of performance data it is evident that, as suggested in Chapter 4, even though the steady-state performance of the modified look-up table method is poor, the rapid change of CHF with quality allowed the modified LUT to give a good prediction of the time to dryout. In fact the modified look-up table predicted more of the data within ± 2 s than the modified Biasi *et al* correlation. This was in spite of its tendency to overpredict the steady-state data that biased it towards slightly late prediction of the onset of dryout—negative dryout delay.

The modified Biasi *et al* correlation overpredicted the steady-state data by a much smaller amount than the modified look-up table. This was reflected in the

mean predicted time being closer to but not exactly zero. The relatively smoother rate of change of the modified Biasi *et al* correlation with respect to quality—the LQR is not represented by the Biasi *et al* correlation—resulted in a slightly larger variance in the distribution of predicted dryout times.

The median values of the dryout delay from Table 5.3 should also be noted. For the modified look-up table the median delay values vary similarly to the mean delay times in magnitude. For the modified Biasi *et al* correlation, however, the MTD data had the smallest mean prediction error while the median prediction error was identical to the PDO data. The reason for this may be seen in the histogram in Figure 5.11: there is an outlying concentration of values in the 4 s histogram bin. These values biased the mean dryout delay value to make it seem that the MTD data was predicted better than the PDO data. The median dryout delay values for the modified Biasi *et al* correlation, however, show that the PDO and MTD data were, overall, predicted with nearly equal accuracy. The median values of dryout delay for the modified look-up table lead to the same conclusion.

5.3.2   Observations from Reduced Data

Overall the distributions of PDO and MTD data differ very little from each other and from the distribution of all of the data together for each correlation. The mean dryout delay values for the PDO and MTD data differ by 0.3 and 0.7 s for the modified LUT and Biasi *et al* correlations. These values are less than 25% of their overall distributions standard deviations that are on the order of 3 s. Furthermore the median dryout delay values for the modified Biasi correlation are equal despite the difference of 0.7 s in their mean values.

For a normal distribution the mean values would need to differ by 1.96 standard deviations in order to state with 95% confidence that they are statistically different. The difference between the distributions of MTD and PDO data is much less than 1.96 times their standard deviations. Therefore there is no statistically significant difference between the effect of these two initial conditions. This renders the author's hypothesis that the initial conditions were responsible for the differing conclusions of Celata *et al* [1, 2] and Lyons and Swinnerton [80, 3] null for the

range of conditions investigated in the present work.

The mean dryout delay times for each dryout prediction method differ from zero by a fraction of the estimated error in the predicted dryout times. Therefore it may be concluded that, within the overall prediction uncertainty of the methods used in the present work, the quasi-steady method is sufficient for predicting OID during pressure transients for the range of conditions investigated in the present work. This supports the conclusion of Lyons and Swinnerton [3].

Chapter 6

Discussion

This chapter discusses the results presented in the previous chapter. Some comparisons are made between the data of Celata *et al* [86] and the data of Lyons and Swinnerton [3] in relation to the author's hypothesis, the data, and the relevant phenomena.

6.1 Relevant Dryout Phenomena

6.1.1 Axial Conduction

Conduction from the region near the test section exit undergoing intermittent dryout to neighbouring wetted regions was postulated to accelerate the onset of dryout in Lyons and Swinnerton's experiments [80]. They stated that for some of their experiments the initial wall temperature occasionally reached 400°C. This effect was tested for steady-state condtions using a steady-state two-dimensional radial conduction model.

25 mm of the test section was modelled with adiabatic boundary conditions at the upstream tube face and the outer tube face. The downstream face of the tube was given a constant temperature boundary condition of 212.4°C to simulate conduction to the bus bars at the end of the heated length. The inside wall of the test section was given a convective boundary condition with a heat transfer coefficient of 100 kW m^{-2} °C^{-1} over the upstream 15 mm and 10 kW m^{-2} °C^{-1} over the final

10 mm.

The resulting temperature distributions at the inside and outside faces of the tube are shown in Figure 6.1. The maximum inside wall superheat in the post-dryout region was 177.8°C while the steady wall superheat away from the wetted region was 26.4°C. This figure shows that the difference in wall superheat between the two regions decreased to 2.3% of its maximum value within 1.5 mm of the boundary between the wetted and post-dryout regions. This represents an extreme case since dryout occurred gradually in the present work. With gradual dryout there would be a transition region with a continuously varying heat transfer coefficient rather than an abrupt step change in heat transfer coefficient as in this model. With a gradual heat transfer transition the axial temperature gradients would be less severe and exert a smaller influence than what was found in this model.

6.1.2 Thermal Energy Storage

Both Celata *et al* [1] and Lyons and Swinnerton [3] made note of the effect of the release of stored energy in pressure transients. This phenomena was central to Celata *et al*'s analysis. It was not modelled in Lyons and Swinnerton's data analysis although its relevance was acknowledged. RELAP5 modelled the release of stored energy in the present work. This effect will be present in any depressurisation experiment that uses a heated boundary with a non-zero heat capacity.

A rewet transient from a failed depressurisation experiment that occurred during the present work is shown in Figure 6.2. In this experiment the power supply was completely shut off when one of the wall temperature thermocouples hit a pre-set temperature limit. When the power supply was shut off the wall superheat was on the order of 250°C above the saturation temperature of the two-phase mixture in the test section. If no thermal energy were stored in the test section wall the wall temperature would drop instantaneously to the ambient temperature. The test section wall has a finite heat capacity and does therefore store energy; as a result it took a finite time for the test section wall to cool. This example was chosen because in this case the wall is cooling slowly due to the poor heat transfer coefficient in the post-dryout regime that remains until the surface rewets. When the rewet
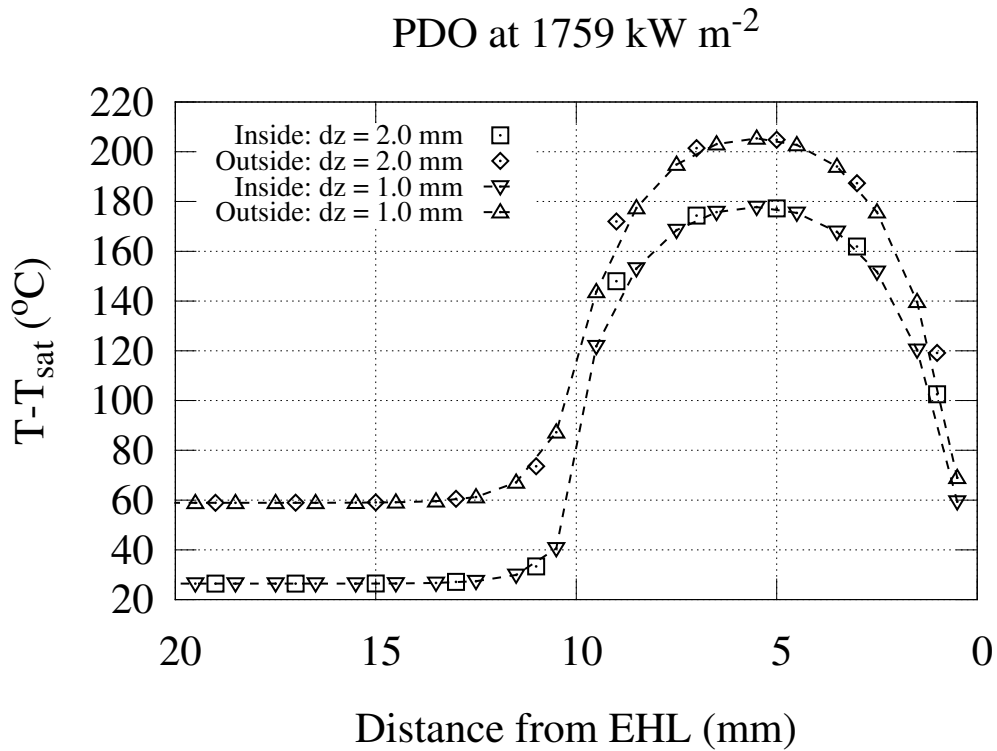
Figure 6.1: 2-D conduction model results that show the effect of conduction from a region of dry-out to a wetted region. Two different discretizations were used. The effect of the region undergoing dryout ($<$10 mm from the EHL) on the neighbouring region was 95% dissipated within 1 mm in the coarse model and 98% dissipated within 1.5 mm in the fine model. The decrease in wall temperature as the EHL was approached was due to the effect of the bus bars. The bus bars were modelled by a constant temperature boundary condition.

occurs at approximately 96 s for all displayed thermocouples the rate of energy release increases because of the increased heat transfer coefficient. The degree to which thermal energy storage affects the results of depressurisation transients in the present work is compared to that of Celata *et al* [1] and Lyons and Swinnerton [3] below.
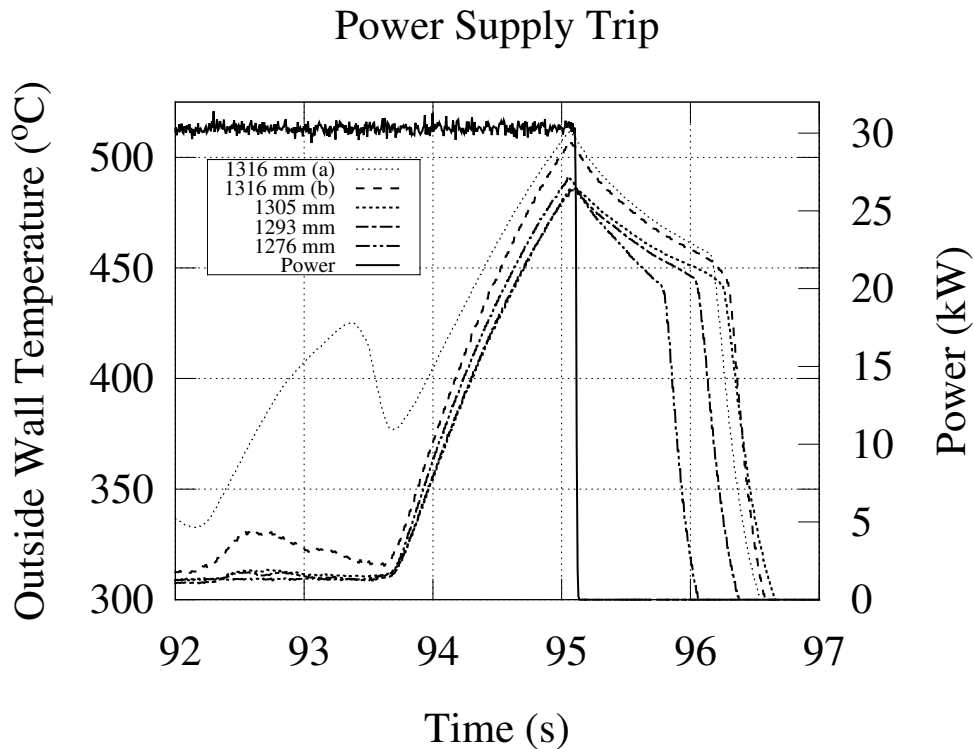
Figure 6.2: Test section thermal energy dissipation following power supply shutoff. This figure shows the heatup and cooldown of the test section wall when dryout was observed during a transient. Dryout was followed by a power supply trip on a high temperature signal. Due to the heat capacity of the test section wall it took a finite time to cool down. This time is initially exaggerated due to the post-dryout heat transfer conditions. It is a good example because it shows that the cooldown time is not due to the time-response of the thermocouples but is actually an energy storage effect.

Using a 1-D lumped capacitance model the heat transferred from the test section wall may be approximated as in Equation 6.1 where c_{pw} is the specific heat capacity of the wall material, ρ_w is the density of the wall, L_w is the wall thickness, and T_{sat} is the saturation temperature that forms the boundary condition for Equation 1.1. A

lumped capacity approach with a constant heat transfer coefficient at the boundary between the heated surface and the fluid was used to solve for the time-dependent heat flux at the wall by Celata $et\ al$ [1] in the initial analysis of their pressure transient only data. The purpose of the present analysis is to find a quantity that allows the experiments of Celata $et\ al$, the experiments of Lyons and Swinnerton [3], and the experiments from the present work to be compared on the basis of the relative importance of the power transients caused by thermal energy storage.

$$\ddot{q}_{st}(t) = c_{pw}\rho_w L_w \frac{dT_{sat}}{dt} \tag{6.1}$$

The rate of change of saturation temperature can be approximated using the known depressurisation rate and the saturation curve for the fluid:

$$\frac{dT_{sat}}{dt} \approx \frac{dT_{sat}}{dp}\frac{dp}{dt} \tag{6.2}$$

Celata $et\ al$ provide boundary conditions for all of their experimental data in [86] including exponential time constants that may be used to approximate the depressurisation transients. Using the 1-D lumped capacitance model from Equation 6.1 that neglects the effects of conduction and evaluating the depressurisation rate using Celata $et\ al$'s provided exponential decay curves yields an upper bound on the maximum heat flux due to thermal storage for each of their data points. An energy storage number, Γ, may be defined as in Equation 6.3 where $\ddot{q}_a$ is the applied heat flux and $\ddot{q}_{st}(0)$ is the approximate initial magnitude of the driving force behind the rate of heat flux increase due to thermal energy storage. This number represents the degree to which thermal energy storage affects the heat flux delivered to the fluid relative to the applied—near CHF—heat flux. It is evident from Equations 6.3 and 6.1 that the effect will increase with depressurisation rate and decrease with as the applied power is increased keeping other values constant.

$$\Gamma = \frac{\ddot{q}_{st}(0)}{\ddot{q}_a} \tag{6.3}$$

This energy storage number was calculated and plotted in Figure 6.3 for all of Celata $et\ al$'s pressure transient data from [86]. It was calculated for Lyons

and Swinnerton's test section [3] for a range of depressurisation rates and initial pressures for a constant applied heat flux of 1000 kW m^{-2}. Similarly it was also calculated for a the same range of conditions for the test section of the present work with an applied heat flux of 1400 kW m^{-2}. These heat flux values represent the approximate lower bounds of the range of CHF values for steady state CHF in Lyons and Swinnerton's study and the present work, respectively. These calculated values of the energy storage number were similarly plotted in Figure 6.3 with Celata *et al*'s data. The data in this figure show that for similar depressurisation rates the energy storage number is an order of magnitude larger for the R-12 data of Celata *et al* [86] than it was for the experiments conducted using water from Lyons and Swinnerton [3] and the present work.

The main reason that the effect of stored thermal energy is much greater on data collected using a refrigerant to simulate the two-phase flow of water is largely because of how the fluid properties are scaled. Using data from [115] the rate of change of the saturation temperature of water decreases from 25 to 11 when the pressure increases from 2 to 6 MPa—the range of the present work. Again using data from [115] but for R-12 the rate of change of saturation temperature decreases from 33 to 20 as the pressure increases from 1.25 to 2.75 MPa—the range of Celata *et al*'s data [86]. Celata *et al*'s data is affected by energy storage to a much greater degree partly because of the slightly faster rate of change of saturation temperature with pressure but mostly because of the low latent heat of R-12. The applied heat fluxes needed to reach CHF in R-12 were on the order of 100 kW m^{-2} [1] or less compared to 1000 kW m^{-2} or more for water with similar boundary conditions. The absolute values of the amount of energy released from the wall were otherwise similar except for variations in wall thickness and material properties.

The effect of conduction on energy storage effects in the present work and Celata *et al*'s data [86] should be nearly identical for similar depressurisation rates: Celata *et al* used a stainless steel test section while Inconel 600 was employed for the present work. Both test sections had wall thicknesses of approximately 0.9 mm. The thermal properties of each material are illustrated in Table 6.1 [116]. Lyons and Swinnerton's Inconel 600 test section had a wall thickness of 1.6 mm [3] and so conduction would reduce the peak heat fluxes predicted using the lumped capac-

Thermal Energy Storage Effect
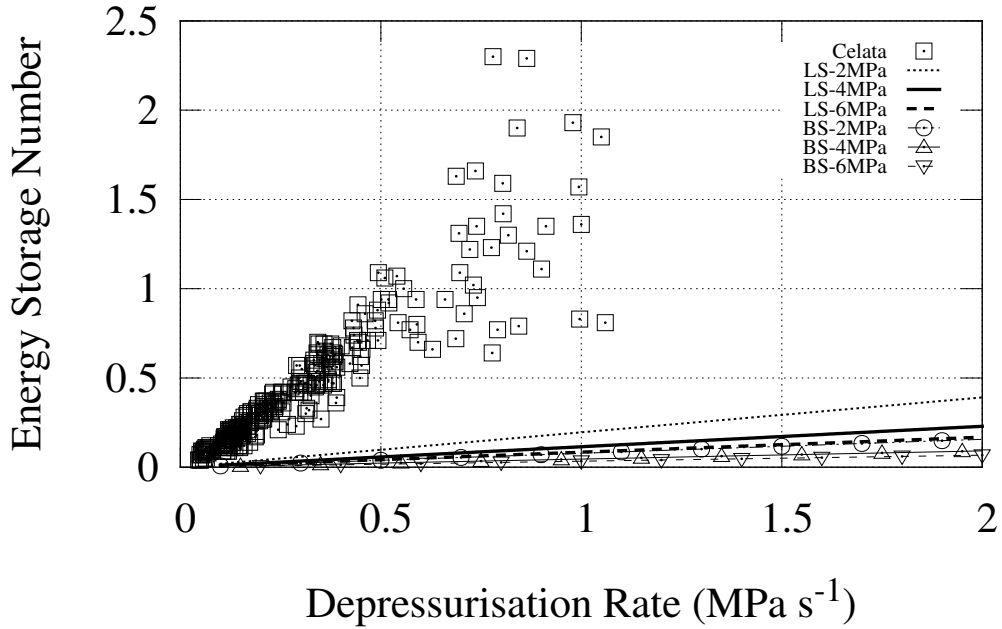
Figure 6.3: Energy storage numbers for Celata *et al*'s pressure transient data [1] and the test sections of Lyons and Swinnerton and the author operating at 1000 kW m^{-2} and 1400 kW m^{-2} respectively. For the depressurisation rates that are shown Celata *et al*'s data is clearly separated from the water data because the nominal effect of the stored thermal energy transient relative to the applied heat flux is much larger for R-12 than for water pressure transient CHF experiments.

itance model by a greater degree than for the other experiments.

Material	Heat Capacity kJ kg^{-1} K^{-1}	Density kg m^{-3}	Thermal Conductivity kW m^{-1} K^{-1}
SS316	0.488	7920	0.0173@100°C
Inconel 600	0.578	8415	0.0186@300°C

Table 6.1: Properties of SS 316 and Inconel 600.

Lyons and Swinnerton [3] concluded that the quasi-steady model reliably pre-dicted the shape—dryout position *vs* time—of the dryout front transient. It is ev-ident from observation of their results that their annular flow model over-predicts

the dryout length for their rapid transients while the annular flow model generally under-predicted the dryout length in their steady state results. It is possible that the slightly earlier onset of dryout predicted by their model for the fast transients is because their data analysis did not model these thermal energy storage effects. The heat flux delivered to the fluid during the transient did increase—as Lyons and Swinnerton demonstrated for one case—but when their model was run this additional heat flux was not included. This error may also be due to their neglect of pressure drop and momentum conservation in their annular film dryout model.

By comparing the relative effect of stored energy on Celata *et al*'s experiments [86] to Lyons and Swinnerton's [3] and the present work it is clear that it is much more important in experiments where refrigerants are used to simulate two-phase flow than in experiments conducted using water. This was also noted by Leung [81] when they analysed their data. In that case dryout occurred much later in the transient than the thermal energy storage peak so the results were not influenced by this effect.

Celata *et al* [2], however, noted that the transient power increase caused by the release of thermal energy was much faster than even their step power transient experiments. The rate of power increase due to stored energy was fast enough to mask the type of imposed power transient—ramp or step—in their pressure and power combined transient experiments.

In their analysis of pressure combined with flow and/or power transients Celata *et al* [2] stated that there was a threshold value of 0.2 MPa s^{-1} above which there was a systematic decrease, from approximately unity, in the ratio of predicted to observed time to dryout. Figure 6.3 is re-plotted with Celata *et al*'s pressure-only transient data [1] in Figure 6.4 at a reduced scale. The threshold depressurisation rate is plotted as a vertical line. If the threshold depressurisation rate that was noted for the combined transients is applied to the pressure-only transients then a critical value of the energy storage number, 0.3, can be deducedfrom this graph. This critical value is plotted as a horizontal dashed line in Figure 6.4.

The application of the combined-transient threshold value to pressure-only data is supported by Celata *et al*'s [85] earlier analysis of combined flow-power transients. In this work the same code was used to analyse flow-power transients as was

Thermal Energy Storage Effect
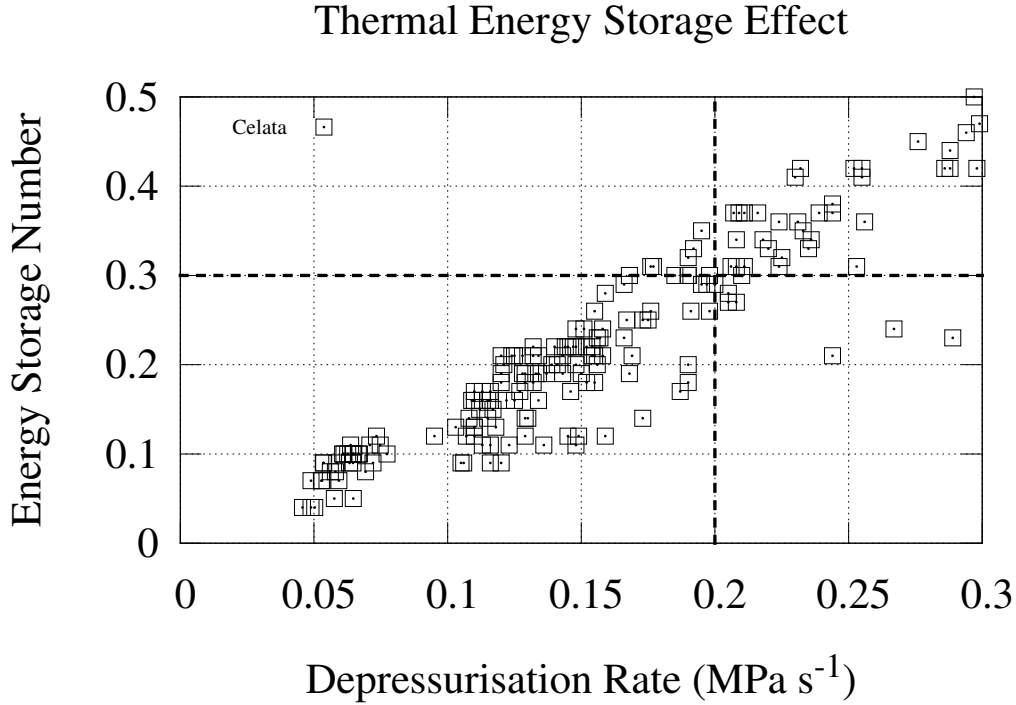
Figure 6.4: Celata *et al's* [1] pressure transient data plotted on energy storage number–depressurisation rate axis. This figure shows that, based on the threshold depressurisation rate from [2], the critical value of the thermal energy storage number is approximately 0.3.

used to analyse pressure-power, pressure-flow and pressure-power-flow transients in [2]. No systematic difference between the predicted and observed dryout times was found when the flow-power transients were analysed. Therefore it is reasonable to conclude that the systematic effect of depressurisation rate observed in [2] was due to the secondary, but very rapid, power transient triggered by the pressure transient. The threshold value may be applied to pressure-only transients because it is this transient that is solely responsible for the observed delay.

Based on the experimental evidence from the present work and the lumped-capacity model comparison of the effect of transient stored energy relative to the applied heat flux it is apparent that the delay in the onset of dryout observed by Celata *et al* [1, 2] was due to the effects of the secondary power transient. This

power transient effect was dominant over any transient effects that may have been caused by the pressure transient itself.

This demonstrates that transient data from experiments that use refrigerants to simulate the two-phase flow of water is inadequate even when the fluid properties scale using, *e.g.*, Ahmad's CHF scaling laws [117]. The delay observed by Celata *et al* [1, 2] may have been due to the time required to evaporate the wetting liquid film as postulated but the results of the present work demonstrate that this is not a significant effect in pressure transients where the energy released from the wall is relatively unimportant. For power transients, *e.g* the energy storage transient that has a significant effect for experiments conducted using refrigerants to simulate the two-phase flow of water, an analogy may be drawn between the annular liquid film evaporating and the evaporation of the liquid sublayer in Serizawa's [63] and Pasamehmetoglu *et al*'s [96] models.

6.1.3   Droplet Heat Transfer

The steady-state results collected during the approach to dryout showed a change in heat transfer mechanism at heat fluxes below the onset of intermittent dryout as can be seen in Figures 4.3, 4.5 and 4.4. This change in heat transfer could be the consequence of a change in flow regime from a dispersed annular flow to a dispersed droplet flow. In this flow regime the heated surface is wetted solely by the deposition of droplets onto the surface as postulated by Hewitt, Groeneveld and others [6, 8]. Based on the steady-state data from this study this transition occurs with a margin to dryout of 5–8%. The margins to dryout in the present work of 1–1.5% were therefore too small for this regime change to affect the results. Since this regime change axially preceded OID in the test section it was unlikely to affect transient OID for the conditions investigated. It was not clear, however, if this regime change would correspond to a liquid film flow of zero if computed by Whalley *et al*'s model and the presence of this regime may have been responsible for the slight underprediction of Lyons and Swinnerton's steady-state data [103].

6.2 Validity of the Quasi-Steady Method

The results and analysis of the transient experiments in the present work have demonstrated the validity of the quasi-steady method for the prediction of the onset of dryout during pressure transients over the range of conditions investigated: upward annular flow in a tube with a length to diameter ratio of 289 at pressures from 2–6 MPa, mass fluxes of 1000–2500 $\text{kg m}^{-2}\text{ s}^{-1}$ and initial inlet subcooling of -0.148 at depressurisation rates of up to 1.0 MPa s^{-1}.

The phenomena discussed above suggest that the validity of the quasi-steady method is not due to a coincidence of combined effects that cancel each other out as Pasamehmetoglu [38] suggested may occur. It is unlikely that axial conduction in the present work acted to accelerate the progression of the dryout front. Furthermore the shift in the wall temperature as dryout is approached suggests that the wall is wetted soley by the deposition of droplets and that a continuous liquid film that would require a finite time to evaporate during a transient does not exist immediately upstream of the location of incipient dryout. The data presented by Celata *et al* [2] do suggest that there may be a delay in the onset of dryout. If this is a real effect and not an artifact of the limitations of their HEM model then it is due to the power transient imposed by the release of stored energy in the test section wall. This effect is also present in water data but is an order of magnitude *relatively* more significant for transient data from experiments where refrigerants were used to simulate the two-phase flow of water.

Dryout prediction methods that are based solely on the local equilibrium quality, mass flow, pressure, and geometry or diameter are empirical representations of the locus of heat transfer deterioration that are controlled by underlying hydrodynamic and thermal phenomena. This includes the flow of a liquid film along the heated wall, entrainment and deposition of liquid droplets to and from the liquid film and the flow of vapour with entrained droplets through the centre of the channel. When these effects are modelled dryout prediction is no more accurate than the empirical correlations [101, 105].

The exceptions to this are circumstances where, for example, an annular flow is allowed to reach equilibrium downstream of a diabatic section in an unheated sec-

tion before entering an additional heated section where dryout occurs. This was the case in Bennet's cold patch data analysed by Biasi *et al* [98]and later re-analysed by Adamsson and Anglart [118]. This data, and other data obtained with two-phase inlet conditions, have dissimilar initial conditions—at the effective onset of annular flow or boiling length that is the beginning of the channel—to data obtained from experiments with single phase inlet conditions. In these experiments the analogy made by the empirical correlations that the local mass flux and quality—which can be derived relatively straightforwardly from experimental boundary conditions—may be used to represent the underlying film flow, droplet entrainment and deposition processes breaks down.

When Whalley, Lyons and Swinnerton [39] removed the transient terms in their annular film flow model they found that the model performed nearly as well at predicting the dryout front progression in their transient experiments as it did when they were included. This suggests that the implicit time scales of the entrainment and deposition rates are very fast. If their model is representative of the governing phenomena of dryout—as suggested by the analyses of the dryout data obtained with effective two-phase inlet conditions—this also suggests that if the quality-mass flux analogy to film flow, entrainment and deposition is valid during steady-state conditions then it is equally valid during transients. This gives credibility to the quasi-steady method for predicting dryout during flow boiling transients for channels with single-phase inlet conditions when the steady-state method applied to the local channel conditions during transients also predicts steady-state dryout well for the same channel.

Chapter 7

Conclusion

7.1 Summary

The most common method to predict OID in the core of nuclear reactors and other industrial systems is to compute the local thermo and fluid dynamic conditions throughout the heated portion of the system and to use those local parameters as input to a dryout prediction method such as a correlation or look-up table. These prediction methods are used to determine whether or not the local heat flux exceeds the CHF associated with dryout for those conditions. These prediction methods are nearly universally based on data collected under steady or near-steady operating conditions. There is some evidence in the literature of a delay in the onset of dryout—or an increase in the transient CHF for power transients—in some transient situations. Some examples that show evidence of a dryout delay include the flow boiling heated wire experiments of Kataoka *et al* [71]with exponentially increasing power or the step power and total loss of flow transient experiments of Moxon and Edwards [46]. There is also some evidence of a delay in OID for pressure transients: Celata *et al* [2]were unable to successfully predict OID in combined transients with maximum depressurisation rates in excess of 0.2 MPa s^{-1} although they had good success with slower depressurisation rates and power-flow transients [85].

Transient-specific models have been used to successfully predict the observed increase in the CHF under exponential power increase conditions for nucleate boiling conditions, *e.g.* [95, 96]. Chang *et al* [107] used a boiling length approach to

B.A. Statham
Ph. D. Thesis

Chapter 7
Conclusion

McMaster University
Engineering Physics

successfully predict the onset of dryout for the power transient data of Moxon and Edwards although how well the model or base correlation was able to predict the steady data was not established. Several others have shown that the quasi-steady approach is sufficient for both refrigerant-based flow transient experiments and a handful of Moxon and Edwards flow transient experiments, *e.g.* [43], [44]. Based on these analyses from the literature there is evidence that there may be a short delay in the onset of dryout for channels undergoing nucleate boiling that experience rapid power transients while flow transients may be predicted well by the quasi-steady method.

Lyons and Swinnerton [3] performed rapid depressurisation experiments with depressurisation rates of more than 5 MPa s^{-1} using water as the working fluid. They found that the inlet-conditions Bowring correlation and the Whalley [39] annular flow model were able to predict the rate of dryout front progression as it moved upstream in their vertical channel. The author of the present work hypothesised that the apparent delay in the onset of dryout observed by Celata *et al* [1, 2] was due to the finite time required for the liquid layer on the test section wall to evaporate since their initial conditions had a small margin to dryout. Concomitantly it was hypothesised that the progression of the dryout front in the Lyons and Swinnerton [3] data was initially accelerated due to axial conduction in the test section wall from the hot dry patch to the wetted region because of the initial conditions of their experiments.

A new experimental facility was constructed in order to perform steady-state and transient dryout experiments. The experimental facility was commissioned with high-accuracy calibrated instrumentation. Data was sampled throughout the experiments and recorded at high data rates for specific steady and transient conditions in order to preserve the data for posterity. This facility enabled both steady and transient data to be collected using the same apparatus and test section. This ensured that the transient data could be analysed in a way that was self-consistent with the steady-state data.

A series of pressure transient experiments were conducted with this facility. These experiments represented both post-dryout and margin-to-dryout initial conditions at the exit of a vertical uniformly heated test section that was internally cooled

147

by the forced flow of water. The purpose of the experiments was to test the author's hypotheses on the effect of initial conditions on the onset of intermittent dryout during pressure transients. Steady state dryout data was collected for the range of initial conditions that were investigated—outlet pressures from 2 to 6 MPa, mass fluxes of 1000–2500 kg m^{-2} s^{-1}, heated length of 1.321 m, 4.6 mm inside diameter, inlet flow quality of -0.148 and uniform electrical heating. Two dryout prediction methods were compared with this data and then modified slightly in order to improve the accuracy of their predictions. This modification was done so that, when the quasi-steady method was used to analyse the transient data, bias in the predicted time to dryout would be reduced. By reducing the bias in the prediction methods they were able to predict dryout when the local conditions were analogous to the steady-state conditions. Any systematic delay—or the opposite—in the onset of dryout was due to either a systematic effect of the initial conditions—MTD or PDO—or an overall systematic effect of the transient that was independent of the boundary conditions.

When the data was analysed using the local conditions computed by a RELAP5 model as input to the modified steady-state CHF prediction methods the quasi-steady method was found to predict the data well overall. Furthermore there was no statistically significant systematic variation between the data collected with the two different initial conditions. This negated the author's hypothesis that the apparent difference between the conclusions of Lyons and Swinnerton [3] and those of Celata *et al* [1, 2] was due to the initial conditions. Furthermore it suggests that there is no delay in the onset of dryout for pressure transients over the range of conditions that were investigated in the present work. The delay observed by Celata *et al* was due to one of two possibilities they had suggested: a limitation of the HEM formulation for pressure transients, or the effect of a rapid and dramatic power transient caused by the release of stored thermal energy as the temperature boundary in Newton's law of cooling changes with pressure. In the present work a change in heat transfer regime was observed before OID that suggests that the flow regime changed to a dispersed droplet flow. This type of flow should be well-approximated using a HEM formulation of the mass, momentum, and energy conservation equations. Therefore it is mostly likely that the observed delay was in fact caused by the rapid thermal power transient that was triggered by the pressure transient.

7.2   Conclusions

Based on the experiments and analysis presented in this thesis the following conclusions may be made:

- The presence or absence of dryout in the initial conditions of a pressure transient does not influence the ability of the quasi-steady method to predict the onset of dryout within the limits of experimental accuracy of the present work.

- Axial conduction in the test section wall does not significantly contribute to the propagation of dryout to neighbouring wetted regions of the test section.

  - For the present test section this effect was modelled and had no influence more than 1.5 mm away from the position of a step change in heat transfer coefficient from 100 to 10 kW m^{-2} K^{-1}.

- The quasi-steady method predicts the onset of dryout with analogous accuracy as the steady-state data during pressure transients when the following criteria are satisfied:

  - The energy storage number is less than 0.3 ($\frac{\ddot{q}_{st}}{\ddot{q}_a} < 0.3$)

  - The steady-state method used to predict transient dryout has been validated against steady-state data from the system that is being analysed.

- Thermal energy storage effects are far more important in transient experiments conducted using scaled simulating fluids (refrigerants) than those with water.

  - For analagous thermalhydraulic conditions the heat fluxes at OID for refrigerants are an order of magnitude smaller than those observed for water. This is largely due to the much lower latent heat of refrigerants compared with water.

  - The fluid properties of refrigerants and water vary at similar rates with respect to pressure and test sections are often constructed of similar materials regardless of the fluid used.

– Therefore the absolute magnitude of the transient heat flux due to the release of stored thermal energy in the test section walls are similar for both refrigerants and water. Since the absolute values of the applied heat fluxes are about an order of magnitude lower in dryout experiments conducted using refrigerants these thermal energy storage transients are an order of magnitude relatively more important.

7.3   Future Work

Several avenues have been opened to pursue in future work that would complement and extend the present work:

- Perform experiments in annular or channel-like geometries

  – Gaspari *et al* [78] postulated that the delay in the onset of dryout they observed was due to a redistribution of liquid from the unheated to the heated surface when they added a depressurisation transient to their flow stoppage experiments.

- Test the postulated value of the critical energy storage number.

  – For what relative magnitude of the transient heat flux increase due to thermal energy storage does the quasi-steady method break down.

  – This is analogous to investigating the threshold rate of power increase that has an effect on OID in annular film dryout.

  – Perform experiments with higher depressurisation rates.

- Perform experiments with larger initial margins to dryout.

  – In the present work all initial conditions were within the range of enhanced (droplet) heat transfer before OID.

  – May the transition from liquid film evaporation to drop deposition heat transfer also influence OID?

- Investigate the region of droplet heat transfer.

- – Over what range of parameters does this occur?

- – Over what range of parameters is the deposition of droplets sufficient to prevent the surface from completely drying out?

References

[1] G. P. Celata, M. Cumo, F. D'Annibale, and G. E. Farello. CHF in flow boiling during pressure transients. In T. N. Veziroglu, editor, *Particulate Phenomena and Multi-phase Transport*, pages 207–223. Hemisphere, Washington, D. C., 1988.

[2] G. P. Celata, M. Cumo, F. D'Annibale, G. E. Farello, and A. Mariani. CHF behaviour during pressure, power and/or flow simultaneous variations. *International Journal of Heat and Mass Transfer*, 34(3):723–738, 1991.

[3] A. J. Lyons and D. Swinnerton. Measurement and prediction of dryout front movement during rapid depressurisation. Technical Report AEEW-R1525, UKAEA, 1983.

[4] L. Biasi, G. C. Clerici, S. Garribba, R. Sala, and A. Tozzi. Studies on burnout: Part 3 - A new correlation for round ducts and uniform heating and its comparison with world data. *Energia Nucleare*, 14:530–536, 1967.

[5] D. C. Groeneveld, J. Q. Shan, A. Z. Vasić, L. K. H. Leung, A. Durmayaz, J. Yang, S. C. Cheng, and A. Tanase. The 2006 CHF look-up table. *Nuclear Engineering and Design*, 237:1909–1922, 2007.

[6] G. F. Hewitt. Experimental studies on the mechanism of burnout in heat transfer to steam-water mixtures. In U. Grigull and E. Hahne, editors, *Heat Transfer 1970: Papers presented at the Fourth International Heat Transfer Conference*, volume VI, Paris-Versailles, France, 1970. Elsevier Publishing Company. Paper B6.6.

[7] V. E. Doroschuk, F. P. Lantsman, and L. L. Levitan. A peculiar type of burnout in evaporative tubes. In U. Grigull and E. Hahne, editors, *Heat Transfer 1970: Papers Presented at the Fourth International Heat Transfer Conference*, volume VI, Paris-Versaille, France, 1970. Elsevier Publishing Company. Paper B6.1.

[8] D. C. Groeneveld. Anomalies and other concerns related to the critical heat flux. *Nuclear Engineering and Design*, 241:4604–4611, 2011.

[9] D. C. Groeneveld. The onset of dry sheath condition–A new definition of dryout. *Nuclear Engineering and Design*, 92:135–140, 1986.

[10] B. A. Statham. Flow boiling heat transfer in a long, small diameter, vertically oriented, uniformly heated tube. Master's thesis, McMaster University, Hamilton, Canada, 2009.

[11] Jonathan E. Guyer, Daniel Wheeler, and James A. Warren. FiPy: Partial differential equations with Python. *Computing in Science & Engineering*, 11(3):6–15, 2009.

[12] Davide Del Col and Stefano Bortolin. Investigation of dryout during flow boiling in a single microchannel under non-uniform axial heat flux. *International Journal of Thermal Sciences*, 57:26–36, 2012.

[13] International Energy Agency. *CO_2 Emissions from fuel combustion*. International Energy Agency, 2013. PDF obtained online through the publisher's website.

[14] International Energy Agency. *Climate and Electricity Annual: Data and Analyses*. International Energy Agency, 2011. PDF obtained online through the publisher's website.

[15] International Energy Agency. *World Energy Outlook*. International Energy Agency, 2013. PDF obtained online through the publisher's website.

[16] Independent Electricity System Operator (Ontario). Supply overview. Accessed 6 December 2013.

[17] Government of Canada. Nuclear safety and control act, 1997. Accessed 5 December 2013.

[18] V. G. Snell. Chapter 5: Safety systems. Engineering Physics 714: Safety Design Course Notes, 2009.

[19] V. G. Snell. Chapter 1: Introduction. Engineering Physics 714: Safety Design Course Notes, 2009.

[20] Canadian Nuclear Safety Commission. Regulatory document RD-337: Design of new nuclear power plants, 2008. Accessed 4 December 2013.

[21] Canadian Nuclear Safety Commission. Regulatory guide G-149: Computer programs used in design and safety analyses of nuclear power plants and research reactors, 2000. Accessed 6 December 2013.

[22] United States Nuclear Regulatory Commission. Glossary: Defense-in-depth, 2013. Accessed 16 February 2014.

[23] P. Saha and N. Zuber. Point of net vapor generation and vapor void fraction in subcooled boiling. In *Heat Transfer 1974: Proceedings of the Fifth International Heat Transfer Conference*, volume IV, pages 175–179, Tokyo, Japan, 1974. Paper B4.7.

[24] Canadian Nuclear Safety Commission. Regulatory guide G-144: Trip parameter acceptance criteria for the safety analysis of CANDU nuclear power plants, 2006. Accessed 31 July 2013.

[25] J. C. Collier and J. R. Thome. *Convective Boiling and Condensation*. Oxford University Press, 3rd edition, 1996.

[26] J. Yang, D. C. Groeneveld, L. K. H. Leung, S. C. Cheng, and M. A. El Nakla. An experimental and analytical study of the effect of axial power profile on chf. *Nuclear Engineering and Design*, 236:1384–1395, 2006.

[27] J. C. Luxat. A technical basis for the flux-corrected local conditions critical heat flux correlation. In *Proceedings of the 29th Annual Conference of the*

Canadian Nuclear Society, Toronto, Canada, 2008. Session F4: Thermalhydraulics II.

[28] A. Olekhnovitch, A. Teyssedou, and P. Tye. Critical heat flux in a vertical tube at low and medium pressures: Part II–new data representation. *Nuclear Engineering and Design*, 193:91–103, 1999.

[29] Y. Haramura and Y. Katto. A new hydrodynamic model of critical heat flux, applicable widely to both pool and forced convection boiling on submerged bodies in saturated liquids. *International Journal of Heat and Mass Transfer*, 26(3):389–399, 1983.

[30] C. H. Lee and I. Mudawwar. A mechanistic critical heat flux model for subcooled flow boiling based on local bulk flow conditions. *International Journal of Multiphase Flow*, 14(6):711–728, 1988.

[31] J. Weisman and B. S. Pei. Prediction of critical heat flux in flow boiling at low qualities. *International Journal of Heat and Mass Transfer*, 26(10):1463–1477, 1983.

[32] Y. Katto and H. Ohno. An improved version of the generalized correlation for the forced convective boiling in uniformly heated vertical tubes. *Inernational Journal of Heat and Mass Transfer*, 27(9):1641–1648, 1984.

[33] D. C. Groeneveld, S. C. Cheng, and T. Doan. The CHF look-up table, a simple and accurate method for predicting critical heat flux. *Heat Transfer Engineering*, 7(1):46–62, 1986.

[34] D. C. Groeneveld, L. K. H. Leung, P. L. Kirillov, V. P. Bobkov, I. P. Smogalev, V. N. Vinogradov, X. C. Huang, and E. Royer. The 1995 look-up table for critical heat flux in tubes. *Nuclear Engineering and Design*, 163:1–23, 1996.

[35] J. D. Jackson, O. Büyükalaca, and S. He. Heat transfer in a pipe under conditions of transient turbulent flow. *International Journal of Heat and Fluid Flow*, 20:115–127, 1999.

[36] E. K. Kalinin and G. A. Dreitser. Unsteady convective heat transfer for turbulent flows of gases and liquids in tubes. *International Journal of Heat and Mass Transfer*, 28(2):361–369, 1985.

[37] H. A. Johnson. Transient boiling heat transfer to water. *International Journal of Heat and Mass Transfer*, 14(1):67–82, January 1971.

[38] K. O. Pasamehmetoglu. *Transient Critical Heat Flux*. PhD thesis, University of Central Florida, 1986.

[39] P. B. Whalley, A. J. Lyons, and D. Swinnerton. Transient critical heat flux in flow boiling. In *1st UK National Heat Transfer Conference*, Leeds, UK, 1984.

[40] David D. Hall and Issam Mudawar. Critical heat flux (CHF) for water flow in tubes–I.: Compilation and assessment of world CHF data. *International Journal of Heat and Mass Transfer*, 43(14):2573–2604, July 2000.

[41] David D. Hall and Issam Mudawar. Critical heat flux (CHF) for water flow in tubes–II.: Subcooled CHF correlations. *International Journal of Heat and Mass Transfer*, 43(14):2605–2640, July 2000.

[42] Y. Katto. Critical heat flux. *International Journal of Multiphase Flow*, 20:53–90, 1994.

[43] M. Cumo, F. Fabrizi, and G. Palazzi. Transient critical heat flux in loss-of-flow-accidents (L.O.F.A.). *International Journal of Multiphase Flow*, 4:497–509, 1978.

[44] T. Iwamura. Transient burnout under rapid flow reduction condition. *Journal of Nuclear Science and Technology*, 24(10):811–820, 1987.

[45] I. Kataoka and A. Serizawa. Transient boiling heat transfer under forced convection. In Nicholas P. Cheremisinoff, editor, *Handbook of Heat and Mass Transfer*, volume Volume 1: Heat and Mass Transfer Operations. Gulf Publishing Company, 1986.

[46] D. Moxon and P. A. Edwards. Dryout during flow and power transients. Technical Report AEEW-R553, UKAEA, 1967.

[47] T. G. Theofanous. Introduction to a round table discussion on reactor power margins. *Nuclear Engineering and Design*, 163:213, 1996.

[48] Pavel Hejzlar and Neil E. Todreas. Consideration of critical heat flux margin by subcooled or low quality critical heat flux correlations. *Nuclear Engineering and Design*, 163:215–223, 1996.

[49] F. Inasaka and H. Nariai. Evaluation of subcooled critical heat flux correlations for tubes with and without internal twisted tapes. *Nuclear Engineering and Design*, 163:225–239, 1996.

[50] G. P. Celata. Letter to the Editor: On the application method of critical heat flux correlations. *Nuclear Engineering and Design*, 163:241–242, 1996.

[51] G. S. Lellouche. Letter to the editor on "Evaluation of subcooled critical heat flux correlations for tubes with and without internal twisted tapes" by F. Inasaka and H. Nariai and "Consideration of CHF margin prediction by subcooled or low quality CHF correlations" by P. Hejzlar and N. E. Todreas. *Nuclear Engineering and Design*, 163:243–244, 1996.

[52] D. C. Groeneveld. On the definition of critical heat flux margin. *Nuclear Engineering and Design*, 163:245–247, 1996.

[53] Moshe Siman-Tov. Technical note: Application of energy balance and direct substitution methods for thermal margins and data evaluation. *Nuclear Engineering and Design*, 163:249–258, 1996.

[54] J. Weisman. Letter: Letter to the editor on "Evaluation of subcooled critical heat flux correlations for tubes with and without internal twisted tapes" by F. Inasaka and H. Nariai and "Consideration of CHF margin predictions by subcooled or low quality CHF correlations" by P. Hejzlar and N. Todreas. *Nuclear Engineering and Design*, 163:259–261, 1996.

157

[55] Pavel Hejzlar and Neil E. Todreas. Letter: Response of Hejzlar and Todreas to contributors' letters and technical notes. *Nuclear Engineering and Design*, 163:273–279, 1996.

[56] H. Nariai and F. Inasaka. Letter to the Editor: Comments on "the Letter to the Editor and some notes". *Nuclear Engineering and Design*, 163:281–282, 1996.

[57] A. Olekhnovitch, A. Teyssedou, and P. Tye. Letter to the Editor: On the round table discussion on reactor power margins published in Nuclear Engineering and Design 163 (12) 1996. *Nuclear Engineering and Design*, 201(2-3):335–346, October 2000.

[58] E. M. Sparrow and R. Siegel. Unsteady turbulent heat transfer in tubes. *Trans. ASME Journal of Heat Transfer*, 82(3):170–180, 1960.

[59] J. D. Jackson and S. He. Experimental investigation of transient turbulent pipe-flow. In *Symposium on Laser Anemometry*, University of Swansea, UK, 1992.

[60] S. He and M. Seddighi. Turbulence in transient channel flow. *Journal of Fluid Mechanics*, 715:60–102, 2013.

[61] S. He and M. Seddighi. A DNS study of effects of Reynolds number on unsteady channel flow. In *International Symposium on Turbulence and Shear Flow Phenomena: TSFP8*, Poitiers, France, 2013.

[62] Kyuong-Ho Kang and Soon-Heung Chang. Experimental study on the heat transfer characteristics during the pressure transients under supercritical pressures. *International Journal of Heat and Mass Transfer*, 52:4946–4955, 2009.

[63] Akimi Serizawa. Theoretical prediction of maximum heat flux in power transients. *International Journal of Heat and Mass Transfer*, 26(6):921–932, June 1983.

[64] A. Sakura and M. Shiotsu. Transient pool boiling heat transfer. Part 1: Incipient boiling superheat. *Trans. ASME Journal of Heat Transfer*, 99(4):547–553, 1977.

[65] A. M. Osman and J. V. Beck. Investigation of transient heat transfer coefficients in quenching experiments. *Trans. ASME Journal of Heat Transfer*, 112(4):843–848, 1990.

[66] Hein Auracher and Wolfgang Marquardt. Experimental studies of boiling mechanisms in all boiling regimes under steady-state and transient conditions. *International Journal of Thermal Sciences*, 41:586–598, 2002.

[67] H. Auracher and W. Marquardt. Heat transfer characteristics and mechanisms along entire boiling curves under steady-state and transient conditions. *International Journal of Heat and Fluid Flow*, 25(2):223–242, April 2004.

[68] H. S. Ragheb, S. C. Cheng, and D. C. Groeneveld. Observations in transition boiling of subcooled water under forced convective conditions. *International Journal of Heat and Mass Transfer*, 24(7):1127–1137, 1981.

[69] W. J. Green. An experimental and analytical study of transient heat transfer in the region of dryout for a heated tube using Freon-12 as coolant. Technical Report AEEC/E452, AAEC Research Establishment, Lucas Heights, 1978.

[70] W. J. Green and K. R. Lawther. An investigation of transient heat transfer in the region of flow boiling dryout with Freon-12 in a heated tube. *Nuclear Engineering and Design*, 55:131–144, 1978.

[71] I. Kataoka, A. Serizawa, and A. Sakurai. Transient boiling heat transfer under forced convection. *International Journal of Heat and Mass Transfer*, 26(4):583–595, 1983.

[72] Robert B. Roemer. The effect of transients on the peak heat flux. *International Journal of Heat and Mass Transfer*, 12:953–964, 1969.

[73] V. A. Gerliga and V. M. Tokarev. Study of the critical heat flux under transient conditions. *Journal of Engineering Physics and Thermophysics*, 21(5):1391–1393, 1971.

[74] V. I. Deev, Htay Lwin Oo, V. S. Kharitonov, K. V. Kutsenko, and A. A. Lavrukhin. Critical heat flux modeling in water pool boiling during power transients. *International Journal of Heat and Mass Transfer*, 50(19-20):3780–3787, September 2007.

[75] K. Fukuda, M. Shiotsu, K. Hata, and A. Sakurai. Transient boiling heat transfer from initial steady state caused by rapid depressurization. *Nuclear Engineering and Design*, 149:91–110, 1994.

[76] O. K. Smirnov, L. T. Pashkov, and V. N. Zaitsev. Investigation of critical heat flux with decrease in flow through a heated tube. *Teploenergetika*, 19(9):122–126, 1972.

[77] O. K. Smirnov, V. N. Zaitsev, and E. E. Serov. Investigation of burnout under transient hydrodynamic conditions. *Teploenergetika*, 24(5):72–74, 1977.

[78] G. P. Gaspari, R. Granzini, and A. Hassid. Dryout onset in flow stoppage, depressurization and power surge transients. *Energia Nucleare*, 20(10):554–570, 1973.

[79] T. Iwamura and T. Kuroyanagi. Burnout characteristics under flow reduction condition. *Journal of Nuclear Science and Technology*, 19(6):438–448, 1982.

[80] A. J. Lyons and D. Swinnerton. A study of transient dryout during depressurisation. In *Heat and Fluid Flow in Nuclear and Process Plant Safety*, London, UK, 1983. Institution of Mechanical Engineers.

[81] J. C. M. Leung. *Transient Critical Heat Flux and Blowdown Heat Transfer Studies*. PhD thesis, Northwestern University, 1980.

[82] J. C. M. Leung, K. A. Gallivan, R. E. Henry, and S. G. Bankoff. Critical heat flux predictions during blowdown transients. *International Journal of Multiphase Flow*, 7(6):677–701, 1981.

[83] G. P. Celata, M. Cumo, F. D'Annibale, G. E. Farello, and T. Setaro. Critical heat flux in flow transients. In *Proceedings of the 8th International Heat Transfer Conference*, pages 2429–2435, 1986.

[84] G. P. Celata, M. Cumo, F. D'Annibale, G. E. Farello, and S. Abou Said. Critical heat flux phenomena in flow boiling during step-wise and ramp-wise power transients. *Revue Génerale de Thermique*, 317:296–303, June 1988.

[85] G. P. Celata, M. Cumo, F. D'Annibale, and G. Farello. Critical heat flux in transient flow boiling during simultaneous variations in flow rate and thermal power. *Experimental Thermal and Fluid Science*, 2(2):134–145, April 1989.

[86] G. P. Celata, M. Cumo, and F. D'Annibale. A data set of critical heat flux of boiling R-12 in uniformly heated tubes under transient conditions. *Experimental Thermal and Fluid Science*, 5(1):78–107, 1992.

[87] G. P. Celata and M. Cumo. An experimental study of CHF under complex and simultaneous transient conditions. *Wärme - und Stoffübertragung*, 27(1):17–28, January 1992.

[88] Mamoru Ozawa, Hisashi Umekawa, Yohji Yoshioka, and Akio Tomiyama. Dryout under oscillatory flow condition in vertical and horizontal tubes— experiments at low velocity and pressure conditions. *International Journal of Heat and Mass Transfer*, 36(16):4076–4078, 1993.

[89] C. H. Lee and K.-W. Lin. Experimental investigation of flow transient critical heat flux at light water reactor conditions. *International Communications in Heat and Mass Transfer*, 20:477–488, 1993.

[90] T. Iwamura, H. Watanabe, and Y. Murao. Critical heat flux experiments under steady-state and transient conditions and visualization of CHF phenomenon

with neutron radiography. *Nuclear Engineering and Design*, 149:195–206, 1994.

[91] D. W. Zhao, G. H. Su, Z. H. Liang, Y. J. Zhang, W. X. Tian, and S. Z. Qiu. Experimental research on transient critical heat flux in vertical tube under oscillatory flow condition. *International Journal of Multiphase Flow*, 37:1235–1244, 2011.

[92] Tomio Okawa, Taisuke Goto, Jun Minamatani, and Yosuke Yamagoe. Liquid film dryout in a boiling channel under flow oscillation conditions. *International Journal of Heat and Mass Transfer*, 52:3665–3675, 2009.

[93] T. Fukano, S. Mori, and T. Nakagawa. Fluctuation characteristics of heating surface temperature near an obstacle in transient boiling two-phase flow in a vertical annular channel. *Nuclear Engineering and Design*, 219:47–60, 2003.

[94] Soon Heung Chang and Won-Pil Baek. Understanding, predicting, and enhancing critical heat flux. In *The 10th International Topical Meeting on Nuclear Reactor Thermalhydrulics (NURETH-10)*, Seoul, South Korea, 2003.

[95] K. O. Pasamehmetoglu, R. A. Nelson, and F. S. Gunnerson. Critical heat flux modeling in pool boiling for steady-state and power transients. *Trans. ASME Journal of Heat Transfer*, 112:1048–1057, November 1990.

[96] K. O. Pasamehmetoglu, R. A. Nelson, and F. S. Gunnerson. Critical heat flux modeling in forced convection boiling during power transients. *Trans. ASME Journal of Heat Transfer*, 112:1058–1062, November 1990.

[97] G. F. Hewitt and N. S. Hall-Taylor. *Annular Two-Phase Flow*. Pergamon Press, 1970.

[98] L. Biasi, G. C. Clerici, R. Sala, and A. Tozzi. A non-equilibrium description of two-phase annular flow: Application to the burnout prediction. *International Journal of Heat and Mass Transfer*, 12:319–331, 1969.

[99] L. K. H. Leung, D. C. Groeneveld, A. Teyssedou, and F. Aubé. Pressure drops for steam and water flow in heated tubes. *Nuclear Engineering and Design*, 235:53–65, 2005.

[100] A. Olekhnovitch, A. Teyssedou, A. Tapucu, P. Champagne, and D. C. Groeneveld. Critical heat flux in a vertical tube at low and medium pressures: Part I. Experimental results. *Nuclear Engineering and Design*, 193(1-2):73–89, September 1999.

[101] P. B. Whalley, P. Hutchinson, and G. F. Hewitt. The calculation of critical heat flux in forced convection boiling. In *Heat Transfer 1974: Proceedings of the Fifth International Heat Transfer Conference*, volume IV, pages 290–294, Tokyo, Japan, 1974. Paper B6.11.

[102] P. Hutchinson and P. B. Whalley. A possible characterisation of entrainment in annular flow. *Chemical Engineering Science*, 28:974–975, 1973.

[103] P. B. Whalley, P. Hutchinson, and P. W. James. The calculation of critical heat flux in complex situations using an annular flow model. In *Sixth International Heat Transfer Conference*, volume 5, pages 65–70, Toronto, Canada, 1978. Hemisphere Publishing Corporation. Paper NR-12.

[104] P. W. James and P. B. Whalley. The calculation of dryout during flow and pressure transients. In *2nd CSNI specialist meeting on transient two-phase flow*, Paris, France, 1978. Accessed 7 June 2013.

[105] A. H. Govan, G. F. Hewitt, D. G. Owen, and T. R. Bott. An improved CHF modelling code. In *Second UK National Heat Transfer Conference*, pages 33–48, 1998. Paper C175/88.

[106] G. F. Hewitt and A. H. Govan. Phenomenological modelling of non-equilibrium flows with phase change. *International Journal of Heat and Mass Transfer*, 33(2):229–242, 1990.

[107] S. H. Chang, K. W. Lee, and D. C. Groeneveld. Transient-effects modeling of critical heat flux. *Nuclear Engineering and Design*, 113:51–57, 1989.

[108] J.-M. Le Corre, I. Trisic, D. Palko, C. Adamsson, and H. Anglart. Transient responses and analyses of three thermal-hydraulic models to synthetic and typical BWR accident scenarios. In *Proceedings of the 15th International Topical Meeting on Nuclear Reactor Thermal-hydraulics, NURETH-15*, Pisa, Italy, 2013. Paper 423.

[109] Micropump. Series GC magnetic drive pump product data sheet. Accessed 6 November 2013.

[110] Regatron Inc. *TopCon Quadro Power Supply: Mains requirements and output specifications*. Accessed 7 Nov 2013.

[111] National Instruments. NI 9203 8 ch, ±20 mA, 200 kS/s, 16-bit C series analog current input module data sheet. Accessed 7 November 2013.

[112] National Instruments. NI 9213 16-channel thermocouple module data sheet. Accessed 7 November 2013.

[113] Regatron Inc. *TopCon Input/Output API: tcio.dll*, 2011. Note: Supplied by manufacturer on DVD supplement: "TopCon TC.P + TC.GSS Series Programmable High-Power DC Supplies: General User Documentation V4.5X, Windows Software TopControl 4.01.72".

[114] Philip R. Bevington and D. Keith Robinson. *Data Reduction and Error Analysis for the Physical Sciences*. McGraw-Hill, third edition, 2003.

[115] NIST. Thermophysical properties of fluid systems web application: R-12. http://webbook.nist.gov/chemistry/fluid/.

[116] R. C. Rice. *Metallic Materials Properties Development and Standardization (MMPDS-1)*, volume 1. National Technical Information Service, 2003.

[117] S. Y. Ahmad. Fluid to fluid modeling of critical heat flux: A compensated distortion model. *International Journal of Heat and Mass Transfer*, 16(13):641–662, 1973.

[118] C. Adamsson and H. Anglart. Influence of axial power distribution on dry-out: Film-flow models and experiments. *Nuclear Engineering and Design*, 240(6):1495–1505, 2010.

[119] Eric Jones, Travis Oliphant, Pearu Peterson, et al. *SciPy: Open source scientific tools for Python*, 2001–. http://www.scipy.org/.

[120] David Ascher, Paul F. Dubois, Konrad Hinsen, Jim Hugunin, Travis Oliphant, et al. *Numerical python*, 2001. Package to speed-up arithmetic operations on arrays of numbers. http://sourceforge.net/projects/numpy.

[121] Magnus Holmgren. XSteam for MATLAB.

[122] W. Wagner, J. R. Cooper, A. Dittmann, J. Kijima, H.-J. Kretzschmar, A. Kruse, R. Mareš, K. Oguchi, H. Sato, I. Stöcker, O. Šifner, Y. Takaishi, I. Tanishita, J. Trübenbach, and Th. Willkommen. The IAPWS industrial formulation 1997 for the thermodynamic properties of water and steam. *Trans. ASME Journal of Engineering for Gas Turbines and Power*, 122(1):150–184, January 2000.

[123] The International Association for the Properties of Water and Steam. Release on the IAPWS formulation 2008 for the viscosity of ordinary water substance, 2008. Accessed 23 January 2014.

[124] The International Association for the Properties of Water and Steam. Release on the IAPWS formulation 2011 for the thermal conductivity of ordinary water substance, 2011. Accessed 23 January 2014.

[125] The International Association for the Properties of Water and Steam. IAPWS release on surface tension of ordinary water substance, 1994. Accessed 23 January 2014.

[126] Information Systems Laboratories Inc. *RELAP5/MOD3.3 Code Manual*. Rockville, MD and Idaho Falls, ID, NUREG-CR5535 edition, October 2010.

[127] D. R. Novog, S. T. Yin, and J. S. Chang. Recent advances in high heat flux
      smooth and swirl flow boiling of water. *Fusion Science and Technology*,
      52:880–884, 2007.

Appendix A

Data Processing

A.1 Data Processing

Steady-state data below and beyond the onset of intermittent dryout were collected for pressures of 2, 3, 4, 5 and 6 MPa and mass fluxes of 1000, 1500, 2000 and 2500 kg m^{-2} s^{-1} by following the experimental procedure described in Chapter 3. The thermodynamic inlet quality was constant for all experiments with a value of -0.148±0.006. Raw data was then post-processed to separate steady-state and transient runs, calculate time-averaged values for the steady-state runs and initial conditions for the transient runs. The process used to post-process the steady data is described in this section. This process is depicted in Figure A.1; conversion to SI units, filtering, mean value and uncertainty calculations will be described in this chapter. The calculations of modal values and the processes that follow the 'Detect Transient YES' branch are described in Section A.2.

The cDAQ modules described in Chapter 3 record raw data as waveforms with a magnitude and a time stamp. For all process measurements—pressure, mass flow rate, test section Voltage, and test section current—these values were stored as raw measured current values that were subsequently converted to units. This is shown in Equation A.1 where x represents the value of any process measurement and units are shown in square brackets. All process measurements were low-pass filtered by performing a discrete Fourier transform on each data sequence using SciPy's `rfft` method, eliminating all components with a freqency greater than 25 Hz using

B.A. Statham
Ph. D. Thesis

Appendix A
Data Processing

McMaster University
Engineering Physics
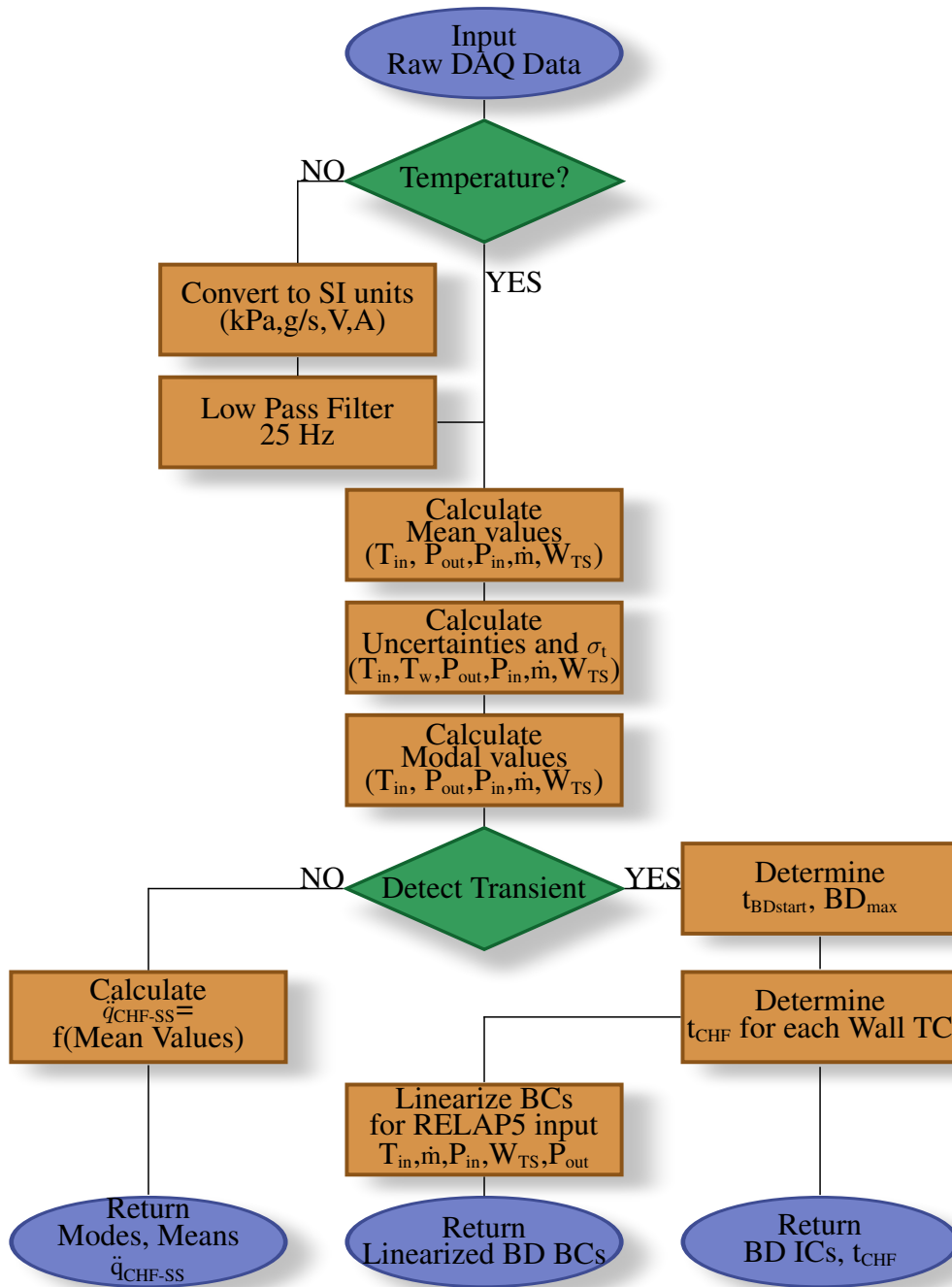
Figure A.1: Raw data post-processing flow chart.

NumPy's `clip` method and inverse discrete Fourier transforming the data back to the time domain using SciPy's `irfft` method [119, 120]. This was found to reduce

the amount of high frequency noise in all signals without losing any of the transient qualities of the data. The observed noise was caused largely by electromagnetic interference from the DC power supplies. The mass flow meter was in particular sensitive to noise from the pump variable frequency drive. Space limitations and ergonomic considerations prevented these noise sources from being moved further away from the instruments.

$$x[SI] = \frac{(x[mA] - 4)}{(20 - 4)} \left(x_{max}[SI] - x_{min}[SI]\right) \qquad (A.1)$$

Temperature data was converted from the NIST thermocouple tables in hardware before being stored in memory. Operation of the power supplies did induce additional noise on the observed thermocouple measurements. The magnitude of the noise was less than the overall thermocouple uncertainty and no filtering of the temperature data was performed.

For steady-state experiments all process measurements were time-averaged to obtain a mean value and a standard deviation. These were performed over the entire measurement interval of 40–120 s. NumPy's `mean` and `std` methods were used to calculate these quantities [120]. The mean values were then used to estimate the systematic and random errors based on the instrument manufacturer's specifications. Systematic and random errors were calculated separately. This allowed the random error to be compared to the overall standard deviation of the data over the same time period. The total uncertainty in each measurement was then straightforward to determine by adding the variances of the random and systematic errors as shown in Equation A.2. The square root of the variance could then be used to approximate the standard deviation of the measurement.

$$\sigma_t^2 = \sigma_r^2 + \sigma_s^2 \qquad (A.2)$$

Data sets selected as dryout points were further processed by using the time-averaged values of the inlet temperature, inlet pressure, inlet mass flow rate, outlet pressure, and test section power as boundary conditions for a RELAP5 simulation. This was done in order to obtain an estimate of the local pressure and quality in the test section with greater accuracy than is possible using a simple linear interpolation

or other method. RELAP5 is able to calculate the pressure gradient based on correlations for two-phase multiplier, frictional pressure drop, gravity, and acceleration. The RELAP5 model was run for 10 s of simulated time which was adequate for the model to achieve steady-state in both the heat structures and hydrodynamic components. Details of the RELAP5 model are identical to the model used for transient data analysis and are discussed in Section A.3

The local values of the pressure and quality from the RELAP5 simulation at the end of the heated length, in addition the inlet mass flux and test section geometry, were used as input to several different CHF correlations: the CHF look-up table, the Biasi correlation, and the Katto-Ohno correlation [5, 4, 32]. Water thermodynamic properties for any calculations external to RELAP5, *i.e.* when necessary to evaluate dryout correlations, were obtained using `PySteam` that was adapted to Python by the author from the MATLAB script `XSteam` based on the IAPWS formulations for water properties [121, 122, 123, 124, 125]. The implementation of the CHF prediction methods is discussed in more detail in Chapter 4.

For each wall temperature thermocouple the run name, run start time, duration, calculated time-averaged process measurements in SI units—mean inlet temperature, mean wall temperature, random and systematic uncertainties for each process measurement and the wall thermocouple and the standard deviation of the wall temperature, inlet temperature, oulet pressure, test section power, mass flow rate and inlet pressure over all samples was written to a text file for further analysis. Recording the data in this way made boundary conditions, experimental uncertainties and local wall temperature values available for later analysis and visualization.

A.2   Transient Data Processing

Transient experiments were conducted by establishing steady-state conditions and then initiating a blowdown sequence that opened a pneumatically operated valve in the top of the condenser downstream of the test section for a preset, user-specified, duration before closing again. Data collection continued until test section conditions returned nominally to the initial conditions. This data was then post-processed to find the transient start time, the maximum depressurisation rate, and the time

of OID at each test section thermocouple position—if any—for each transient experiment. The data post-processing algorithms are described in this section. The boundary conditions were linearized and used as input to RELAP5. RELAP5 was used to simulate the effect of energy storage in the test section wall and to obtain an estimate of the local pressure, quality, and mass flow rate in the test section during the transient. The linearization process and the RELAP5 model nodalisation were described in Section A.3

The local conditions obtained from the RELAP5 output were post-processed using the modified dryout prediction methods described in Chapter 4 to obtain predicted times to dryout. At each thermocouple location the CHF was predicted using the transient local conditions and compared to the wall heat flux including the release of stored thermal energy. The time to dryout was predicted when the local wall heat flux exceeded the predicted CHF value for the local conditions at that time. The final part of the analysis was to compare the observed and predicted dryout times for the data as a whole and for the PDO and MTD data separately to test the author's hypothesis. The following subsections describe each stage of the data processing.

A.2.1   Transient Characteristics and Dryout Times

Due to the large amount of transient data recorded some algorithms were developed to systematically process the transient data to determine the dryout times and compare the prediction methods. This was done to improve the reproducibility of the dryout detection and transient parameter identification—transient start time, maximum blowdown rate, etc.—by developing consistent quantitative techniques to reduce the data. These methods are described in this section.

The statistical mode of each process measurement was calculated in order to obtain an initial estimate of the average initial and/or boundary conditions for each experimental run. For steady-state runs this was not necessary but taking the mean over all time during a transient is not meaningful. Data was recorded for 20–60 s before blowdown was initiated during each transient run. The process measurements and wall temperatures varied substantially during and after blowdown. By

171

appropriately binning the measured data the transient values of each measurement would be ignored when the mode of the data was calculated.

The bins for each process measurement were based on operational experience with the experiment: each measurement was binned into a range related to the smallest increment by which each process could be adjusted. These bins are shown in Table A.1. The binning process was aided by taking the moving average of each signal over 1 s for the inlet temperature, mass flow, and power measurements and 0.1 s for the pressure measurements. Each sample of each measurement was then divided by the bin size to scale the measurement by bin size, rounded to the nearest single digit. The mode over all samples was calculated using NumPy's `mode` method and multiplied by the bin size to convert back to SI units from the modal bins.

Pressure (MPa)	Mass Flow (kg s^{-1})	Inlet Temperature ($^{\circ}$C)	Power (kW)
0.005	0.0002	0.1	0.02

Table A.1: Process measurement modal bins.

The modal value of the outlet pressure was then used as a reference to determine if a transient occurred during a run as illustrated in Figures A.2. Once a transient was detected the time derivative of the outlet pressure was taken using forward, backward and central finite difference formulas to obtain an estimate with O^6 accuracy. To eliminate large rapid fluctuations the derivative was further smoothed over a window of 5 samples. The minimum value of the slope—since the pressure decreased in time—was taken as the maximum blowdown rate and the corresponding time recorded as the maximum blowdown time. The transient start time was found by stepping backwards in time from the maximum blowdown until the pressure time derivative was greater than zero. An additional 0.05 s—one half the pressure smoothing window length—was then subtracted from this time in order to compensate for the effect of smoothing the original signal.

If a transient was detected the data was then further processed to detect the onset of dryout. For each thermocouple dryout was detected by taking a running

B.A. Statham
Ph. D. Thesis

Appendix A
Data Processing

McMaster University
Engineering Physics
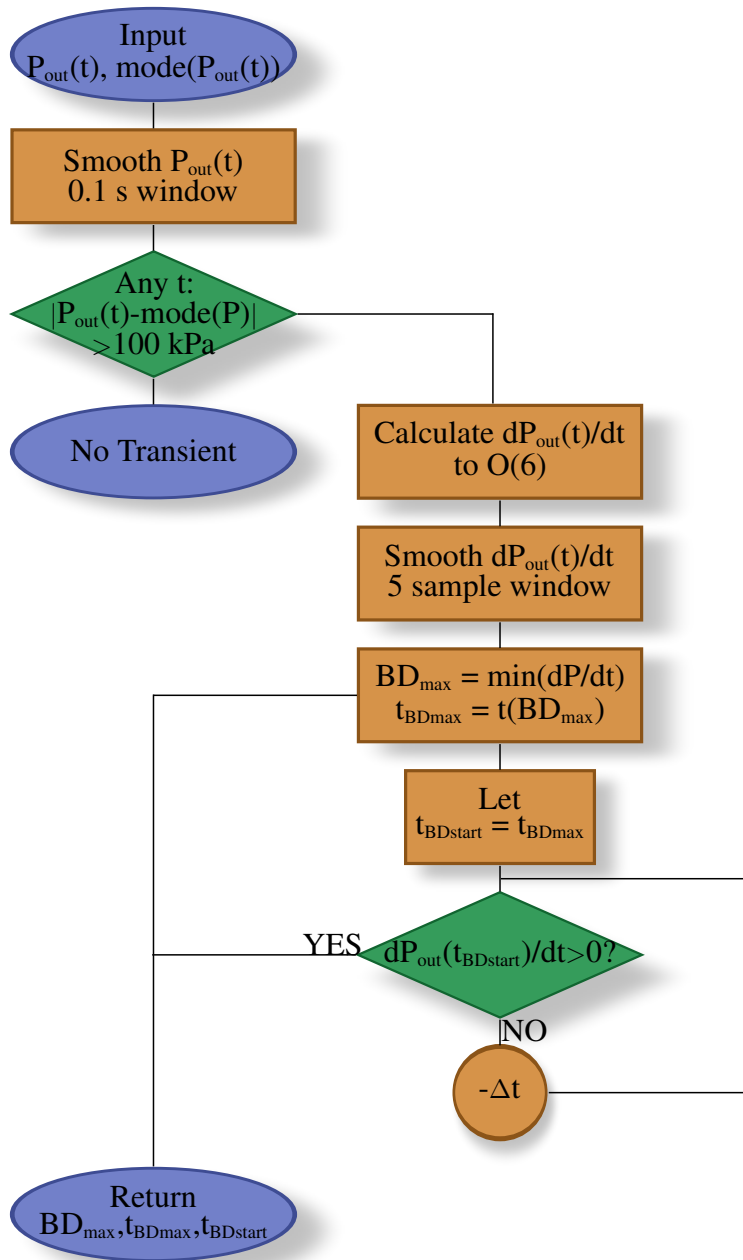
Figure A.2: Transient start time and max blowdown rate flow chart.

average—over $t - \Delta t < t$ rather than $t - 0.5\Delta t < t < t + 0.5\Delta t$ as in a moving average—of each wall temperature measurement and testing whether the tempera-

ture exceeded the moving average by more than 3°C. If dryout was detected then the exact time to dryout was determined by taking the moving standard deviation of the wall temperature measurement over 0.1 s starting at the beginning of the transient. Dryout was assumed to occur at the first time during the transient where this moving standard deviation exceeded 0.7°C as illustrated in Figure A.3. This dryout detection method is discussed in more detail in Appendix F.
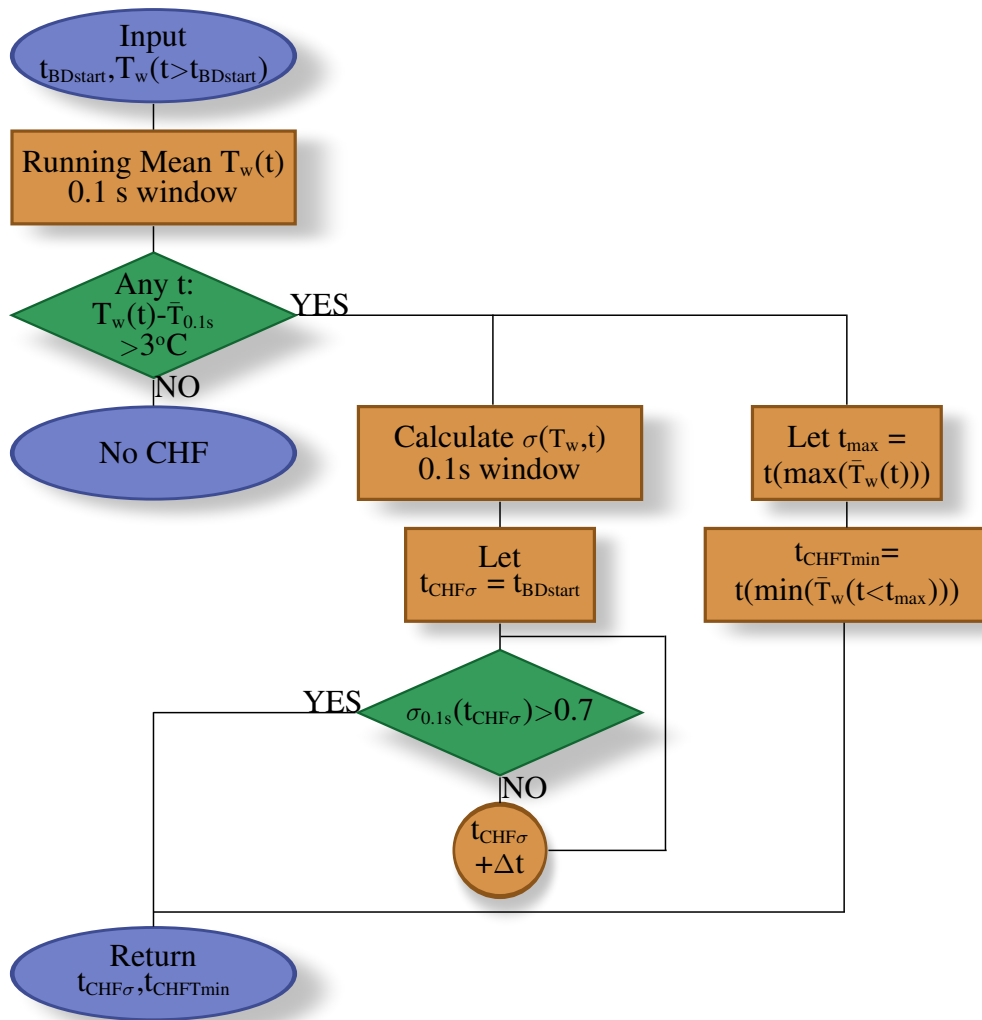
Figure A.3: Dryout time detection flow chart.

A.2.2   Predicted Dryout Times

For each thermocouple location in each transient the time to dryout was predicted based on the instantaneous values of the local conditions predicted by the RELAP5 model and the dryout prediction methods discussed in Section 4.3. Time data for a specific simulated test section volume was read into computer memory and scanned through until the steps between entries decreased to less than 0.015 s. This was done simply because the time interval between recorded data points from the RELAP5 simulation was 0.01 s during the transient and 3–10 s elsewhere. The index of this time value was then saved as the dryout detection starting point. The predicted CHF value at this time was calculated using the modified Biasi and look-up table methods and compared with the convective heat flux at this time. The convective heat flux includes both the heat generated in the test section wall and the release of stored thermal energy as the test section wall cooled down during the transient. The code stepped forward in time until the convective heat flux exceeded the predicted CHF at that time. This time is recorded as the predicted time to dryout along with the other relevant local quantities from the RELAP5 simulation for that volume at that time. This is repeated starting again from the dryout detection starting index for the other dryout prediction method. If no dryout was predicted by any of the employed methods then the time and values recorded correspond to the last data point recorded during the transient.

This process is repeated for every thermocouple location in every run by reading every detected CHF point from the output file that was generated during the experimental data post-processing. This file contains the run name, thermocouple location, boundary condition mode values, transient start time, maximum blowdown rate, and observed dryout times for all of the experimental data. As each line of this file was read a function was called that reads the RELAP5 data from the appropriate columns in the corresponding `stripf` file and performs the operation described in the previous paragraph to obtain the predicted dryout time. The original results of the post-processed raw data, the predicted dryout times and predicted CHF values and the local properties from the RELAP5 simulation for each dryout prediction method were then written in a line to a new output file. The output of the entire script produced a tab-delimited text file that contained the run name, test

175

section positions, boundary condition mode values, transient properties, observed dryout times, predicted dryout times, and simulated local properties from the RE-LAP5 output for every data point. This file could then be easily read by Excel or other software for further analysis and visualization.

Data points with dryout predicted before the beginning of the pressure transient were identified by subtracting the data's transient start time from the predicted dryout time. Negative values indicated dryout was predicted before the beginning of the transient. Similarly, the data points where no dryout was predicted were identified by comparing the difference between the transient start time and the predicted dryout time with the valve opening time recorded for each transient run. Data with predicted dryout times within 0.5 s or less of the total length of the blowdown were then identified as points where no dryout was predicted.

A.3   RELAP5 Model

The test section, from the Swagelok elbow where the inlet temperature was measured to the T-junction where the outlet pressure measurement was made, was modelled in RELAP5 for each transient experiment [126]. RELAP5 uses a two-fluid—liquid and vapour— and six-equation—one equation for each fluid for mass, energy, and momentum conversation—model to simulate fluid transport in one-dimension. The purpose of modelling the test section in RELAP5 was to determine the local conditions in the heated section as a function of time. When implementing the model several aspects needed to be considered: the test section geometry, how to represent time-dependent boundary conditions in 99 points or less, and the thermal and physical properties of the test section and water in the test section itself. These are described in this section.

A.3.1   Model Nodalisation

The heated length of the test section was divided into 99 sections of equal length. The dimensions of the modelled section are illustrated in Figures 3.2 and 3.4 including process measurement locations. Single components—fittings and intersti-

tial spaces—were modelled as single volumes using the `SNGLVOL` component while sections of tubing were modelled with `PIPE` components. The number of elements in each `PIPE` component were chosen so that each volume would be between 0.01 and 0.02 m long.

The inlet temperature was specified using a `TMDPVOL` component. The pressure in this volume was fixed to the modal value of the inlet pressure for all values of time since the subcooled enthalpy is only weakly dependent on pressure in comparison to temperature. Inlet mass flux was controlled using a `TMPDPJUN` component and the outlet pressure was fixed using another `TMDPVOL` component. This exit volume was specified to contain saturated steam and does not affect the upstream calculations unless a flow reversal were to occur. Flow reversal was not observed in the present work. The total test section power over time was specified using a table that was then used as an input to the heat structures described below.

Each volume element of the test section was coupled to a one dimensional heat structure. Each heat structure modelled one-dimensional radial conduction with convective internal and adiabatic external boundary conditions. Wall heat structures were modelled using 5 equally spaced radial nodes. The power in each heat structure was calculated as $^{1}/_{99}$ of the total power from the input table. It was assumed that the power was uniformly distributed throughout the test section wall. Axial conduction was not modelled but the radial conduction model was sufficient to estimate any additional power-to-fluid due to thermal energy storage effects.

A.3.2 Material and Fluid Properties

The thermal conductivity values that were used are shown in Table A.2. They were extracted from a graph of the properties of Inconel 600 in [116]. Intermediate values were linearly interpolated by RELAP5 from the table. A constant volumetric heat capacity of 4.241 MJ m^{-3} K^{-1}, Inconel 600's value at approximately 316ºC, was used. This was satisfactory over the range of wall temperatures observed in the simulation simulation results—250–350ºC—to the level of precision that was possible using the temperature-heat capacity graph from which the volumetric heat capacity was derived [116].

Temperature (K)	Thermal Conductivity (W m^{-1} K^{-1})
255.4	13.8
310.9	14.5
366.5	15.4
422.0	16.2
477.6	17.0
533.2	17.8
588.7	18.7
644.3	19.6
699.8	20.6
755.4	21.5
810.9	22.4
866.5	23.4
922.0	24.2
977.6	25.2
1033.2	26.1
1088.7	27.0
1144.3	27.9

Table A.2: Thermal conductivity values used for the RELAP5 model [116].

RELAP5's own fluid property tables based on the IAPWS-1995 formulations for steam tables were used for internal calculations [126].

A.3.3   Boundary Condition Linearisation

Boundary conditions were controlled using time-dependent components. The inputs to these components were based on a sequence of linear fits that were generated from the experimental measurements. This was done in-line with the identification of transient *vs* steady-state data, the evaluation of transient parameters, and determination of the experimental dryout time as illustrated in Figure A.1. Each time-dependent component in RELAP5 allows up to 99 different time–boundary value pairs for each input file. Values at intermediate times are linearly interpolated between table entries. In order to reduce tens of thousands of sampled data points to 99 or less a method was developed to systematically produce time-sequences of

boundary condition inputs for RELAP5. These quantities included the inlet temperature, inlet mass flow rate, outlet pressure, and test section power.

The first step in this process was to determine the time intervals over which the data could be fit to a reasonable level of accuracy. *E.g.* steady initial conditions may require only one pair of time values to represent the time before the beginning of the transient. Rapidly changing conditions required a series of fits with short time intervals to achieve a reasonable degree of accuracy. These linear sequences were calculated using a recursive algorithm. Beginning with the entire time range of each run's experimental data a linear fit was produced using SciPy's `linregress` method from the `stats` module. The error in the fit at every point in time over the interval— the difference between the value generated using the linear fit and the value of the original signal—was checked to verify whether or not it had exceeded a maximum critical value. If the value of the error in the fit at every point in time satisfied this criteria then these time indices and the calculated slope and intercept were saved. If the error exceeded the critical value then the time interval was bisected, a new fit was generated over the new time interval, and checked again using a new criteria based on the new time interval. This process continued until a series of points were generated over which a linear fit could be made in each interval that satisfied the critical value.

The critical value was based on the mean RMS fluctuations of the measurement relative to its moving average at each sample time. This is shown in Equation A.3 where ϵ is the critical value, ϕ_ϵ is the measurement-dependent fraction of the RMS error that is different for each measurement type, N is the total number of samples, x_i represents the sample value and $\bar{x}_i$ is the value of the moving time-average. This was based on all recorded time values for the measurement rather than simply the interval of interest. The impetus for this was that if the fluctuations in the signal were on the order of magnitude of the uncertainty of each sample then a linear fit whose values lay within the boundaries of these fluctuations would be representative of the signal to within some fraction of the measurement uncertainty.

$$\frac{\epsilon}{\phi_\epsilon} = \frac{1}{N-1} \sum_{i=1}^{N} \sqrt{(x_i - \bar{x}_i)^2} \tag{A.3}$$

The fraction of the RMS value, ϕ_ϵ, used as the critical value, ϵ, and the time over which the moving average was taken was different for each signal being fit. The values are listed in Table A.3. The time window over which the moving average was taken and the critical value were tuned to balance the desire to obtain the most accurate representation of the signals possible without needing more than 97 time-domain pairs. The allowable number of time pairs for RELAP5 boundary condition control was limited to 97 since the first 10 seconds of simulated time were run with the boundary conditions fixed to the modal values for the entire run. This was done to allow the initial conditions to become steady before beginning the simulation of the transient data and required two of the allowed 99 time-value pairs.

Measurement Type	Moving Average Interval (s)	ϕ_ϵ
Outlet Pressure (150 Hz)	0.5	4.7
Outlet Pressure (1000 Hz)	0.5	5.1
Mass Flow Rate (150 Hz)	0.5	2.4
Mass Flow Rate (1000 Hz)	0.5	3.2
TS Power (150 Hz)	0.5	6.0
TS Power (1000 Hz)	0.5	4.8
Inlet Temperature	0.5	5.0

Table A.3: Fitting algorithm critical values and moving average intervals.

The first set of linear fits that were generated for each time interval were allowed to be discontinuous with one another. No restrictions were placed on the intercept values of adjoining interval fit equations. The time boundaries of the intervals were interpolated to the intersection points of neighbouring linear fits. Fit intervals that generated end indices earlier than their start indices were eliminated. These intervals were replaced by single points generated from the intercepts of their earlier and later neighbouring intervals. Each of the linear fits was then used to update the time

variation of the appropriate boundary condition in the RELAP5 input file for each run. An example of two resulting fits compared with the original signals is shown in Figure A.4.

Once the boundary conditions were fully specified each RELAP5 input file was run to obtain local values of the total—both phases—mass flux, pressure, and quality in the heated section. It was *not* used to estimate the onset of dryout or the progression of the dryout front. RELAP5's CHF multiplier was adjusted to a very large value in the RELAP5 input files to ensure that dryout would not be predicted. The onset of dryout in the model could have affected the power-to-fluid. At dryout the heat transfer model would change from saturated boiling to post-dryout conditions. As the test section wall heated up in the post-dryout region thermal energy would accumulate in the wall instead of being delivered to the fluid. This way the local parameters predicted by RELAP5, including energy storage effects, could be externally post-processed to obtain estimates of the time to dryout. Simulating the post-dryout conditions was not of interest in the present work so the simulation behaviour after the prediction of dryout was not important.

It should be noted that RELAP5 does not directly calculate the equilibrium quality needed as input to the CHF prediction methods. Closure models are used to represent the thermo and hydro-dynamic non-equiluibrium present in evaporating flows. The RELAP5 six-equation solution plus these closure models yield a flow quality—the actual fraction of the total mass flow as vapour—as well as enthalpies for each phase. RELAP5 calculates the equilibrium quality by using the flow quality and phasic enthalpies to obtain a mixture enthalpy as shown in Equation A.4. The equilibrium quality is then obtained using this mixture enthalpy and the liquid and vapour saturation enthalpies at the local pressure.

$$h_e = h_{va} \cdot x_a + h_{la} \cdot (1 - x_a) \tag{A.4}$$

RELAP5 saved data to a RESTART file for each run at user-specified intervals. For a period of time at least 2 s before the beginning of the transient and 2 s following the end of the blowdown period data was saved every 0.01 s. In advance of this period data was recorded every 3 s and following the blowdown period every

B.A. Statham
Ph. D. Thesis

Appendix A
Data Processing

McMaster University
Engineering Physics

Linearisation (0904-no016)
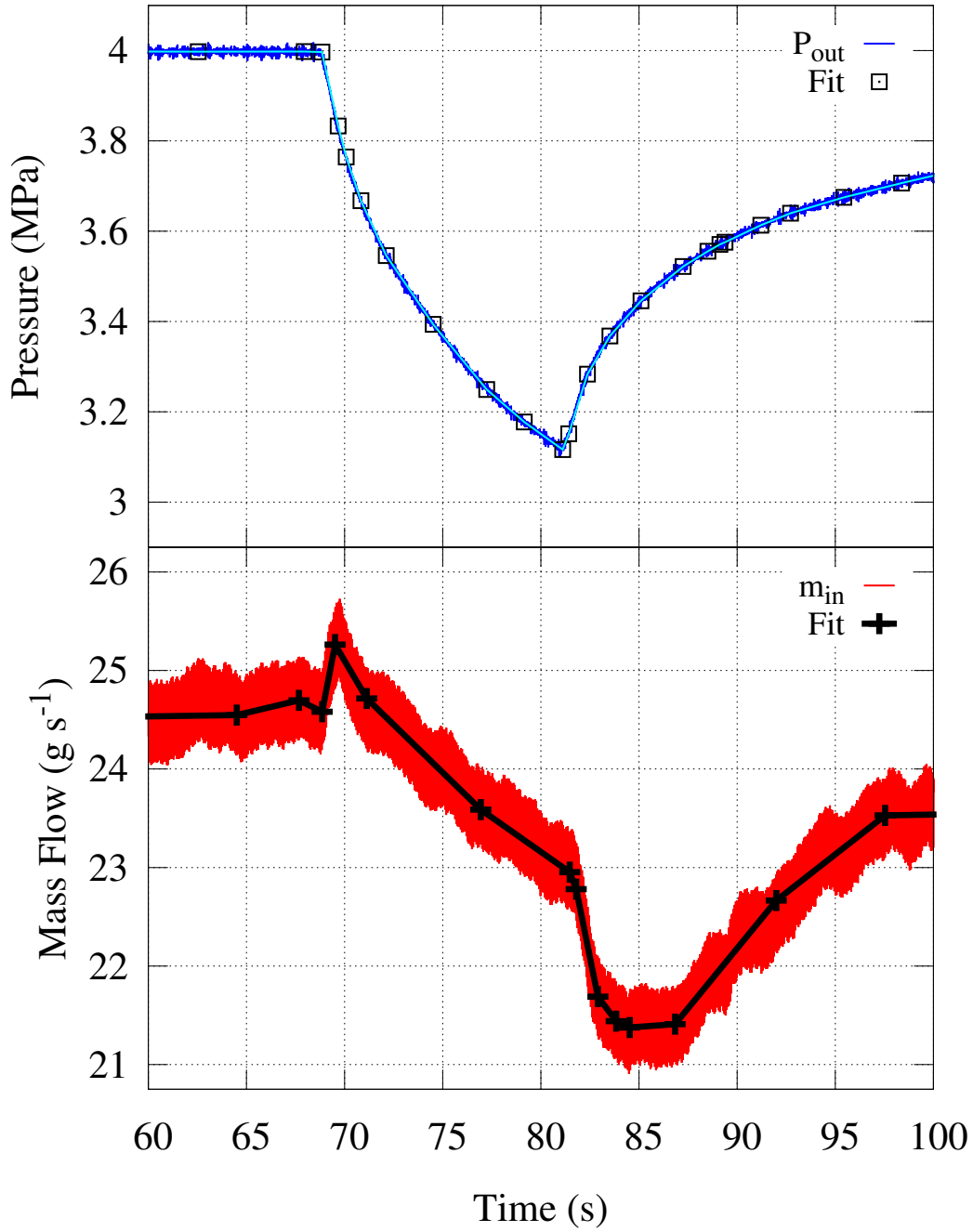
Figure A.4: Example series of linear fits used to reduce sampled data for input to RELAP5.

10 s. RELAP5 was then used to export the pressure, equilibrium quality, upstream mass flow rate, downstream mass flow rate, convective heat flux, liquid density and vapour density for all recorded time values at each volume that corresponded to a test section thermocouple location. The resulting `stripf` file was then further processed so that the data could be read like a spreadsheet as a tab-delimited text file. This tab-delimited file of time-data for each volume was then used as input to the time-to-dryout prediction script written by the author.

A.3.4   Model Sensitivity

The RELAP5 model's sensitivity to variations in modelling parameters was tested for run 0913-no013. In addition to the control model used for all simulations in this thesis—abrupt area change junctions with unequal fluid velocities and thermodynamic disequilibrium—five other variations were tested: The homogeneous equilibrium model (HEM), inhomogeneous equilibrium—thermodynamic equilibrium with unequal fluid velocities, the control model with wall friction disabled, and the control model with the junction hydraulic diameter used in the interphase friction calculations both halved and doubled for all components.

The computed local pressures and qualities for each model are depicted for the furthest upstream and downstream thermocouple positions in Figures A.5 and A.6 respectively. In both figures the only model that shows a visible variation from the others is the model with zero wall friction. Without the effect of wall friction the pressure drop is effectively reduced. In this case the local pressure differs in this model by an increasing amount as the distance from the outlet pressure boundary condition increased.

The effect of these models on the predicted time to dryout for the modified Biasi correlation and the modified look-up table is small. The means and standard deviations in dryout delay—for run 0913-no013 only—for each model are shown in Table A.4. Note that for this run three data points were used to compute the mean and standard deviation of dryout delay for the modified Biasi correlation data— the thermocouple at the text section exit was predicted to be in dryout before the beginning of the transient—while there were four predicted dryout times for the
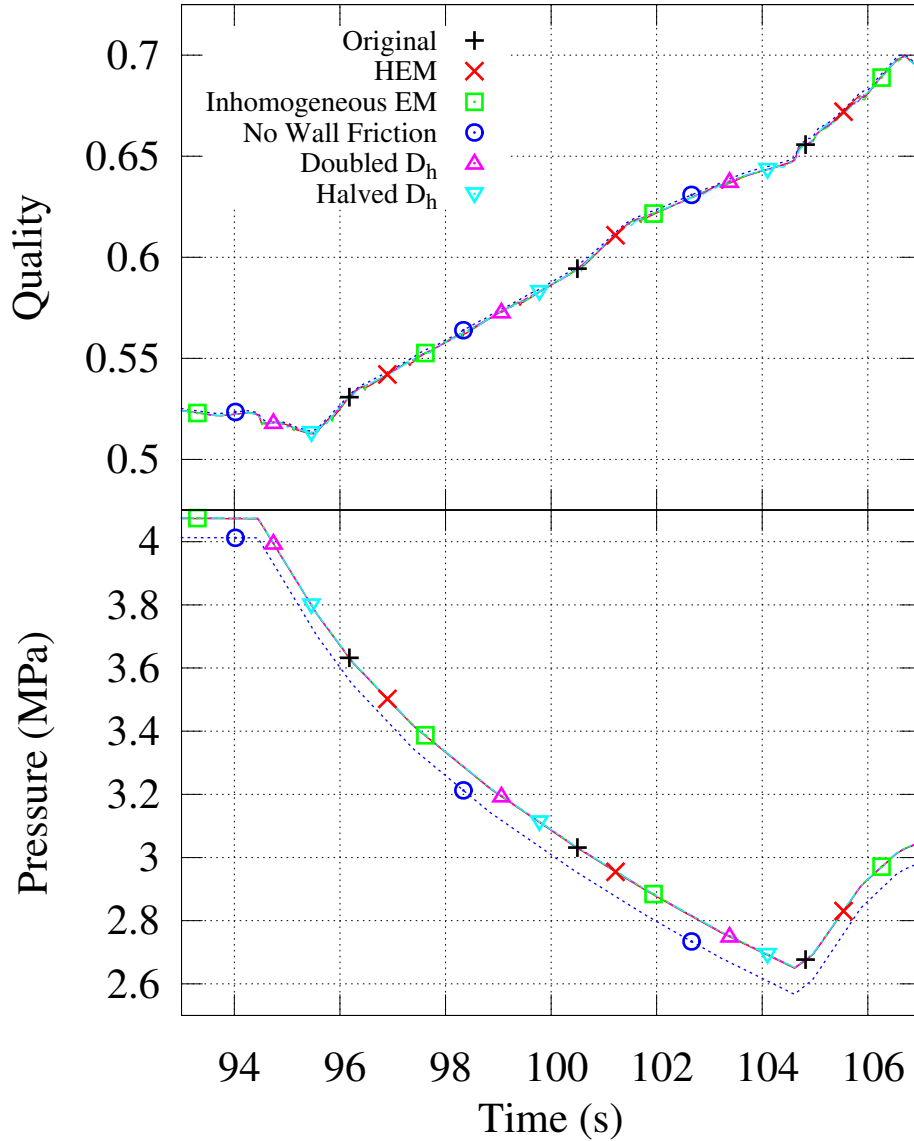
Figure A.5: Local pressure and quality computed by RELAP5 for transient run 0913-no013 with six different variations on the thermalhydraulic model at L_h = 955 mm.

Model Sensitivity at L_h=1316 mm
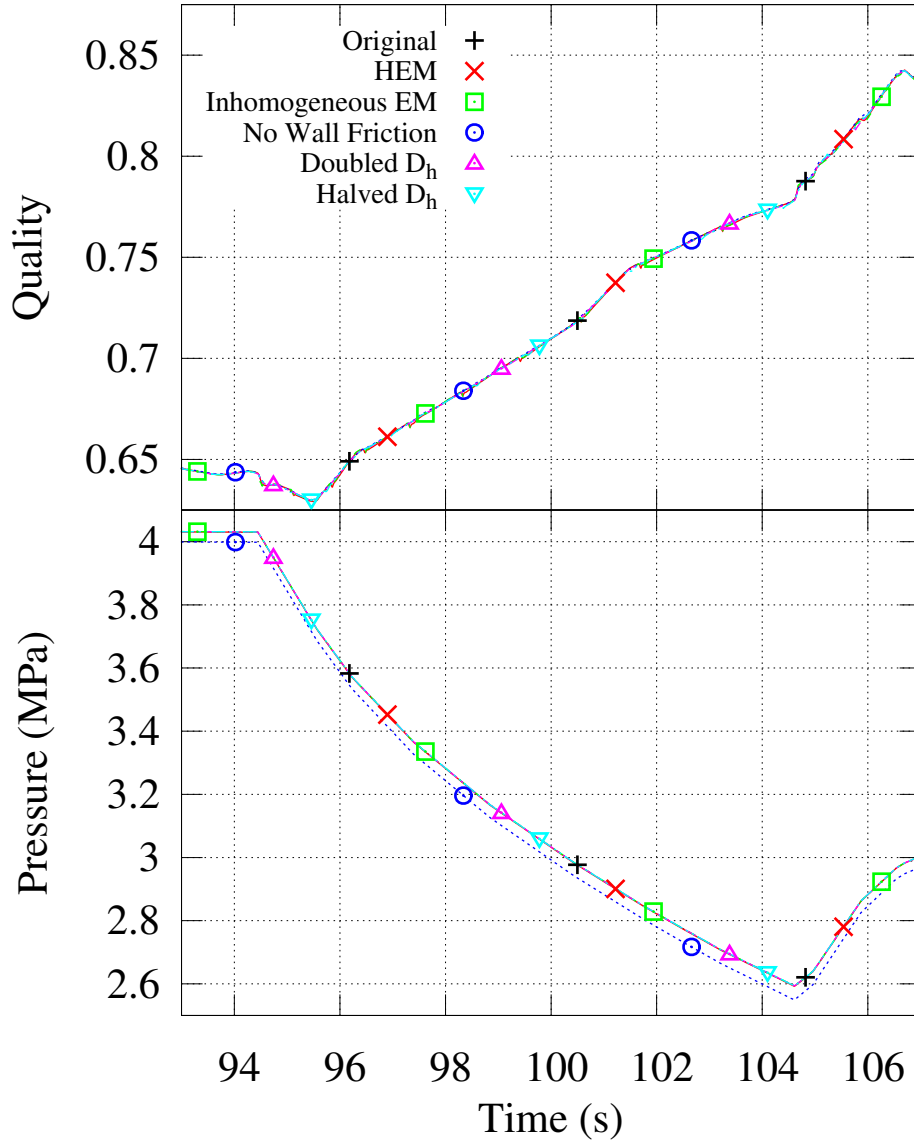
Figure A.6: Local pressure and quality computed by RELAP5 for transient run 0913-no013 with six different variations on the thermalhydraulic model at L_h = 1316 mm.

Model	Mean Delay (s) Biasi*	Std Dev (s) Biasi*	Mean Delay (s) LUT*	Std Dev (s) LUT*
Control	-0.32	0.62	-0.59	0.48
HEM	-0.33	0.60	-0.59	0.45
Inhomogeneous Equilibrium	-0.32	0.61	-0.58	0.45
No Wall Friction	-0.28	0.56	-0.51	0.42
Double d_{hyd}	-0.33	0.62	-0.59	0.47
Half d_{hyd}	-0.32	0.62	-0.60	-0.49

Table A.4: Variation in dryout delay times due to variation of the RELAP5 thermal-hydraulic model

modified LUT data.

The effect of removing wall friction was much larger overall than any of the other variations in thermalhydraulic parameters: the mean dryout delay decreased by 0.04 s for the modified Biasi correlation and by 0.08 s for the modified CHF look-up table when wall friction was removed from the model. The mean variation was on the order of 0.01 s for the other models. A change of less than 0.1 s is insignificant relative to the overall scatter in the dryout delay times and the estimated uncertainties in the predicted dryout times that were on the order of 2 s or more.

Appendix B

Standard Operating Procedures

B.1   Operating Fluid and Filling Procedure

The operating fluid of the experiment is de-oxygenated distilled water obtained from dedicated taps in the Arthur Bourns Building undergraduate chemistry labs at McMaster University. Early flow boiling experiments at this facility showed that corrosion of the test section was a problem. The solution was to de-oxygenate the filling water prior to charging the experiment. This significantly reduced but did not eliminate the problem completely.

The method used to prepare the filling fluid, flush the experiment, and charge it with water is outlined below:

1. Completely depressurise loop.

   (a) Gradually open the back pressure nitrogen regulator to fully open. Wait until the accumulator stops discharging nitrogen.

2. Drain the loop through the outlet ports at the lowest elevations of the loop.

   (a) Ensure that all bleed lines—except preheater discharge drain—and the pump suction line are terminated in the storage tank and that the bleed isolation valve, flow control valves and condenser spray valve are open.

   (b) Open all bleed line plug valves and filling line—at the filling pump discharge—and allow loop to drain as much as possible.

(c) Open preheater discharge drain and allow to empty before closing again.

(d) Close the filling line valve.

3. Flush the loop.

   (a) Remove the accumulator bleed line from the lid of the storage tank and connect it to the nitrogen supply line using a Swagelok NY-400-6 fitting.

   (b) Make sure that the bleed valves are open then carefully adjust a nitrogen regulator to obtain a slow, steady flow of nitrogen into the loop.

   (c) Close all of the bleed valves except the accumulator bleed valve—where the nitrogen enters the loop—and the pump suction pressure gauge bleed line. Allow this line to flush.

   (d) Close the bleed isolation valve. Open the first bleed valve in the experimental flow path: the flow meter discharge/preheater inlet bleed valve. Close the gauge pressure bleed valve. Allow the open valve to flush.

   (e) Open the preheater discharge drain and close the flow meter discharge bleed valve. Allow the preheater discharge drain valve to flush.

   (f) Proceed in the manner above for all bleed valves in the experimental loop until the last valve in the flow path is reached.

   (g) Open the bleed isolation valve and close the flow control and condenser spray valves. Follow this procedure from the previous step in reverse until all lines have been flushed in forward and reverse order.

   (h) Close the experimental loop.

      i. Open the gauge pressure bleed valve and close all others.

      ii. Stop the flow of nitrogen from the regulator and wait until any accumulated pressure in the loop has dissipated.

      iii. Close the gauge pressure and accumulator bleed valves.

   (i) Fully open the flow control, condenser spray, and bleed isolation valves.

4. Refresh water supply.

(a) Remove bleed lines and pump suction line from the storage tank cover. Hang the lines from their associated valves; the pump suction line should be kept clean—this is usually done by storing it in a tank of clean (distilled) water. Empty the storage tank.

(b) Rinse the tank out with distilled water from tap and discard water.

(c) Fill tank until water level reaches ledge near top of container.

5. De-oxygenate water.

(a) Re-insert all bleed lines and pump suction line back through the lid of storage tank.

(b) Prime the filling pump by filling it with distilled water from the storage tank using a clean plastic beaker.

(c) Flush the filling pump by running the discharge line into a clean tank until any gas bubbles have been eliminated in the suction and discharge lines.

(d) Fit the pump discharge to the loop's filling inlet. The experimental loop's bleed lines, the storage tank, and the filling pump should form a closed, but not airtight, system when the lid is secured to the storage tank.

(e) Attach the nitrogen supply line to the inlet of the nitrogen bubbling assembly that protrudes out of the top of the storage tank using a Swagelok NY-400-6 fitting.

(f) Slowly open the nitrogen supply regulator to allow a small, steady flow of nitrogen to the porous stone blocks. The flow rate should be enough to see a steady stream of small bubbles from at least one of the blocks but not enough to cause a violent disruption of the water surface. Once a continuous nitrogen flow is established re-close the lid and leave for 10-12 hours (overnight) to allow dissolved oxygen to diffuse out of the water.

6. Fill and bleed loop.

(a) Listen through the side of the storage tank to check that nitrogen continues to be bubbled through the water. If not the nitrogen supply may need to be adjusted and left to continue de-oxygenating.

(b) Disconnect the filling pump discharge and siphon 2 L of water to flush out the water from the pump, suction, and discharge lines that my not have been deoxygenated. 2 L is approximately one and a half times the volume of the filling pump.

(c) Reconnect filling pump discharge to loop filling connection.

(d) Make sure that flow control, condenser spray and bleed isolation valves are fully open.

(e) Open all bleed lines except the preheater discharge drain.

(f) Start the filling pump and slowly open the loop filling line valve.

(g) Follow the same procedure for bleeding gas from the loop as was used to flush the loop with nitrogen. When this process is complete leave the accumulator bleed valve open and the filling pump running.

(h) Use the nitrogen regulators to pressurize the accumulator to 1–2 MPa. This will not pressurize the loop but will cause the nitrogen bladder to expand to its full size. This will squeeze gas out of the accumulator. Continue until the accumulator has reached its full extension—there is usually an audible 'click' as the blow-out prevention device in the accumulator is depressed completely.

(i) Depressurise the accumulator by discharging all nitrogen through the back-pressure regulator.

(j) Close the accumulator bleed valve, close the filling line valve and stop the filling pump.

(k) Stop the nitrogen bubbling supply. This is only necessary if it was not stopped when filling and discharging the accumulator.

The next step must be performed before the loop can be left alone otherwise damage to the accumulator bladder may occur. The bleed lines may be removed from the storage tank lid and hung from their respective plug valves.

The filling pump can be removed for storage and the storage tank moved to a more convenient location.

7. Charge accumulator.

   This step must be performed shortly after the previous step is completed to prevent damage to the bladder in the accumulator.

   (a) Pressurise the accumulator to 1–2 MPa.

   (b) This will happen very quickly since very little nitrogen will be needed to completely fill the compressed volume of the accumulator bladder.

   (c) Discharge liquid through the condenser level bleed lines and the condenser bleed line.

      Small vapour bubbles that may have been entrained during the filling process tend to get trapped in the condenser bleed lines and this is a good way to eliminate them. The liquid should be discharged into a graduated cylinder or other measuring device. Continue this process until approximately 4.5 L has been discharged. This ensures that the accumulator bladder is relaxed while the loop is idle. It also allows for enough expansion volume for the condenser to completely fill with steam during the first run of the loop before any liquid is discharged during blowdown experiments. If no blowdown experiments are planned before the loop will be flushed and refilled then 6–8 L should be bled out since no extra liquid inventory is required to allow for blowdown discharge.

8. Depressurise the loop.

   (a) Close the supply valve on the nitrogen cylinder then allow all nitrogen in the accumulator to discharge through the back-pressure valve.

   (b) Completely relax the pressure regulators by turning their handles fully anti-clockwise and close the nitrogen supply isolation valves. The loop is now charged.

191

B.2   Startup Procedure

The procedure outlined below should be followed to start the loop *every time it is run* in order to perform experiments safely and make sure the pump and other components are performing as expected.

1. Test the electrical isolation of powered components.

   (a) Make sure that the test section and preheater power supply main switches are 'off' and that their supply breakers are open.

   (b) Ensure that there is no electrical continuity between the test section and preheater heating circuits and the rest of the loop. This should ideally be done using a high-potential tester but a digital multimeter can be used to test the resistance and continuity if a high-potential tester is not available.

2. Start the Instrumentation and Control VI in LabVIEW

   (a) Make sure that the instrument and DAQ power supplies are plugged in

   (b) Run the VI

3. Pressurise the secondary (heat removal) loop and charge the blowdown valve opening air supply.

   (a) Check that the secondary loop is depressurised by checking the pressure gauges at the chilled water supply tube side inlet and outlets read zero.

   (b) Check that the secondary loop pressure-reducing and back-pressure regulator handles are turned anti-clockwise as far as they will go. Close the back-pressure regulator by turning the handle three turns clockwise.

   (c) Open the secondary loop supply shutoff valve. If a blowdown experiment is planned open the blowdown valve supply shutoff valve.

   (d) Open the gas cylinder shutoff valve slowly until the cylinder pressure registers on the inlet gauge of the pressure-reducing regulator.

(e) Turn the pressure-reducing regulator's handle slowly clockwise until the outlet gauge registers a pressure increase.

(f) Slowly increase the pressure to 550 kPa and adjust the back-pressure regulator until a just-detectable amount of leakage is present. The small amount of leakage will reduce hysteresis in pressure control as the blow-down valve is opened and closed and when the fluid in the loop expands due to heating.

4. Pressurise the loop.

   (a) Make sure the loop is completely depressurised and that the regulator handles have been turned fully counter clockwise.

   (b) Make sure that the bleed isolation valve is open and that at least one of the flow control or condenser spray valves is partly open. This will prevent the loop from becoming partially pressurized and reverse-loading the bleed isolation valve. Fully open the orifice valve.

   (c) Open the nitrogen cylinder's shutoff valve slowly until it is fully open and the cylinder pressure is shown on the pressure-reducing regulator's input gauge.

   (d) Close the back-pressure regulator slightly by turning the handle clockwise a few full turns.

   (e) Slowly turn the pressure-reducing regulator's handle clockwise until the accumulator begins to fill and the pressure increase registers on the VI's display. Continue until either the back-pressure regulator begins to leak or the desired loop pressure has been reached.

   (f) Adjust the back-pressure regulator so that leakage is eliminated. If a higher pressure than the current pressure is desired then the handle should rotated an additional clockwise turn.

   (g) Repeat the previous two steps until the desired pressure is reached. Adjust the back-pressure regulator until a barely detectable amount of leakage is present. This will allow pressure relief while the loop is warmed up and the liquid expands.

5. Start the low-pressure subcooler.

   (a) Fully open the subcooler's cooling water supply valve. For the present experiments this was the cold water tap for the lab's sink.

   (b) Make sure that there is sufficient flow, there are no leaks in the low-pressure flow path and the water temperature is cool—approximately 15°C.

6. Start the pump.

   (a) Close the bleed isolation valve and set the flow control and condenser spray valves so that they are slightly open. The bleed isolation valve decouples the pump suction from the pump discharge. When the pump is started the (absolute) discharge pressure may be observed using the outlet pressure transducer's displayed value on the VI. The suction (gauge) pressure is read by the pump suction pressure gauge and should change very little when the pump is started.

   (b) Set the pump recirculation valves to three turns open. These may be adjusted during loop operation to adjust the operating position on the pump curve. Care should be taken to make sure that the total flow does not fall below the manufacturer's recommended minimum nor exceed the maximum limit. If these limits are disregarded damage to the pump or the motor may occur.

   (c) Check that the Basic Operator Panel (BOP) display on the VFD is alternating between '0.00' and '30.00'. This means that the motor is off but will be ramped up to 30 Hz when started.

   (d) Check the oil in the pump casing. The oil level should be halfway up the sight glass. If there is not enough oil it should be topped up or changed. Check the operating manual for the recommended frequency of oil changes and type of oil.

   (e) Press the green on button on the VFD. The motor should begin turning and the displayed frequency will ramp up to '30.00' in 10 s. If it does

194

not consult the pump and VFD operating manuals. The outlet pressure shown on the VI's display should increase by approximately 190 kPa when the pump is started. If it does not or if the pump makes any unusual noises stop it immediately so that the problem may be identified and fixed if possible. Continue to the next step if everything is working correctly.

    (f) Slowly open the bleed isolation valve. A few grams per second of flow should register on the flow meter's LCD display.

7. Set the flow control valve positions.

    Open the fine and very fine flow control valves three turns anti-clockwise. Adjust the orifice valve and the pump frequency so that the desired mass flow rate is achieved without changing the flow control valves positions and the pump's frequency does not exceed 32.50 Hz. This is not a hard limit but one that has been arrived at through operating experience.

8. Run the experiment.

B.3   Basic Procedure Outline

This section describes the procedure for performing a steady-state experiment. Before performing a CHF experiment the final test section power—*i.e.* the CHF power—was estimated using the Katto-Ohno correlation and the 2006 CHF look-up table using the heat balance method.

1. Follow the loop start-up procedure outlined in Section B.2.

2. Start the preheater and test section power supplies

    (a) Check that the hard-wired Emergency Stop switches are available by depressing and releasing them. Each power supply has one switch on the front of its enclosure and a remote switch is mounted in the polycarbonate shielding on the North side of the experimental apparatus between the VFD and the flow control valves.

(b) Check that both power supply front panel switches are set to off.

(c) Throw the power supply breakers for 'Power Supply One' and 'Power Supply Two'. These correspond to the test section and preheater power supplies, respectively.

(d) Turn the power supply front panel switch to on.
The HMI on each power supply will start but will not supply any power to the test section or preheater.

(e) Check the current and voltage limits for each unit.
Record these values for reference during the experiment. They should be adjusted so that they exceed the anticipated maximum values for the experiment by between 5 and 10%. If the power supply's internal sensors detect that either of these limits have been exceeded the power supply will be tripped and an error message will be displayed. This is an important safety feature but if the power supplies are operated near these limits then spurious trips can occur.

(f) Ensure the output settings are set to reasonable 'turn-on' values.
For the test section good starting values are 20.1 A, 2 V and 0.5 kW while 33.2 A, 5 V and 0.5 kW should be used for the preheater.

(g) Load and run the test section and preheater power supply control VIs.
An RS-232 serial cable with DB-9 terminating connections should connect the HMI of the power supplies with the serial inputs of the controlling computer. Press the Connect button on each VI and set the control interface to RS-232 as shown in Figure 3.7. All power supply control actions described below are performed using this VI.

(h) Set the power supply control values to the settings described above using the power supply VIs.

(i) Switch 'Voltage On Set' to on. The fluid and wall temperatures downstream of the test section should rise when the preheater is started and the wall temperatures and outlet temperature of the test section should rise slightly when the test section power supply is started.

3. Start the closed-loop heat exchanger pump—i.e. the secondary loop.

   (a) Open the chilled water supply shutoff valve and make sure that the chilled water flow control valve is fully open.

   (b) Set the secondary flow control valve to 0.25 turns open. This valve has a position indicator. Set the secondary loop recirculation control valve to approximately $1/16$ of a turn open.

   (c) Plug the secondary loop pump cord into the wall.
   The pump should start abruptly and the pressure gauges at the inlet and outlet of the tube side of the chilled water heat exchanger should rise by approximately 70 kPa. Open the secondary flow control valve completely. This corresponds to a valve position of approximately 4.25 turns.

4. Adjust the preheater power.
   The preheater power needed to raise the inlet temperature to the desired value can be calculated using a single phase heat balance. During all of the experiments conducted for the present work the current was used as the power limiting value.

5. Adjust the test section power.

6. Adjust the primary loop pump's frequency as needed to maintain the desired mass flow rate.

7. Adjust the pressure.
   During single phase and low steam quality operation this must be done by manipulating the pressure-reducing and back-pressure regulators. If the test section exit steam quality exceeds 20% the pressure can be controlled precisely by balancing the volume of steam in the condenser. The recommended condenser level is between 3 and 5 inches. At this level the free surface of the liquid is below the end of the test section discharge tube but sufficient liquid inventory is available to prevent vapour bubbles from entering the condenser

discharge tube. Operating experience also suggests that the flow is more stable when the free surface is below the test section discharge. The procedure for establishing a steady condenser level follows. Maintaining a nominally constant mass flow rate through this process is very important because of the strong interaction between the pressure, mass flow rate, and test section inlet temperature.

(a) The test section and preheater power are kept constant during the following steps.

(b) Open the back-pressure regulator so that there is a steady flow of nitrogen and the outlet pressure begins to decrease slowly. The condenser level should also begin to decrease.

(c) Adjust the condenser spray control valve to moderate the rate of change of the condenser level and the pressure.

(d) Repeat the previous two steps until the desired condenser level is reached.

(e) Close the back-pressure regulator until there is no nitrogen leakage. For the rest of the experiment the pressure should be controlled by balancing the steam volume in the condenser. This is done by manipulating the flow rate of liquid through the condensing spray nozzle using a flow control valve.

8. Repeat the previous steps to obtain the desired inlet temperature—i.e. preheater power—test section power, mass flow rate, and pressure reach steady-state.

9. Record high-speed data.

(a) Set the thermocouple DAQ mode on the VI to 'Speed.'

(b) Activate high speed logging on the VI. Continue recording data for approximately 1 minute. For the present work the time that logging began was written down along with the measured test section and preheater supply powers, the power supplies' current limit values, and the pump

frequency. This was done so that any anomalous behaviour observed during the recording period could be noted for future reference.

(c) Switch high speed logging off.

B.4   Shutdown from Two-Phase Conditions

In order to safely shutdown the experiment without damage to the pump or test section the following procedure was used:

1. Gradually reduce test section power

2. Maintain the mass flow rate approximately constant while power is decreased.

3. Allow the pressure to decrease slowly. Use the condenser spray valve to control the rate of increase of the condenser level and thereby limit the depressurisation rate. The nitrogen supply should make up for the decreasing steam volume in the condenser. Ensure that the pump has sufficient NPSH at all times.

4. Continue to control the flow and the rate of depressurisation until the test section reaches its turn-on power. Shut off the test section power supply. The flow in the test section and condenser should now be completely single phase.

5. Ramp down the preheater power gradually while maintaining a constant flow rate—no flow control valve or pump frequency adjustments should be necessary.

6. Turn off the preheater power supply output.

7. Gradually open flow control, condenser spray, and orifice valves until they are fully open.

8. Reduce pump frequency to 30 Hz.

9. Allow loop to cool down to room temperature.

10. Follow the reverse of the startup procedure to stop the pump and depressurise the experiment.

Appendix C

Raw Data

C.1 Heat Balance Data

Heat balance data are shown in Figure C.1 with error bars. Fluid properties were calculated using the IAPWS-97 formulation [122]. Heat losses were less than 1% for test section powers above 10 kW.

The heat balance was calculated using Equation C.1 where W_{meas} is the measured electrical power applied to the test section. Uncertainties were propagated through Equation C.1 in order to calculate the overall uncertainty using Equation 3.2. For this calculation the mean and standard deviation of the temperature calibration curves were used to represent the overall systematic and random error, respectively, for the fluid temperatures. These values are given in Section D.3. The root sum square of these values was taken as shown in Equation C.2 to calculate an overall calibrated fluid temperature uncertainty for each. These uncertainties, $\pm 0.4^{\text{o}}$C and $\pm 0.1^{\text{o}}$C for the inlet and outlet temperatures respectively, were much smaller than the results that were obtained by propagating the manufacturer-specified uncertainties which was on the order of $\pm 1.4^{\text{o}}$C.

$$\Delta W = \frac{W_{fluid} - W_{meas}}{W_{meas}} = \frac{\dot{m} \cdot (h_{out}(T_{out}, p_{out}) - h_{in}(T_{in}, p_{in})) - W_{meas}}{W_{meas}} \quad \text{(C.1)}$$

$$\sigma_{Tcal} = \sqrt{\sigma_{sTcal}^2 + \sigma_{rTcal}} \qquad\qquad (C.2)$$

Heat Balance Data
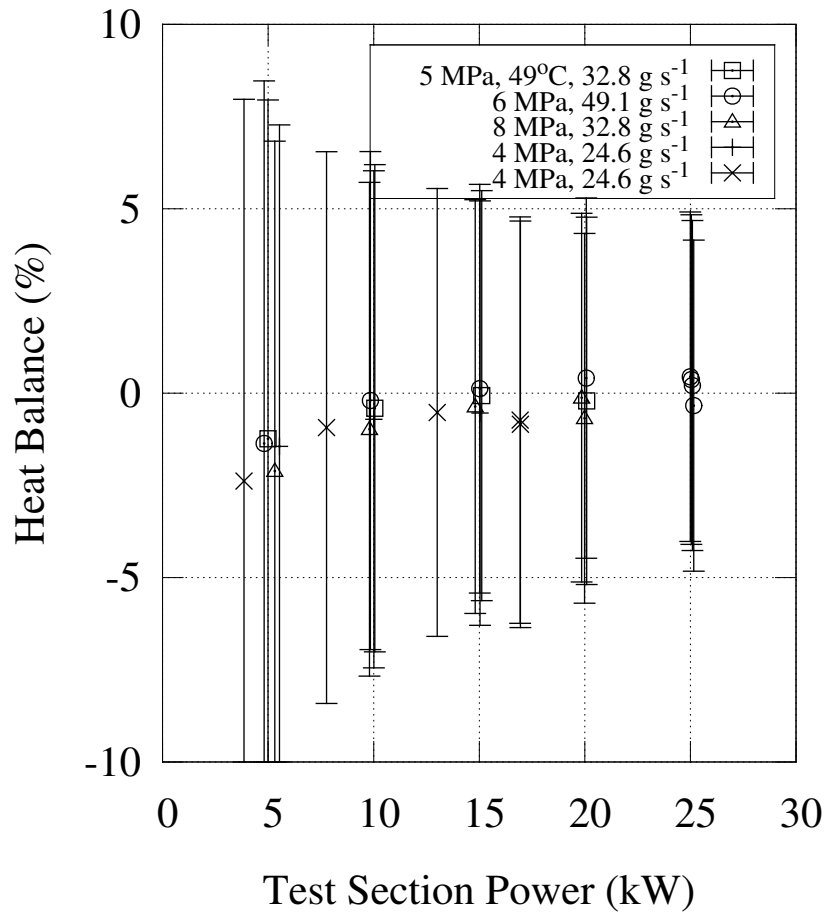
Figure C.1: Heat balance data.

C.2   Wall Temperature and σ_{Tw} *vs* Heat Flux Data for Steady OID

Wall temperature *vs* heat flux plots are given in this section for each series of steady-state data collected. Separate plots are shown for each set of boundary conditions in each test series. The plots are sorted into sections by mass flux and are presented in order of increasing pressure for each mass flux. Repeated tests are shown in chronological order.

The heat flux is also co-plotted against the wall temperature standard deviations in this section. The standard deviation axes are reversed relative to the wall temperature axes. Two standard deviations are plotted. The first standard deviation is calculated as the overall standard deviation in temperature for each steady data set in each series. The second was the maximum value of the standard deviation calculated in a 0.1 s interval for all values of time in the data set. These standard deviations were used as criteria for selecting the OID points from the steady-state data and to find the time OID occurred during transient runs respectively.

C.2.1   1000 kg m^{-2} s^{-1}

T$_{wall}$ and SD$_{Twall}$ vs. Heat Flux at L$_h$=1316 mm
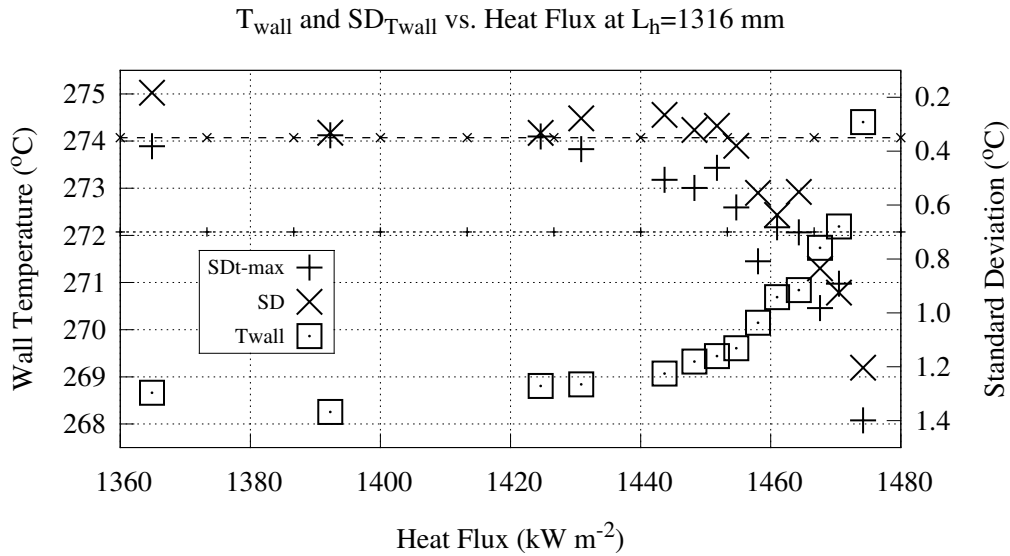
Figure C.2: T$_{wall}$ and σ_{Tw} *vs* $\ddot{q}$ for 2 MPa, 1000 kg m^{-2} s^{-1}, series 0909.

T$_{wall}$ and SD$_{Twall}$ vs. Heat Flux at L$_h$=1316 mm
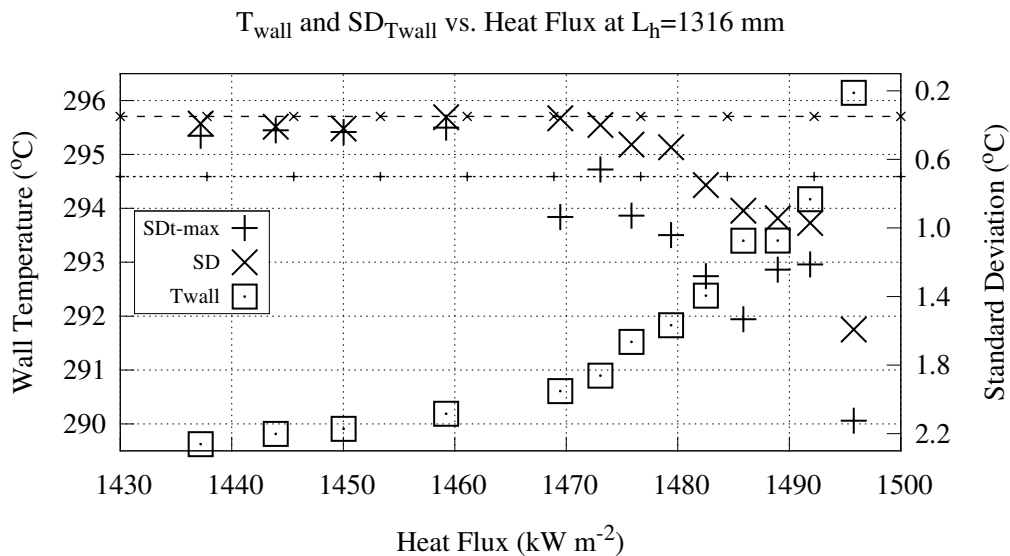
Figure C.3: T$_{wall}$ and σ_{Tw} *vs* $\ddot{q}$ for 3 MPa, 1000 kg m^{-2} s^{-1}, series 0910.

T_{wall} and SD_{Twall} vs. Heat Flux at L_h=1316 mm

Figure C.4: T_{wall} and σ_{Tw} *vs* $\ddot{q}$ for 4 MPa, 1000 kg m^{-2} s^{-1}, series 0910.

T_{wall} and SD_{Twall} vs. Heat Flux at L_h=1316 mm
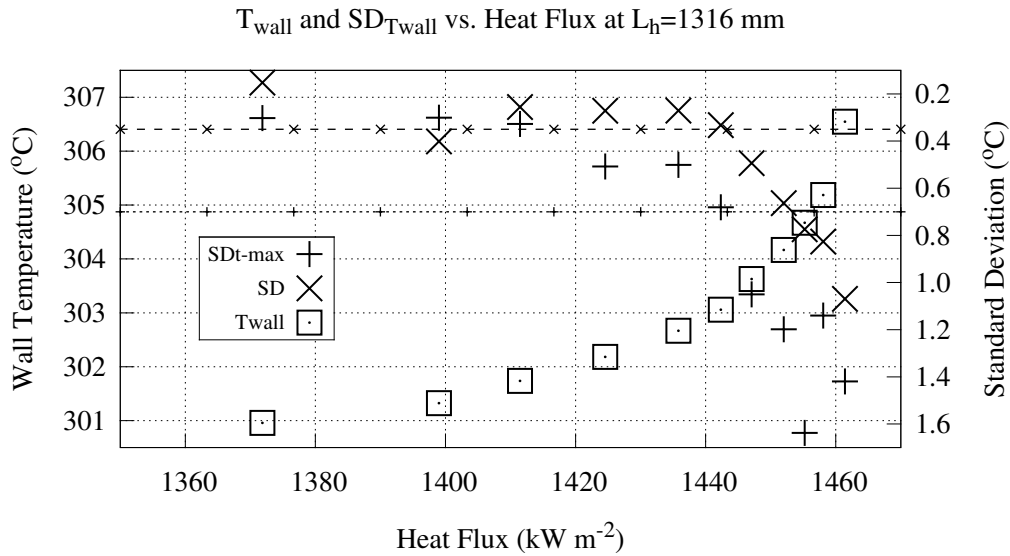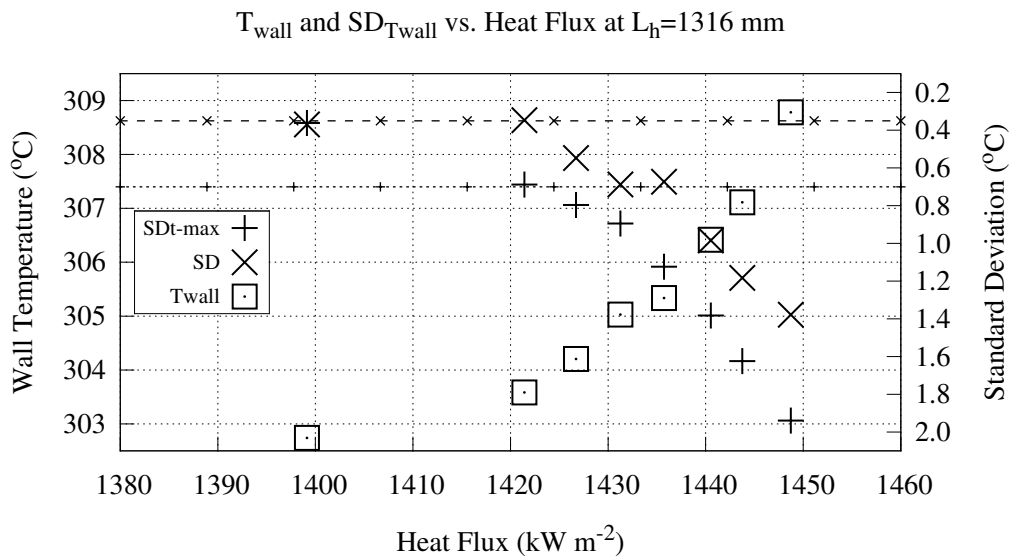
Figure C.5: T_{wall} and σ_{Tw} *vs* $\ddot{q}$ for 4 MPa, 1000 kg m^{-2} s^{-1}, series 0917.
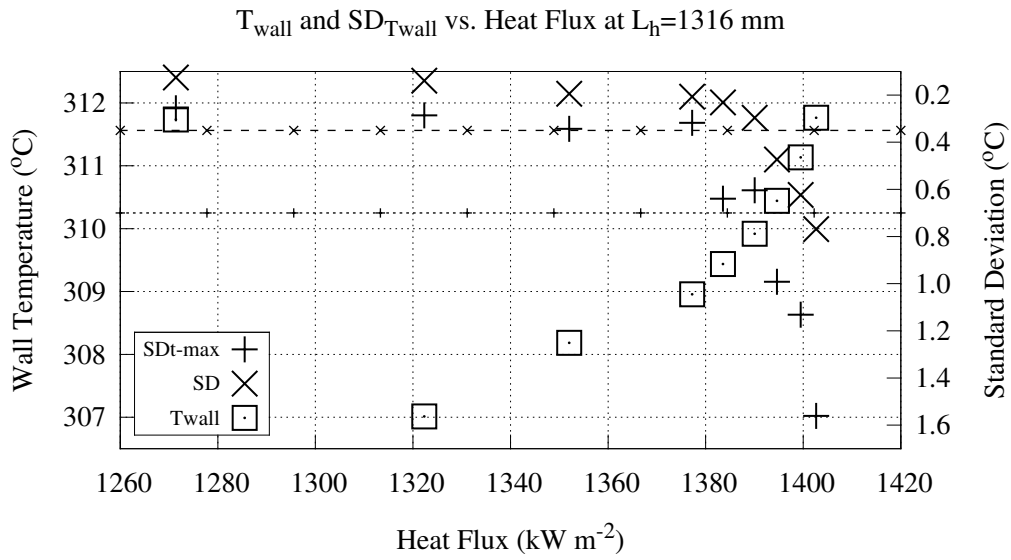
Figure C.6: T_{wall} and σ_{Tw} *vs* $\ddot{q}$ for 5 MPa, 1000 kg m^{-2} s^{-1}, series 0829.

C.2.2   1500 kg m^{-2} s^{-1}

T$_{wall}$ and SD$_{Twall}$ vs. Heat Flux at L$_h$=1316 mm
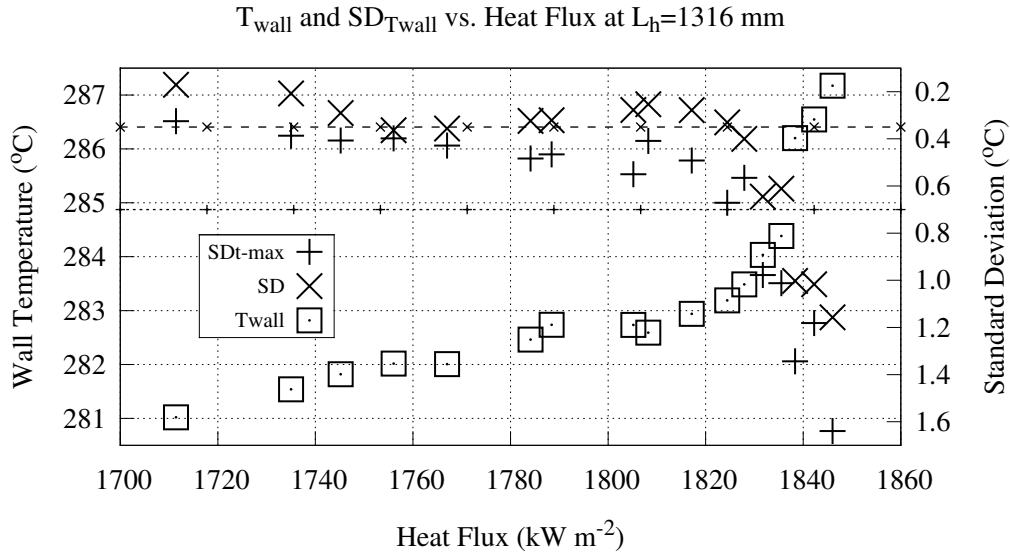
Figure C.7: T$_{wall}$ and σ_{Tw} *vs* $\ddot{q}$ for 2 MPa, 1500 kg m^{-2} s^{-1}, series 0909.

T$_{wall}$ and SD$_{Twall}$ vs. Heat Flux at L$_h$=1316 mm
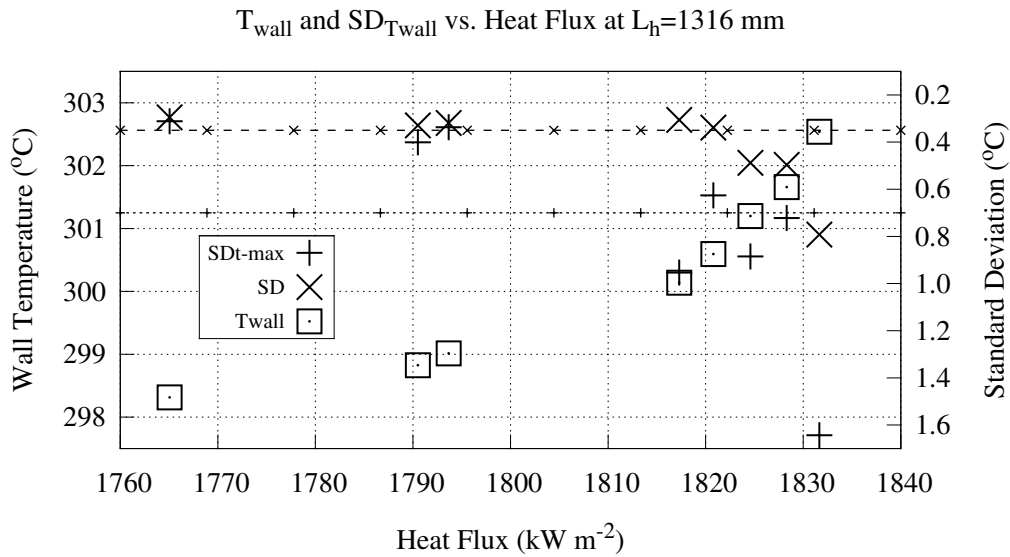
Figure C.8: T$_{wall}$ and σ_{Tw} *vs* $\ddot{q}$ for 3 MPa, 1500 kg m^{-2} s^{-1}, series 0904.
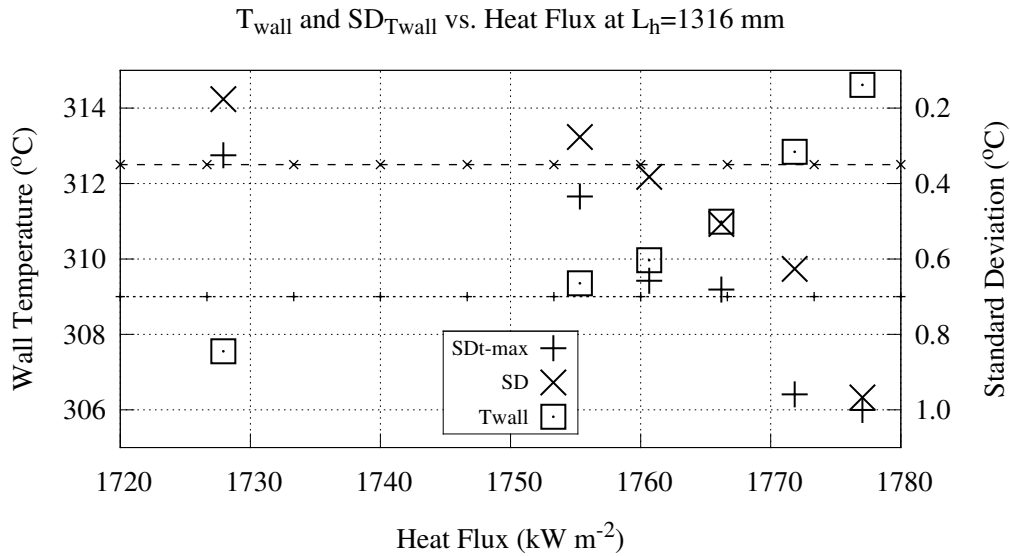
Figure C.9: T_{wall} and σ_{Tw} *vs* $\ddot{q}$ for 4 MPa, 1500 kg m^{-2} s^{-1}, series 0826.

Figure C.10: T_{wall} and σ_{Tw} *vs* $\ddot{q}$ for 4 MPa, 1500 kg m^{-2} s^{-1}, series 0904.

T_{wall} and SD_{Twall} vs. Heat Flux at L_h=1316 mm

Figure C.11: T_{wall} and σ_{Tw} *vs* $\ddot{q}$ for 4 MPa, 1500 kg m^{-2} s^{-1}, series 0911.

T_{wall} and SD_{Twall} vs. Heat Flux at L_h=1316 mm

Figure C.12: T_{wall} and σ_{Tw} *vs* $\ddot{q}$ for 4 MPa, 1500 kg m^{-2} s^{-1}, series 0913.

T_{wall} and SD_{Twall} vs. Heat Flux at L_h=1316 mm

Figure C.13: T_{wall} and σ_{Tw} *vs* $\ddot{q}$ for 4 MPa, 1500 kg m^{-2} s^{-1}, series 0917.

T_{wall} and SD_{Twall} vs. Heat Flux at L_h=1316 mm

Figure C.14: T_{wall} and σ_{Tw} *vs* $\ddot{q}$ for 4 MPa, 1500 kg m^{-2} s^{-1}, series 1114.

T_{wall} and SD_{Twall} vs. Heat Flux at L_h=1316 mm

Figure C.15: T_{wall} and σ_{Tw} *vs* $\ddot{q}$ for 6 MPa, 1500 kg m^{-2} s^{-1}, series 0827.

T_{wall} and SD_{Twall} vs. Heat Flux at L_h=1316 mm

Figure C.16: T_{wall} and σ_{Tw} *vs* $\ddot{q}$ for 6 MPa, 1500 kg m^{-2} s^{-1}, series 0829.

C.2.3 2000 kg m^{-2} s^{-1}
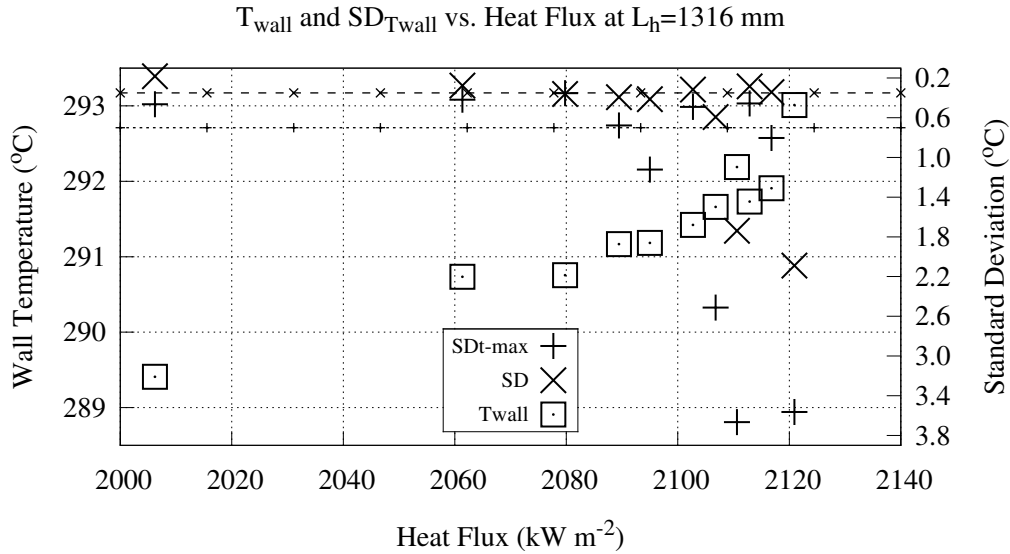
T_{wall} and SD_{Twall} vs. Heat Flux at L_h=1316 mm

Figure C.17: T_{wall} and σ_{Tw} *vs* $\ddot{q}$ for 2 MPa, 2000 kg m^{-2} s^{-1}, series 0908.

T_{wall} and SD_{Twall} vs. Heat Flux at L_h=1316 mm

Figure C.18: T_{wall} and σ_{Tw} *vs* $\ddot{q}$ for 2 MPa, 2000 kg m^{-2} s^{-1}, series 1115.

B.A. Statham
Ph. D. Thesis

Appendix C
Raw Data

McMaster University
Engineering Physics
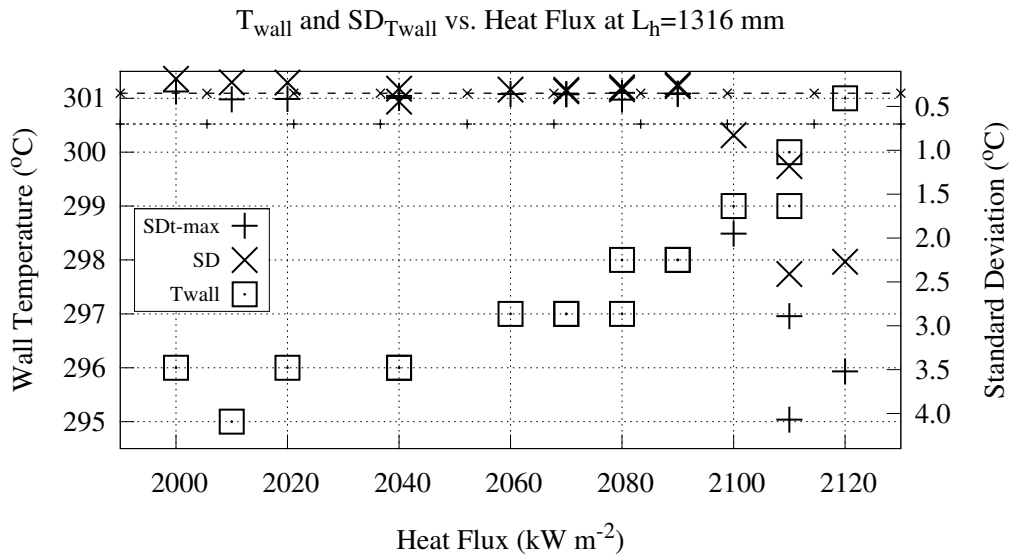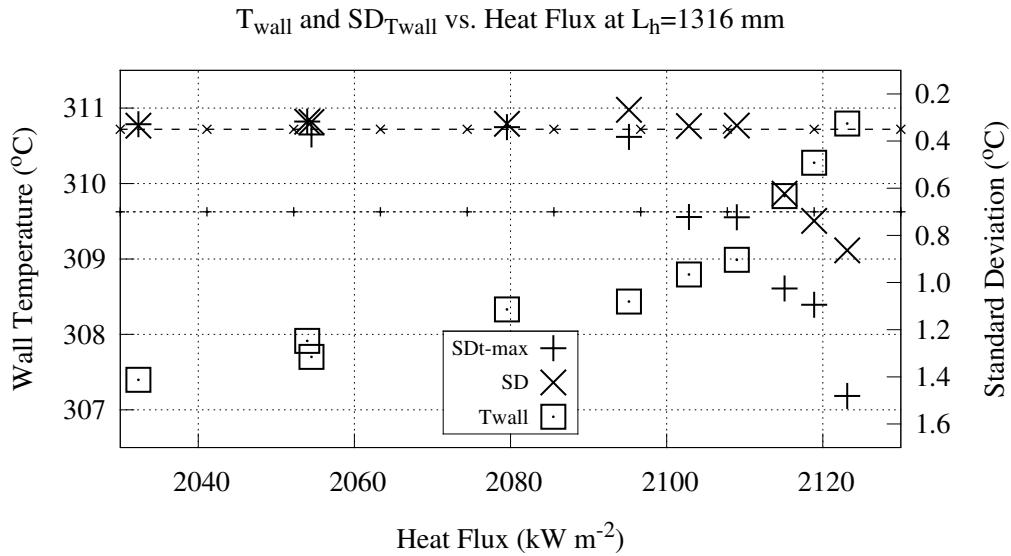
Figure C.19: T_{wall} and σ_{Tw} *vs* $\ddot{q}$ for 3 MPa, 2000 kg m^{-2} s^{-1}, series 0906.
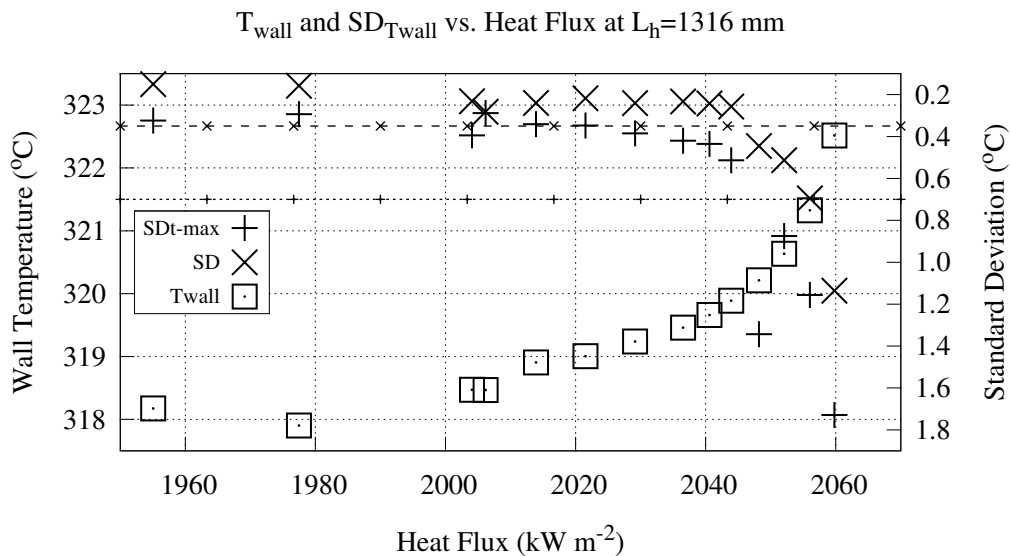
Figure C.20: T_{wall} and σ_{Tw} *vs* $\ddot{q}$ for 4 MPa, 2000 kg m^{-2} s^{-1}, series 0906.

T$_{wall}$ and SD$_{Twall}$ vs. Heat Flux at L$_h$=1316 mm

Figure C.21: T$_{wall}$ and σ_{Tw} *vs* $\ddot{q}$ for 5 MPa, 2000 kg m^{-2} s^{-1}, series 0826.

T$_{wall}$ and SD$_{Twall}$ vs. Heat Flux at L$_h$=1316 mm
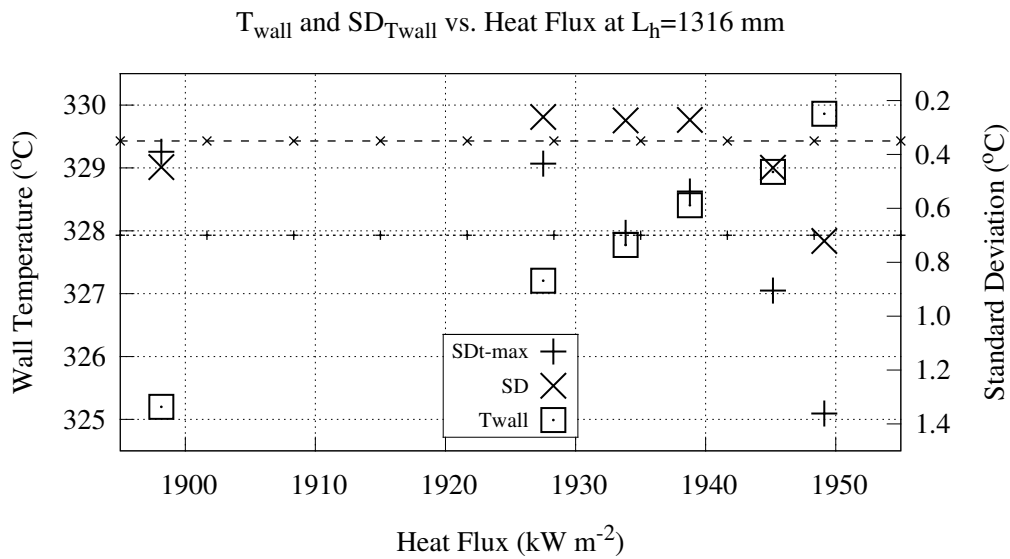
Figure C.22: T$_{wall}$ and σ_{Tw} *vs* $\ddot{q}$ for 5 MPa, 2000 kg m^{-2} s^{-1}, series 0827.

Figure C.23: T_{wall} and σ_{Tw} *vs* $\ddot{q}$ for 6 MPa, 2000 kg m^{-2} s^{-1}, series 1113.

C.2.4   2500 kg m^{-2} s^{-1}

T_{wall} and SD_{Twall} vs. Heat Flux at L_h=1316 mm
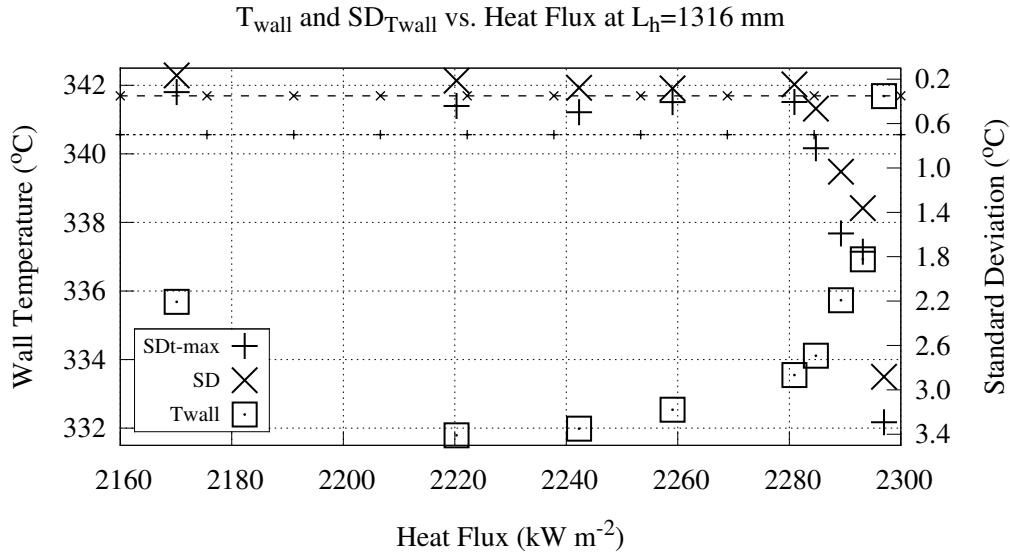
Figure C.24: T_{wall} and σ_{Tw} *vs* $\ddot{q}$ for 4 MPa, 2500 kg m^{-2} s^{-1}, series 0918.

T_{wall} and SD_{Twall} vs. Heat Flux at L_h=1316 mm
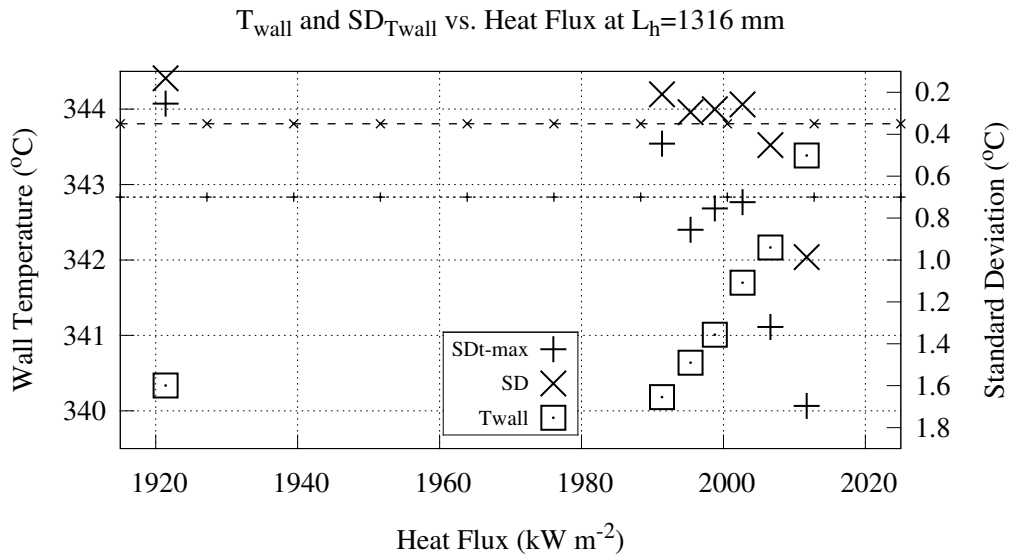
Figure C.25: T_{wall} and σ_{Tw} *vs* $\ddot{q}$ for 6 MPa, 2500 kg m^{-2} s^{-1}, series 0827.

C.3 OID Conditions

C.3.1 Steady Conditions

Table C.1 contains local values for the steady experimental dryout data points. The reported heat and mass fluxes are the mean measured value while the local pressure and quality were computed by RELAP5. The RELAP5 model was run as a transient with steady boundary conditions for 10 s which was sufficient for all local conditions reach steady values.

Run Identifier	Heat Flux ($kW\ m^{-2}$)	Pressure (MPa)	Mass Flux ($kg\ m^{-2}\ s^{-1}$)	Quality
0826-no004	1770	4.04	1490	0.649
0827-no005	1950	5.04	1990	0.538
0827-no019	2010	6.05	2490	0.442
0827-no028	1620	6.03	1490	0.651
0829-no007	1400	5.02	993	0.842
0829-no013	1620	6.02	1490	0.651
0904-no010	1780	4.03	1490	0.656
0904-no023	1820	3.05	1490	0.637
0906-no015	2050	4.04	1990	0.545
0906-no028	2110	3.06	1990	0.533
0908-no010	2110	2.14	1990	0.494
0909-no009	1450	2.04	993	0.746
0909-no031	1830	2.07	1500	0.595
0910-no008	1450	4.02	993	0.836
0910-no021	1480	3.02	999	0.803
0911-no006	1790	4.03	1490	0.659
0913-no006	1780	4.03	1490	0.654
0917-no004	1430	4.02	999	0.815
0917-no015	1780	4.03	1490	0.653
0918-no010	2280	4.06	2490	0.467
1113-no015	1800	6.04	1990	0.515
1114-no017	1770	4.04	1490	0.651
1115-no027	2100	2.14	2000	0.491

Table C.1: Steady dryout local conditions at L_h = 1316 mm.

C.3.2 Transient Conditions

Tables C.2–C.7 and C.8–C.13 list the transient local dryout conditions for PDO and MTD data respectively. The local conditions were computed by RELAP5 for all transients and are listed at the time dryout was experimentally observed and at the time dryout was predicted by both modified prediction methods.

L_h (mm)	Type	Dryout Time (s)	Heat Flux (kW m^{-2})	Pressure (MPa)	Mass Flux (kg m^{-2} s^{-1})	Quality
			Run Identifier			
			0826-no007			
1316	Exp.	0.69	1790	3.90	1538	0.638
1293	Exp.	3.29	1781	3.61	1506	0.639
	Biasi*	2.75	1781	3.66	1512	0.635
	LUT*	4.78	1780	3.51	1485	0.650
1276	Exp.	3.95	1781	3.56	1497	0.636
	Biasi*	4.94	1780	3.50	1483	0.643
	LUT*	6.24	1781	3.43	1466	0.653
			0827-no007			
1316	Exp.	3.14	1951	4.65	2016	0.537
	LUT*	4.21	1950	4.57	1996	0.545
1293	Exp.	6.96	1948	4.40	1954	0.548
	LUT*	8.10	1952	4.34	1948	0.552
1276	Exp.	10.11	1949	4.25	1914	0.557
	Biasi*	3.20	1951	4.66	2015	0.517
	LUT*	10.68	1948	4.22	1906	0.560
			0827-no020			
1316	Exp.	6.00	2009	5.33	2441	0.465
			0827-no022			
1316	Exp.	3.93	2018	5.46	2481	0.457
	LUT*	9.19	2013	5.11	2363	0.489
1293	Exp.	11.17	2011	5.02	2334	0.484
	LUT*	13.61	1976	5.15	2134	0.526
1276	Exp.	12.99	1967	5.07	2249	0.485
	LUT*	13.99	1977	5.20	2096	0.530

Table C.2: Transient local conditions for PDO data (1).

Run Identifier

L_h (mm)	Type	Dryout Time (s)	Heat Flux (kW m^{-2})	Pressure (MPa)	Mass Flux (kg m^{-2} s^{-1})	Quality
			0827-no031			
1316	Exp.	6.97	1636	5.02	1479	0.672
1293	Exp.	15.18	1595	4.71	1354	0.707
			0829-no010			
1316	Exp.	2.72	1399	4.47	999	0.846
	LUT*	3.19	1399	4.39	994	0.851
1293	Exp.	4.45	1401	4.22	983	0.842
	LUT*	6.00	1400	4.02	970	0.854
1276	Exp.	6.07	1400	4.01	970	0.845
	Biasi*	4.07	1401	4.28	986	0.829
	LUT*	7.28	1401	3.85	960	0.854
1230	Exp.	11.40	1406	3.41	921	0.864
	Biasi*	8.61	1408	3.69	958	0.828
	LUT*	10.63	1407	3.48	928	0.858
			0829-no017			
1316	Exp.	5.59	1630	5.34	1478	0.667
	Biasi*	9.64	1630	5.13	1434	0.692
1293	Exp.	10.96	1627	5.13	1415	0.685
			0904-no016			
1316	Exp.	1.14	1804	3.82	1543	0.642
1293	Exp.	2.75	1799	3.64	1509	0.644
	LUT*	3.16	1798	3.61	1503	0.647
1276	Exp.	4.61	1797	3.51	1485	0.649
	Biasi*	2.29	1799	3.69	1515	0.632
	LUT*	4.75	1797	3.50	1483	0.650
1230	Exp.	10.59	1796	3.23	1419	0.663
	Biasi*	8.95	1796	3.29	1434	0.654
	LUT*	10.35	1796	3.24	1422	0.661
			0904-no026			
1316	Exp.	2.76	1835	2.88	1520	0.631
	LUT*	6.25	1833	2.77	1493	0.646
1293	Exp.	6.37	1833	2.77	1492	0.630
	Biasi*	8.47	1833	2.72	1476	0.639
1276	Exp.	7.29	1833	2.75	1484	0.627

Table C.3: Transient local conditions for PDO data (2).

Run Identifier

L_h (mm)	Type	Dryout Time (s)	Heat Flux (kW m^{-2})	Pressure (MPa)	Mass Flux (kg m^{-2} s^{-1})	Quality
			0906-no019			
1316	Exp.	0.10	2068	4.03	1992	0.551
1293	Exp.	4.51	2064	3.67	1978	0.547
	LUT*	3.67	2064	3.72	2003	0.537
1276	Exp.	4.86	2064	3.65	1967	0.543
	Biasi*	5.45	2064	3.62	1949	0.550
	LUT*	4.78	2064	3.66	1969	0.542
			0906-no031			
1316	Exp.	0.67	2130	2.98	2045	0.521
	Biasi*	3.98	2125	2.80	1991	0.542
	LUT*	2.27	2125	2.88	2029	0.527
1293	Exp.	3.32	2125	2.84	2006	0.522
	Biasi*	6.61	2125	2.73	1941	0.547
	LUT*	4.55	2125	2.79	1978	0.533
1276	Exp.	5.20	2125	2.78	1966	0.530
	Biasi*	8.03	2126	2.70	1915	0.550
	LUT*	6.38	2125	2.74	1945	0.538
			0909-no016			
1316	Exp.	0.17	1480	2.03	1008	0.749
	LUT*	6.45	1477	1.87	994	0.761
1293	Exp.	4.97	1478	1.90	1003	0.736
	Biasi*	0.77	1480	2.01	1007	0.732
1276	Exp.	6.55	1476	1.88	994	0.734
	Biasi*	3.83	1477	1.93	1003	0.726
			0909-no037			
1316	Exp.	0.11	1851	2.06	1500	0.604
1293	Exp.	3.57	1848	1.95	1492	0.594
	Biasi*	5.33	1848	1.92	1499	0.591
1276	Exp.	3.52	1848	1.96	1492	0.586
	Biasi*	6.31	1847	1.90	1478	0.594
	LUT*	0.08	1852	2.07	1499	0.581

Table C.4: Transient local conditions for PDO data (3).

Run Identifier

L_h (mm)	Type	Dryout Time (s)	Heat Flux (kW m^{-2})	Pressure (MPa)	Mass Flux (kg m^{-2} s^{-1})	Quality
0910-no013
1316	Exp.	0.81	1459	3.86	1015	0.827
1293	Exp.	6.33	1461	3.48	982	0.838
	LUT*	6.32	1461	3.48	983	0.837
1276	Exp.	6.24	1463	3.49	983	0.827
	LUT*	9.13	1463	3.35	972	0.838
0910-no028
1316	Exp.	0.01	1498	3.03	998	0.816
1293	Exp.	4.80	1496	2.75	1003	0.796
	LUT*	4.37	1496	2.77	1005	0.794
1276	Exp.	5.98	1496	2.72	999	0.790
	LUT*	7.40	1496	2.67	995	0.794
0911-no011
1316	Exp.	0.07	1808	4.01	1511	0.657
1293	Exp.	5.26	1803	3.59	1494	0.654
	LUT*	3.94	1804	3.67	1506	0.647
1276	Exp.	6.23	1803	3.55	1485	0.651
	Biasi*	2.18	1805	3.79	1521	0.630
	LUT*	5.92	1803	3.56	1488	0.649
0913-no012
1316	Exp.	0.11	1809	4.00	1504	0.663
1293	Exp.	0.66	1805	3.87	1519	0.639
1276	Exp.	2.32	1804	3.58	1504	0.643
	Biasi*	0.05	1804	4.03	1494	0.641
	LUT*	2.59	1804	3.54	1496	0.647
1230	Exp.	5.26	1802	3.23	1432	0.659
	Biasi*	4.54	1802	3.30	1445	0.651
	LUT*	5.25	1802	3.24	1432	0.659

Table C.5: Transient local conditions for PDO data (4).

Run Identifier

L_h (mm)	Type	Dryout Time (s)	Heat Flux (kW m^{-2})	Pressure (MPa)	Mass Flux (kg m^{-2} s^{-1})	Quality
			0917-no011			
1316	Exp.	0.17	1460	3.97	1023	0.818
	LUT*	4.75	1449	3.21	1023	0.818
1293	Exp.	0.73	1459	3.83	1034	0.786
	Biasi*	3.61	1457	3.40	1023	0.798
	LUT*	6.09	1460	2.98	1014	0.810
1276	Exp.	4.23	1457	3.30	1022	0.789
	Biasi*	4.88	1458	3.19	1022	0.792
	LUT*	6.50	1459	2.91	1011	0.804
1230	Exp.	7.57	1457	2.76	1001	0.785
	Biasi*	7.20	1459	2.81	1006	0.781
			0917-no020			
1316	Exp.	0.10	1812	4.00	1545	0.642
1293	Exp.	1.66	1808	3.62	1530	0.638
	LUT*	2.66	1806	3.45	1517	0.646
1276	Exp.	2.27	1807	3.52	1523	0.634
	Biasi*	2.09	1807	3.55	1525	0.633
	LUT*	3.29	1805	3.35	1504	0.645
1230	Exp.	4.46	1806	3.18	1481	0.636
	Biasi*	5.34	1808	3.03	1463	0.648
	LUT*	5.54	1809	3.00	1457	0.652
			0918-no015			
1316	Exp.	0.00	2301	4.05	2490	0.473
1293	Exp.	0.56	2311	3.93	2546	0.453
1276	Exp.	1.87	2308	3.69	2516	0.458
1230	Exp.	3.44	2307	3.49	2396	0.472
			1113-no019			
1316	Exp.	0.09	1829	6.01	2013	0.520
	Biasi*	7.38	1818	5.11	1882	0.571
			1113-no020			
1316	Exp.	5.02	1818	5.25	1922	0.554
	Biasi*	9.42	1819	5.06	1885	0.570
	LUT*	15.15	1821	4.80	1834	0.593
1293	Exp.	13.71	1818	4.86	1850	0.571
	Biasi*	15.39	1820	4.80	1827	0.581

Table C.6: Transient local conditions for PDO data (5).

Run Identifier

L_h (mm)	Type	Dryout Time (s)	Heat Flux (kW m^{-2})	Pressure (MPa)	Mass Flux (kg m^{-2} s^{-1})	Quality
			1113-no021			
	Exp.	5.10	1819	5.28	1927	0.553
1316	Biasi*	9.65	1819	5.07	1884	0.571
	LUT*	17.00	1818	4.77	1832	0.593
1293	Exp.	17.58	1816	4.77	1826	0.581
	Biasi*	18.04	1817	4.76	1824	0.582
1276	Exp.	18.16	1817	4.76	1823	0.576
			1114-no022			
1316	Exp.	0.15	1810	3.99	1526	0.652
	Exp.	0.61	1800	3.87	1528	0.631
1293	Biasi*	0.03	1797	4.03	1506	0.639
	LUT*	2.21	1798	3.63	1503	0.647
	Exp.	0.58	1800	3.88	1527	0.624
1276	Biasi*	1.70	1798	3.70	1516	0.632
	LUT*	2.95	1798	3.53	1486	0.649
	Exp.	5.75	1795	3.25	1416	0.664
1230	Biasi*	4.94	1797	3.32	1437	0.653
	LUT*	5.57	1795	3.26	1420	0.662
			1115-no031			
	Exp.	0.64	2125	2.02	2021	0.493
1316	Biasi*	1.32	2123	1.96	1984	0.506
	LUT*	0.11	2128	2.08	2022	0.491
	Exp.	1.68	2123	1.96	1963	0.500
1293	Biasi*	2.17	2123	1.93	1938	0.509
	LUT*	0.86	2125	2.01	2015	0.482
	Exp.	1.70	2123	1.97	1961	0.493
1276	Biasi*	2.75	2123	1.91	1917	0.510
	LUT*	1.23	2123	1.99	1989	0.483
	Exp.	2.69	2123	1.94	1920	0.488
1230	Biasi*	4.98	2124	1.85	1878	0.511
	LUT*	6.66	2129	1.80	1801	0.542
1113	Exp.	3.78	2124	1.96	1916	0.428

Table C.7: Transient local conditions for PDO data (6).

Run Identifier

L_h (mm)	Type	Dryout Time (s)	Heat Flux (kW m^{-2})	Pressure (MPa)	Mass Flux (kg m^{-2} s^{-1})	Quality
			0826-no008			
1316	Exp.	3.14	1755	3.62	1499	0.646
	Biasi*	2.15	1754	3.71	1508	0.640
	LUT*	3.86	1753	3.56	1490	0.650
1293	Exp.	5.62	1751	3.46	1473	0.644
	Biasi*	6.86	1751	3.41	1461	0.651
	LUT*	8.18	1750	3.35	1447	0.658
1276	Exp.	7.38	1751	3.38	1456	0.646
	Biasi*	9.13	1750	3.32	1437	0.656
	LUT*	10.46	1750	3.27	1426	0.663
			0827-no009			
1316	Exp.	7.16	1921	4.34	1941	0.556
	LUT*	6.29	1922	4.39	1947	0.554
1293	Exp.	10.60	1920	4.20	1898	0.559
	Biasi*	4.72	1922	4.50	1967	0.532
			0827-no023			
1316	Exp.	9.70	1978	5.05	2325	0.489
	LUT*	14.81	1976	4.83	2261	0.508
			0829-no011			
1316	Exp.	5.70	1381	4.25	989	0.842
	LUT*	7.50	1381	4.06	976	0.854
1293	Exp.	8.84	1385	3.94	967	0.844
	Biasi*	6.96	1386	4.12	980	0.831
	LUT*	12.12	1383	3.70	952	0.857
1276	Exp.	12.65	1383	3.66	947	0.853
	Biasi*	8.58	1386	3.97	968	0.832
	LUT*	13.27	1383	3.62	940	0.859
			0829-no018			
1316	Exp.	10.26	1605	4.89	1417	0.691
	Biasi*	13.76	1604	4.69	1394	0.705

Table C.8: MTD Transient local conditions (1).

<div align="center">Run Identifier</div>

L_h (mm)	Type	Dryout Time (s)	Heat Flux (kW m^{-2})	Pressure (MPa)	Mass Flux (kg m^{-2} s^{-1})	Quality
			0829-no019			
1316	Exp.	9.65	1607	4.81	1421	0.690
	Biasi*	11.70	1606	4.66	1397	0.704
1293	Exp.	14.81	1605	4.48	1365	0.706
	Biasi*	16.97	1605	4.38	1359	0.711
	LUT*	8.18	1607	4.94	1439	0.664
1276	Exp.	19.56	1599	4.38	1327	0.718
	Biasi*	19.72	1599	4.39	1326	0.719
			0904-no017			
1316	Exp.	4.43	1770	3.63	1496	0.655
1293	Exp.	9.54	1769	3.42	1464	0.657
	Biasi*	4.21	1770	3.65	1497	0.638
	LUT*	6.81	1769	3.53	1469	0.654
1276	Exp.	10.16	1768	3.41	1454	0.655
	Biasi*	6.86	1769	3.53	1468	0.646
	LUT*	10.49	1768	3.40	1449	0.657
			0904-no027			
1316	Exp.	5.00	1807	2.79	1504	0.628
	Biasi*	8.90	1806	2.69	1485	0.639
	LUT*	12.31	1804	2.63	1465	0.650
1293	Exp.	10.28	1805	2.67	1479	0.626
	Biasi*	14.06	1801	2.70	1432	0.649
	LUT*	14.61	1810	2.72	1417	0.661
1276	Exp.	14.11	1801	2.71	1430	0.642
	Biasi*	14.54	1810	2.72	1421	0.651
			0906-no020			
1316	Exp.	3.71	2035	3.72	1997	0.543
	LUT*	3.08	2032	3.76	2008	0.538
1293	Exp.	7.04	2030	3.56	1943	0.549
	Biasi*	8.62	2030	3.50	1918	0.559
	LUT*	7.03	2030	3.56	1943	0.549
1276	Exp.	8.92	2030	3.50	1913	0.554
	Biasi*	11.95	2030	3.40	1886	0.565
	LUT*	10.15	2030	3.45	1902	0.558

<div align="center">Table C.9: MTD Transient local conditions (2).</div>

L_h (mm)	Type	Dryout Time (s)	Heat Flux (kW m^{-2})	Pressure (MPa)	Mass Flux (kg m^{-2} s^{-1})	Quality
				Run Identifier		
			0906-no032			
1316	Exp.	3.69	2094	2.82	2000	0.529
	Biasi*	5.96	2093	2.74	1943	0.550
	LUT*	4.00	2094	2.81	1995	0.531
1293	Exp.	6.63	2092	2.74	1937	0.538
	Biasi*	9.91	2091	2.66	1894	0.554
	LUT*	7.70	2092	2.71	1917	0.545
1276	Exp.	7.51	2092	2.72	1923	0.536
	Biasi*	12.53	2091	2.62	1869	0.557
	LUT*	10.73	2091	2.65	1886	0.550
1230	Exp.	15.50	2091	2.60	1853	0.542
			0909-no017			
1316	Exp.	4.30	1454	1.91	999	0.742
	Biasi*	0.59	1457	2.00	1013	0.731
	LUT*	15.54	1452	1.76	971	0.769
1293	Exp.	9.58	1453	1.83	986	0.737
	Biasi*	5.25	1453	1.90	997	0.726
1276	Exp.	12.01	1451	1.81	979	0.733
	Biasi*	8.32	1452	1.85	989	0.724
			0909-no038			
1316	Exp.	3.83	1821	1.93	1498	0.595
	Biasi*	3.70	1821	1.93	1499	0.595
1293	Exp.	8.31	1820	1.87	1466	0.597
	Biasi*	7.63	1820	1.88	1471	0.595
	LUT*	1.50	1822	2.00	1514	0.571
1276	Exp.	8.70	1820	1.87	1463	0.591
	Biasi*	9.76	1820	1.85	1455	0.595
	LUT*	4.30	1821	1.94	1495	0.574

Table C.10: MTD Transient local conditions (3).

Run Identifier

L_h (mm)	Type	Dryout Time (s)	Heat Flux (kW m⁻²)	Pressure (MPa)	Mass Flux (kg m⁻² s⁻¹)	Quality
0910-no014						
1316	Exp.	4.30	1439	3.60	996	0.830
	LUT*	6.23	1438	3.49	989	0.837
1293	Exp.	8.28	1441	3.38	981	0.825
	Biasi*	4.59	1442	3.59	995	0.812
	LUT*	11.23	1440	3.26	964	0.842
1276	Exp.	8.70	1441	3.37	979	0.817
	Biasi*	7.06	1442	3.44	986	0.811
	LUT*	16.97	1440	3.09	957	0.840
0910-no029						
1316	Exp.	4.22	1472	2.76	1006	0.797
	LUT*	3.60	1473	2.78	1006	0.797
1293	Exp.	8.83	1474	2.61	990	0.794
	LUT*	9.04	1474	2.61	988	0.797
1276	Exp.	8.78	1474	2.62	991	0.784
	Biasi*	4.83	1475	2.74	995	0.780
	LUT*	12.48	1473	2.53	976	0.798
0911-no012						
1316	Exp.	4.60	1776	3.63	1496	0.657
1293	Exp.	9.62	1775	3.43	1459	0.662
	Biasi*	3.79	1777	3.69	1504	0.636
	LUT*	6.79	1779	3.54	1479	0.652
1276	Exp.	10.87	1775	3.39	1449	0.660
	Biasi*	6.77	1779	3.54	1479	0.643
	LUT*	10.06	1775	3.42	1456	0.656
0913-no013						
1316	Exp.	1.56	1773	3.63	1523	0.642
	LUT*	1.70	1773	3.60	1514	0.647
1293	Exp.	2.66	1769	3.43	1482	0.648
	Biasi*	2.32	1769	3.49	1490	0.643
	LUT*	2.91	1768	3.39	1475	0.652
1276	Exp.	2.96	1768	3.38	1473	0.645
	Biasi*	3.38	1765	3.32	1461	0.651
	LUT*	3.75	1765	3.27	1450	0.657

Table C.11: MTD Transient local conditions (4).

Run Identifier

L_h (mm)	Type	Dryout Time (s)	Heat Flux (kW m^{-2})	Pressure (MPa)	Mass Flux (kg m^{-2} s^{-1})	Quality
0913-no013					
1230	Exp.	4.98	1762	3.13	1416	0.651
1230	Biasi*	5.87	1760	3.02	1393	0.665
1230	LUT*	6.14	1759	2.99	1383	0.670
0917-no012					
1316	Exp.	3.40	1429	3.33	1048	0.784
1316	Biasi*	4.49	1430	3.10	1052	0.785
1316	LUT*	5.48	1431	2.87	1042	0.796
3 129	Exp.	4.68	1443	3.06	1051	0.768
3 129	Biasi*	5.37	1445	2.90	1043	0.777
3 129	LUT*	6.16	1446	2.71	1034	0.788
1276	Exp.	5.07	1443	2.97	1046	0.764
1276	Biasi*	5.83	1445	2.79	1038	0.774
1276	LUT*	6.62	1446	2.60	1028	0.785
1230	Exp.	6.72	1448	2.58	1028	0.759
1230	Biasi*	6.96	1448	2.52	1025	0.763
1230	LUT*	7.70	1451	2.32	1017	0.774
0917-no022					
1316	Exp.	1.72	1777	3.66	1530	0.640
1316	LUT*	2.35	1776	3.55	1518	0.647
1293	Exp.	3.69	1776	3.36	1494	0.645
1293	Biasi*	3.42	1776	3.40	1499	0.642
1293	LUT*	4.00	1776	3.32	1489	0.649
1276	Exp.	3.85	1776	3.34	1492	0.639
1276	Biasi*	4.64	1777	3.23	1479	0.648
1276	LUT*	4.94	1777	3.18	1474	0.651
1230	Exp.	6.16	1778	3.01	1448	0.644
1230	Biasi*	7.00	1778	2.88	1430	0.656
1230	LUT*	7.06	1778	2.87	1428	0.656
0918-no016					
1316	Exp.	1.40	2273	3.75	2541	0.460
1316	Biasi*	2.14	2271	3.62	2482	0.476
1316	LUT*	1.97	2271	3.65	2491	0.473

Table C.12: MTD Transient local conditions (5).

L_h (mm)	Type	Dryout Time (s)	Heat Flux (kW m^{-2})	Pressure (MPa)	Mass Flux (kg m^{-2} s^{-1})	Quality
				Run Identifier		
			0918-no016			
1293	Exp.	2.39	2271	3.60	2467	0.468
	Biasi*	3.47	2269	3.46	2399	0.487
	LUT*	3.01	2271	3.51	2430	0.479
1276	Exp.	2.78	2271	3.55	2444	0.468
	Biasi*	4.12	2270	3.39	2361	0.492
	LUT*	3.59	2269	3.45	2392	0.482
1230	Exp.	4.97	2268	3.34	2308	0.487
	Biasi*	6.12	2268	3.24	2245	0.506
	LUT*	5.28	2269	3.31	2290	0.493
			1113-no022			
1316	Exp.	16.75	1794	4.84	1837	0.581
	Biasi*	20.14	1789	4.76	1819	0.589
	LUT*	23.32	1790	4.65	1806	0.601
1293	Exp.	23.19	1790	4.67	1807	0.586
	Biasi*	24.67	1791	4.63	1801	0.592
	LUT*	27.73	1789	4.56	1783	0.605
1276	Exp.	23.86	1789	4.66	1802	0.582
	Biasi*	26.71	1792	4.58	1792	0.594
	LUT*	29.71	1789	4.51	1770	0.607
			1114-no023			
1316	Exp.	0.59	1770	3.88	1523	0.637
	Biasi*	0.02	1770	4.03	1503	0.646
	LUT*	1.97	1769	3.72	1506	0.648
1293	Exp.	4.67	1768	3.46	1474	0.652
	Biasi*	2.71	1770	3.64	1495	0.639
	LUT*	4.90	1768	3.44	1471	0.653
1276	Exp.	5.76	1767	3.38	1462	0.650
	Biasi*	5.62	1767	3.39	1463	0.649
	LUT*	7.07	1763	3.31	1445	0.658
1230	Exp.	15.36	1765	3.22	1381	0.670
	Biasi*	9.77	1762	3.30	1388	0.666
	LUT*	15.64	1765	3.21	1379	0.672

Table C.13: MTD Transient local conditions (6).

C.4   Pressure Drop Data

Pressure drop data is presented in this section. The data are plotted as measured pressure drop against total test section power. Figure C.26 shows the pressure drop for all tested pressures for a mass flux of 2000 kg m^{-2} s^{-1} with error bars. It is evident that the uncertainty in the pressure drop is small—typically on the order of 6 kPa—and it is not plotted in the remaining plots in this chapter. Uncertainty in the heat flux varies from ± 0.3–0.9 kW as power increases from 4 to 40 kW.

Figure C.27 depicts the effect of mass flux on pressure drop at 4 MPa for all tested mass fluxes. It is evident that, against test section power, the mass flux only weakly influences the pressure drop in the test section. The axial quality gradient in the test section is inversely proportional to mass flux. Therefore it should be noted that the test section exit quality for the highest tested power at 1000 kg m^{-2} s^{-1} is much higher than—nearly double—the exit quality at the highest power for 2500 kg m^{-2} s^{-1}.

Figures C.28–C.31 depict the effect of test section exit pressure on total pressure drop for each tested mass flux. In comparison with Figure C.27 it is evident that, as a function of test section power, the influence of boundary pressure on pressure drop is much larger than that of mass flux. The effect of boundary pressure on pressure drop was larger at lower boundary pressures.
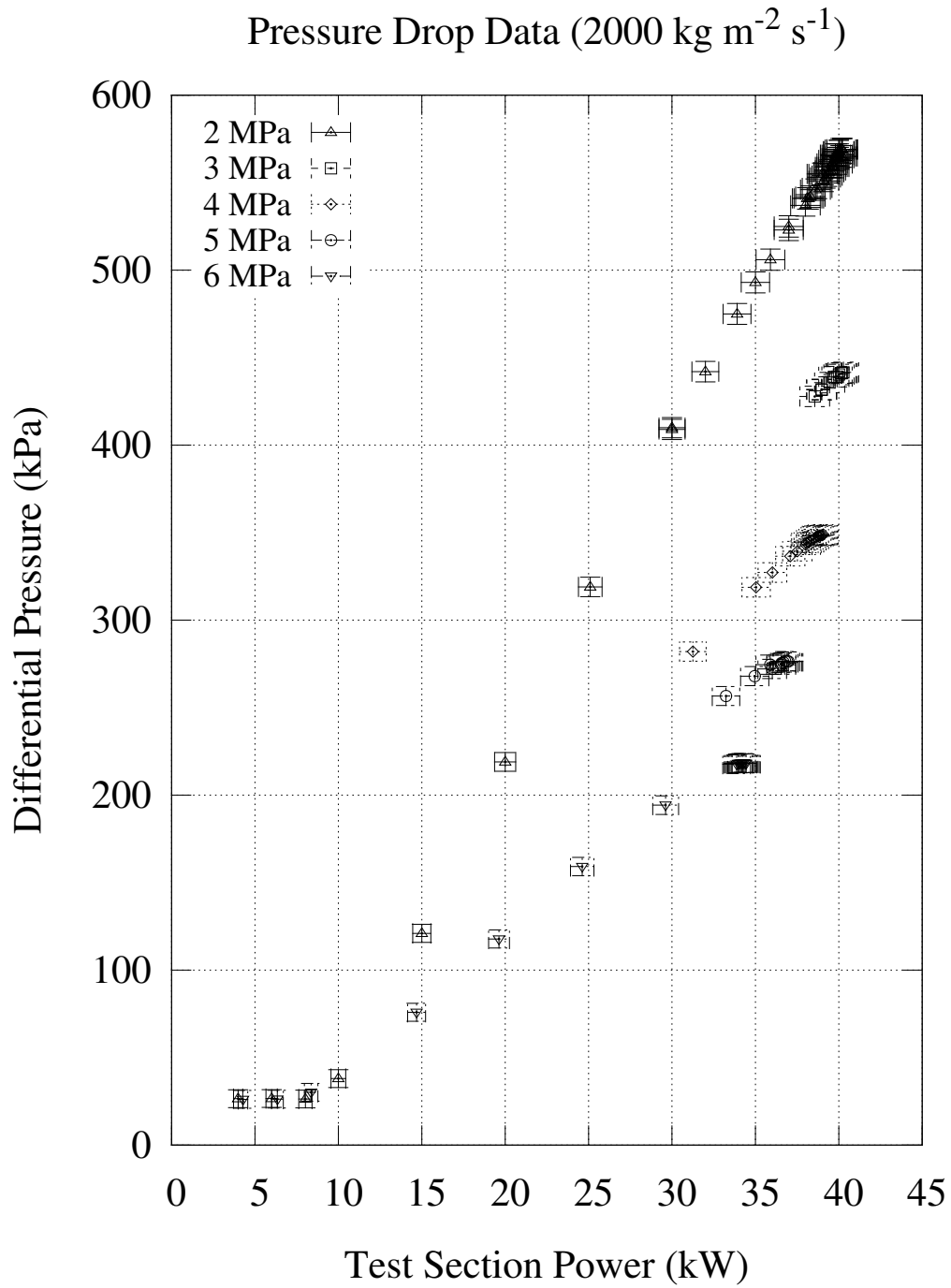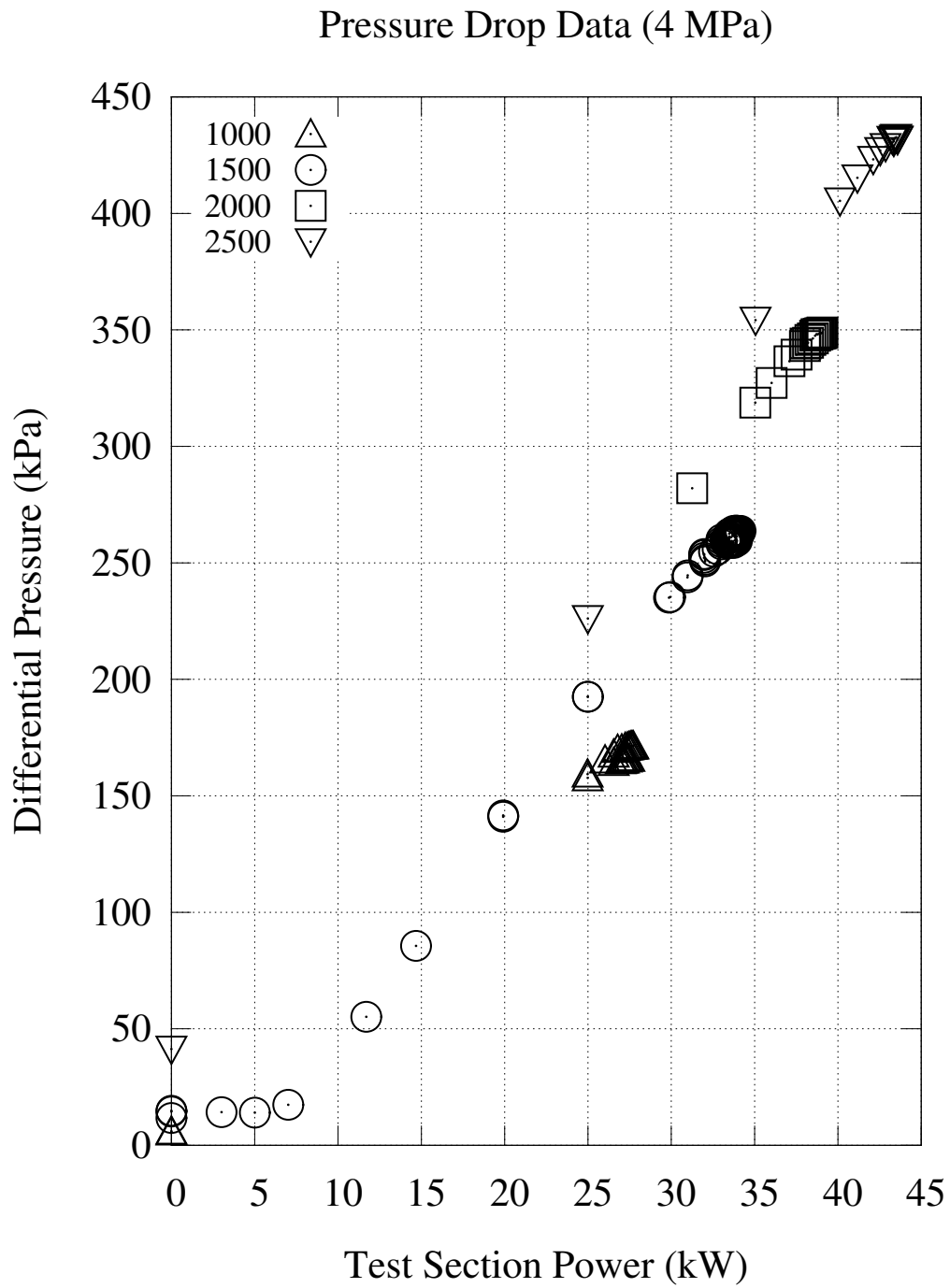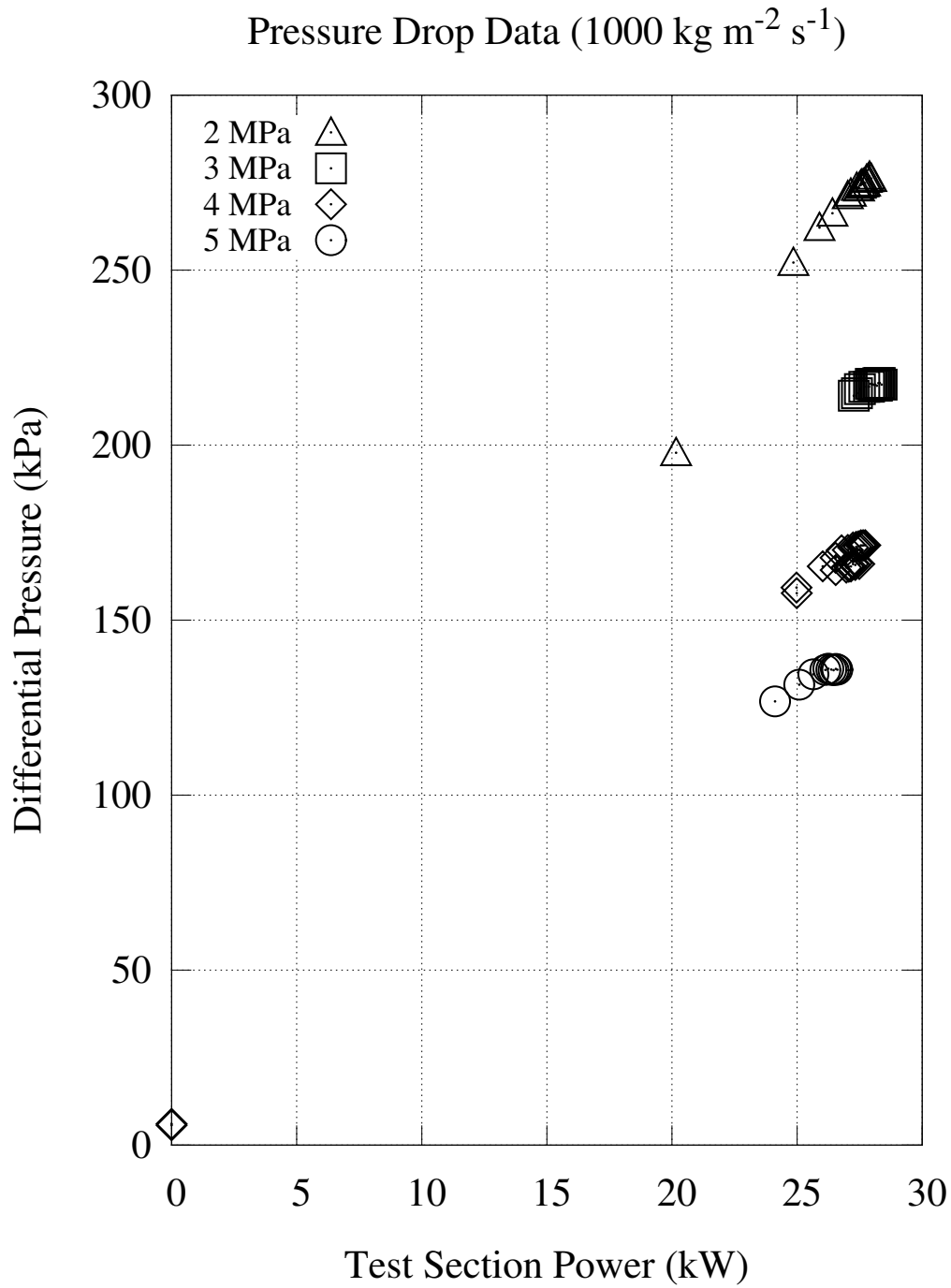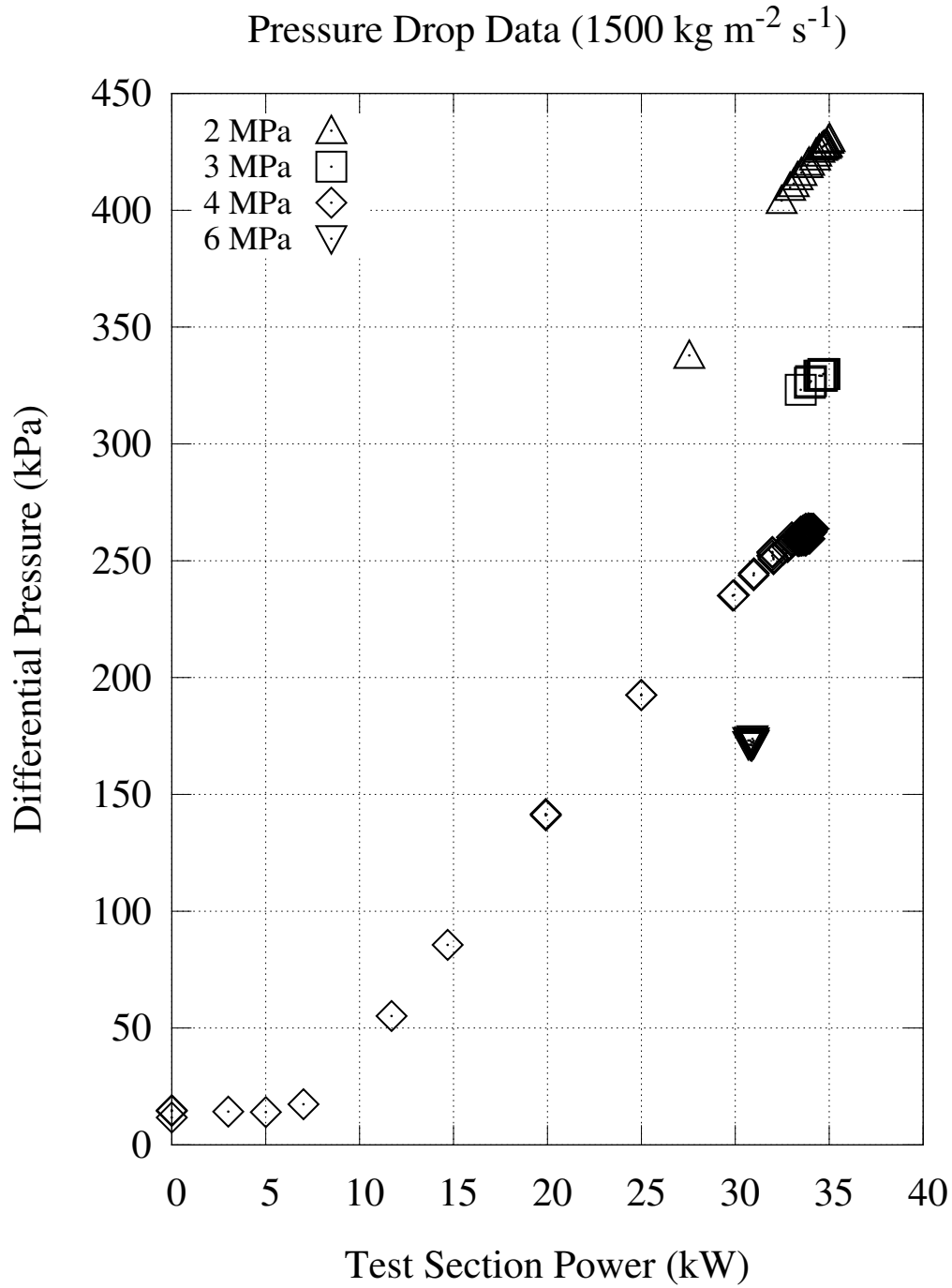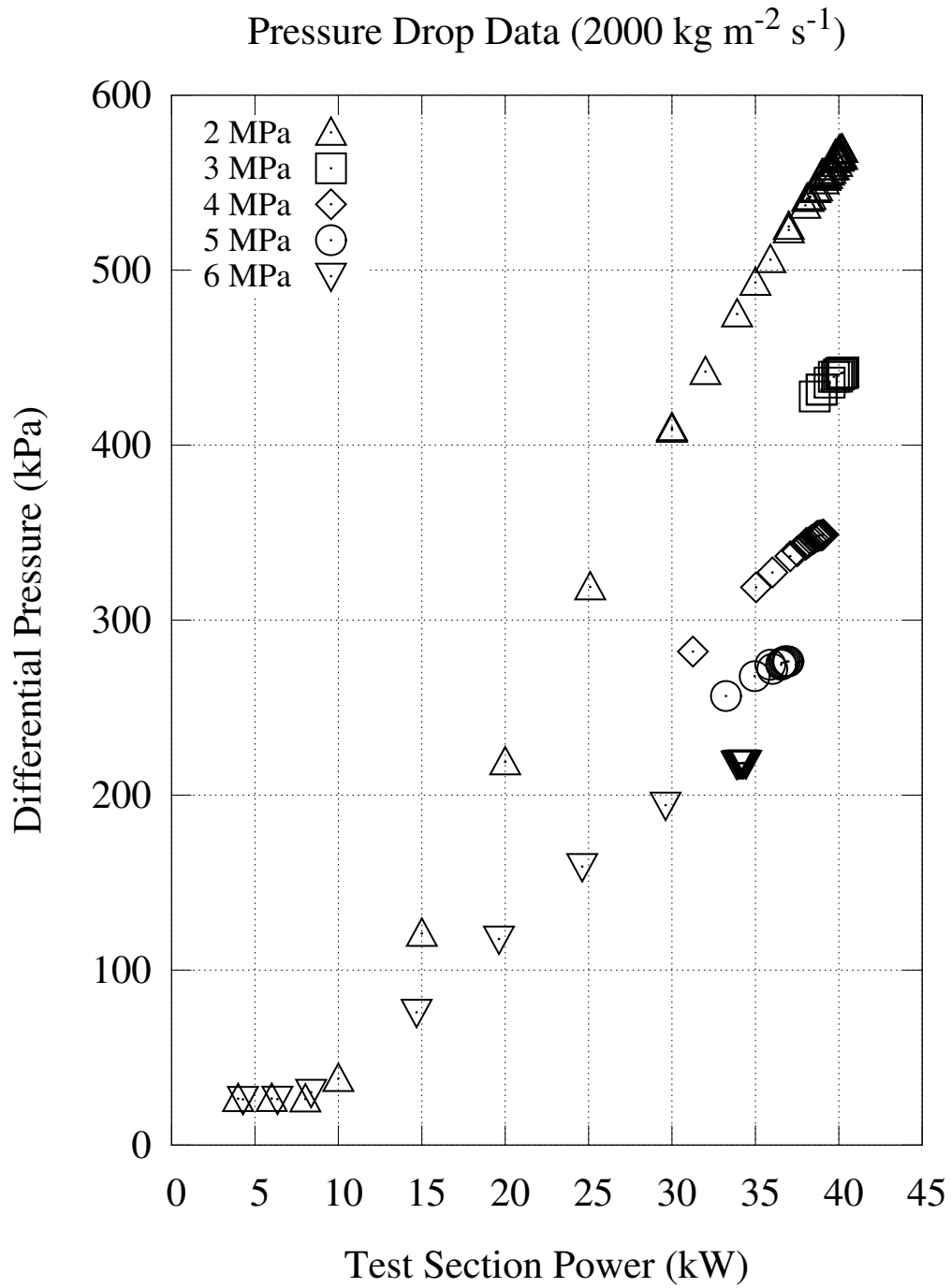
Figure C.26: Pressure drop data with error bars.

Pressure Drop Data (4 MPa)

Figure C.27: Mass flow effect on pressure drop at 4 MPa.

Figure C.28: Pressure drop for 1000 kg m^{-2} s^{-1}.

Pressure Drop Data (1500 kg m^{-2} s^{-1})

Figure C.29: Pressure drop for 1500 kg m^{-2} s^{-1}.

Figure C.30: Pressure drop for 2000 kg m^{-2} s^{-1}.
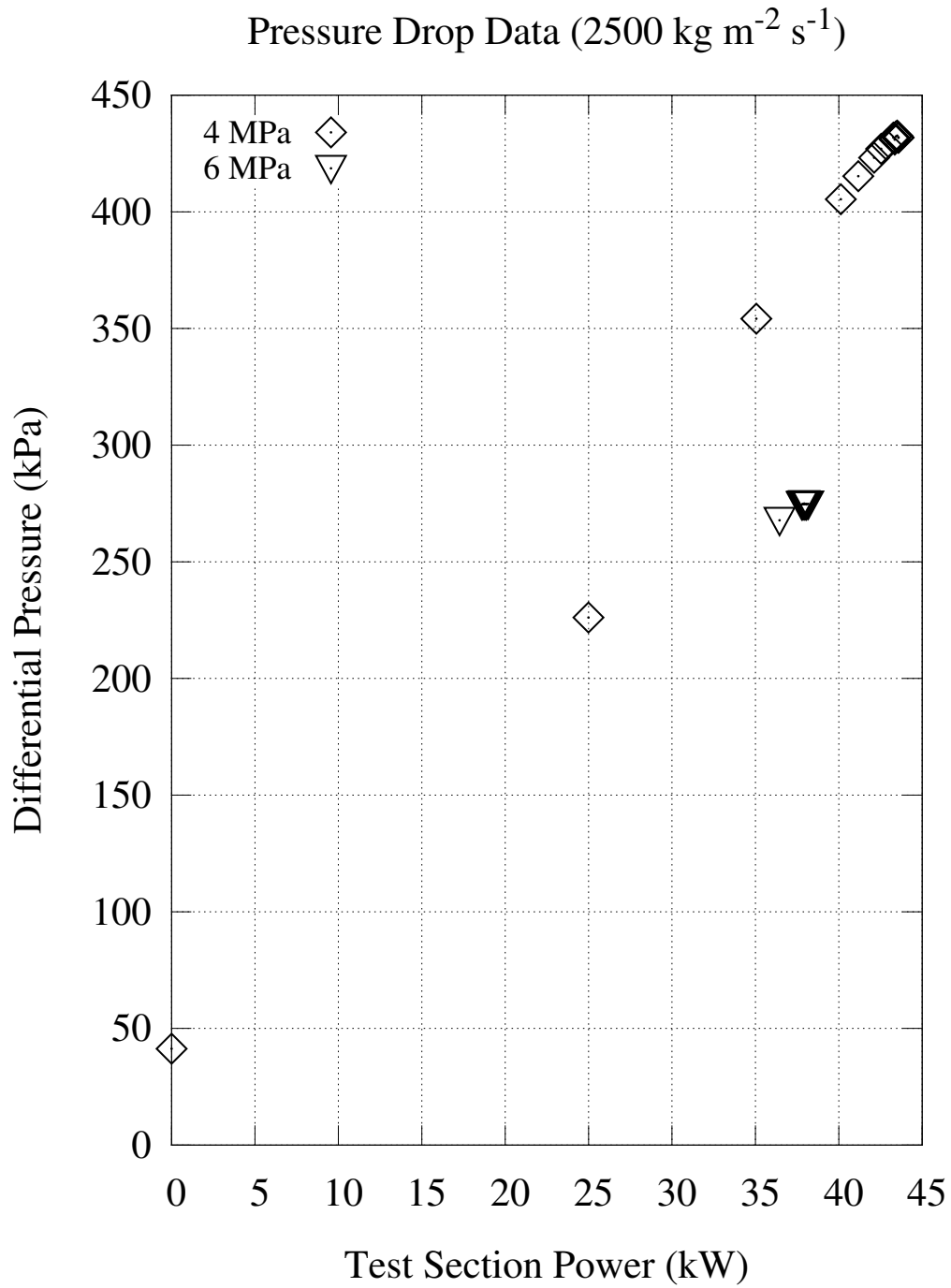
Figure C.31: Pressure drop for 2500 kg m^{-2} s^{-1}.

C.5   Heat Transfer

C.5.1   Heat Transfer Calculation

This section presents heat transfer coefficients obtained from the data. Inside wall temperatures were estimated based on the outside wall temperature measurements. Local fluid properties were extrapolated, based on enthalpy, from the inlet conditions, *i.e.* mass flow and temperature, and test section power. Bulk fluid temperatures for single phase flow were calculated using a heat balance. It was assumed that pressure drop was zero before the onset of annular flow. The bulk temperature in the single phase region was used as the boundary temperature, T_∞, to calculate the heat transfer coefficient by re-arranging Newton's law of cooling as shown in Equation C.3.

$$h = \frac{\ddot{q}}{T_w - T_\infty} \tag{C.3}$$

The pressure distribution inside the test section was interpolated from the outlet pressure and differential pressure measurements. The pressure profile in the annular flow region was assumed to have a parabolic profile—to vary continuously as $1-z^2$—throughout the two-phase region of the test section as shown in Equation C.4. The two-phase region included both the diabatic portion of the test section and the adiabatic region downstream of the test section before the flow area was increased at the outlet of the electrical isolation fitting. The test section pressure drop was assumed to be negligible between the area expansion and the outlet pressure measurement. This assumption was supported by the results of the steady RELAP5 simulations that were used to estimate the pressure distribution inside the test section for the steady-state CHF data.

$$p(z) = p_{in} - \left(\frac{z - z_{OAF}}{z_{EOL} - z_{OAF}} \right)^2 \cdot (p_{in} - p_{out}) \tag{C.4}$$

The quality at the onset of annular flow was estimated using the Levitan and Borevskiy correlation cited by Olekhnovitch *et al* and shown in Equation 2.7 [28]. The position of the onset of annular flow was estimated by assuming that the pres-

sure drop upstream of the onset of annular flow was zero and linearly interpolating the quality within the heated portion of the test section. This was also similar to the method used in [28]. The outlet quality was estimated using the measured outlet pressure and the outlet enthalpy based on the heat added in the test section. No iteration was performed after the parabolic pressure profile was obtained. Thermodynamic equlibrium was assumed in the two-phase region so that the saturation temperature at the local, interpolated, pressure was used as the boundary temperature value T_∞ in Equation C.3.

Interior wall temperatures were calculated from exterior wall temperature measurements using the 2-D steady conduction equation for a uniformly distributed source term in radial co-ordinates that was presented by Novog *et al* [127]. Thermal conductivity data for Inconel 600 were taken from [116], converted to SI units and fitted to the quadratic function shown in Equation C.5. This function had an RMS error of less than 0.3% when compared with 17 evenly spaced data points from 255.4 to 1144.3 K. The calculated inside wall temperatures were used in Equation C.3 to calculate the final estimate of the local heat transfer coefficient for each thermocouple location.

$$k(T(K)) = 10.1 + 0.014 \cdot T(K) + 1.54 \times 10^{-6} \cdot T^2(K) \text{ W m}^{-1} \text{ K}^{-1} \qquad \text{(C.5)}$$

C.5.2   Heat Transfer Coefficient Data

Figure C.32 depicts the heat transfer coefficient plotted against the estimated local quality with error bars. Uncertainty in h was estimated by propagating uncertainties using Equation 3.2. The uncertainties are on the order of 10–30% for two-phase data and well over 100% for single phase data. Temperature measurement errors were compounded in the difference term of Equation C.3. It was assumed that the uncertainty in the saturation temperature was proportional to the outlet pressure measurement uncertainty. The sensitivity of the pressure distribution to the uncertainty in the position of the OAF and the accuracy of the parabolic pressure profile were not taken into consideration in the uncertainty calculation. The heat transfer data are included for reference and were not the primary objective of the present

work.

Some aging of the surface due to oxidation and/or drift in the thermocouple readings over time was evident. Figure C.33 shows the heat transfer results for the repeated steady state experiments at 4 MPa and 1500 kg m^{-2} s^{-1}. The earliest experiments, series '0826' and series '0904' show 25% higher heat transfer coefficients, h, than data collected later. This may be due to thermocouple drift or surface aging *i.e.* corrosion.

The change in observed heat transfer coefficients over time had no significant effect on the observed CHF. The heat transfer data from Figure C.33 is re-plotted against surface heat flux instead of local quality with error bars in Figure C.34 . OID data points correspond to the sharp downturn in observed heat transfer coefficient. The qualitative behaviour of the h–$\ddot{q}_{CHF}$ curve is nearly identical for all data points and the heat flux at which the sharp downturn in h occurs changes, over time, by much less than the overall uncertainty in the surface heat flux alone. Overall the effect of aging on the heat transfer coefficient is on the order of the uncertainty in the HTC itself.

Surface aging or temperature drift affected thermocouples located further upstream from the test section exit to an approximately equal degree. Data from the thermocouple located at a heated length of 1113 mm are shown in Figure C.35 for the same series of experiments and axes as in Figure C.33. The difference between the heat transfer coefficients derived from the earliest experiment, '0826', and the later experiments is similar to the difference observed for the thermocouple nearest the test section exit—on the order of 20 compared to 25 kW m^{-2} $^{\circ}$C^{-1}.

Series '0917' are outliers; the difference in h corresponds to a difference in wall superheat of slightly less than 3°C from the other data collected after '0826'. There is no systematic variation in the boundary conditions for these experiments and this outlier behaviour was not observed in the HTC data from the thermocouple further downstream. One possible explanation for this anomalous behaviour is the heat transfer regime has begun to transition to the postulated droplet regime in both the '0826' and '0917' series. This is supported by the observation that, in both cases, the heat transfer coefficient appears to decrease with increasing local quality. Aside from this anomalous series the aging effect settled to a constant value after

the initial series of experiments.

The earliest experiment conducted for the data presented in this text was for the repeated boundary conditions of 4 MPa 1500 kg m^{-2} s^{-1}. Aside from this series the earliest data collected were for 5 MPa, 1000 and 2000 kg m^{-2} s^{-1}, and 6 MPa, 1500 and 2500 kg m^{-2} s^{-1}. These series may represent HTCs from a heater that is somewhat less aged than for the remaining data. *i.e.* the HTCs in these series may be biased to a slightly higher value than the remaining data. It is evident from Figure C.34 that this aging process did not affect the CHF within the bounds of experimental uncertainty in the present work.
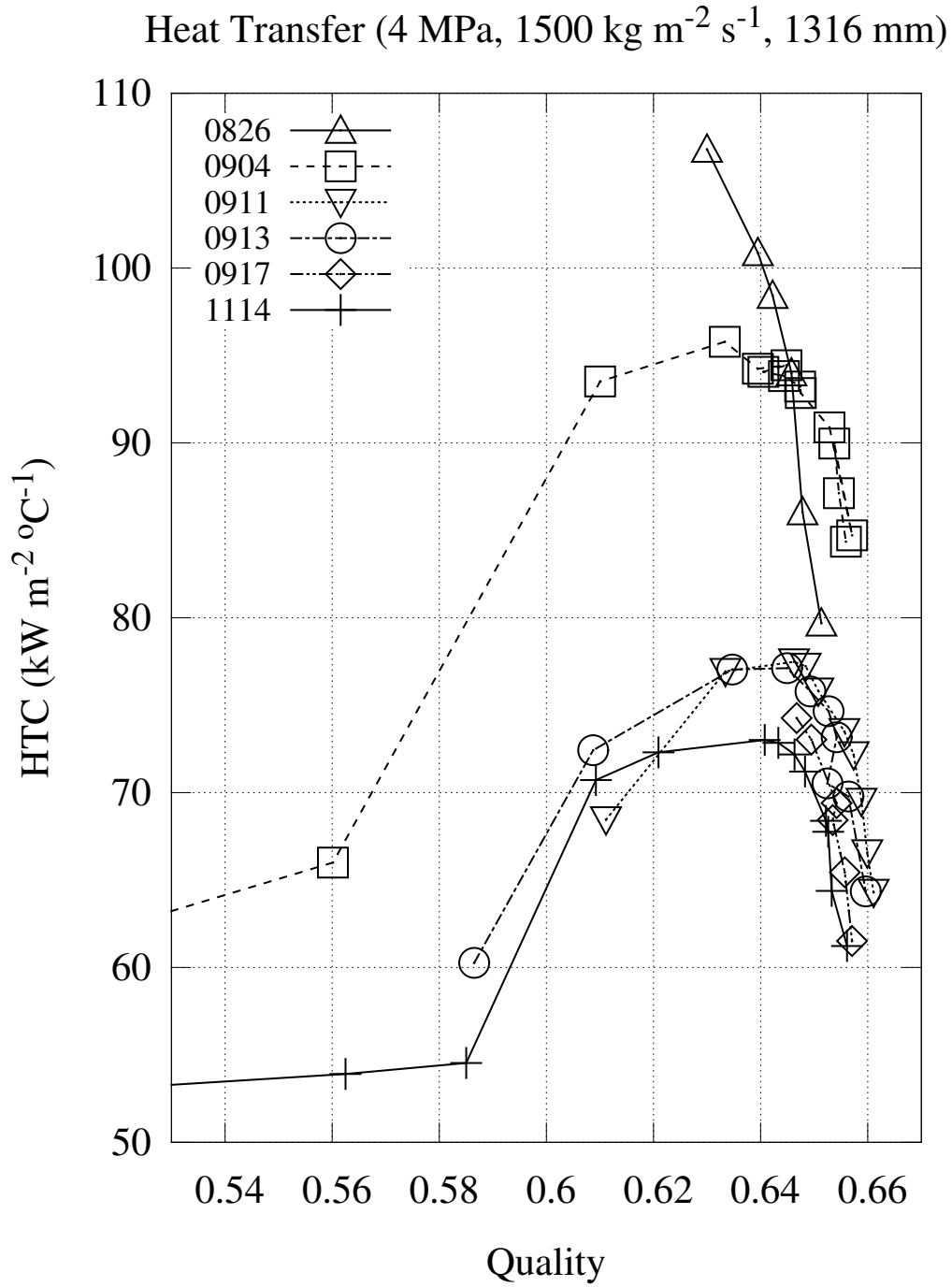
Wall temperatures were measured at several different test section locations. Results are shown in Figure C.36 for one test series at all test section locations. The thermocouples at 1113, 1230, 1276 and 1293 mm are self-consistent while the thermocouples at 955 and 1316 mm yield systematically higher and lower HTC values. For the purpose of depicting heat transfer data the results from the thermocouple at 1113 mm will be used as a representative value in subsequent figures.

Heat transfer coefficients for 4 MPa at all tested mass fluxes are plotted in Figure C.37. If the boiling curves for each mass flux are extrapolated to lower local qualities a systematic dependence on mass flux is evident. The effect is on the order of a 30% increase in HTC as the mass flux increases from 1500 to 2500 kg m^{-2} s^{-1} at constant quality. Several data points for the mass flux of 1500 kg m^{-2} s^{-1} show a higher heat transfer coefficient than the rest. These data correspond to the series '0826' and '0917' data depicted in Figure C.35 and were discussed above.
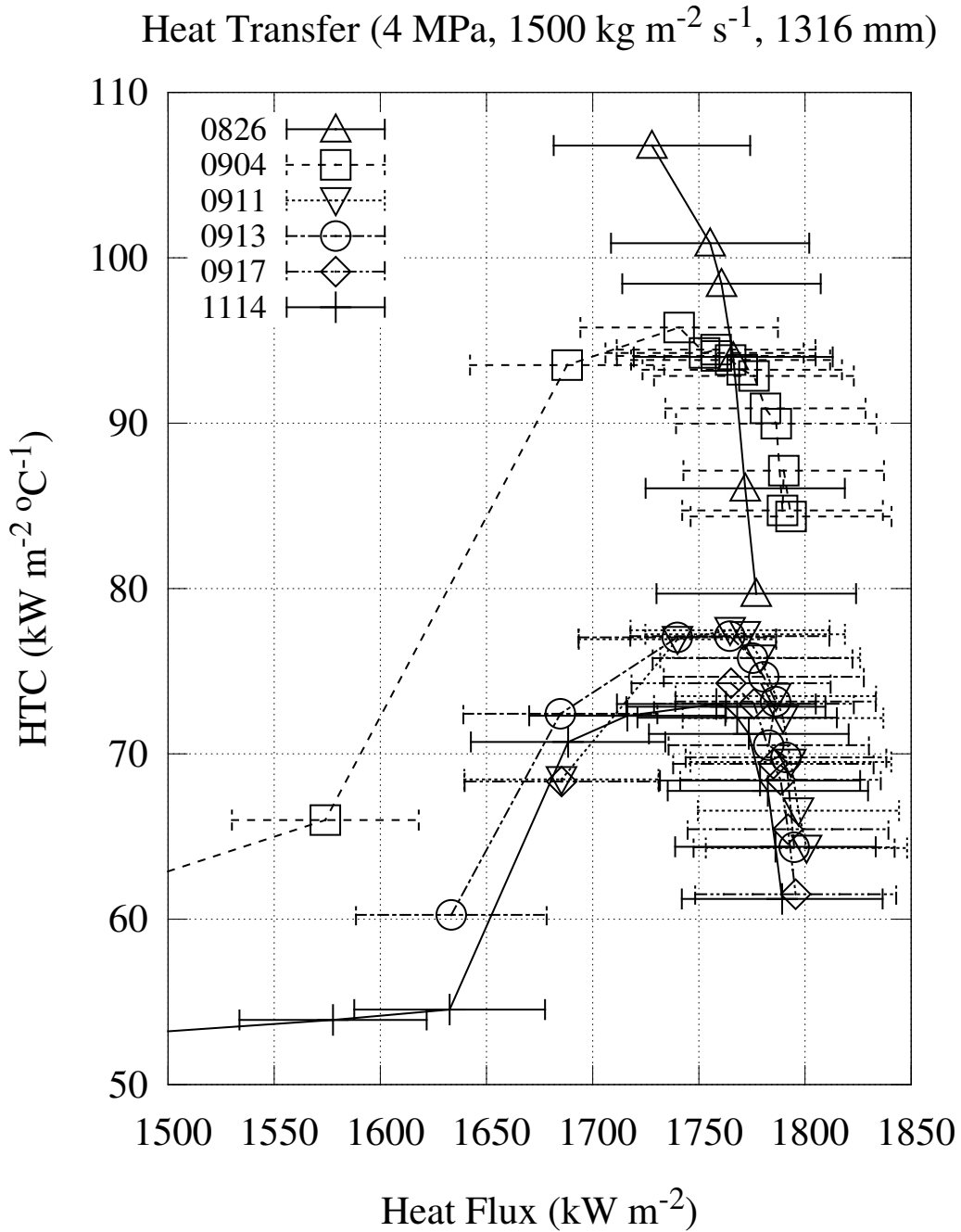
The remaining heat transfer data are plotted in Figures C.38–C.41. It is evident that the effect of pressure on the observed heat transfer coefficient is small. In all of these figures the variations in heat transfer with pressure at constant quality is on the order of 2–4 kW m^{-2} s^{-1} with the exception of the unaged data and the '0917' series for 4 MPa and 1500 kg m^{-2} s^{-1} discussed above. This variation is a fraction of the overall uncertainty in h for the present work.

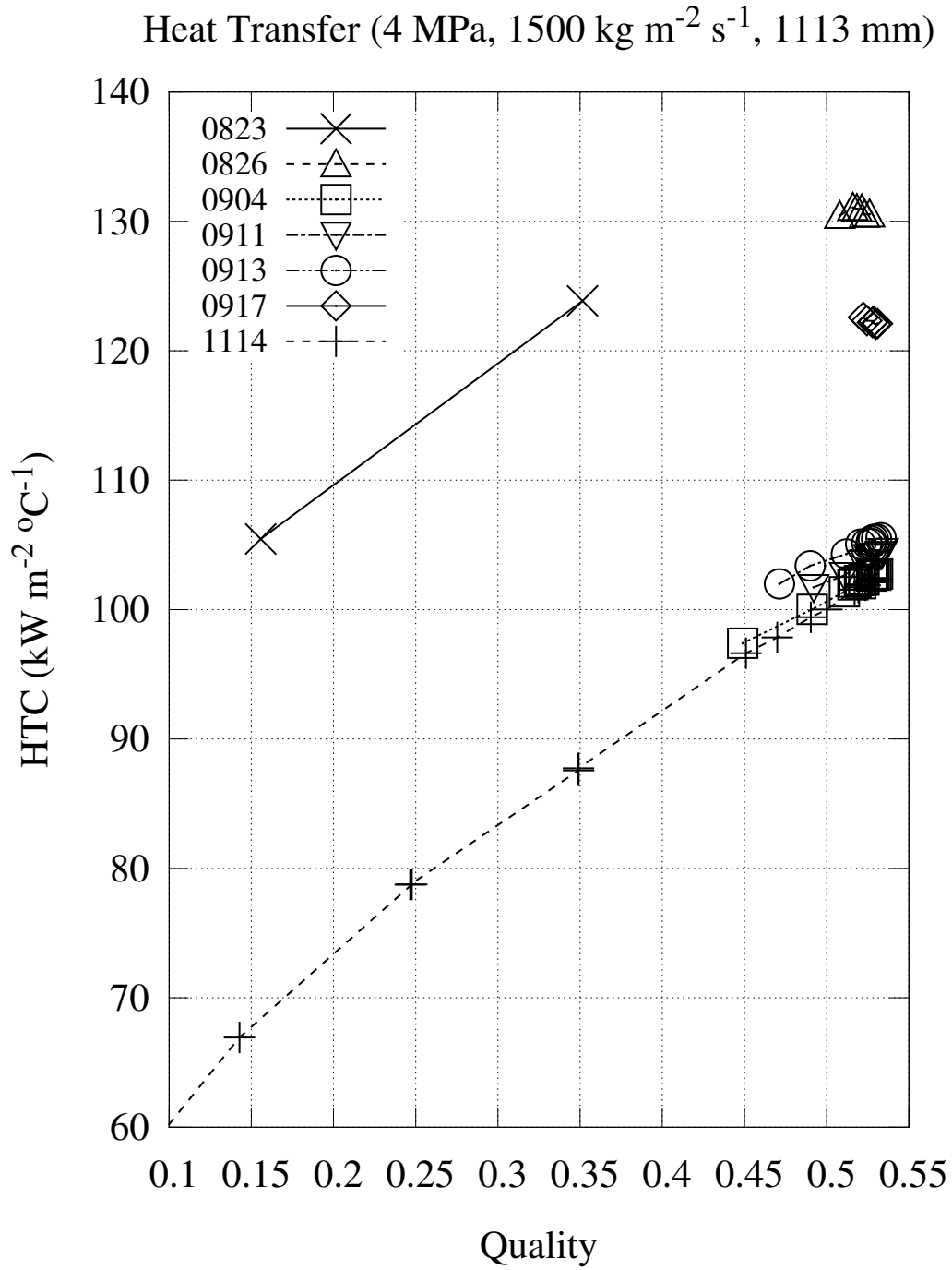## Heat Transfer (4 MPa 1500 kg m^{-2} s^{-1})
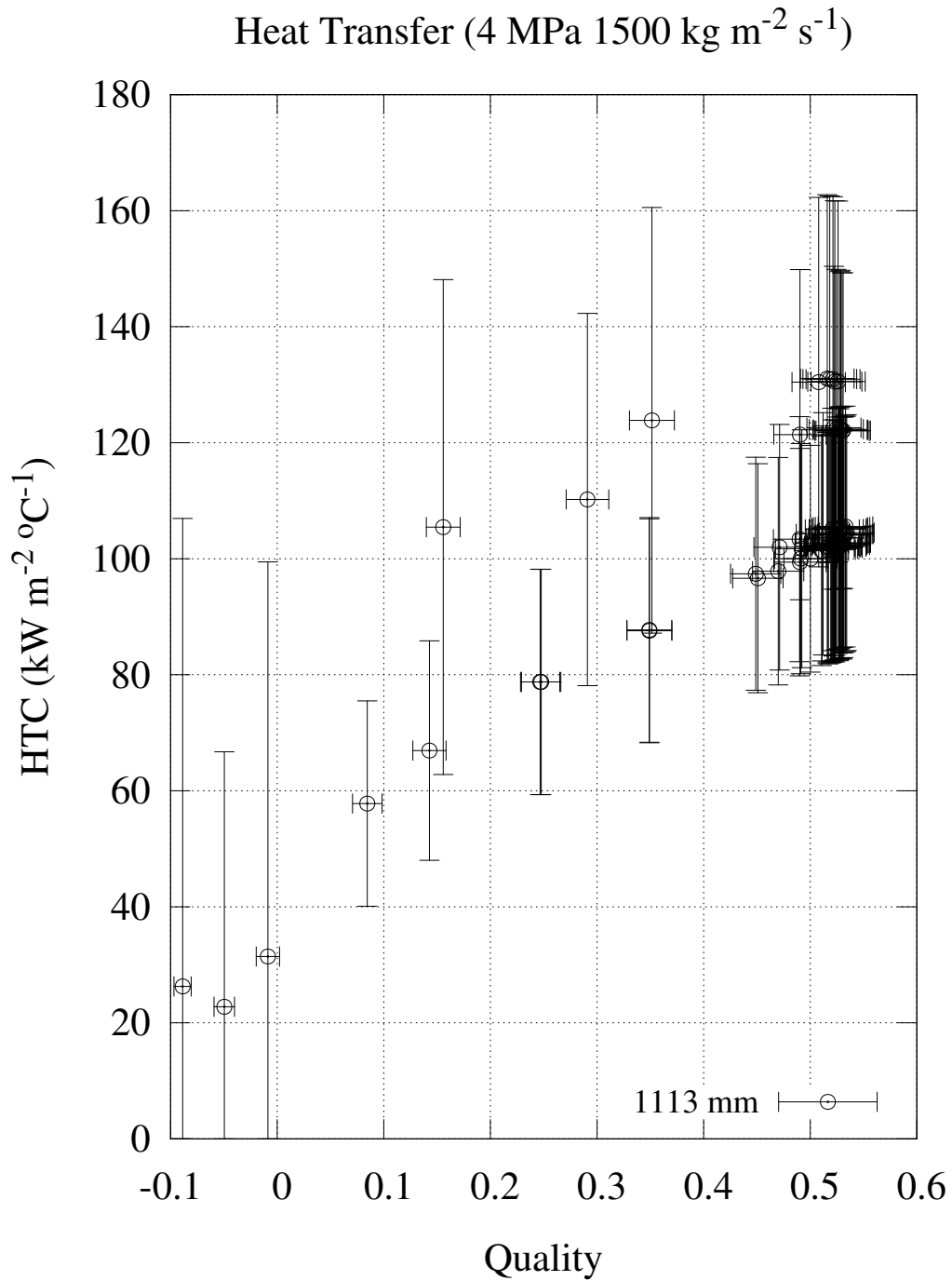
Figure C.32: Heat transfer data with error bars at 4 MPa and 1500 kg m^{-2} s^{-1}.

Figure C.33: Thermal drift or aging effect on HTC at 1316 mm *vs* Quality.

B.A. Statham
Ph. D. Thesis

Appendix C
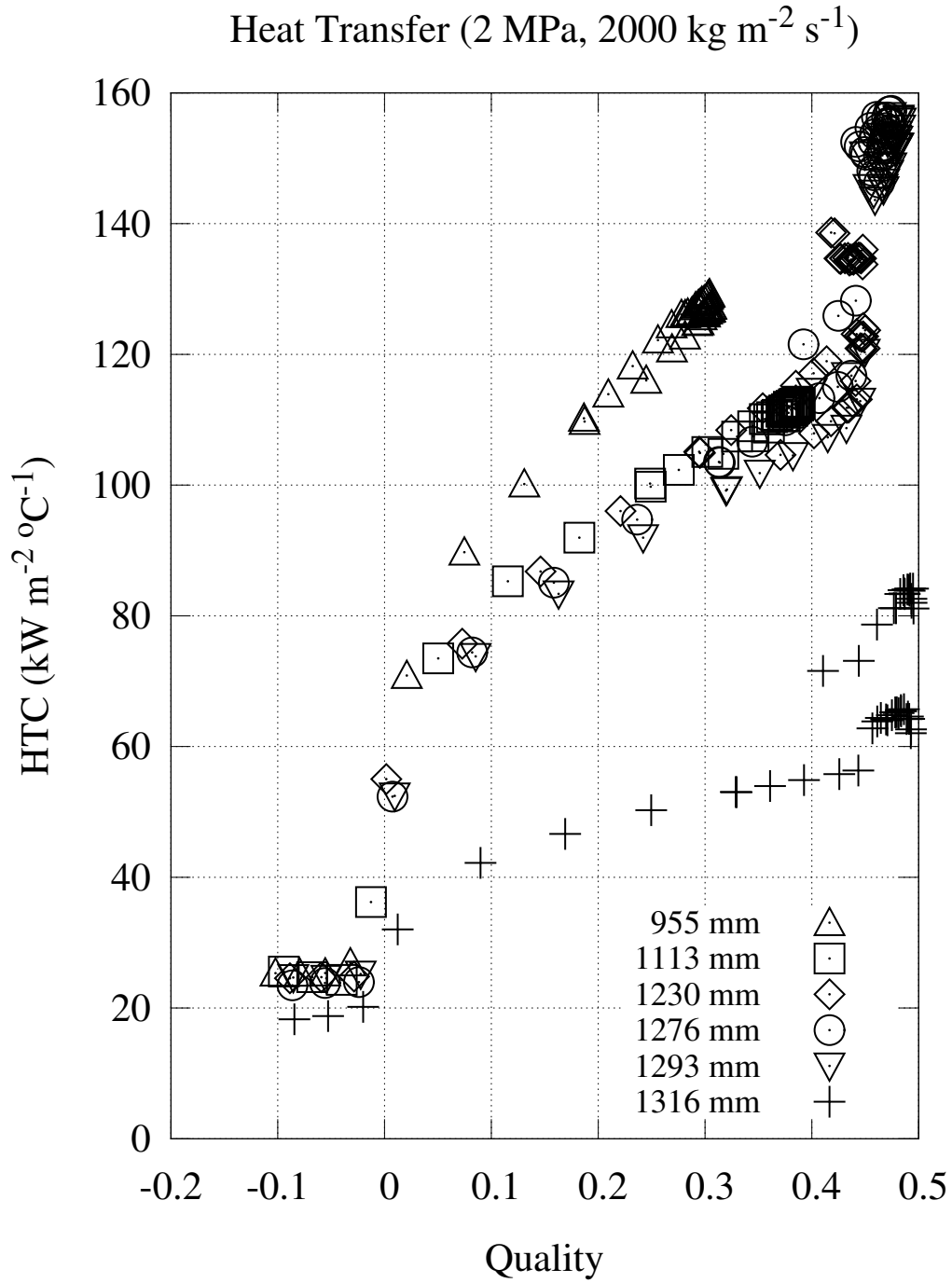Raw Data

McMaster University
Engineering Physics

Figure C.34: Thermal drift or aging effect on HTC at 1316 mm *vs* $\ddot{q}$.

Figure C.35: Thermal drift or aging effect on HTC at 1113 mm *vs* Quality.

Figure C.36: HTC at various test section locations for 2 MPa, 2000 kg m^{-2} s^{-1}.

B.A. Statham
Ph. D. Thesis

Appendix C
Raw Data

McMaster University
Engineering Physics

Heat Transfer (4 MPa 1113 mm)
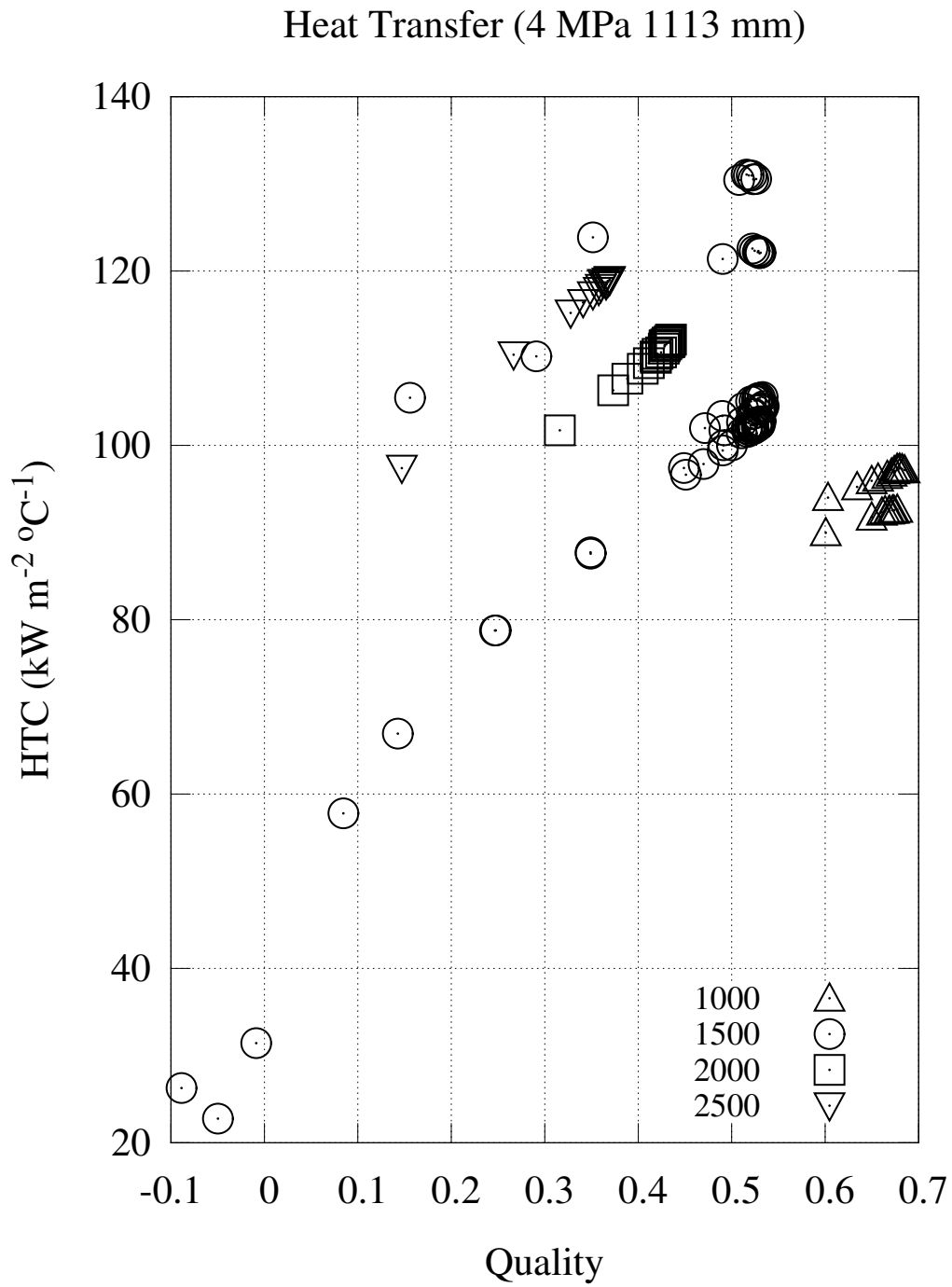
Figure C.37: Mass flux effect on heat transfer at 4 MPa.
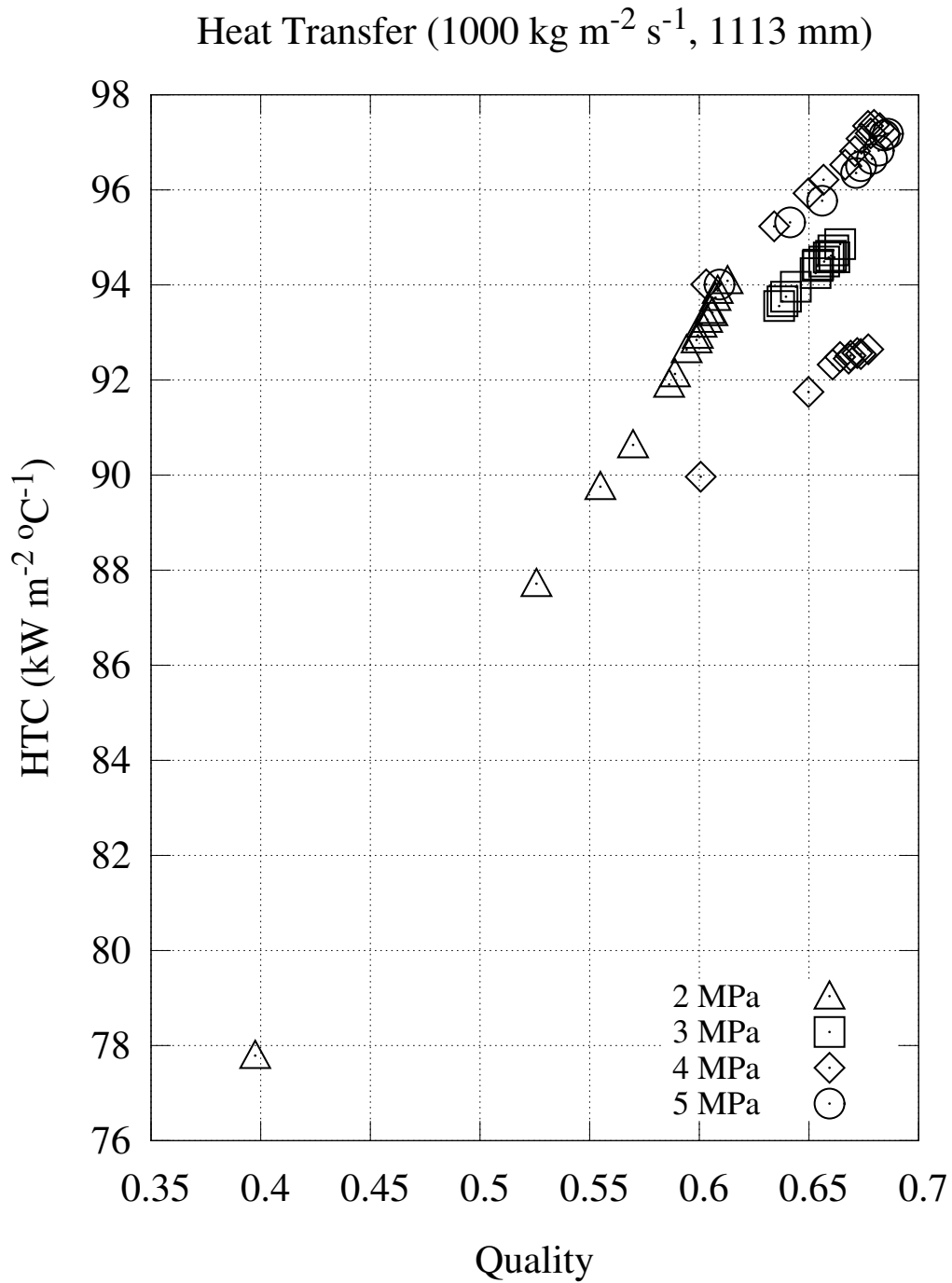
Figure C.38: Pressure effect on heat transfer at 1000 kg m^{-2} s^{-1}.

Figure C.39: Pressure effect on heat transfer at 1500 kg m^{-2} s^{-1}.

Figure C.40: Pressure effect on heat transfer at 2000 kg m^{-2} s^{-1}.

Heat Transfer (2500 kg m^{-2} s^{-1}, 1113 mm)

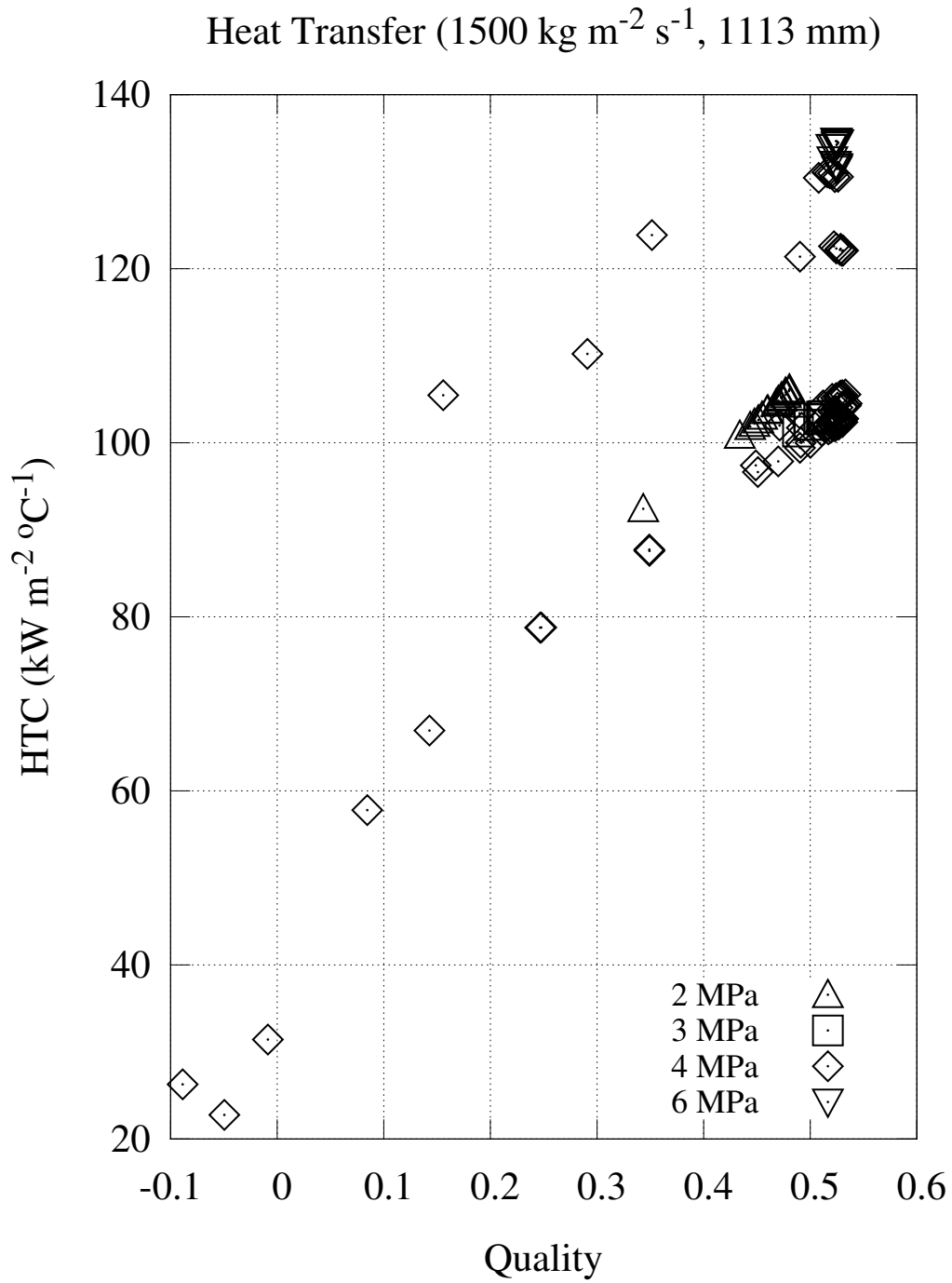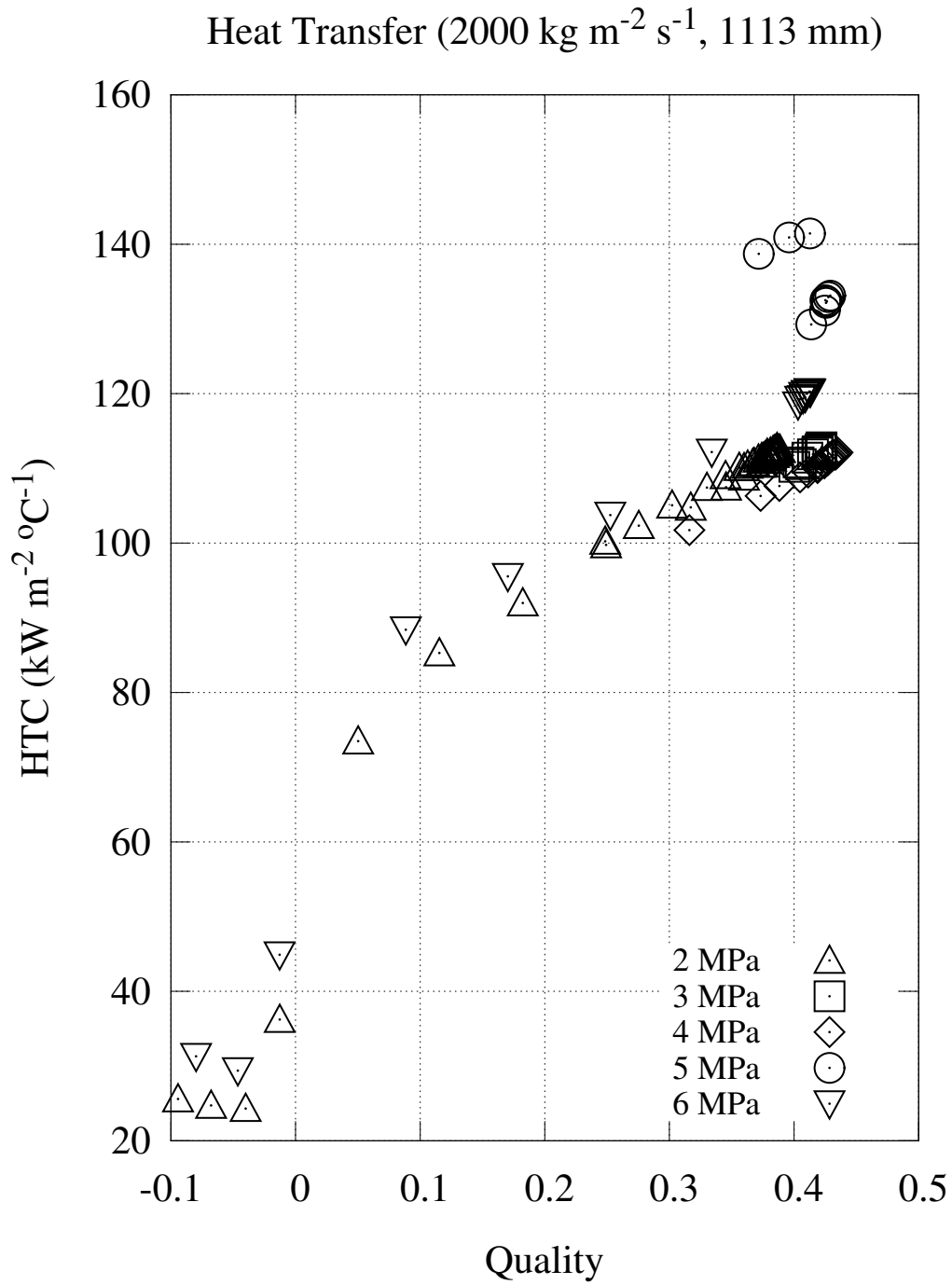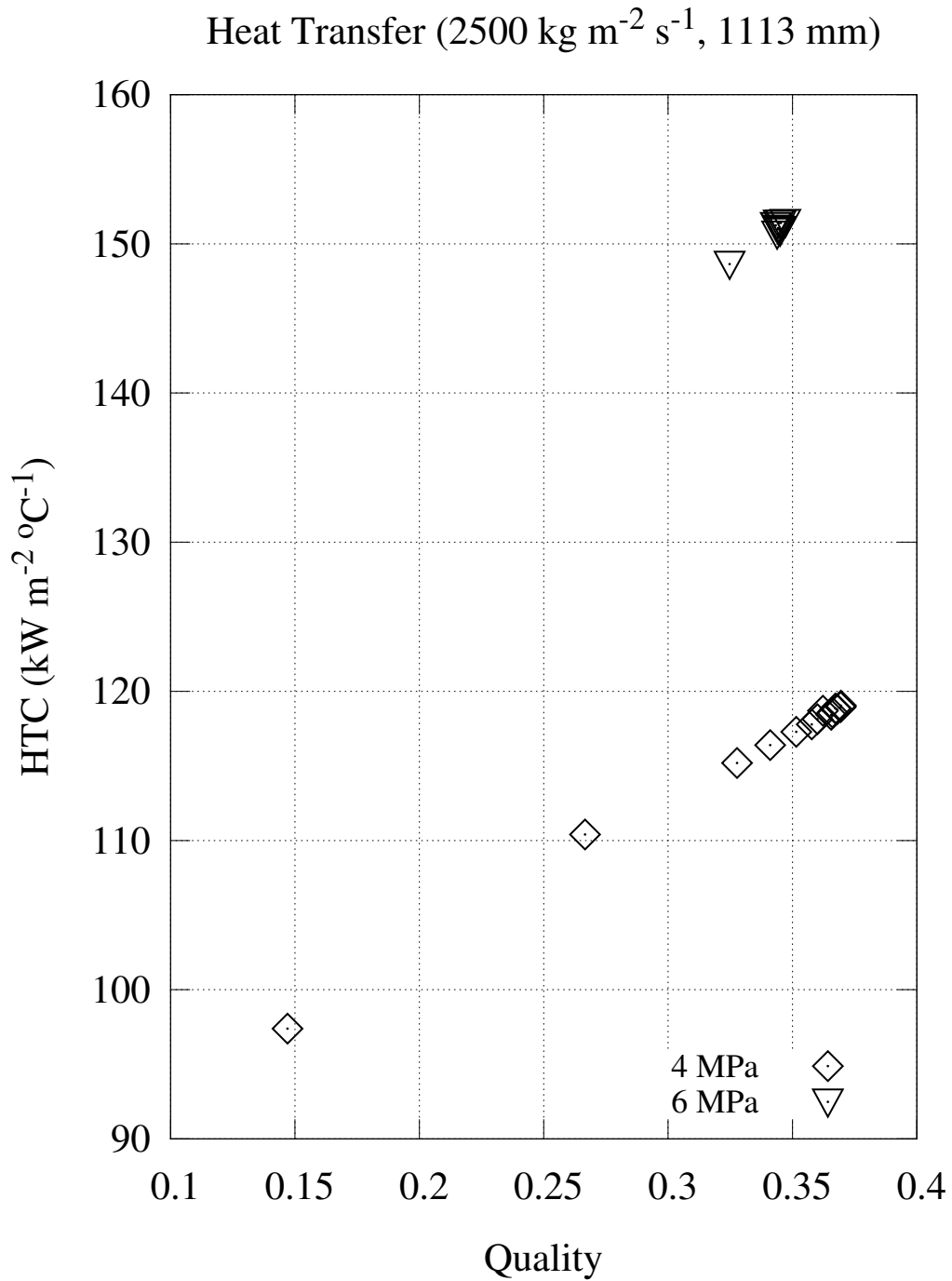**Figure C.41:** Pressure effect on heat transfer at 2500 kg m^{-2} s^{-1}.

Appendix D

Calibration Data

D.1   Power Measurement

Tables D.1 and D.2 contain manufacturer-supplied calibration data for the 100 V and 50 mV transmitters. The 100 V transmitter was used to measure the test section voltage directly. The mV transmitter measured the voltage drop across a calibrated shunt to indirectly measure the current supplied to the test section. The manufacturer specified tolerances are denoted as 'Tol.'

Calibrated Input (V)	Tol. (V)	Output (V)
0.000	±0.1	0.0
25.000	±0.1	12.5
50.000	±0.1	25.0
75.000	±0.1	37.5
100.000	±0.1	50.0

Table D.1: Transmitter calibration data for test section voltage measurement.

D.2   Pressure Transducers

The outlet and differential pressure transducers were calibrated by Cal-Matrix in Burlington, ON on 11 October 2013. Calibration data from their test standards is

Calibrated Input (mV)	Tol. (mV)	Output (mV)
0.000	±0.05	0.01
12.500	±0.05	12.49
25.000	±0.05	24.99
37.500	±0.05	37.49
50.000	±0.05	50.01

Table D.2: Transmitter calibration data for the test section current shunt.

shown in Tables D.3 and D.4 respectively. Both transducers were within manufacturer specified limits and were returned without any modifications.

Calibrated Pressure (psia)	Tol. (psia)	Output (psia)
0.0	±3	0
400.0	±3	401
800.0	±3	801
1200.0	±3	1200
1500.0	±3	1500
2000.0	±3	2002

Table D.3: Outlet pressure transducer calibration data.

D.3   Thermocouple Calibration Data

With one exception all thermocouples were calibrated in an insulated isothermal mineral oil bath apparatus called 'Excalibrator'. This calibration bath was borrowed from the McMaster Department of Mechanical Engineering. The oil bath is thoroughly insulated and a range of calibration temperatures may be obtained by heating the oil using a central and a guard heater. The guard heater ensures that the temperature distribution within the oil is uniform. Both heaters are temperature controlled using a built-in PID algorithm. The calibrations were performed against a reference standard RTD that was also generously loaned from the Department of

Calibrated Pressure (bar)	Tol. (bar)	Output (bar)
0.00	±0.012	0.006
1.60	±0.012	1.606
3.20	±0.012	3.206
4.80	±0.012	4.804
6.40	±0.012	6.403
8.00	±0.012	8.004

Table D.4: Differential pressure calibration data.

Mechanical Engineering. Thermocouple readings were made during the calibration process by the same DAQ and VI system used for the experiments described in the body of the present work. Therefore the tolerance limits are given as one standard deviation of the total manufacturers' specified uncertainties for the thermocouple readings.

Calibration data for the test section inlet temperature thermocouple are given in Table D.5. Calibration data for each wall temperature thermocouple was obtained before silver soldering to the outside of the test section wall. Wall temperature thermocouple calibration data are given in Tables D.7–D.8. The highest temperature calibration point for the thermocouple that was used at the heated length of 1293 mm was out of specification. Its performance at all other calibration points, and in the heat transfer data presented in Figure C.36, is nearly identical to the other thermocouples. It is possible that it may have become partially withdrawn from the mineral oil bath near the end of the calibration procedure but this cannot be confirmed.

The exception to the use of Excalibrator for thermocouple calibrations was the outlet temperature measurement. Its Swagelok ferrule prevented it from being fully inserted into the Excalibrator guide tubes for immersion in the mineral oil calibration bath. Saturation temperatures obtained using the IAPWS-97 formulation for water properties based on the measured outlet pressure were used as a proxy for calibration temperatures. The results are shown in Table D.6.

The outlet temperature measurement location is 70mm downstream of the outlet

pressure measurement port. The test secction is well insulated in this region but non-coincidence of these measurement locations contributed to a slight bias in this calibration technique. For the conditions with the highest experimental pressure drop—post-dryout power at 2MPa, 2000 kg m^{-2} s^{-1}—the pressure gradient *upstream* of the outlet pressure tap was approximately 50 kPa m^{-1}. This estimate was based on the output of the RELAP5 model for run 1113-no031 during the steady period before the beginning of the transient. Extrapolating this pressure gradient 70 mm downstream of the pressure tap to the temperature measurement location gives a 3.5 kPa difference in local pressures. The corresponding difference in saturation temperature at 2 MPa is less than 0.1°C. The magnitude of this slight bias varies with the slope of the saturation curve and the two-phase multiplier for pressure drop. Both of these quantities vary inversely with pressure and therefore this estimate of the bias represents a maximum value.

Calibration curves were generated for the inlet and outlet temperature measurements and used in the data analysis. The equation of the inlet temperature calibration curve is given in Equation D.1 and similarly for the outlet temperature in Equation D.2.

$$T_{cal} = -0.00003 \cdot T_{raw}^2 + 1.00631 \cdot T_{raw} - 1.06 \qquad \text{(D.1)}$$

$$T_{cal} = 1.0027 \cdot T_{raw} + 0.41 \qquad \text{(D.2)}$$

Using these curves the inlet temperature measurement accuracy improved from a mean error of +0.9°C using the raw DAQ output to -0.02°C using the calibration curve. The standard deviation was 0.4°C in both cases. Using the saturation temperature data the mean error in the outlet temperature measurement improved from -1.1°C to +0.02°C. The standard deviation of the error in both cases was 0.1°C. The standard deviation for the inlet temperature was slightly higher because there was only one series of data from which to draw an average calibration point for each calibrated temperature. Between 6 and 8 data points for each of the three saturation pressures were used for the outlet temperature calibration. Each calibration data point was generated from the mean values of a series of thousands of sampled pressure and outlet temperature points.

Calibrated Temperature (ºC)	Measured Temperature (ºC)
22.2	22.9 ±1.4
34.1	35.5 ±1.4
80.2	80.4 ±1.4
120.5	121.0±1.4
150.5	151.6±1.4
176.0	177.1±1.4
200.9	201.9±1.4
221.0	221.8±1.4

Table D.5: Inlet temperature calibration data.

Saturation Temperature (ºC)	Measured Temperature (ºC)
275.6	274.5±1.4
275.6	274.6±1.4
275.7	274.6±1.4
275.6	274.6±1.4
275.6	274.5±1.4
275.6	274.5±1.4
275.6	274.5±1.4
250.4	249.3±1.4
250.5	249.4±1.4
250.3	249.1±1.4
250.4	249.2±1.4
250.4	249.3±1.4
250.5	249.4±1.4
212.5	211.6±1.4
212.5	211.6±1.4
212.4	211.5±1.4
212.5	211.3±1.4
212.4	211.4±1.4
212.5	211.5±1.4
212.4	211.5±1.4

Table D.6: Saturation data used to 'calibrate' the outlet temperature thermocouple.

Calibrated	Measured Temperature (^{o}C) for TC installed at L_h			
Temperature (^{o}C)	1316 mm (a)	1316 mm (b)	1305 mm	1293 mm
219.9	220.1±1.4	220.0±1.4	220.0±1.4	218.3±1.4
210.2	210.6±1.4	210.4±1.4	210.4±1.4	209.0±1.4
191.2	191.7±1.4	191.7±1.4	191.4±1.4	190.9±1.4
169.2	169.8±1.4	169.8±1.4	169.6±1.4	169.3±1.4
150.0	150.8±1.4	150.8±1.4	150.6±1.4	150.3±1.4
130.1	130.8±1.4	130.7±1.4	130.6±1.4	130.3±1.4
120.1	120.8±1.4	120.7±1.4	120.6±1.4	120.3±1.4
110.1	110.6±1.4	110.6±1.4	110.5±1.4	110.2±1.4
100.1	100.5±1.4	100.5±1.4	100.3±1.4	100.1±1.4
90.0	90.3±1.4	90.3±1.4	90.1±1.4	89.9±1.4
80.4	80.6±1.4	80.6±1.4	80.4±1.4	80.2±1.4
70.3	70.5±1.4	70.4±1.4	70.3±1.4	70.1±1.4
60.2	60.4±1.4	60.4±1.4	60.2±1.4	60.0±1.4
50.1	50.3±1.4	50.2±1.4	50.1±1.4	49.9±1.4
39.0	39.1±1.4	39.0±1.4	38.9±1.4	38.7±1.4
31.1	31.0±1.4	31.0±1.4	30.9±1.4	30.7±1.4
21.1	20.9±1.4	20.8±1.4	20.8±1.4	20.7±1.4

Table D.7: Calibration data for wall temperature thermocouples (1).

| Calibrated | Measured Temperature (°C) for TC installed at L_h | | | |
Temperature (°C)	1276 mm	1229 mm	1113 mm	955 mm
219.9	219.9±1.4	219.9±1.4	219.6±1.4	219.9±1.4
210.2	210.2±1.4	210.2±1.4	210.0±1.4	210.2±1.4
191.2	191.3±1.4	191.3±1.4	191.1±1.4	191.3±1.4
169.2	169.4±1.4	169.4±1.4	169.3±1.4	169.4±1.4
150.0	150.4±1.4	150.4±1.4	150.3±1.4	150.4±1.4
130.1	130.4±1.4	130.4±1.4	130.3±1.4	130.4±1.4
120.1	120.4±1.4	120.4±1.4	120.3±1.4	120.4±1.4
110.1	110.3±1.4	110.3±1.4	110.2±1.4	110.3±1.4
100.1	100.2±1.4	100.2±1.4	100.1±1.4	100.1±1.4
90.0	90.0±1.4	90.0±1.4	89.9±1.4	89.9±1.4
80.4	80.3±1.4	80.3±1.4	80.2±1.4	80.2±1.4
70.3	70.2±1.4	70.2±1.4	70.1±1.4	70.1±1.4
60.2	60.1±1.4	60.1±1.4	60.1±1.4	60.0±1.4
50.1	50.0±1.4	50.0±1.4	49.9±1.4	49.9±1.4
39.0	38.8±1.4	38.8±1.4	38.8±1.4	38.7±1.4
31.1	30.8±1.4	30.8±1.4	30.7±1.4	30.7±1.4
21.1	20.8±1.4	20.8±1.4	20.7±1.4	20.7±1.4

Table D.8: Calibration data for wall temperature thermocouples (2).

D.4 Pump and Flow Meter

Manufacturer supplied calibration data for the pump and coriolis mass flow meter are given in Table D.9 and Figure D.1, respectively.

| Speed	Q	Discharge Head	Suction Head	Velocity Head	Motor Power	Pump Power
(RPM)	(USgpm)	(ft)	(ft)	(ft)	(hp)	(hp)
3560	4.9	263.6	1.27	0.0	10.32	8.41
3557	13.5	260.5	1.26	0.3	10.88	8.90
3550	35.7	253.5	1.22	2.1	12.30	10.12
3538	66.9	233.7	1.16	7.3	14.22	11.71
3530	89.1	213.5	1.08	12.9	15.59	12.82
3520	116.0	187.3	0.97	21.9	17.06	14.00

Table D.9: Pump calibration data supplied by the manufacturer.

AW Company Calibration Data

8809 Industrial Dr., Franksville, WI 53126 Ph: 262-884-9800 Fax: 262-884-9810 Email: aw@awcompany.com

Date	4/30/2010	**SoftwareVersion**	M 1.80 MD 1.
Mass Meter Type	ACM-1500	**Natural Freq Air (Hz):**	123.312
Meter Serial Number	01067420	**Natural Freq. H20 (Hz)**	112.956
Electronic Serial Number	co 8042	**Meter Variable:**	8.5855

```
ACM-300   100%  range  is  5Kg/min
ACM-600   100%  range  is  10Kg/min
ACM-1500  100%  range  is  25Kg/min
ACM-3000  100%  range  is  50Kg/min
```
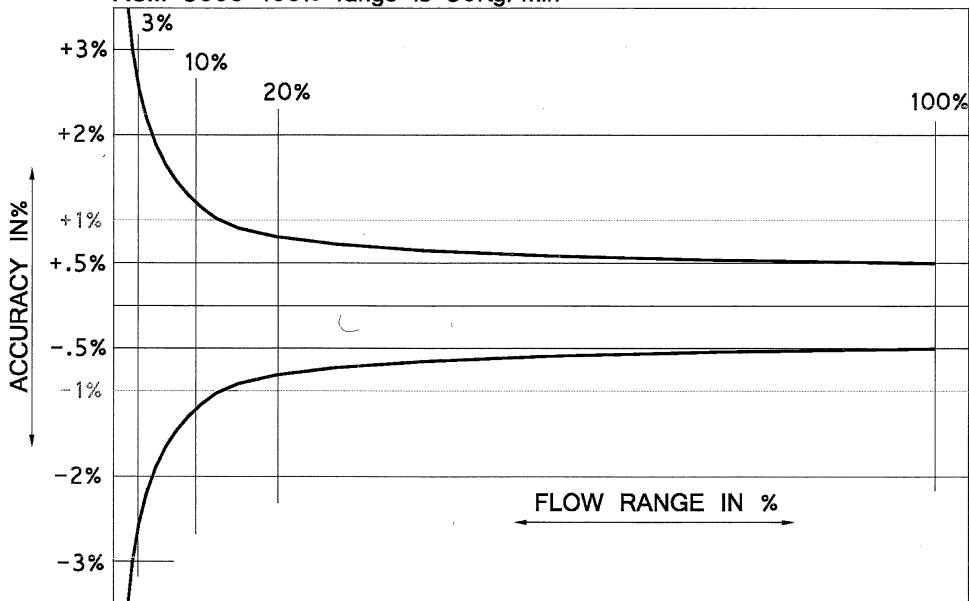

Friday, April 30, 2010

Figure D.1: Flow meter calibration certificate supplied by the manufacturer.

259

Appendix E

Bus Bar Conduction Effect on OID

The copper bus bars that were used to connect the power supply cables to the ends of the test section heated length had a high thermal mass. A steady 2-D radial conduction model was used to model their effect on thermocouple measurements near the end of the heated length. The `FiPy` transport equation solver from NIST was used to implement the model [11].

Heat generation in the test section was calculated by specifying a total applied current boundary condition. It was assumed that the voltage drop across each axial section was equal for all radial positions. Radial heat source distribution was calculated iteratively: each radial shell was treated as a parallel resistor with its resistance value calculated using its axially perpendicular area and the solution iteration's temperature-dependent resistivity value. The heat source–material properties–heat conduction solutions were iterated upon until steady-state was reached.

The model geometry was a 100 mm length of 4.572 mm ID by 6.35 mm OD Inconel 600 tube divided into 400 axial and 30 radial volumes of uniform dimensions. The heat capacity, density, and thermal conductivity data for Inconel 600 were taken from [116]. The electrical resistivity of Inconel 600 was obtained using the exponential fit from [127].

Adiabatic boundary conditions were specified on the outer radial and upstream axial faces of the model. The downstream face of the model was given a constant temperature boundary condition of 485.55 K, *i.e* the saturation temperature at 2 MPa, to model the effect of the bus bar. A convective boundary condition

with a constant heat transfer coefficient of 100 kW m^{-2} and a boundary temperature of 485.55 K was used on the inside radial face of the model. A constant current boundary condition of 603 A was used as the heat generation source term.

The results of the present model are shown in Figure E.1. The constant current boundary condition resulted in an inside surface heat flux of 1755 kW m^{-2}. T_w-T_∞ reaches 99% of its constant value at the upstream end of the modelled length 2.8 mm and 1.4 mm from the bus bar at the outside and inside walls respectively. The nearest thermocouple location to the bus bar at the end of the heated length is located 5 mm upstream in the present work. The results of the conduction model demonstrate that the bus bars will not affect the temperature measurements nor the detection of OID at the location of the thermocouple nearest the bus bars in the present work.
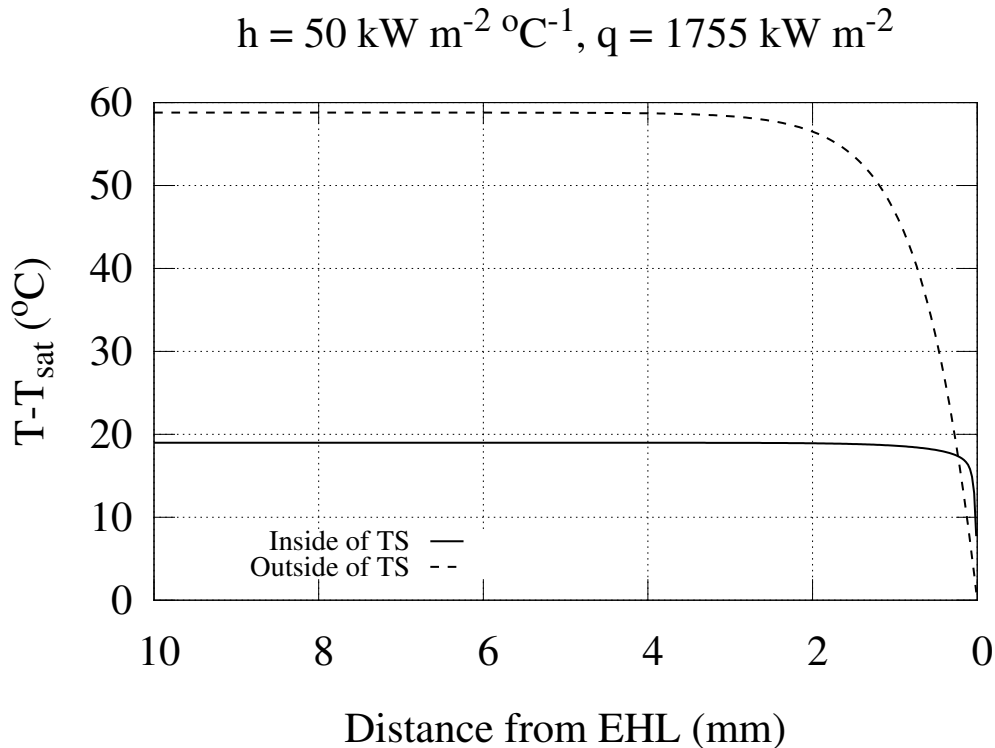
Figure E.1: Steady conduction model results for bus bar influence on OID.

Appendix F

Dryout Detection

F.1 Steady-State Dryout Detection

Steady dryout data were selected based on two criteria derived from the wall temperature measurement located nearest the end of the heated length. The point must lie on the region of the boiling curve where the wall temperature increases at a higher rate per increase in heat flux compared to data points at lower heat fluxes. Secondly the overall standard deviation of the wall temperature measurement for all samples must be greater than 0.35°C.

The wall temperature and standard deviation are plotted against the applied heat flux for one data series in Figure F.1. Data in this form from every steady-state series may be found in Section C.2.

These criteria were used for phenomenological and practical reasons. In general dryout, or CHF, is based on a condition where the rate of heat transfer begins to deteriorate in a way that cannot be predicted based on data collected under conditions away from the dryout point. This is the physical basis for the use of the change in boiling curve slope as a steady OID criteria. The term onset of intermittent dryout was coined by Groeneveld in 1986 [9] to describe the gradual deterioration in heat transfer observed in high-quality channels in contrast to the sudden heat transfer deterioration observed for subcooled channels. 'Intermittent' implies that the heated surface repeatedly dries out and rewets although this may occur at irregular intervals. This implies that there is a time-dependence on the surface heat transfer

262
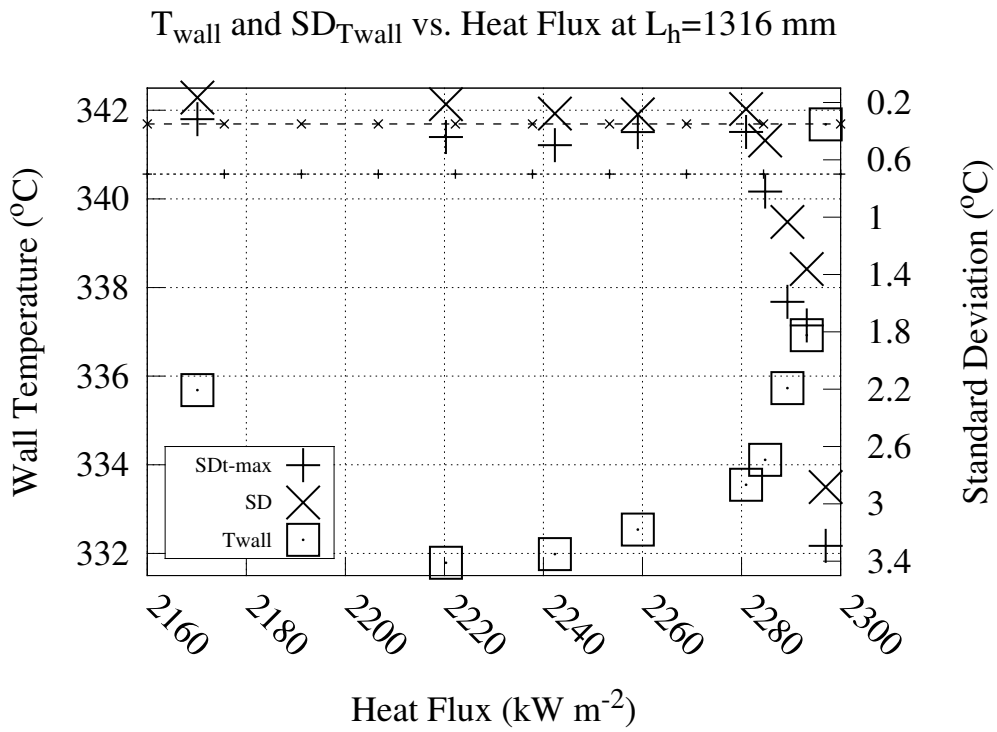
Figure F.1: Wall temperature and its standard deviation vs. Heat Flux.

and this is the physical basis for using the wall temperature standard deviation as a dryout criteria. This criteria has previously been used by, *e.g.*, Del Col and Bortolin who found that the standard deviation of the wall temperature roughly tripled at the onset of intermittent dryout in their fluid-heated microchannel [12].

Using two criteria to determine the onset of intermittent dryout improved the consistency of the data point selection. The conditions at OID vary with pressure and mass flux. Concomitantly the slope of the boiling curve will also vary with these parameters. This makes it difficult to derive a consistent OID criteria based on boiling curve slope alone. The wall temperature standard deviation varies within a very small range—approximately 0.1–0.3ºC—for the entire boiling curve until the region of heat transfer deterioration where it begins to increase strongly with increasing heat flux. The use of these two criteria gives both a quantitative basis— the standard deviation—and a qualitative phenomenological check—the change in boiling curve slope—that together ensure consistent selection criteria for steady OID data.

F.2 Transient Dryout Detection

A strong physical basis exists for the use of wall temperature standard deviation as an OID criteria for steady data. In order to adapt this criteria to transient situations the standard deviation must be calculated using samples collected over a limited period of time. The time window over which the standard deviation is calculated must be determined with care: increasing the time period increases the number of samples and therefore the accuracy of the estimate of the standard deviation. Increasing the number of samples simultaneously decreases the time-precision of the calculated standard deviation. Conversely decreasing the number of samples increases the time-precision of the calculated standard deviation but increases the likelihood of spurious values of standard deviation.

In other works on transient dryout, *e.g.* of Celata *et al* and Lyons and Swinnerton, the OID criteria were based on wall temperature alone. Lyons and Swinnerton based their time to dryout on the last time where the wall temperature time rate of change was zero or less that preceded an observed wall temperature of 400ºC

[3]. Lyons and Swinnertons' sample rate was 10 s^{-1}—more than an order of magnitude less than in the present work—and their test section wall was twice as thick as in the present work. Therefore their time-dependent thermocouple measurements were relatively more damped than in the present work. Celata *et al* marked the time where the wall temperature began to increase as the onset of dryout [83].

In the present work neither of these techniques was satisfactory. Fluctuations in the measured wall temperature between OID and the time the wall temperature reached 400ºC would result in the detection of dryout at intermediate times using Lyons and Swinnerton's method. To combat this a substiantial amount of data smoothing would be required and the intermittent nature of the OID would be lost. Celata *et al* were not specific as to what magnitude or rate of change of wall temperature constituted the "first indication" of a rise in wall temperature [83]. Based on the information from their publications it is likely that the time at which a temperature increase was registered as the dryout point was taken from a graphical data recorder. This could have been performed manually in the present work but it does not lend itself to a quantification. Therefore the problem of transient dryout detection has changed as data acquisition systems have become more powerful.
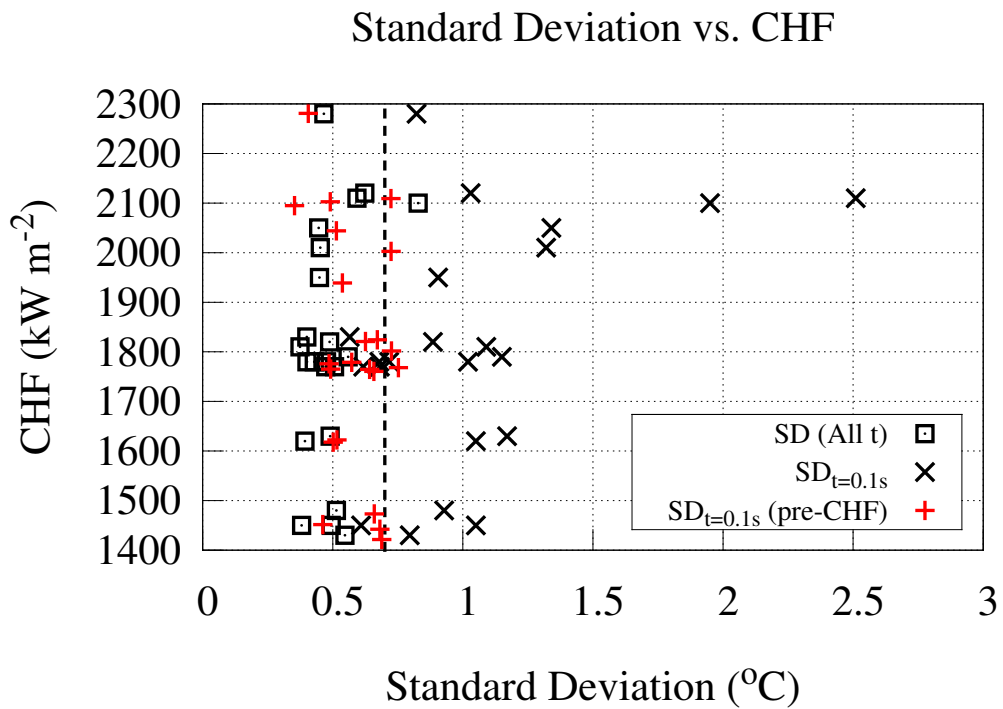
In the present work the maximum rate at which temperature data could be sampled was limited by the DAQ to 150 s^{-1}. A window of 0.1 s, or 15 samples, was chosen to calculate the time-dependent standard deviation with. This time window is slightly smaller but on the same order of magnitude of the time period of the temperature variations observed at OID. The characteristic time scale for thermal diffusion in the wall, L^2/α, was approximately 0.2 s using the test section wall thickness for the length scale. This type of temperature fluctuation can be seen in the example wall temperature transient data shown in Figures 5.1–5.3. Increasing the number of samples would yield a diminishing return in the accuracy of the standard deviation. The standard deviation is based on the sample mean and the uncertainty in the sample mean—assuming that the parent distribution is normal—nominally varies with the inverse square of the number of samples. Therefore the chosen window size would not benefit from being made larger and it was sufficiently short to capture the underlying physical fluctuations in wall temperature with good precision.

A threshold time-dependent standard deviation value of 0.7°C was chosen as the transient dryout criteria. This was based initially on inspecting the behaviour of the transient data—both the time-dependent standard deviation and the wall temperature. A value was chosen that was low enough to capture the obvious early stages of OID without being so small as to count spurious variations in wall temperature and detect OID obviously earlier than when it occurred. The selection of this value was confirmed by the steady state data. The maximum observed value of the time-dependent standard deviation calculated using the 0.1 s window for all sampled time is plotted in Figure F.1 and in Section C.2 for all steady-state data series. These values can be compared with the standard deviations calculated based on all sampled values from the recorded time. From these data it is evident that the maximum value of the time-dependent standard deviation is larger than the overall standard deviation as expected and that the maximum value of the time-fluctuating standard deviation behaves similarly to the overall standard deviation as OID is reached and exceeded.

Figure F.2 shows the overall and time-dependent maximum standard deviations for all dryout data plotted against the CHF value. In addition to the dryout data the time-dependent maximum standard deviations for the data collected at one heat flux-step below the OID points are also shown. The threshold value of 0.7°C is depicted as a vertical dashed line. 18 of the 23 pre-dryout data lie below—to the left—of the boundary line while 16 of the 23 dryout data lie to the right. The mean and standard deviation of the pre-CHF time-dependent standard deviations was 0.6±0.1°C and 1.0±0.4°C for the dryout data. This data suggests that the boundary value was appropriately chosen since, based on the fraction of data above and below the threshold value, roughly equal probabilities—within 10%—of counting a spurious fluctuation as OID, 5 of 23, as of late detection of OID, 7 of 23.

In practice the exact threshold value of the standard deviation used to indicate dryout is not of great importance. Once OID occurs, the standard deviation value varies quickly. This is shown in the bottom portion of Figure 5.5 where the wall temperature and standard deviation are plotted against time and the threshold value is plotted as a straight line. For the transient depicted in this figure the standard deviation value remains less than 0.4°C until rapid temperature fluctuations begin.

Once the wall temperature fluctuations began the standard deviation spiked to well over 1.5°C twice in the first 0.5 s. The evidence presented in this section supports the use of the method used to determine the experimental OID time in the present work.


Figure F.2: Time-maximum and overall σ_{Tw} for steady OID data and one preceding heat flux value.

Appendix G

Pneumatic Valve Opening Time

The valve opening and closing time was measured using a high speed video camera. A frame rate of 1000 frames per second was used to film the valve opening and closing 4 times each. Frames from the video that depict the opening and closing, respectively, are shown in Figures G.1 and G.2. The frames that corresponded to the initiation and termination of the actuation process were determined from the video for each of the four valve opening and closing sequences. The number of frames that passed between the beginning and end of each valve initiation process were counted as 0.001 s for each frame. The mean and standard deviation from the four sequences was 0.087 ± 0.008 s for the valve opening time and 0.16 ± 0.01 s for the valve closing time.

| 0 ms | 23 ms | 47 ms | 70 ms | 93 ms |
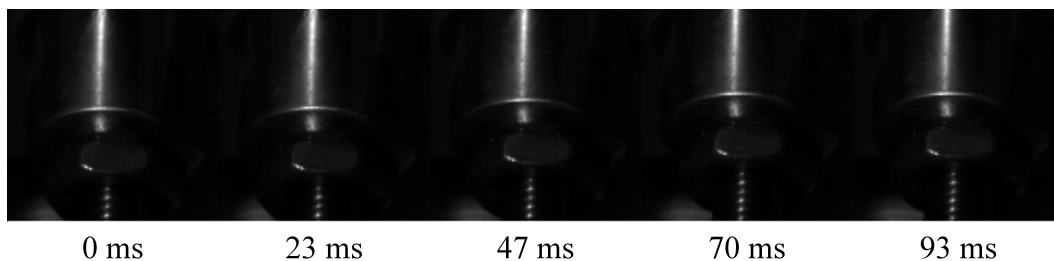
Figure G.1: Pneumatic valve opening.

0 ms   40 ms   80 ms   120 ms   160 ms
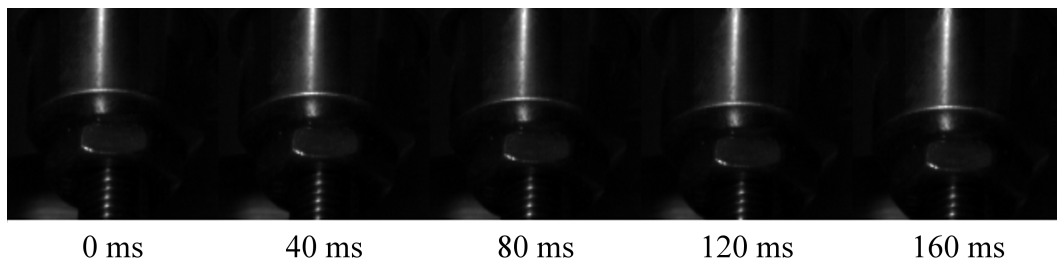
Figure G.2: Pneumatic valve closing.